UNIVERSITAT DE BARCELONA

Desenvolupament de models per nanopartícules de TiO_2 i ZnO en fotocatàlisis

Josep Oriol Lamiel Garcia

UNIVERSITAT DE BARCELONA

Desenvolupament de models per nanopartícules de TiO_2 i ZnO en fotocatàlisis

Josep Oriol Lamiel Garcia

Programa de doctorat de Química Teòrica i Computacional

Desenvolupament de models per nanopartícules de TiO_2 i ZnO en fotocatàlisis

Dirigida per:

Dr Francesc Illas Riera
(Universitat de Barcelona)

Dr Stefan T. Bromley
(Universitat de Barcelona Institució Catalana de Recerca i Estudis Avançats)

Tutor:

Dr Francesc Illas Riera

(Universitat de Barcelona)

UNIVERSITAT DE BARCELONA

UNIVERSITAT DE BARCELONA

FACULTAT DE QUÍMICA

DEPARTAMENT DE CIÈNCIA DE MATERIALS I QUÍMICA FÍSICA

INSTITUT DE QUÍMICA TEÒRICA I COMPUTACIONAL

Desenvolupament de models per nanopartícules de TiO_2 i ZnO en fotocatàlisis

Josep Oriol Lamiel Garcia

2017

UNIVERSITAT DE BARCELONA

Institut de Química Teòrica i Computacional
UNIVERSITAT DE BARCELONA

A tots vosaltres

The work done in this doctoral thesis has been carried out at the Material Science and Physical Chemistry Department of the Chemistry Faculty of the University of Barcelona (UB), and within the Institut of Theoretical and Computational Chemistry (IQTCUB) and the Reference Network of Theoretical and Computational Chemistry of Catalunya (XRQTC).

This project has been possible in virtue of the financial support provided by the "Ajut de personal investigador predoctoral en formació per a alumnes de tercer cicle de la universitat de Barcelona (APIF), from Spanish Ministerio de Ciencia e Innovación MINECO/FEDER grant CTQ2015-64618-R grant and, in part, by Generalitat de Catalunya grants 2014SGR97, XRQTC is acknowledged. Also the European Union's Horizon 2020 research and innovation programme under grant agreement No 676580). The access to supercomputer resources was provided through grants from the Red Española de Supercomputación (RES) and the COMPHOTOCAT project 2014112608 of the Partnership for Advanced Computing in Europe (PRACE).

Agraïments

M'agradaria començar donant les gracies especialment als meus directors de tesis Francesc i Stefan. Primer de tot per confiar en mi per a dur a terme el treball presentat en aquesta tesis. També per tot el suport que m'han donat durant aquests anys, durant el màster i el doctorat, tant en temes acadèmics com personals, sempre he pogut contar amb el seu ajut i suport. Primerament vaig conèixer al Francesc en una de les últimes assignatures de la llicenciatura de Química i, entre d'altres coses relacionades amb la Fisicoquímica de superfícies, em va ensenyar que a la facultat també hi havien grups de recerca teòrics; que no necessàriament tota la química es fa al laboratori i que els treballs teòrics i computacionals com els que s'han realitzat en aquesta tesis poden aportar molt a la ciència. Em va informar de la recerca que es realitza als grups teòrics de la universitat i de l'existència del màster de química teòrica i computacional i l'opció de cursar aquest màster i posteriorment el doctorat al seu grup. D'aquesta manera vaig conèixer també a l'Stefan que ha estat el meu director de màster i codirector de doctorat i va ser qui em va iniciar en l'estudi computacional de nanopartícules durant el meu màster i amb qui ha sigut un plaer parlar de ciència i de qualsevol tema en general. A tots dos, uns grans professionals i grans persones, els vull agrair tot el que han fet per mi durant aquests anys. La confiança que han demostrat en mi en tot moment i per suposat també tot el que he après d'ells (que es molt, però també em queda molt per aprendre). Moltes gracies per tot.

Seguint amb l'entorn universitari també vull agrair especialment el suport de tots els companys de despatx, grup i departament que han estat sempre que els he necessitat i amb qui he compartit moltes hores de feina i fora de la feina. Francis, quasi codirector de tesi, company i amic de qui també he aprés molta ciència i metodologies de treball. De mateixa manera vull agrair a Sergio Tosoni, Rosendo i Angel, els postdocs que treballen o han treballat al grup i amb qui he col·laborat, de qui he aprés i també m'han donat grans consells durant el temps que hem treballat junts i de qui m'emporto també un gran record. Gracies també a tots els companys que han passat per el despatx durant aquest temps: Sergi, Gian, KC, Cho, Sun, Almudena, Noelia, Anderson, Politi, Juanjo i Lorena; gracies per totes les hores compartides discutint ciència i altres temes i també per la paciència que heu tingut. No dins el despatx però igualment propers; gracies també als companys de departament Alberto, Julia, Sonia, Cristina, Raúl, Andy,Toni, Arnau, Melchor, Anna, Albert, Sergey i molts altres professors del departament companys i de màster i doctorat; amb vosaltres també he compartit moltes moments durant el transcurs d'aquesta tesis i os agraeixo moltíssim el vostre suport tot aquest temps i ajut.

Ja fora de l'àrea de treball. També dedico aquesta tesis a bons amics de fora de l'ambient acadèmic. Amb qui he passat hores de lleure i moments importants durant aquesta tesis; Judit, Miguel, Lara, Marc, Ivan, Carlos, Juan Carlos, Magda, Melania, Pedro, Anna, i molts altres a qui demano disculpes per no mencionar-los. Durant

aquests anys de tesis també m'heu ajudat molt, heu sigut un gran suport i especialment comprensius quan he estat ocupat escrivint.

També voldria dedicar aquest treball als companys de l'agrupació fotogràfica de Gavà amb qui he passat grans estones i de qui he aprés molt.

Òbviament també vull agrair molt especialment a la meva família. Primerament gracies als meus pares Josep i Anna, no nomes per el suport durant el transcurs de tesis, si no per fer possible que arribés a ferla, per criar-me i educar-me, per la confiança mostrada sempre, el suport en els bons i mals moments, per tots aquests anys. En definitiva, per donar-me la vida. Moltes gracies. També vull dedicar especialment aquest treball als meus avis Teresa, Daniel, Delia, Ismael. Aquesta tesis també es gracies a vosaltres. Daniel, Luis i Mayte gracies a per tot el vostre suport. Os estimo família.

En resum, aquest treball ha estat possible gracies a tots vosaltres, a tots els que heu estat durant tot el procés, en una part,o abans. Gracies per ajudar-me a arribar fins aquí.

Every so often, you have to unlearn

what you thought you already knew,

and replace it by something more subtle.

Terry Pratchett (1948-2015)

Chapter 1:

Introduction

1.1. Overview

The research presented in this thesis is aimed at studying the electronic structure, energetic stability and intrinsic photocatalytic properties of the semiconductors TiO_2 and ZnO. These studies have been performed using theoretical and computational models and in some cases complemented with experimental work from collaborators.

Before describing the work done during this thesis we will start with a brief summary of the most relevant historical discoveries up to the present day. The origin of the interest in TiO_2 and ZnO as possible photocatalysts started in the sixties where several research groups studying photo-induced processes in solids (TiO_2 and ZnO for example) found that certain molecules like H_2O and O_2 were adsorbed and desorbed from the surface of these semiconductors. This phenomena was explained years later by the d-band theory.[1–3] Soon after these observations S. Kato and F. Masuo reported the first photocatalyzed reaction by TiO_2; the oxidation of tetralin in liquid phase irradiated with UV light.[4] This result triggered the interest of the scientific community towards TiO_2 in this field whereby different gas phase reactions based on TiO_2 irradiated with UV light were reported.[5–8] Fujishima and Honda were the first to report the photocatalytic decomposition of water by using a TiO_2 electrode and under UV radiation. This publication showed how the bias voltage needed to perform the electrolysis was considerably lower compared with normal electrolysis.[9] In 1977 Scrauzer and Guth reported the photocatalytic decomposition of H_2O on powdered TiO_2 photocatalysts with small amounts of Pt or Rh metal particles[10]. The photo-induced electrons in TiO_2 move to the Pt metal site where they promote reduction reactions, while photo-induced holes remain in the TiO_2 particle and migrate to its surface where they promote oxidation reactions.[11,12]

At this point the importance of the electron-hole separation in photocatalytic processes arose. These works by Honda/Fujishima and Schrauzer/Guth led to an intense research effort to design photocatalytic systems able to exhibit a high conversion efficiency of light into chemical energy. The decomposition of H_2O into H_2 and O_2, and some other reactions like decomposition of pollutant compounds, motivated this work,

Some research groups have focused on colloidal semiconductors,[13] small nanoparticles which display quantum confinement effects, as well as on semiconductors incorporated on inert supports such as porous glass and zeolites. Various binary oxide catalysts have also been shown to be promising photocatalysts.[14–19]

Before continuing is important to briefly review the known basis of photocatalysis in order to understand the results presented in this work. The photocatalytic processes consists of the absorption of solar radiation by a semiconductor material therefore the electrons that occupy the higher levels of the valence band are promoted to the lower levels of the conduction band. This generates electrons in the conduction band and holes in the valence band that can either recombine again after certain time, or react separately with molecules adsorbed on the surface of the material reducing and oxidizing them respectively; this is summarized in Figure 1.

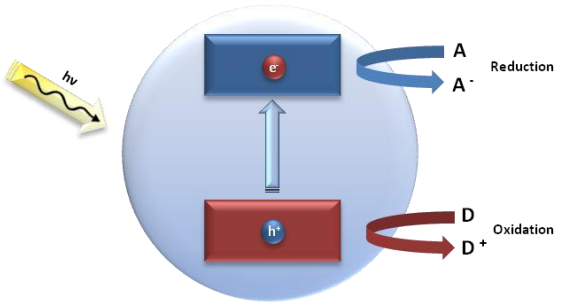

Figure 1 Diagram summarizing the photocatalytic processes. The blue circle represents the photocatalyzer. The red rectangle represents the valence band, blue rectangle represents the conduction band. The yellow arrow represents the radiation of a certain wavelength adsorbed by the material.

Knowing this, one of the most crucial point that affects the efficiency of photocatalysts is the capability of absorbing the most amount of light to promote as many electrons as possible in order to be able to reduce and oxidize more of the adsorbed molecules. The amount of light that can be absorbed is directly related to the energy difference between the valence band and the conduction band of the material. This energy, to promote the electrons between VB and CB, is provided by solar radiation. Therefore the band gap of the material determines the wavelength of the radiation that can be absorbed and subsequently is able to produce the electron promotion and the electron-hole separation needed for catalyzing the redox reactions.

The band gap of titanium dioxide and zinc oxide are both near 3 eV. This amount of energy corresponds to a wavelength that belongs to the UV region. This is in agreement with the fact that the photoactivity of these materials reported in the literature is always

under UV radiation. That is why one of the main objectives of the research in this field is to modify these materials to reduce their band gaps and subsequently shift the radiation absorption from the UV spectra to the visible region.

Another important factor that can lead to an increase in the photoactivity is the type of surfaces exposed by the photocatalyst. It is well known that for anatase TiO_2, for example, most of the synthesized nanoparticles tend to expose mainly the [101] surface which is the most thermodynamically stable for this polymorph. However, the next most stable [001] surface shows a much higher reactivity and subsequently a better efficiency in the photocatalytic processes. It would thus be desirable to understand which factors affect to the stability of the different surfaces and to find a way to modify these factors in order to increase the ratio of [001] surface in such nanoparticles. In this work we performed several studies on how the stability of the surfaces in anatase TiO_2 can be influenced to modify this ratio.

Over the last few years another factor has been shown to be also of great importance for photocatalysis is the recombination effect of the electrons and holes generated by light absorption. As mentioned previously the excitation of electrons from the valence band to the conduction band is a process that creates electron-hole pairs. These excited species can react separately oxidizing and reducing the compounds adsorbed on the nanoparticle (which is the desired process for photocatalysis) or on the other hand can rapidly recombine losing the capability to perform such reactions. The way to avoid this recombination is yet not clear, but it is known that is related with the mobility of electrons and holes in the system and that it depends on the electronic structure of system.

The objective of this thesis is to perform theoretical studies and *ab initio* calculations focused on finding the intrinsic properties that cause the previously mentioned drawbacks of these materials as high efficient photocatalizers. In this way it is hoped that the work herein may assist in overcoming these drawbacks and help improve the efficiency of photocatalysts designed in the future.

In this chapter we will present an overview of TiO_2 and ZnO with special interest on their properties applied to photocatalytic processes.

The results obtained are presented in four blocks, the organization of these blocks include the published articles on the respective topics and do not always follow a chronological ordering. The different publications have been ordered accordingly to their topic: (i) TiO_2 bulk studies, (ii) effect of fluorine on the photocatalytic activity of TiO_2, (iii) TiO_2 clusters and nanoparticles, and (iv) results for ZnO. This ordering has been chose to clarify the connection between the different works and topics inside the thesis.

Titanium dioxide (TiO_2), also known as Titania, is a white colored semiconductor material, as most of the transition metal oxides. It has been widely used for a long time as white pigment in paints, paper and cosmetics, and also as colorant in the food industry and has many other applications. This thesis, however, has been mainly motivated by the photocatalytic potential of TiO_2.

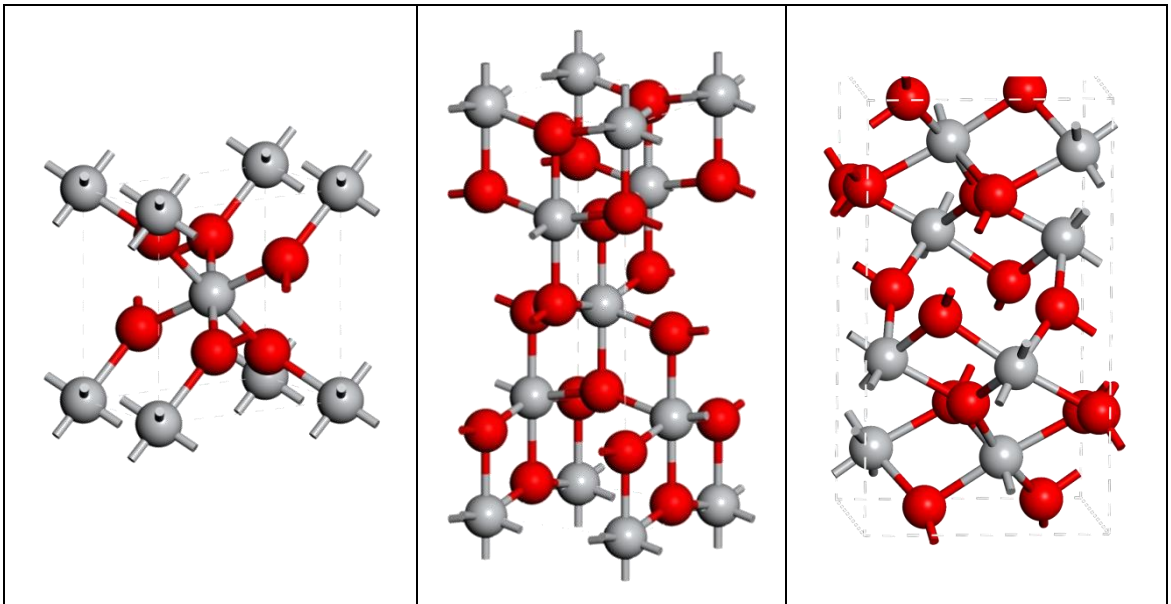

Rutile	Anatase	Brookite

Figure 2. Most stable Crystal structures for titanium dioxide (TiO_2)

The three most common polymorphs of TiO_2 are Rutile, Anatase and Brookite (see Fig. 2).Additionally,TiO_2 has a number of high pressure forms including a monoclinic baddeleyite-like form,11% more dense than Rutile, and an orthorhombicα-PbO_2-like form. These last two forms will not be considered in this work due to the extreme

conditions needed for their synthesized. The different solid phases presented by TiO_2 depend on the crystalline structure of the system. In the case of Rutile and Anatase they present a tetragonal cell and for Brookite an orthorhombic cell. In all three cases the titanium atoms are coordinated to six oxygen species in an octahedron. The oxygen atoms are bonded to three Ti species with a planar coordination environment. Rutile is the most thermodynamically stable bulk polymorph. Anatase and Brookite are metastable phases, but stable until high temperatures (~600-800 ºC). However, Anatase is most stable at nanometric sizes and its unique photocatalytic properties in this size range are the reasons to study these TiO_2 polymorphs at both the bulk scale and the nanoscale.

Another material studied in this thesis because of its promising photocatalytic activity is zinc oxide (ZnO). This material is also a metal oxide semiconductor but its most stable crystal structure is wurtzite (see Figure 3). ZnO has also been predicted to have a rich low energy polymorphism[20] although most of these polymorphs are yet to be experimentally stabilized. We highlight two particularly well-studied low energy polymorphs: the body centered tetragonal (BCT) structure and sodalite (SOD), which were also studied in the present work.

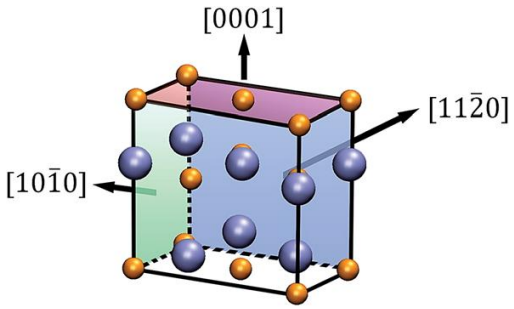

Figure 3: Orthorhombic unit cell of wurtzite ZnO on the showing the preferential surface orientations.

The appearance wurtzite ZnO is a white solid; often used in industry as additive in plastics, rubber, ceramics, glass and in other wide range of products, often, as it happens, together with TiO_2. Apart from these industrial applications, the interesting optical and electronic properties of ZnO make this material very useful for other technological applications such as protective devices in electric circuits (namely varistors), semiconductors, field-effect transistors, photodetectors, blue- and UV light emitting and laser diodes, gas sensors, piezoelectric generators, transparent electrodes, and directly related with its photocatalytic properties, cells for solar light harvesting.[21–29]

For both TiO_2 and ZnO, their applications are directly related to their electronic structures. One of the most representative parameters related with the electronic

structure of a semiconductor is its band gap. In the case of TiO_2 the gap is between 3 and 3,2 eV depending on the polymorph and for zinc oxide the gaps is ~3,3 eV which is clearly close to that of TiO_2. For this reason and taking into account its high electron mobility, ZnO constitutes a promising candidate to become an efficient photocatalyst, although so far it does not outperform TiO_2.

Even with the intense interest in these materials and the processes that are able to photocatalyze, the complete mechanisms of the photocatalytic processes such as water splitting, are unknown. Also the key properties and features that make these materials able to perform such reactions efficiently are not at all clear. Here is where computational chemistry becomes a powerful tool to shed some light and knowledge on the electronic structure of these materials. Such an approach provides the possibility to analyze in more detail features where experiments cannot. For example we can begin to probe a range of important questions such as: Why certain nanoparticles are more active than others? Which are the most important features that make a catalyst effective? How can these materials be tuned to improve their efficiency? How the different modifications on the material modify its properties? Which are the intrinsic features of the nanoparticles that make them to have different activity that the bulk?

A large number of theoretical works have been carried out in recent years but have mostly employed periodic models. Taking advantage of crystal symmetry means that relatively small unit cells can be used in such modelling making such an approach relatively computationally efficient. However, such modelling thus assumes perfect infinite symmetry and is thus not so realistic for nanoparticles. Fortunately, in the past few years the power of the computers and codes has increased exponentially and nowadays sophisticated methods can be applied to more realistic systems. The idea behind this thesis is that a combination of periodic modelling and large scale explicit modelling of nanoparticles can be extremely helpful in clarifying some of the important issues regarding the electronic properties of (nano)TiO_2 and (nano)ZnO.

In the present work we apply computational modelling to study TiO_2 and ZnO as they are good representative of the most promising photocatalysts. We have studied the energetic stability and electronic structure of different systems, going from extended

periodic systems (e.g. bulk structures and their most stable surfaces), nanoparticles with sizes similar to the ones used in experiments, and smaller nanoclusters with a few atoms. All these studies have been performed in order to reach an accurate description of these systems and also a global vision of the properties of these materials and their evolution with their size. These studies highlight the intrinsic electronic structure based properties of titanium dioxide and zinc oxide that make them unique for photocatalytic applications. The work in this thesis will also be useful to predict properties and specific behavior of these materials depending on their phase, geometry, size, or composition and also give some hints on how they can be modified to enhance their properties and be able to produce more efficient photocatalyst based on TiO_2 and ZnO.

As it has been pointed previously the main goal of this thesis is to describe in a comprehensive way the most important properties of TiO_2 regarding photocatalysis. Titania has been shown to be a very promising material in this field. Probably what greatly has increased the interest in these materials and opened them up towards green chemistry, was the discovery of the capability of TiO_2 to catalyze certain reactions of great interest not only for the scientific community but for the whole society. It has been proven that, under certain conditions, TiO_2 is able to catalyze several redox reactions. For example, one of the most important and that in great part motivated this work, the water splitting reaction. This reaction consists on the production of H_2 and O_2 from water using UV light as the only external energy. The thermodynamics of this reaction shows that in normal conditions this redox reaction is non spontaneous and needs 475 kJ/mol to occur.

$$H_2O + 2h^+ \rightarrow 2H^+ + \frac{1}{2}O_2 \qquad E^o_{ox} = -1.23V$$

$$2H^+ + 2e^- \rightarrow H_2 \qquad E^o_{red} = 0.00V$$

$$H_2O \rightarrow H_2 + \frac{1}{2}O_2$$

The use of UV radiation opens the possibility to provide this energy from sunlight. This is an extremely interesting way to obtain energy since H_2 is then produced in a clean way, without harmful effects on the environment. This makes H_2 a serious candidate to replace fossil fuels in the near future taking advantage of the energy of the solar

radiation to produce energy only using water as a reactant. However, the amount of UV radiation from sunlight arriving at the surface of the earth is very limited with respect to its spectral range, and modification of materials is needed so that their bang gap is reduced, shifting the radiation adsorbed by the photocatalyst to the more plentiful visible spectrum of light.

Finally we note that water splitting is only a part of the full potential of photocatalysis. Photoactive materials such as TiO_2 and ZnO also present interesting applications in other fields due to their unique photocatalytic properties. Some examples are the photocatalytic cleaning effect of TiO_2 coated materials[30]and their photocatalytic anti-bacterial properties[31]

Chapter 2:

Theoretical background

2.Theoretical background

In this section we will summarize the theory behind the methodology used to carry out these studies. We start from the basics of quantum mechanics with the Schrödinger equation and how it is applied to Hartree-Fock method. We further continue with density functional theory (DFT), the different basis sets that can be used in these computational approaches and several models and techniques applied during this thesis.

2.1 Schrödinger equation.

The Schrödinger equation[32] is the basis of quantum mechanics, it was developed in 1926 by the physicist Erwin Schrödinger, this equation is one of the most important equations of physics and is as important as the Maxwell equations for electromagnetism or the equations of motion from Newton for macroscopic systems. The main aim of first principle calculations is to describe the electronic structure of the molecules and systems under study. This is where the Schrödinger equation needs to be used. For static systems, which are the cases studied in this work, the non-relativistic time independent Schrödinger equation appropriately describes the electronic structure of the system.

The Schrödinger equation establishes that the only possible values of the energy of a system (E_n) are eigenvalues of the Hamiltonian operators $\hat{H}$ with the eigenfunctions Ψ_n representing stationary quantum states of the system.

$$\hat{H}\Psi_n = E_n\Psi_n$$

Where $\hat{H}$ includes the kinetic operator for electrons and the nuclei, and a potential for electrons and atoms.

$$\hat{H}(r, R) = \hat{T}(\dot{r}) + \hat{T}(\dot{R}) + \hat{V}(r) + \hat{V}(R) + \hat{V}(r, R)$$

This operator, known as Hamiltonian includes; the kinetic energy for both, electrons and nuclei of the system, which are the first two terms respectively, the third term is the attractive interaction between electrons and nuclei, the fourth and fifth terms are the repulsive contributions to the energy as the electron-electron repulsion and the last term the nuclei-nuclei repulsion. The Hamiltonian takes the form.

$$\widehat{H} = -\sum_{i=1}^{N}\frac{1}{2}\nabla_i - \sum_{A=1}^{M}\frac{1}{2m_A}\nabla_A^2 - \sum_{i=1}^{N}\sum_{A=1}^{M}\frac{Z_A}{r_{i,A}} + \sum_{i=1}^{N}\sum_{j=1}^{N}\frac{1}{r_{i,j}} + \sum_{A=1}^{M}\sum_{B=A}^{M}\frac{Z_A \cdot Z_B}{R_{A,B}}$$

Where M_A is referred to the mass of the nucleus, Z_A is the atomic number for the nucleus A, r_{iA} is the distance between the electron (i) and nuclei (A), r_{ij} is the distance between electron(i) and electron(j) and R_{AB} is the distance between nucleus (A and B). ∇_i and ∇^2 are the Laplacian operators that correspond to the differentiation with respect the position of the electron i in the first term, and with respect to the nuclei A for the second term.

To solve this equation is not trivial, in fact it's impossible to find the exact solution for systems with more than one electron. Therefore quantum chemistry uses some approximations that make it possible to solve the equation with reliable results.

2.2 Hartree-Fock method

As was pointed in the previous section the electron-electron interaction cannot be described exactly for systems with more than one electron, for that reason an approximation needs to be used to achieve the resolution of the Schrödinger equation in order to get reliable results of energy and other properties. In the Hartree-Fock (HF) method[32] the interaction between electrons in the Hamiltonian of the Schrödinger equation is treated as the potential that a single electron feels with respect to an average of all the other electrons in the system. It's in that way how we can get accurate results for systems with more than one electron.

In the Hartree-Fock (HF) method the wavefunction that describes the system is represented as a combination of approximated wavefunctions $\Psi = \prod_{i=1}^{N}\psi_i$. The first attempt to construct this wavefunction was the Hartree product. Latterly, in order to account for Pauli principle Slater determinants were used. This form ensures that the wavefunction is antisymmetric as defined by Pauli's principle for fermions. The assumption that the system can be described by a single Slater determinant implies the mean field approximation, which replaces the many-particle problem with a one-particle problem in an approximate field representing the rest of the electrons. In turn this leads to an overestimation of the electron repulsion. This approximation is the main source of errors of the method, since it does not take into account the so-called electronic correlation. The HF method is based on the variational principle, where the energy of

the system is minimized with respect to the orbitals. This procedure needs to be carried out iteratively and the solution depends on the orbitals. The final approach to solve it is called Self Consistent Field method (SCF). However, the energy thus obtained is always an upper limit to the exact energy of the system due to the lack of correlation and is given by:

$$E^{HF} = 2\sum_{i} h_{ii} + \sum_{i}\sum_{j}(2J_{ij} - K_{ij})$$

where ,h_i, J_{ij} and K_{ij} are respectively, matrix elements of the one-electron Hamiltonian, the Coulomb terms accounting for electron repulsion and the exchange terms which are a consequence of the antisymmetric principle of quantum mechanics.

One of the main goals of quantum chemistry is to solve the problems related to the lack of correlation in the HF method. There are several post-HF methods that try to include the correlation in the calculations. The most important and well known are Moller-Plesset (MP), the configuration interaction (CI), and coupled cluster (CC). As these methods are not applied in this study we will just mention them briefly.

The first approach to improve the HF results is the Moller-Plesset method (MP) which solves the Schrödinger equation using a perturbation operator and not the variational method commented before. The configuration interaction method (CI) solves the problem of the electron correlation by taking into account not only one Slater determinant but a linear combination of different Slater determinants corresponding to different electronic configurations, not only the ground state.

$$\Psi_{CI} = c_0\Psi + \sum_{i}^{a} c_i^a \Psi_i^a + \sum_{ij}^{ab} c_{ij}^{ab} \Psi_{ij}^{ab} + \sum_{ijk}^{abc} c_{ijk}^{abc} \Psi_{ijk}^{abc} + \cdots$$

In this method if we include in the expansion all the possible electronic configurations the result will be “exact” for a given basis set. If this basis would be infinite then we would obtain the exact non relativistic result for the energy of our system. This method makes great improvements on the results obtained by the HF method, but the main drawback of the method is its computational cost which is much more expensive than HF. It is important to point out that this method may also lead to size-consistency

problems besides the mentioned computational cost when millions of configurations need to be included.

The Coupled Cluster method is very similar to the CI method mentioned previously but solves the problem of the size consistency. In this case the method is based on an exponential expansion of the wave function and a non-variational methodology for solving the equation. The cluster operators (T) that represent the possible excitations of our system are similar to the results of the CI method:

$$|\Psi_{cc}\rangle = e^{\hat{T}}|\Phi_{HF}\rangle$$

$$\hat{T} = \sum_{i}^{N} \hat{T}_i$$

$$\hat{T}_1\Psi = \sum_{i}^{a} c_i^a \Psi_i^a$$

$$\hat{T}_2\Psi = \sum_{i}^{a}\sum_{i}^{b} c_{ij}^{ab} \Psi_{ij}^{ab}$$

…

where the coefficients need to be found.

2.3 Density Functional Theory

Another different approach to the problems of solving the Schrödinger equation isDFT[33,34]. The origin of this theory is the statistical model established by Thomas and Fermi for the electron gas model[35,36]. This model expressed the energy of a system constituted by electrons uniformly distributed under the influence of a nuclear field as a function of electron density only.

The density functional theory is an alternative to wavefunction based methods, this methodology although approximate, gives quite accurate results for the exchange and correlation energies in a more simplified way compared to post-HF methods and subsequently requires less computational cost.

The basis of the DFT method is that the energy of the ground state of a poly-electronic system depends on the density only. Although the energy of a system with N electrons depends on a wavefunction that also depends on 3N coordinates (4 including the spin), in DFT the energy depend on only the 3 coordinates of the electronic density, independently of the size of the system. This is very useful when studying large systems that would have a huge number of variables to treat in a HF or post-HF calculation. The density function could be explained as the probability to find an electron in a certain volume. This function has to satisfy a number of conditions such as: (i) the integral of the density function over the whole space should to be equal to the number of electrons in the system, (ii) the value of the function at an infinite distance should be equal to zero. In short,

$$E_0 = E_0[\rho]$$

$$\rho(r) = N \int \dots \int |\Psi(x_1, x_2, \dots x_n)|^2 dx_1, dx_2 \dots dx_N$$

$$\int \rho(r)\, dr = N$$

$$\rho\left(r \to \infty\right) = 0$$

DFT was not broadly used until Hohenberg and Kohn formulated their two fundamental theorems which are the base of modern DFT formalisms. Its computational implementation was accomplished by Kohn-Sham a year later.

2.3.1 Hohenberg-Kohn Theorem first theorem

The first Hohenberg-Kohn theorem[37] also known as existence and unicity theorem, establishes that the electronic density of the ground state $\rho_0(r)$cannot arise from two different external potentials $V_{ext}(r)$, except in the case that the difference between both is only a constant. This proves that any observable correspondent to a stationary non-degenerate ground state (including the energy) is exactly determined by $\rho_0(r)$ and can be writen as a functional of the electronic density function. For the energy one has:

$$E_0 = E_0[\rho(r)]$$

In other words, the electron density becomes determined by the external potential (potential produced by the nuclei) and the inverse relation (V-representability).

$$V_{ext}(r) \rightarrow \rho(r)$$

Each external potential builds a different Hamiltonian with two fundamental functions also different.

$$\widehat{H} = H_0 + V_{ext} \qquad \widehat{H}\Psi = E_0\Psi$$

$$\widehat{H}' = H_0 + V'_{ext} \qquad \widehat{H}'\Psi' = E_0'\Psi'$$

The first Hohenberg-Kohn theorem is only valid for non-degenerate ground states and always when $\rho(r)$ is N-representable and V-representable[37]. For thesecases

$$E_v[\rho] = T[\rho] + \int V_{ext}(\vec{r})\delta\vec{r} + F_{HK}[\rho]$$

Where $E_v[\rho]$ indicates that, for a specific external potential,$V_{ext}(r)$, the energy is a functional of the density.

2.3.2 Hohenberg-Kohn Theorem second theorem

The second theorem of Hohenberg-Kohn[37] or variational principle, says that the energy in a non-degenerate ground state can be obtained by the variational method and that the electronic density that minimizes the total energy is the exact electronic density of that state and therefore defines correctly the external potential.

$$E_0 \leq E[\rho]$$

Except if we have ρ_0 in that case we obtain the exact energy of the ground state. The interest is to find the electronic density functional. This functional can be divided in two parts, one that includes the interaction between the electronic density and the external potential, and another one contribution $F[\rho]$

$$E[\rho_r] = \int \rho(r)V_{ext}(r)\delta r + F[\rho(r)]$$

Where $F[\rho]$ is a universal functional that depends on the electronic component of the system and includes a part corresponding to electrons $T[\rho]$ and another part $V_{ee}[\rho]$ that includes the Coulomb repulsion and the energies of exchange and correlation.

$$F[\rho(r)] = T[\rho] + V_{ee}[\rho]$$

2.3.3 Kohn-Sham method

The last step on the development of the DFT methodology was the formalism of Kohn-Sham[33,34], mentioned previously. These authors pointed that in a poly-electronic system described by a density,$\rho(r)$ could be substituted by another system of non interacting electrons with the same density $\rho(r)$ that can be expressed as the sum of the squares of the N mono-electronic spin-orbitals, known as Kohn-Sham orbitals.

$$\rho(r) = \rho_{ks}(r) = \sum_{i=1}^{N} |\Phi(r)|^2$$

For this system of non-interacting electrons, the kinetic energy of the electrons is described by the following expression.

$$T_s[\rho] = \sum_{i=1}^{N} \langle \Phi_i | \frac{-1}{2} \nabla^2 | \langle \Phi_i \rangle$$

The energy of the real system can be expressed as functional of the density of the non-interacting system, and the energy of the fundamental system E_0, can be determined by minimizing the following expression:

$$E[\rho(r)] = T_s[\rho(r)] + \int \rho(r)\, V_{ext}(r) dr + \frac{1}{2} \frac{\int \rho(r)\, \rho(r')}{r - r'} dr dr' + E_{xc}[\rho(r)]$$

$$E = T_s + E_{ext} + J + E_{ex}$$

The first term,T_s, corresponds to the kinetic energy of the electrons, E_{ext} refers to the attractive external potential within the electronic density. The third term J represents the Coulombic repulsion between electrons. The last term,E_{ex},is the most hard to handle and represents the difference between the kinetic energy of the real system and the non-interacting electron system. This term also includes the correlation and exchange contributions. This last part is not an exact functional and there are many different

E_{ex} functionals which try to represent as accurately as they can, interactions mentioned which do not have an exact density dependent expression.

$$E_{xc}[\rho(r)] = T[\rho] - T_s[\rho] + V_{ee}[\rho] - J[\rho]$$

$V_{ee}[\rho] - J[\rho]$ is the non classical part, and $(T[\rho] - T_s[\rho])$is the contribution to the kinetic energy that comes from the inter-electronic interactions.

We can use Lagrange multipliers to minimize the functional, applying the restrictive effect of the equation commented previously. From which we obtain the total energy functional of Kohn-Sham. This does not depend on the electronic density directly but depends on a series of doubly occupiedΦ_i states. In order to solve the equation with spin polarization two different sets of states, α and β, are needed. The group of states that then minimizes the Kohn-Sham functional is obtained by solving the self-consistent system known as the Kohn-Sham equations.

$$\left(-\frac{1}{2}\nabla^2 + \mathrm{V_{eff}}(\mathrm{r})\Phi_\mathrm{i}(\mathrm{r})\right) = \varepsilon_i\Phi_i(r)$$

Where $\mathrm{V_{eff}}(\mathrm{r})$ is an effective potential that can be decomposed into:

$$\mathrm{V_{eff}}(\mathrm{r}) = \mathrm{V_{ext}}(\mathrm{r}) + \int \frac{\rho(r')}{|r - r'|} dr' + \mathrm{V_{xc}}(\mathrm{r})$$

Where the first part corresponds to the external potential, the second, represents the Coulomb interactions and the last one is the exchange-correlation term with respect to the electron density.

$$\mathrm{V_{xc}}(\mathrm{r}) = \frac{\mathrm{dE_{xc}}[\rho(\mathrm{r})]}{\rho(\mathrm{r})}$$

The Hamiltonian shown before depends on $\mathrm{V_{eff}}(\mathrm{r})$ and this, at the same time, depends also on the electronic density $\rho(\mathrm{r})$ that is obtained from the Kohn-Sham equations. This allows the system to be solved iteratively until the electronic density is constant and then can be used to find the energy of the system.

The main disadvantage of the DFT methodology introduced previously is the fact that there is no universal expression for the exchange-correlation functional. It is interesting to point out that the Kohn-Sham equations are formally equivalent to the Hartree-Fock

equations, just changing the $V_{eff}(r)$ for the HF exchange but in DFT also the correlation is included. It's interesting to note that if the exact exchange-correlation functional would be known the DFT methodology could lead us to the exact solution of the system on study. But as it has been commented previously by now, the universal functional has yet to be found.

2.3.4Exchange-Correlation Functionals

The choice of an exchange-correlation functional is not trivial, probably it is one of the most critical choices in the computational DFT calculations. The performance of different functionals can be very different and lead to very different, and sometimes unrealistic, results. Roughly speaking, functionals can be divided into four groups: Local density approximation (LDA), Generalized Gradient Approximation (GGA), meta Generalized Gradient Approximation (meta-GGA) and Hybrid functionals.

Local Density Approximation (LDA):

The LDA approach was the first one used and is the most simple to be taken. It assumes that the exchange-correlation functional depends only on the local density ρ

$$E_{xc}[\rho] = f(\rho)$$

$$E_{xc}[\rho] = \int \rho\,(r)\varepsilon_{xc}[\rho(r)]dr = \int \rho\,(r)\varepsilon_{x}[\rho(r)]dr + \int \rho\,(r)\varepsilon_{c}[\rho(r)]dr$$

$$E_{xc}^{LDA}[\rho] = \varepsilon_x(\rho) + E_c[\rho]$$

$$E_{xc}[\rho] = -\frac{3}{4}\left(\frac{3}{\pi}\right)^{1/3}\rho(r)^{(1/3)}$$

This kind of functional gives good results for metals in which electrons present a similar behavior to those in the free electron gas. Indeed that is the basis of the method. However, LDA fails when try to one needs to describe strongly correlated materials such as magnetic oxides, and other semiconductors as TiO_2 or ZnO. It also tends to overestimate the bonds. Some examples of this type of functionals are the Vosko-Wilk-Nusair (VWN) functional[38], or the Cole-Perdew (CP) functional[39].

Generalized Gradient Approximation (GGA):

These functionals depend on the local density and also on the gradient of the density.

$$E_{xc}^{GGA}[\rho(r)] = \int f\big(\rho(r)\big), \nabla\rho(r))dr$$

In most of the cases this type of functional can be split in two parts. One for the correlation and another one for the exchange allowing different combinations of the two kind of functionals. An example of this is the BLYP which combines the exchange functional from Becke (B88)[40] and the correlation functional from Lee, Yang and Parr (LYP)[41]. Some of the most common GGA functionals used are PW91[42], PBE[43] etc.

Meta-Generalized Gradient Approximation (meta-GGA):

This functional depends on the density, the gradient of the density and also the Laplacian of the density.

$$E_{xc}[\rho] = f(\rho, \nabla\rho, \nabla^2\rho)$$

This kind of functional initially appeared to have few advantages over GGA functionals and some of the first meta-GGA functionals even failed when they were applied to extended systems. However, nowadays they have been significantly improved and have been applied to extended systems with good results.

Hybrid functionals:

These functionals, as their name indicates, use a mixture of the exact exchange from the HF method with different exchange-correlation contributions from the above mentioned DFT functionals as LDA and GGA the proportion of these different contributions are defined by empirical parameters.

Some examples of well-known hybrid functionals are B3LYP[38,40],[41] and PBE0[44]. In the case of B3LYP it includes three empirical parameters (α, β and c) as shown below.

$$E_{xc}^{B3LYP} = \beta E_x^{HF}[\psi_i] + (1-\beta)E_x^{LDA}[\rho] + \alpha\Delta\mathrm{E_x^{B88}} + \mathrm{E_c^{LDA}}, VWN[\rho] + c\Delta E_c^{LYP}[\rho]$$

In the case PBE0 functional 25% of Hartree-Fock exchange is used and the other 75% of exchange belongs to the GGA functional PBE and also the correlation.

$$E_{xc}^{PBE0} = {}^{1}/_{4}\, E_{x}^{HF} + {}^{3}/_{4}\, E_{x}^{PBE} + E_{c}^{PBE}$$

The inclusion of the Hartree-Fock exchange can compensate the lack of localization presented in LDA and GGA functionals, resulting from the electron gas treatment of the exchange and correlation. For this reason pure GGA functionals can also fail when describing highly correlated systems. But the performance of the Hybrid functions can in some way overcome this problem.

2.3.5 On-site Coulomb interaction: DFT+U

In systems with electrons in the d or f orbitals are strongly correlated, these electrons are localized in the orbitals due to the Coulomb repulsion which increase the exchange effect between occupied and empty eigenstates. This large Coulombic repulsion between localized electrons might not be well represented by LDA or GGA functionals. This bad description of the strong correlated systems comes from the self-interaction error present in this type of functional. One option to overcome this problem is the introduction of a Hubbard-like potential,[45–50]it is a localized term, to the LDA or GGA density functional. This approach is known as DFT+U. The usual implementation of the method consists of separate localized d or f electrons, on which the Hubbard term will act. The delocalized s and p electrons are correctly described by the usual LDA/GGA calculation. In the calculations performed in this work where this approach has been applied it was used following the implementation introduced by Dudarev,[51] where the spin-dependent on-site density matrix ρ^{σ} is used to define the DFT+U energy functional as follows:

$$E_{DFT+U} = E_{DFT} + \frac{(U—J)}{2} \sum_{\sigma} \left[\left(\sum_{m1} \rho^{\sigma}{}_{m1,m1} \right) - \left(\sum_{m1,m2} \hat{\rho}^{\sigma}_{m1,m2}\, \hat{\rho}^{\sigma}_{m2,m1} \right) \right]$$

Where σ is the orbital momentum quantum number, and $\hat{\rho}^{\sigma}_{m1,m2}$ and $\hat{\rho}^{\sigma}_{m2,m1}$are the occupation matrices for the orbital with m_i spin angular momentum, and $\hat{\rho}^{\sigma}_{m1,m1}$ the total occupation matrix, respectively. U is a Hubbard parameter that measures the increase in energy derived from adding an electron in a particular orbital and J is a Stoner-like exchange parameter (usually zero).

By using this methodology the occupied states are shifted decreasing their energy meanwhile it increases the energy for the unoccupied states by the same amount but

positive. Adding a penalty to the partially occupied orbitals forcing in this way to have fully occupied or fully unoccupied levels and subsequently localizing the electrons.

It is important to point that this methodology has to be used carefully as can lead to artifacts or unrealistic results. For every different system, one should pay attention to the value of the parameter U needed to describe properly the features of the system without misleading results.

2.4 Basis functions

Basis sets

Orbitals (one-electron wave functions) can be expressed in different ways depending on the kind of calculation we want to do. We typically divide wavefunctions into two types: body-centered wave-functions, and periodic plane-wave-based wavefunctions. These orbitals usually are expressed as linear combinations of more simple functions in order to afford the computational cost in an efficient way. There are four main types of basis set used in computational chemistry first three would belong to the body centered wave-functions and the forth one is the main option of non-body centered wave-functions. We comment on all four below.

-Gaussian Type Orbitals (GTOs):

The Gaussian type functions are, as their name suggests, a kind of Gaussian shaped function expressed in the following form.

$$\eta^{GTO} = N x^{l} y^{m} z^{n} e^{[-\alpha r^{2}]}$$

Where *N* is the normalization factor, α is the exponent which makes the function more compact or diffuse, and *l,m, n* are the symbols that make correspond the Gaussian function with the s, p, d or f, orbitals.

-Slater-Type Orbitals (STOs):

These Slater-Type Orbitals[52] are another approach similar to GTO functions. These functions were developed by Slater and the main difference with the GTO is that in this case the functions are split in a radial part and an angular part and are expressed in the following way.

$$\eta^{GTO} = Nr^{n-1}e^{[-\zeta r]}Y_{lm}(\Theta\varphi)$$

In this expression *n* corresponds to the principal quantum number, the orbital exponent is termed $\zeta$and Y_{ml} are the usual spherical harmonics that describe the angular part of the function. The main deficiency of this type of function is that the many-center integrals are a lot more difficult to compute with the STO functions than with the GTO or the planar waves commented below. The localized functions usually are contracted to reduce the computational cost of the calculation. Taking this form:

$$\eta^{Contracted\ \ form} = \sum_{a}^{A} d_a \eta_a^i$$

Where d_a corresponds to the contracting coefficients andη_a^i are the non contracted wave-functions.

-Numerical atomic orbitals (NAOs):

Numerical atomic orbitals[53] were recently developed with the aim to improve scalability of quantum mechanics calculations, in order to be able to perform calculations of larger systems. But they imply a non-negligible drawback which is the lack of systematics for energy convergence.

NAOs have this form:

$$\varphi_{i[lm]}(r) = \frac{u_i(r)}{r} \cdot Y_{ml}(\Omega)$$

The $u_i(r)$ is a numerically tabulated function obtained by calculating the numerical solution of the Kohn-Sham Hamiltonian for isolated pseudoatoms. This procedure implies that the NAOs are fully optimized for different types of atoms and thus attempt to be compact as possible while maintaining the accuracy.

$Y_{ml}(\Omega)$ denotes the real parts (m = 0,...,l) and imaginary parts ($m = -l,\ldots,-1$) of complex spherical harmonics, and l, m are implicit functions of the basis function index i.

Apart from the usual Hamiltonian, for these types of basis set a potential term ($V_{cut}(r)$) in included which is an imposed potential that allow the numerical function to decrease

smoothly with the distance from the center of the atom. This term helps to reduce the computational cost of using NAOs.

$$\left[-\frac{1}{2}\frac{d^2}{2dr^2}+\frac{l(l+1)}{dr^2}+v_i(r)+V_{cut}(r)\right]u_i(r)=\epsilon_i u_i(r)$$

-Plane Wave Functions:

This type of functionis specially designed for periodic systems because of their periodic boundary conditions. These basis functions are expressed in the following way.

$$\eta^{PW}=e^{[i\vec{k}\vec{r}]}$$

Where the vector $\vec{k}$is related with the momentum $\vec{p}$of the wave through$\vec{p}=\hbar\vec{k}$ these plane waves as have been said before are not centered at the nuclei but extended throughout space, filling the entire box which is repeated in one, two, or three dimensions, depending on the periodicity conditions of the system studied. The shape of these functions is specially appropriated for extended system calculations. However, a large number of plane waves are needed to describe the systems in an accurate way. For this reason effective core potentials (also known as pseudopotentials) were developed to reduce the number of plane waves needed and subsequently the computational cost.

2.5 Core electrons and Pseudopotentials

The use of pseudopotentials came from the high computational cost of studying systems with a large number of electrons. Pseudopotentials are based on the idea that internal electrons known as core electrons usually remain unaltered during system changes (e.g. optimizations and reactions). For these reasons the effect that these electrons on the valence electrons can be parameterized, saving a lot of computational resources with no little of accuracy in the results. The way in which these core electrons are parameterized can be quite different depending on the approach used, some examples are shown below.

In this first approximation we setup the Schrödinger equation for an atom in its referential configuration and define the core radius Ω_c. After solving the equation we obtain the radial wave functions, also known as Bessel functions:

$$-1\frac{1}{r}\frac{d^2}{dr^2}\left(r\psi_{nl}(r)\right)+\frac{l(l+1)}{r^2}\psi_{nl}(r)+V_{sc}\psi_{nl}(r)=\varepsilon_{nl}\psi_{nl}(r)$$

Inside the previously defined core radius Ω_c these wavefunctions are substituted by pseudowavefunctions $\tilde{\psi}_{nl}$. The application of pseudopotentials ensures that ψ_{nl} must be equal to $\tilde{\psi}_{nl}$, outside the core radius. These pseudowavefunctions include relativistic effects that are very important in the most internal electrons due to their high kinetic energy and also these pseudofunctions donot show any nodes. Below we briefly comment the most important kinds of pseudopotential.

2.5.1 Norm-conserving

These pseudopotentials were the first created, and were developed by Hamann in 1979,[54]these potentials obeyed the following constraints:

- The partial wavefunctions including all electrons and the pseudofunctions for a determined atom must coincide beyond the core radius.

- The eigenvalues and the first logarithmic derivate of the all electrons wavefunction and the pseudofunction must coincide.

- The norm must be conserved when we integrate the same charge of the all-electron wavefunction in the pseudofunction.

$$4\pi \int_0^{\Omega c} \psi_{nl}(r)^2 r^2 dr = \int_0^{\Omega c} \tilde{\psi}_{nl}(r)^2 r^2 dr$$

These kinds of potentials usually work well with most of the elements but fall in to trouble when the element has strongly localized valence orbitals.

2.5.2 Ultra-soft

These ultra-soft potentials were first reported out in the 1990s to overcome the deficiencies that norm-conservant potentials had. In this kind of potential the condition of conserving the norm is no longer used. For this reason the pseudofunctions are not normalized and subsequently the electronic density is not complete and a charge increaser operator is needed to balance the effect on the valence functions. These pseudopotentials, compared with the norm-conserving potentials, reduce the number of basis functions which lead to a significantly lower computational cost.

2.5.3 Projector-augmented-wave

The projector-augmented-wave (PAW) method was developed by Blöch in 1994,[55] the PAW allows to introduce the advantages from the pseudopotentials with an accurate description of the core electrons, giving similar results as the all-electrons calculations.

In general wavefunctions tend to be smooth in the bonding regions far from the nuclei but at shorter distances they change abruptly due to the huge electron-nuclei potential. For these reasons the PAW approximation splits the wavefunctions into two zones, one for the bonding zone and another for the core region.

The bonding region is described with expanded planar waves or similar base functions. The core section is represented by spherical partial wave functions centered in the atoms forcing both functions to have the same value and first derivative in the edge zone.

This method applies a lineal transformation T which connects the all-electron wavefunction ψ with the $\tilde{\psi}$ pseudowavefunction in the following form.

$$T = 1 + \sum_R \tilde{T}_R$$

In this way $\tilde{T}_R$only acts on the regions below the core radius of each atom, this transformation affects both the wavefunction and its properties.

When r < Core radius

$$|\psi\rangle = 1 + \tilde{T}_R|\tilde{\psi}\rangle$$

When r > Core radius

$$|\psi\rangle = |\tilde{\psi}\rangle$$

Inside the core radius region the pseudowavefunction is described as a linear combination of partial wavefuncions, usually planar waves.

$$\widetilde{|\psi\rangle} = \sum_i |\tilde{\phi}_i\rangle \cdot c_i$$

$$|\psi\rangle = T|\tilde{\psi}\rangle \qquad\qquad |\phi_i\rangle = T|\tilde{\phi}_i\rangle$$

$$|\psi\rangle = T|\tilde{\psi}\rangle = \sum_i |\tilde{\phi}_i\rangle \cdot c_i$$

Where the sub index i refers to the atomic position and also the quantum numbers n, m and l.

The coefficients used in that linear combination can be expressed as products between the pseudowavefunctions and the projection functions.

$$c_i = \langle \tilde{p}_i|\tilde{\psi}\rangle$$

These projection functions must obey:

$$\sum_i |\tilde{\phi}_i\rangle \langle \tilde{p}_i| = 1$$

That means that both groups of functions are orthogonal

$$\langle \tilde{p}_i|\tilde{\phi}_j\rangle = \delta_{ij}$$

Then the linear transformation can be expressed as:

$$T = 1 + \sum_i (|\phi_i\rangle - |\tilde{\phi}_i\rangle) \langle \tilde{p}_i|$$

and the all-electron wavefunctions can be described as a function of the pseudowavefunctions:

$$|\psi\rangle = |\tilde{\psi}\rangle + \sum_i (|\phi_i\rangle - |\tilde{\phi}_i\rangle) \langle \tilde{p}_i|\tilde{\psi}\rangle$$

$$\tilde{A} = A + \sum_{i,j} |\tilde{p}_i\rangle (\langle \phi_i|A|\phi_j\rangle - \langle \tilde{\phi}_i|A|\tilde{\phi}_j\rangle) \langle \tilde{p}_i|$$

To obtain a physical magnitude, A, from the ground state implies the use of the wavefunction.

This methodology requires less computational resources due to the lower number of plane waves needed. This pseudopotential method is also the most similar to an all-electron calculation. This method has been used in all the calculations where was not possible to perform an all electron calculation.

2.6 Structural models for extended systems: The periodic model

2.6.1 Periodic models

In order to study large systems where their properties are intrinsically related with their periodic structure, there is a computational methodology that allows us to take into account the periodicity of the system in order to describe accurately all their properties. This methodology is known as the periodic model. Some examples where this methodology is extremely useful is for studying systems like bulk structures, which present 3D periodicity, surfaces with 2D periodicity and nanotubes or nanowires where the periodicity is only in one dimension.

The periodic model is the based on taking advantage of the use of the periodicity of crystalline systems to save computational cost and also to describe the properties that inherently result from periodic symmetry.

The periodicity is understood as the ordered distribution of atoms in a certain way along 1, 2, or 3 dimensions, depending on the system. For understanding and working with periodicity is necessary to understand first the concept of the Bravais lattice. The Bravais lattice is an infinite array of discrete points with an arrangement and orientation that looks exactly the same, independently from which point of the array is viewed. For example a 3-dimensional Bravais lattice consists of a set of points that can be expressed in the following form.

$$R = n_1\boldsymbol{a_1} + n_2\boldsymbol{a_2} + n_3\boldsymbol{a_3}$$

Where $\boldsymbol{a_1}$,$\boldsymbol{a_2}$ and $\boldsymbol{a_3}$ represent the three vectors of the "box/lattice" which include the motive repeated in the three dimensions, this box is called unitary cell, and n_1, n_2, and n_3 are integer numbers that make possible to represent any point R of the periodic structure as a combination of the three vectors $\boldsymbol{a_i}$. Each point can be reached by moving n_i times a length of a_i in the direction of the vector $\boldsymbol{a_i}$.

To define where the atoms are located inside the lattice, one simple way is to use the atomic fractional coordinates. It can be expressed in the following way.

$$\sum_{i=1}^{3} X_i\boldsymbol{a_i}$$

Where X_i is a number between 0 and 1 that define the relative position of the atom in a certain direction referred to $\boldsymbol{a_i}$ that is a certain vector of the unit cell.

From a three dimensional periodicity there are only 14 different possible lattices, which are defined by the a, b, c which are the length of the thee vectors, and the angles α, β, γ as is shown Fig. 4.

This motif repeated through all the lattice is known as the primitive cell, or unit cell. This cell is not unique, some different versions of that cell can be chosen for the same Bravais lattice, but usually the most common is the Wigner-Seitz cell, which is the simplest or smallest cell that contains all symmetry operations applicable to the lattice.

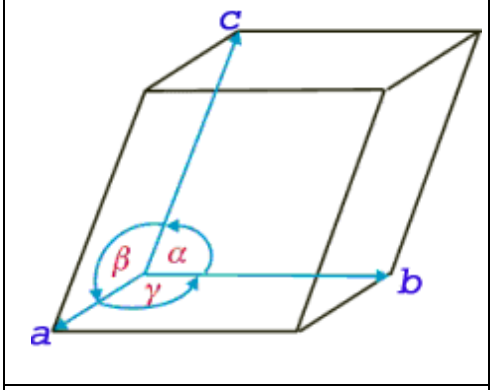

Figure 4: Example of lattice cell

One of the most interesting aspects of the periodic model is the use of the reciprocal space, also known as k-space. The reciprocal space allows performing analytic studies of infinite periodic systems by the construction of a reciprocal lattice of the Bravais lattice. In reciprocal space we have a set of vectors K that yield plane waves with the periodicity conditions from the Bravais lattice in the direct space. K belongs to the reciprocal lattice of Bravais lattice if point R, provides that relation

$$e^{iK\cdot(r+R)} = e^{iK\cdot r}$$

The reciprocal lattice is the set of vectors K that satisfy the following condition.

$$e^{iK\cdot R} = 1$$

The reciprocal lattice can be generated by the 3 primitive vectors of the real space Bravais lattice in the following way.

$$b_1 = 2\pi \frac{a_2 \times a_3}{a_1 \cdot (a_2 \times a_3)} \qquad b_2 = 2\pi \frac{a_1 \times a_3}{a_1 \cdot (a_2 \times a_3)} \qquad b_3 = 2\pi \frac{a_2 \times a_1}{a_1 \cdot (a_2 \times a_3)}$$

This set of vectors is equivalent to the vectors $\mathbf{a_1}$, $\mathbf{a_2}$, $\mathbf{a_3}$ in direct space and the equivalent of the Wigner-Seitz cell in reciprocal space is known as the first Brillouin Zone.

2.6.2 Bloch theorem

The Bloch theorem[56]is also crucial in the periodic model formalism. This theorem says that in a periodic system each electronic wavefunction can be expressed as a product of two functions, one with the periodicity of the cell and a planar wave.

$$\Psi_i(r) = e^{ikr}\upsilon_i(r)$$

The first part of the previous equation is the planar-wave with wave vector k, υ(r) is the periodic function that can be expanded as a linear combination of plane waves, but with wave vectors G that are reciprocal to the vectors in the direct space as is shown below.

$$\upsilon_i(r) = \sum_G c_{i,G} e^{iGr}$$

$$Ga_i = 2\pi m$$

$$\Psi_i(r) = \sum_G c_{i,k+G}\, e^{i(k+G)r}$$

This theorem states that the values of all observables at a certain position of a lattice will be the same for equivalent positions of the system. This allows us to consider only the first Brillouin zone in order to reproduce the properties of the entire lattice. Combining both equations shown above, we can represent the wavefunctions of the real system as a combination of the plane-waves from the reciprocal space. Every plane-wave is characterized by a kinetic energy $|k+G|^2\ h^2/2m$. Due to this we can increase the basis of plane-waves defining a limit for its kinetic energy, obtaining in that way a finite set of basis functions.

As it has been mentioned these methodologies are extremely useful when the properties we want to evaluate are closely related with the periodicity of the system, as could be most of the electronic properties like for example the density of states or the band gap. Also one of the most interesting characteristics of this methodology is the reduction of the computational cost due to the reciprocal space which allows us to use a small cell and a certain number of plane-waves to describe correctly the systems with infinite number of electrons. Another example is the calculations for large nanoparticles with extended exposed periodic surfaces. In this case one can study the reactivity of the different surfaces using this methodology, by applying the slab model where a certain

vacuum is added to the cell in order to avoid periodic interactions in the direction perpendicular to the surface that we want to study. Another methodology that take advantage of the reduction of computational cost of this method consists in performing calculations of 0D systems like clusters and nanoparticles from a periodic point of view. In this way we study the nanoparticle inside a large cell with enough vacuum to ensure no interaction with its periodic replicas. This methodology takes some advantages from the periodic formulation to save computational cost. The periodicity can be used in favor to study macrostructures as nanocables or zeolites etc. In our case, taking into account the system studied, this methodology is the one used to study the bulk and surfaces of ZnO and TiO_2.

2.6.3 Top down and bottom up approaches

In order to describe accurately some of the properties of ZnO and TiO_2, a large number of different types of systems need to be studied. In the work presented in this thesis we have performed studies on different types of TiO_2 and ZnO systems going from small clusters with a few atoms to large nanoparticles with more than 1000 atoms, apart also from the periodic systems like bulks and extended surfaces. For the extended systems the periodic model explained in the previous section has been used; but in the case of smaller clusters and larger nanoparticles different methodologies are needed in order to obtain reliable results.

To study the smaller systems like the nanoclusters, we need to take into account the large amount of different isomers possible and that most of them present relatively similar energetic stability. To explore the shape of these clusters we have used a bottom up approach. This approach consists on a systematic study of the most stable isomers for a certain size by applying a global optimization technique combined with data mining. The global optimization methodology allows us to explore the potential energy surface of small clusters in an efficient way. We note that a study of all possible structures after a certain nanocluster size is not possible since the number of different possible isomer configurations increases exponentially with the number of atoms of the system. This scaling makes it almost impossible to perform a complete study of all the possible structures when the system is larger than ~25 atoms. For this reason the global optimization algorithms are the unique opportunity to perform a search of the most stable isomers.

The global optimization methodology used in this work is based on the basin hopping algorithm.[57] This algorithm works as follows:

The first step consists in provides an initial cluster geometry of certain size, this structure is evaluated and if accomplishes the conditions imposed (number of structures obtained, or other criteria) in the algorithm it stops, if not, it continues to the next step which consists in to modify the position of the atoms in the cluster in a random way, moving them or interchanging their positions. The next step consists in an optimization of the position of the atoms by using interatomic potentials or *ab initio* methods. The energy of the optimized structure is checked in the next step and saved if accomplishes one of the two conditions. The first one is if the energy of the structure is lower than the energy for the previous one. If the structure obtained does not fulfill the condition is rejected goes to the second filter. The energy difference between the structure and the previous one is introduced in a normalized Boltzman distribution generating a number between zero and one. If the number calculated by the Boltzman distribution is higher than a number randomly generated the structure is also accepted and saved, otherwise if is

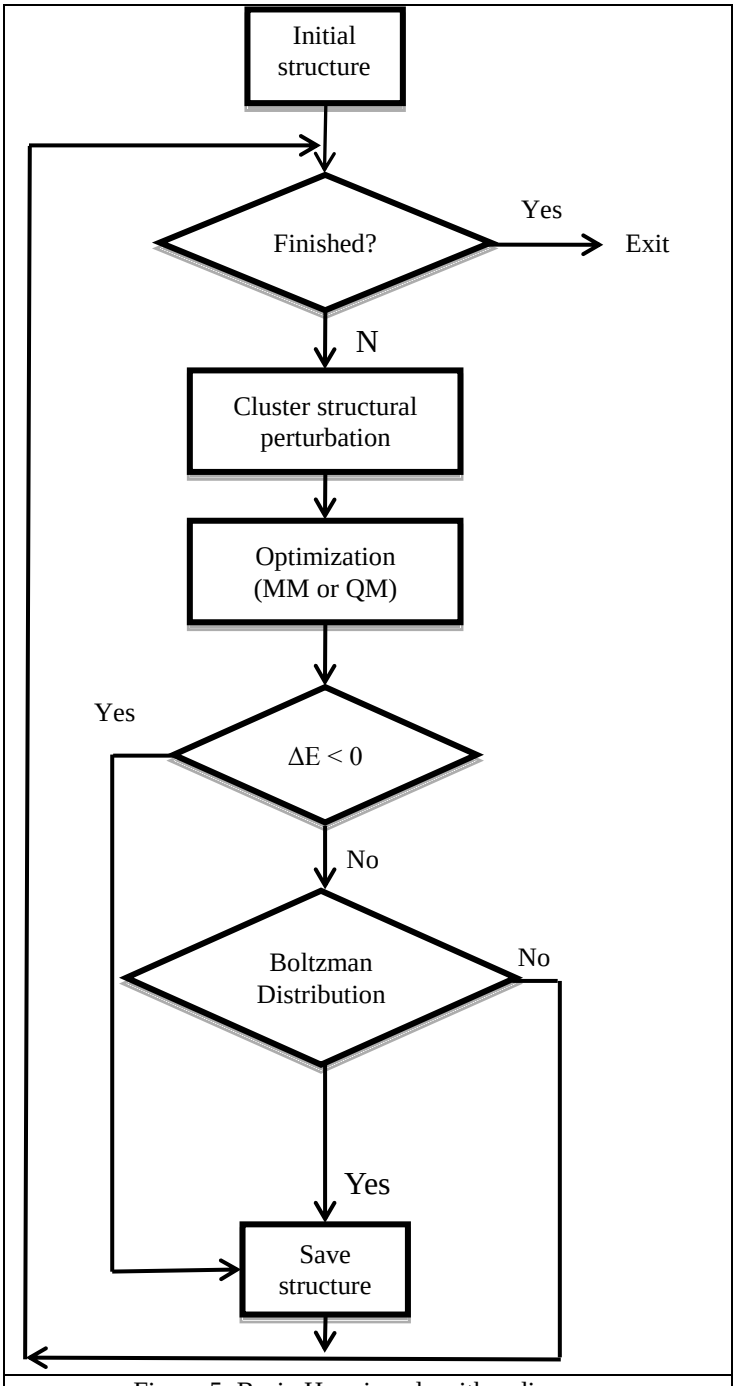

Figure 5: Basin Hopping algorithm diagram

rejected the structure goes to the first steep as a new starting point for the cycle. What we do by applying this methodology is to explore the potential energy surface of the different isomers for a certain size and selecting the most suitable candidates to be the ground state structure for this size. Combining this technique with data mining we have performed an systematic study of the small sized clusters of TiO_2 and ZnO.

In the case of larger nanoparticles with hundreds of atoms also studied in this thesis; this bottom up methodology fails as it is not possible to study a significantly large part of the potential energy surface to have reliable results. For this reason a different approach was used for these larger systems; the top down approach. This methodology is based in the fact that while small clusters can have very diverse isomers, with different shapes, but similar stability. The larger nanoparticles tend to become bulk-like as their size increases, showing bond distances and coordination almost equal to the ones presented in the bulk material. Taking this into account, we follow the premise developed by Gibbs who enounced that a crystal (or nanoparticle in our case) will present a shape having the minimal surface free energy. Based on this, Wulff[58] developed a model in order to build nanoparticles with the shape that accomplish the Gibbs condition.

The Wulff construction takes the information of the bulk material, its most stable surfaces and their surface energies in order to construct the nanoparticle that exposes a larger surface area of the most stable surface and smaller surface areas of the subsequent less stable surfaces. This methodology will lead to nanoparticles that maintain a certain ratio between the most stable surfaces and subsequently maintaining the shape independently of the size of the nanoparticle. This methodology minimizes the free energy of the system surfaces, providing rational and stable shapes for these larger nanoparticles. This methodology is very useful for modeling very large nanoparticles with properties expected to be closer to the bulk ones than to small molecules of the same system. In our case this methodology has been used to model the large nanoparticles of Anatase TiO_2, wurtzite ZnO and Body Centered Tetragonal (BCT) ZnO presented in the results chapter.

2.7 *Ab initio* thermodynamics

A great part of the experiments regarding surface science, catalysis and photocatalysis are performed at low temperature and ultra-low pressures. For this reason the results obtained by the static *ab initio* calculations that are performed at zero Kelvin and vacuum conditions, are easily comparable with the experimental results and very reliable. Nevertheless, in some cases depending on the experimental conditions, or the work conditions desired for the material, the effect of pressure, composition, and temperature not only cannot be neglected but they have a great effect on the energetic stability of different systems. As a consequence sometimes this effect need be taken into account after the *ab initio* calculations are performed, using the results obtained from the static *ab initio* calculation and applying *ab initio* thermodynamics in order to obtain accurate result for specific systems. Also these kind of calculations are needed to compare the stability of different surfaces from different systems presenting different compositions.

One way to be able to do this is by applying *ab initio* thermodynamics method. This methodology was presented by Scheffler and Reuter[59] in order to relate the surface stability with the effects of temperature and pressure for different surfaces from different metal oxides. This is done by calculating the Gibbs free energy of the different systems. In our cases it is applied to the stability of different surfaces with different coverages. We define the Gibbs adsorption energy per surface area γ^{cover} for different coverages (N) as function of pressure (p) and temperature (T). The γ^{cover} can be calculated as the sum of the surface free energy for the clean surface (γ^{clean}) plus the Gibbs free energy related to the atoms adsorbed (γ^{ads}), both normalized per surface area. The equation is represented as follows.

$$\gamma^{cover}(T,p,N) = \gamma^{clean}(T,p) + \gamma^{ads}(T,p,N)$$

The expression of the Gibbs free energy for a clean surface is defined as:

$$\gamma^{clean}(T,p) = \frac{1}{A}[G^{slab} - N_a\mu_a(T,p) - N_b\mu_b(T,p)]$$

Where G^{slab} corresponds to the Gibbs free energy of the surface, μ_a and μ_b correspond to the chemical potential of the atoms forming the surface, normally obtained from their bulk reference. N_a and N_b are the number of atoms of each kind that form the surface.

The adsorption Gibbs free energy ($\gamma^{ads}(T,p,N)$) can be estimated as follows

$$\gamma^{ads}(T,p,N_{molec}) = \frac{1}{A}[G^{cover}(T,p,N_{molec}) - G^{slab}(T,p) - \mathrm{G_{molec}}(T,p)]$$

Where $G^{cover}(T,p,N_{molec})$ is the Gibbs energy of the surface with the atoms adsorbed at a certain T and p, containing N_{molec} number of atoms or molecules adsorbed, $\mathrm{G_{atom}}(\mathrm{T,p})$is the Gibbs energy of the molecule at T and p. $G^{cover}(T,p,N_{molec})$ and $G^{slab}(\mathrm{T,p})$ can be obtained from the *ab initio* calculation. From the covered and clean slabs since:

$$G^{cover}(T,p,N_{molec}) = (E^{cover} - TS^{cover} + pV)$$

$$G^{slab}(\mathrm{T,p}) = (\mathrm{E^{slab}} - \mathrm{TS^{slab}} + \mathrm{pV})$$

Where E^{cover} and $\mathrm{E^{slab}}$ are the total energy of the covered and clean surfaces obtained from the *ab initio* calculation (E^{total}) plus the zero point vibrational energy. S^{cover} and S^{slab} are the entropic contributions and pV is the pressure-volume term. In the case of solid state, the entropic terms and the pV term can be usually neglected, this is due to the order of magnitude of this term is considerably smaller compared with the E^{cover} and $\mathrm{E^{slab}}$. This reduces also the computational cost. For example the pV term and S terms usually are of the order of several meV which is much smaller than the total energy of most bulk and surface obtained from the computational calculation. Therefore the Gibbs free energy of the clean and covered surface can be expressed as their total energies E^{cover} and $\mathrm{E^{slab}}$. In the case of the molecules adsorbed, the pV and S terms cannot be neglected as they are of the same order of magnitude as the total energy. When we consider all the equations and approximations shown previously, the expression of the surface free energy (γ^{ads}) can be expressed in the following way.

$$\gamma^{ads}(T,p,N_{molec}) = \frac{1}{A}\left[[E^{cover} - E^{slab} - N_{molec}\left(\frac{E_{molec}}{2} + \frac{E^{ZPE}_{molec}}{2} + \Delta\mu_{molec} + k_B T \cdot ln\frac{p}{p_0}\right)\right]$$

$\mathrm{E_{molec}}$ and $\mathrm{E^{ZPE}_{molec}}$ are divided by 2 in the case of a diatomic molecule that is adsorbed as individual atoms like for example an Hydrogen molecule. k_B is the Boltzmann constant, p is the working pressure and $\Delta\mu_{molec}$ is the chemical potential of the molecule calculated as follows.

$$\Delta\mu_{molec} = -\frac{1}{2}k_B T \cdot lnQ_{total}$$

Where Q_{total} is the sum of the electronic, rotational, translational and vibrational partition functions of the gas phase molecule.

Chapter 3

Results

Chapter 3.1

Titanium dioxide (TiO_2)

3.1.1 Studies for bulk TiO_2

Motivated by the work done in the field mentioned in previous sections, we started our research in this area by focusing the problem on finding a suitable computational models able to describe the most important and crucial properties of TiO_2 in an accurate and reliable way. In particular we sought models able to describe the crystal structure, geometrical features, energetic stability and, what is probably the most complex part, the electronic structure and band gap which are directly related with the photocatalytic reactivity of TiO_2. Finding suitable models is a crucial issue and allows us not only to describe properly the bulk properties but also to perform reliable calculations for surfaces and nanoparticles, small clusters, and each for various polymorphs. In our studies we have performed calculations on three different TiO_2 polymorphs: anatase, rutile and brookite.

In the first work presented in this thesis we studied the atomic and electronic structure of clean and fluorine-doped (F-doped) rutile, anatase, and brookite polymorphs of TiO_2.In a first step, we present a methodological analysis of the performance of several density functional schemes (GGA, GGA+U, and hybrid functionals) with respect to reproducing experimental structures, cell parameters, and band gap for rutile and anatase. It is important to remark that the study of the performance of the different functionals is crucial for this type of systems, since its well know that GGA functionals tend to underestimate the band gap of oxides and semiconductors while hybrid functionals often tend to overestimate it.[60,61] For a reliable DFT-based description of the electronic structure we need to carefully study the performance of different functionals. Later on, and taking into account the results obtained in the first part of the work, we have studied the effects that doping TiO_2 polymorphs with fluorine has on the electronic structure of the bulk. We especially focused on how fluorine affects the band gap, as it is a determining feature related with the absorption of light by the material.

Beyond assessing previously reported functionals we also looked into adapting these functionals in order to accurately and simultaneously describe the geometry, stability and electronic structure of TiO_2. To this end we modified the amount of Fock exchange included in the hybrid functional PBE0 to improve its description of TiO_2, not only the band gap but the energetics and structural parameters too. We carefully analysed the performance of this modified hybrid functional for the considered TiO_2 systems. This study is reported in the second article presented in this chapter.

With this modified PBE0 functional tested and validated for anatase and rutile TiO_2 polymorphs, and taking into account the results obtained in the previous work, we decided to study the effect of the internal parameters of the HSE06 and PBE0 functionals on the description of the band gap of some other metal oxides apart from TiO_2. This work has been carried out with the aim to find a range of values for these parameters, that allow one to describe properly different types of metal oxides and other systems with similar features. This research was also motivated by the lack of accuracy on the electronic structure description provided by the most extended LDA and GGA DFT functionals. The methodology and results obtained from this research are shown below.

3.1.1.1 Electronic Structure of F-Doped Bulk Rutile, Anatase, and Brookite Polymorphs of TiO_2

THE JOURNAL OF PHYSICAL CHEMISTRY C

Article

pubs.acs.org/JPCC

Electronic Structure of F-Doped Bulk Rutile, Anatase, and Brookite Polymorphs of TiO_2

Sergio Tosoni,[†,‡] Oriol Lamiel-Garcia,[†] Daniel Fernandez Hevia,[‡,§] José Miguel Doña,[‡] and Francesc Illas*[,†]

[†]Departament de Química Física & Institut de Química Teòrica i Computacional (IQTCUB), Universitat de Barcelona, C/Martí i Franquès 1, E-08028 Barcelona, Spain

[‡]Departamento de Química, Universidad de Las Palmas de Gran Canaria, Campus Universitario de Tafira, 35017 Las Palmas de Gran Canaria, Spain

[§]INAEL Electrical Systems S.A., C/Jarama 5, 45007 Toledo, Spain

ABSTRACT: This work investigates the atomic and electronic structure of fluorine-doped (F-doped) rutile, anatase, and brookite polymorphs of TiO_2. In a first step, we present a methodological analysis of the performance of several density functional schemes (GGA, GGA+*U*, and hybrid functionals) in reproducing experimental structures and band gap of rutile and anatase. The PBE+*U* functional appears to provide the best choice, and it is the one chosen to study suitable supercell models of F-doped bulk rutile, anatase, and brookite. We find that F-doping is thermodynamically stable for all polymorphs. In anatase, the Ti^{3+} gap states arising from doping are well located in the middle of the band gap which is convenient for photocatalysis purposes. However, in the case of rutile and brookite, F-doping does not lead to a remarkable reduction of the band gap. We present also results concerning F-doping on reduced titania and provide evidence that the presence of oxygen vacancies does not change significantly the electronic properties of F-substituted TiO_2, albeit slightly stabilizing the resulting system.

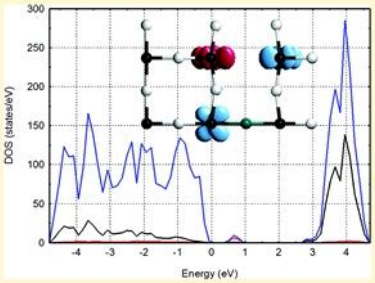

INTRODUCTION

The interesting photocatalytic properties of titanium dioxide, often referred to as titania, have been known for almost 40 years, and the properties of titania-based materials exposed to UV light have been reviewed in detail by several authors.[1−4] These materials proved to be very good catalysts for many chemical reactions, from water splitting to the decomposition of organic molecules,[1] to mention just two important cases. In addition, the potential applications of titania span from design of new materials for the exploitation of renewable energy sources to water and air purification and chemical synthesis.[2] In the past few years, titania-based materials have been at the focus of the search for new candidates suitable for photovoltaic and photocatalytic applications. However, the rather wide band gap of titania, which is close to 3 eV, represents a clear drawback and precludes its direct use under sunlight irradiation. This is because this rather broad band gap implies that a only small percentage of the incoming photons can be absorbed by the TiO_2 substrate, thus considerably reducing the efficiency of the photocatalytic process.[1] Doping with nonmetallic elements (n-doping) has been suggested as a method to reduce the band gap of titania by populating it with exceeding electrons coming from donor impurities.[3] To harvest the largest possible number of sunlight photons for photocatalytic processes, an ideal doped-TiO_2 material should have a band gap close to 1.2 eV. This would ensure an optimal performance under sunlight irradiation.[5] Nevertheless, the situation is not that simple since several factors influence the performance of the resulting photocatalytic system, and parameters such as the position of the band edges of the valence and conduction bands have to be taken into account; these should fit with redox potential of the reaction substrate.[6] Also, kinetic effects concerning the recombination of photogenerated holes and free electrons are relevant and are likely to play a significant role.[4]

From the brief discussion above, it is already clear that the photocatalytic process has a very complex nature where several interconnected elementary steps play a role. Nevertheless, the magnitude of the band gap remains the first parameter to be checked to screen out potentially interesting structures. Consequently, a vast amount of work has been devoted to engineer this electronic structure feature by designing a convenient n-doping of titania. Among the different solutions, nitrogen doping appears to be especially attractive, and various studies concerning nitrogen doping of different titania phases have been published (see ref 4 and references therein). Another potential candidate for reducing the band gap of titania is fluorine doping, and even if the information about the resulting doped systems is less exhaustive than in the case of doping with nitrogen, there is evidence that the photocatalytic activity of TiO_2 toward the organic pollutant mineralization increases in

Received: February 9, 2012
Revised: May 16, 2012
Published: May 23, 2012

the presence of F and, more importantly, under both UV[7] and visible light.[8] Interestingly, it has been shown that anatase, brookite, and rutile phases are all present in TiO_2 nanocrystals depending on the preparation conditions.[7,9−11] It has been mentioned that the presence of F alters the relative concentration of the different polymorphs[7] but also that the presence of heterojunctions between the different phases enhances the photocatalytic activity.[12] There is also a clear interplay between acid/basic media and the relative concentration of each of the TiO_2 polymorphs,[13] although this appears to be highly complex. The interest in TiO_2 nanoparticles containing brookite has recently been enhanced by the report of remarkable high photocatalytic activity of anatase−brookite−rutile composite TiO_2 nanocrystals with a narrow particle size distribution.[14]

F-doping in itself has become a most relevant topic because of the recently discovered fluorine-based stabilization of highly active anatase {001} facets in anatase titania nanocrystals.[15] In nonconventional powders with morphology controlled crystals, it is expected that the presence of only one crystal phase will suffice to achieve high-quality materials because both oxidation and reduction reactions are expected to happen in different facets of the same crystalline particle.[16] Fluorine is the most common surfactant or capping agent for morphology control of TiO_2 surfaces, and any conceivable preparation method will most certainly lead to partial diffusion of fluorine into the host structure and, hence, to F-doping of the bulk material. Fluorine doping of TiO_2 has already been studied from a more fundamental point of view. In particular, in a joint experimental−computational work, Czonska et al.[17] performed some simulation of substitutional F in the anatase bulk. Later, these authors extended their work to the case of N−F codoping.[18] However, these studies are limited to the anatase phase, and the presence of oxygen vacancies is considered only in the absence of dopants.[19] In a related study, Sun et al.[20] considered the interaction of water with a fluorine-covered (001) anatase surface, but the main focus is on the influence of the presence of F at the anatase (001) surface toward water dissociation rather than on the electronic structure modification. F doping and N−F codoping of the anatase (101) surface have also been considered by Chen and Tang who report that F-doping results in a band gap narrowing.[21]

In spite of the almost countless number of experimental and theoretical works on the photocatalytic properties of differently prepared stoichiometric, nonstoichiometric, and doped TiO_2 samples, there are several issues needing further attention. In particular, recent experimental trends point toward preparation of TiO_2 through low-cost/high-yield synthesis techniques that could eventually lead to a new generation of ultrareactive and cost-efficient materials. Mechanochemical doping is one of the main techniques being explored, and it is known that different phases tend to appear during the high-energy milling processes:[22] variable fractions of well-known and widely studied rutile and anatase are usually detected, but as mentioned above, also brookite tends to appear, often with positive effects on photocatalysis, although the amount of this phase is strongly dependent on preparation conditions.[7] In addition, it is known that a balance between anatase and rutile phases is a key ingredient for the current commercial TiO_2-based photocatalyst to work properly. This is often explained by assuming that the anatase phase provides favorable sites for oxidation reactions, while the rutile phase provides favorable sites for the accompanying reduction reactions. Therefore, the joint appearance of rutile and anatase during mechanochemical F-doping experiments is also expected, and a consistent and simultaneous study of the properties of each phase will provide a basic framework for understanding the average properties that are later observed in experiments.

Given the extreme complexity of polycrystalline nanoparticles, a strategy for a theoretical modeling based on quantum chemistry and/or solid state physics methods of electronic structure is to treat several ideal simple structures separately, to identify the most stable configurations and the underlying physics. This is precisely the approach followed in the present work to obtain a comprehensive picture of the effect of fluorine doping on TiO_2. Henceforth, we present a systematic study of F-doped bulk titania by considering explicitly the rutile, anatase, and brookite polymorphs. In particular, band gaps and electronic properties are described in detail. The combined effect of doping and oxygen vacancy is also considered, and finally, the thermodynamic stability of the doped phases is discussed.

Methodological Considerations and Computational Details. Before describing the theoretical approach used in the present work, we find it convenient to point out that the characterization of metal oxides by means of quantum mechanical simulation is a complicated issue. Generally speaking, methods based on the density functional theory (DFT), either in the commonly used Local Density Approach (LDA)[23,24] or, in particular, within the generalized gradient approximation (GGA),[25] provide a very good compromise between the accuracy of the calculation and the required computational effort, at least as long as the structural properties of oxides, and also ground state chemical reactivity, are concerned. However, the prediction of the magnitude of the band gap in these materials is a very delicate issue. In fact, LDA and GGA methods are both affected by the well-documented self-interaction error[26] which is responsible for the systematic underestimation of the magnitude of the band gap either by standard LDA or GGA functionals to the point that some well-characterized antiferromagnetic oxides such as NiO or superconducting cuprate parent compounds are predicted to be metallic.[27,28] A possible remedy to the shortcoming of LDA and GGA is the use of hybrid functionals like B3LYP[29,30] or PBE0[31] (or PBE1PBE[32]) which have become very popular and extremely useful in quantum chemistry and are nowadays increasingly used in condensed matter applications especially after the proposal of Scuseria et al.[33,34] to fix the incorrect asymptotic behavior of LDA and GGA by introducing range separation into the exchange component of the potential and the recent implementation in a periodic code using plane waves.[35−40] The common feature of hybrid DFT methods is that the exchange functional mixes the local Slater exchange with a part of exact nonlocal Fock exchange, the latter usually chosen in an empirical way. However, while hybrid functionals largely improve the description of band structure and band gap of oxides,[25,41−45] there is also evidence that the standard hybrid functionals tend to overestimate the calculated bad gap.[46]

Apart from the aforementioned hybrid approaches to circumvent the deficiencies of the LDA and GGA methods in the description of the electronic structure of oxides, one must mention the ad-hoc correction introduced in the so-called LDA $+U$ or GGA$+U$ approaches,[47,48] where the exchange-correlation functional is corrected by introducing a Hubbard-like term, usually affecting the 3d band only. The introduction of the U(3d) term penalizes double occupancy and, hence, is able to

properly represent complex antiferromagnetic insulators such as cuprates[49] including the rather complex family of $HgBa_2Ca_{n-1}Cu_nO_{2n+2}$ (n = 1, 2, 3) superconductor parent compounds.[49] Most often the effective U term is chosen in an empirical way by fitting to experiment, but the ratio between computational cost and accuracy justifies somehow the introduction of some empiricism. Nevertheless, including the U(3d) term only may not be enough in a compound such as TiO_2, where states mostly localized on oxygen atoms are the main constituent of the valence band. It has been proposed[50] that adding a similar term to the O(2p) level improves the description of the electronic structure of TiO_2, although authors caution that U(3d) values higher than 7 eV can lead to unphysical results. The use of a O(2p) has recently been shown to improve the description of the electronic features of CeO_2.[51] A similar strategy is adopted in the present work as discussed later on.

The more physically grounded methods based on the random phase approximation (RPA)[52] have proved to be very accurate in the prediction of band gaps of metal oxides.[53] However, the relative high computational cost involved in the RPA calculations makes this otherwise excellent choice unsuitable to handle the large supercell models which have to be adopted to describe doping in physically meaningful concentrations in oxides. A similar problem occurs when using hybrid methods within a plane wave basis set or even when employing a localized basis set because the necessary geometry optimization step becomes exceedingly costly. Therefore, the GGA+U appears to be an attractive approach and is the one chosen in the present work to study the doped phases, whereas the bulk of the three titania polymorphs is studied using GGA, GGA+U, and hybrid functionals. The setting of the (U−J) parameter with the aim to tune the band gap with respect to the experiment introduces no doubt some empiricism in the adopted computational scheme. The choice to adopt the same parameter for O and Ti, however, confines the arbitrariness to a level which is in line with widely accepted DFT schemes: the very popular B3LYP, for instance, has three arbitrarily fitted parameters, one of them concerning the amount of exact Fock exchange included in the exchange-correlation functional.

The DFT-based calculations reported in the present work have been carried out with the version 5.2 of the VASP package.[54] The standard DFT part of the calculations has been carried out adopting the PBE form of the GGA exchange-correlation functional,[55] whereas the hybrid calculations employ the B3LYP, PBE0, and HSE06[33] functionals. The effective U potential has been added within the scheme suggested by Dudarev,[47] and the U value has been chosen by comparing to experiment but constraining U(3d) and U(2p) to be the same, to avoid an excessive parametrization. In the case of rutile (anatase), we varied U between 2 and 6 eV, and the band gap thus predicted varies between 1.96 and 2.69 eV (2.54 and 2.95). Larger values of U can slightly increase the band gap, but they are also likely to introduce spurious effects discussed by Park et al.[50] Therefore, U = 6 eV for both Ti(3d) and O(2p) bands has been found to provide the best possible comparison to experiment. The Ti(3p,4s,3d), O(2s,2p), and F(2s,2p) electrons are treated as valence states. The valence states are expanded in a plane wave basis set within a cutoff of 400 eV for the kinetic energy. The effect of the core electrons in the valence density is described through the projector augmented wave (PAW) method.[56,57] The primitive cells' parameters obtained via X-ray diffractions[58−60] have been relaxed using a cutoff of 900 eV and a Monkhorst-Pack[61] grid of 8 × 8 × 4 K points for anatase, 6 × 6 × 8 for rutile, and 8 × 8 × 4 for brookite, respectively. The structures have been relaxed within a gradient threshold of 0.005 eV/Å. The larger supercells employed to study F-doping (vide infra) have been treated with a 2 × 2 × 2 K-mesh.

Model Structures. Rutile and anatase exhibit a tetragonal primitive cell, while brookite is orthorhombic; Figure 1 shows a view of rutile, anatase, and brookite along the [010] direction. In a first step, cell parameters and internal coordinates of atoms in the primitive cells are optimized using several DFT-based methods. Then, in a second step, models for the F-doped structures are built for a realistic concentration of this point defect. Thus, a single F-for-O substitution has been performed on supercells large enough to keep the fluorine concentration close to 1%. For anatase, a 3 × 3 × 2 supercell is adopted corresponding to a $Ti_{48}O_{96}$ repeated unit. For rutile, a 3 × 3 × 3 supercell ($Ti_{54}O_{108}$) is necessary to keep such a low defect concentration, whereas for brookite a 1 × 2 × 2 supercell is sufficient ($Ti_{48}O_{96}$).

Figure 1. View of the atomic structure of rutile, anatase, and brookite along the [010] direction. Ti centers are represented by black and oxygen white spheres, respectively.

RESULTS AND DISCUSSION

Stoichiometric Rutile, Anatase, and Brookite. The relaxed lattice parameters for rutile, anatase, and brookite obtained with different functionals are summarized in Table 1. In the case of rutile, a more systematic study has been carried out which included two GGA functionals (PW91 and PBE), on-site corrected PBE+U, and several hybrid functionals (PBE0, B3LYP, and HSE06). Comparing to experimental data, it appears that HSE06 provides the best performance, as in all the symmetry unconstrained parameters the discrepancy from the experiment is on the order of magnitude of 10^{-3} Å only. As a result, there is a negligible underestimation of the cell volume (−0.6%). On the contrary, the popular B3LYP hybrid functional slightly overestimates the cell volume (2.3%), corresponding to a concomitant error of the order of 10^{-2} Å on the cell parameters. The PW91 and PBE GGA functionals overestimate the cell volume even slightly more than B3LYP (2.4% and 2.5%, respectively). Finally, PBE+U provides the worse performance with an error of 6% on the cell volume. While this overestimation is large compared to hybrids, it is not dramatic, as it corresponds to a maximum deviation from the experiment of 0.1 Å. In the case of anatase, the calculated PBE and B3LYP structural parameters are in good agreement with

Table 1. Relaxed Cell Parameters of Rutile, Anatase, and Brookite with PBE and PBE+*U* (Å) and Δ*V*% Compared to the Experiment

		a	*b*	*c*	Δ*V*%
rutile	PW91	4.648	4.648	2.968	2.4
	PBE	4.652	4.652	2.970	2.5
	PBE+*U*	4.671	4.671	3.046	6.2
	PBE0	4.583	4.583	2.943	−1.2
	B3LYP	4.640	4.640	2.975	2.3
	HSE06	4.592	4.592	2.952	−0.6
	exp[a]	4.602	4.602	2.956	–
anatase	PW91	3.803	3.803	9.720	3.3
	PBE	3.806	3.806	9.734	3.6
	PBE+*U*	3.878	3.878	9.770	8.0
	B3LYP	3.797	3.797	9.757	3.4
	exp[b]	3.796	3.796	9.444	–
brookite	PBE	9.276	5.513	5.182	2.9
	PBE+*U*	9.366	5.561	5.296	7.2
	exp[c]	9.18	5.43	5.16	–

[a]Ref 58. [b]Ref 57. [c]Ref 59.

reported values obtained from different computational codes.[62,63] However, in terms of comparison to experimental cell volume, the overall situation is less satisfactory than in the case of rutile, although this has not been previously particularly highlighted. In fact, all the functionals employed in this work overestimate the cell volume. The PW91, PBE, and B3LYP exhibit an error of 3% with respect to the experiment, whereas PBE+*U* overestimates this property by 8%, with an error of 0.3 Å on the longer c lattice parameter. In the case of brookite, the calculations have been carried out with PBE and PBE+*U* only. The results are in line with what has been reported for rutile and anatase. The systematic study of the structure discussed above reveals that, at least as long as the structure is concerned, all the adopted density functional schemes provide reasonable performances and exhibit similar shortcomings. The hybrid functionals, in particular, the screened functional HSE06, are generally more accurate than GGA, while PBE+*U* performs slightly worse than the other DFT schemes.

Next, let us focus on the electronic structure features of these three polymorphs and, in particular, on the eigenvalue gap between the highest occupied band and the first unoccupied band, as reported in Table 2. The situation is as documented in the literature. Thus, GGA-type functionals lead to a serious underestimation: the PBE band gaps, for instance, span from 1.8 eV (rutile) to 2.1 and 2.3 eV for anatase and brookite, respectively, where the experimental values are 3.0, 3.2, and 3.1 eV, respectively. Note that even the qualitative band gap sequence is not in agreement with the experiment where rutile < brookite < anatase. Hybrid functionals, on the contrary, consistently overestimate the band gap. B3LYP and PBE0 provide band gaps between 3.7 and 4 eV quite above the experiment, although the absolute error is smaller than for the GGA functionals. The PBE+*U* method, applied according to the approach from Dudarev with an effective (*U*−J) parameter of 6 eV, leads to results in good agreement with the experimental data which is not surprising since this value is precisely chosen to reproduce experimental data in the best possible way. In many transition metal oxides such as iron oxide, both the valence band and the conduction band have a d-character, and applying the effective interatomic term (*U*−J) to the d-band of the metals only leads generally to good enough results.[64] The situation of TiO_2 is quite different; here the valence band is mainly constituted by O(2p), orbitals and it makes sense to apply the same (*U*−J) term to both Ti d and O p states as recently suggested for CeO_2.[51] As already mentioned, the value of 6 eV has been chosen on an empirical base; i.e., it yields band gaps in reasonable agreement with the experiment.

In the framework of the present work, it appears that the PBE+*U* method provides a good compromise between accuracy and computational effort, especially for the large supercells which are necessary to simulate isolated defects. A price is paid in terms of accuracy when the structure is calculated, but reasonable band gaps are provided, allowing us to evaluate the effects of F-substitution in the perspective of possible photocatalytic applications.

F-Doped Stoichiometric and Reduced Rutile, Anatase, and Brookite. To study the effect of F-doping on the different TiO_2 polymorphs considered in the present work, substitutional F-defects have been created by introducing one F atom on one O site in the corresponding supercells of rutile, anatase, and brookite described above. The supercell size is large enough to ensure that the concentration of defects remains close to 1% in all cases, which is also close to the typical experimental concentration of dopants. Compared to the stoichiometric systems, the substitution of F for O results in one extra electron in the supercell which leads to the concomitant appearance of a Ti^{3+}, as already reported in the literature.[19] Note, however, that the physically correct description involving one reduced Ti^{3+} center only with a well-localized spin density requires us to use either hybrid functionals, or the already commented GGA+*U* approach.[19] This is clear from the left panel of Figure 2 which shows the

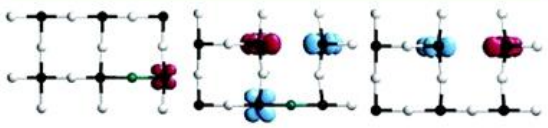

Figure 2. Calculated PBE+*U* spin density in F doped anatase (left), in an oxygen vacancy in anatase (right) and in a supercell containing both F and oxygen vacancy (center). Ti centers are represented by black, oxygen white, and fluorine green spheres, respectively.

spin density of F-substituted anatase calculated at the PBE+*U* level. A similar qualitative result is obtained for F-doped rutile and brookite. In all cases, a well-localized reduced Ti^{3+} center is created on a site directly connected with the fluorine atom. We will consider two different situations, one where, as described above, there is a simple substitution of F for O (doping of a stoichiometric sample) and one where F substitutes an O site close to an oxygen vacancy (doping of a reduced sample).

The qualitative effect of F substitution on the electronic structure of stoichiometric samples can be readily seen in the density of states plots summarized in Figure 3. A more accurate description of the optical absorption energies can be obtained by the calculation of the dielectric function. However, the lack of experimental data does not justify the use of a more expensive and accurate description of the excited states. In fact, the density of states shows that in the case of anatase and brookite the electronic state induced by doping is localized in the gap between the valence and conduction bands of TiO_2, whereas in the case of rutile it is located just within the valence

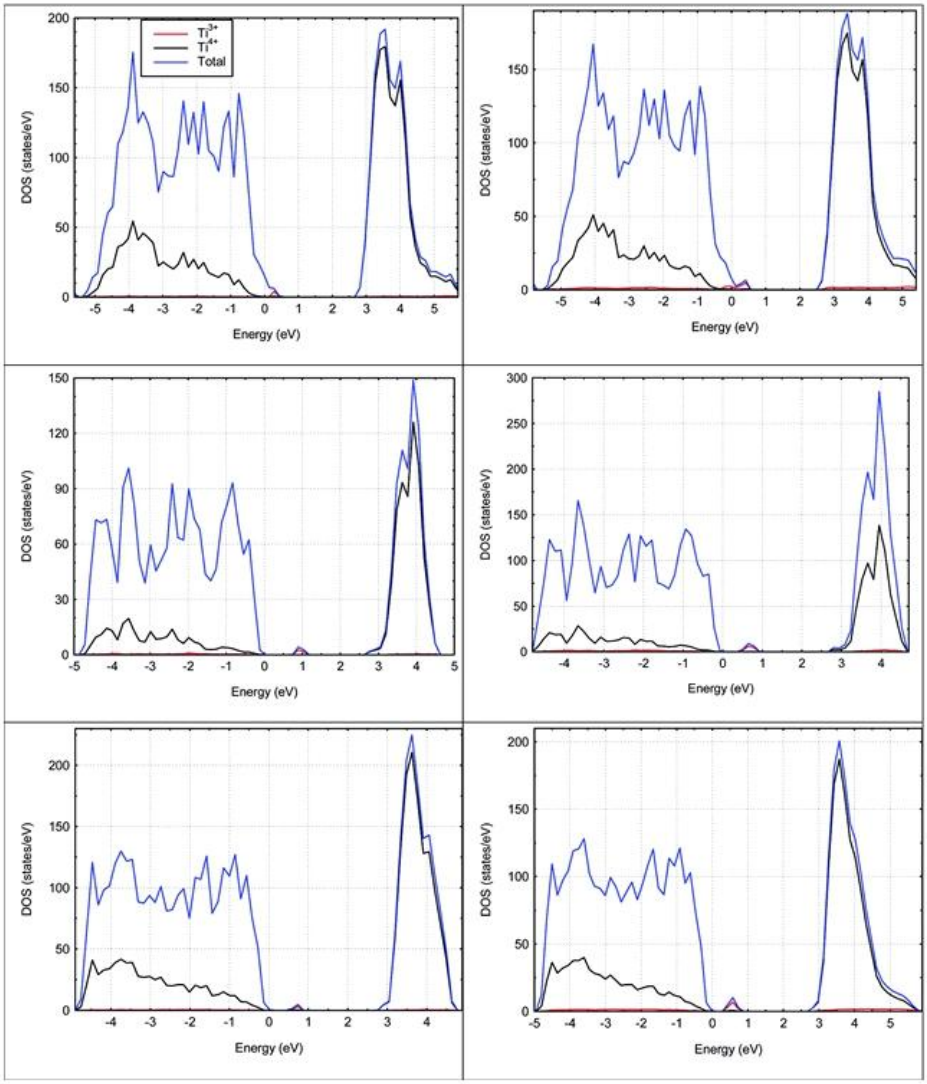

Figure 3. PBE+*U* density of states (DOS) of F-doped rutile (top), anatase (middle), and brookite (bottom). DOS for F-doped stoichiometric titania is reported on the left panels, whereas the right panels report the DOS for F-doped reduced titania.

band; this is schematically illustrated in the energy levels diagrams in Figures 4–6. Hence, the precise location of the impurity state depends notably on the polymorph considered, and the structural differences between the TiO_2 polymorphs are reflected in a remarkably different location of the gap state. In the case of F-substituted anatase (middle left panel in Figure 3), the gap state lies 1.2 eV above the valence band and only 1.8 eV apart from the empty conduction band (see Figure 5, Anatase-F) making it an excellent candidate for photocatalysis in the visible part of the solar spectrum, in agreement with previous work using the B3LYP functional within a local atomic basis set.[17] Nevertheless, it is important to remark that in the present PBE+*U* calculations the impurity state is closer to the top of the valence band than is predicted by the hybrid B3LYP calculations of Czoska et al.,[17] evidencing that the description of the electronic structure depends on the choice of the exchange-correlation functional. It is worth noting that while B3LYP and PBE+*U* lead to a qualitatively similar description of F-doped anatase, including the localization of the extra electron in a single Ti^{3+} site, a pure GGA approach fails to locate the impurity state in the gap. In fact, using the PBE functional, Yang and Zhang[65] found that, in spite of a good description of the crystal structure of anatase, the band gap of this polymorph and of the F-doped material is almost unaffected which is likely to be due to the delocalization of the extra electron in the valence band, as already pointed out by these authors. This is a clear indication that either the on-site correction *U* or a hybrid exchange-correlation potential is required to properly describe the electronic structure of these materials. However, one must also warn that the numerical predictions exhibit notable dependency from the adopted functional and must be taken with care. In the cases of F-doped rutile and brookite, the

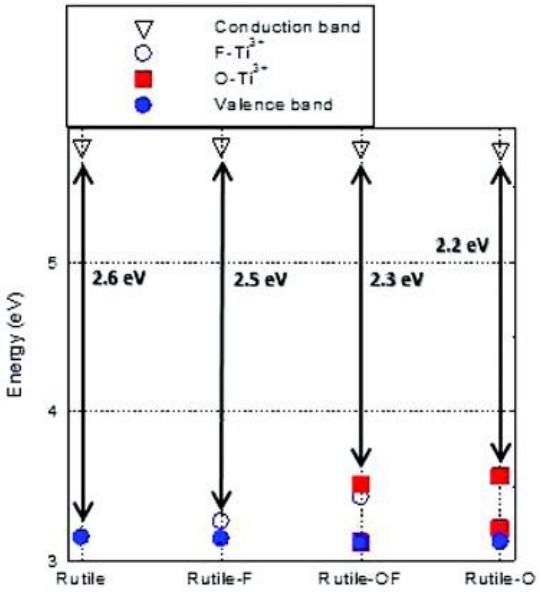

Figure 4. Electronic levels of stoichiometric rutile, F-doped stoichiometric rutile, F-doped reduced rutile, and reduced rutile.

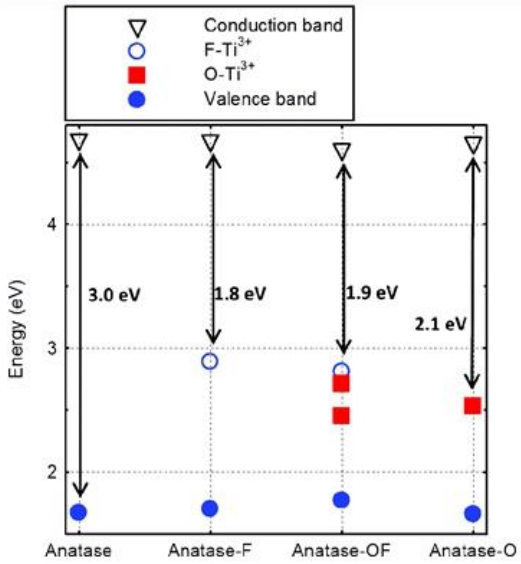

Figure 5. Electronic levels of stoichiometric anatase, F-doped stoichiometric anatase, F-doped reduced anatase, and reduced anatase.

impurity state introduced by doping is far apart from the conduction band (2.5 and 2.2 eV, respectively, as shown in Figures 4 and 6) and thus very close to the top of the valence band. Clearly, F-doping of these two polymorphs will not help too much to increase the photocatalytic activity of this material in the visible.

Next we consider F-doping on supercell models of reduced titania. We already mentioned that two situations are possible depending on whether the F is close to or far from the oxygen vacancy. We will only consider the former since the electronic

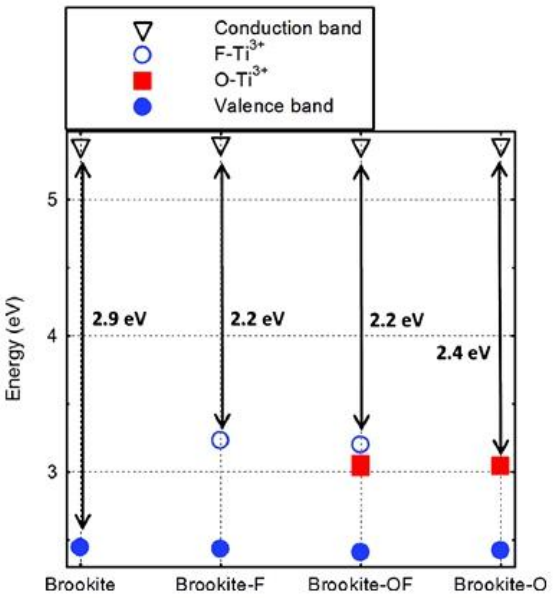

Figure 6. Electronic levels of stoichiometric brookite, F-doped stoichiometric brookite, F-doped reduced brookite, and reduced brookite.

Table 2. Calculated and Experimental Band Gap (eV) of Rutile, Anatase, and Brookite

	PW91	PBE	PBE0	B3LYP	HSE06	PBE+*U*	Exp
rutile	1.83	1.78	4.24	3.68	3.57	2.65	3.0
anatase		2.11	--	4.01	--	3.01	3.2
brookite	–	2.31	--	--	--	2.94	3.1

structure of the latter is just the superposition of the F-doped and oxygen vacancy cases. In any case, the creation of an oxygen vacancy in the bulk leads to two Ti^{3+} centers located in the cavity where the O has been removed as shown in Figure 2 (right panel), and the two unpaired electrons antiferromagnetically coupled even in a triplet high spin state are very close in energy (around 1 kJ/mol). The removal of one O atom leads to two electrons in the supercell which, as in the case of the F-substitution, are localized Ti^{3+} states located in the gap and separated from the conduction band by 2.2 eV (reduced rutile), 2.1 eV (reduced anatase), and 2.4 eV (reduced brookite). Figures 4–6 provide a schematic diagram of the electronic structure of the stoichiometry, reduced, F-doped stoichiometric, and F-doped reduced polymorphs of TiO_2. We now center our attention on the simultaneous presence of a F substitution and an oxygen vacancy. This leads to three unpaired electrons per unit cell well localized on three reduced Ti atoms. Also in this case, the low spin doublet configuration is slightly more stable than the high spin quadruplet. The present calculations also suggest that F substitution on a site close to the oxygen vacancy is energetically slightly more favorable as compared with the case where the two point defects are well separated. Figures 4–6 show that the states introduced by the oxygen vacancy lie slightly below those corresponding to the F impurity, and as a result, the energy between the gap states and the bottom of the conduction band remains unaltered: 2.3, 1.9,

and 2.2 eV for F-doped reduced rutile, anatase, and brookite, respectively.

Finally, we comment on the thermodynamic stability of F-substituted structures at 0 K which has been estimated by calculating the ΔE of the following exchange reaction\

$$(TiO_2)_x + \frac{1}{2}F_2 \rightarrow TiOF(TiO_2)_{x-1} + \frac{1}{2}O_2 \quad (1)$$

The results (normalized per TiO_2 formula unit) reported in Table 3 show that F-substitution turns out to be thermodynamically favored in all cases with an energy gain of 2.3 kJ/mol for brookite and almost 2 kJ/mol for both rutile and anatase.

Table 3. Energy Cost for F-Doping in Rutile, Anatase, and Brookite Normalized per TiO_2 Unit (kJ/mol)[a]

	F-sub	F-int	Vac-F-close	Vac-F-far
rutile	−1.99	--	−2.41	−2.32
anatase	−1.96	+0.15	−1.98	−1.97
brookite	−2.31	--	−2.31	−2.30

[a]Negative values indicate that F-doping is energetically favorable. F-sub stands for direct substitution of O by F; F-int corresponds to interstitial F; Vac-F-close indicates O substitution by F near an O vacancy; and Vac-F-far indicates O substitution by F far from an O vacancy.

We have also considered the possibility for F to occupy an interstitial site of the anatase lattice. The corresponding formation energy according to

$$(TiO_2)_x + \frac{1}{2}F_2 \rightarrow F{:}(TiO_2)_x \quad (2)$$

is found to be unfavorable by 0.15 kJ mol^{-1} per TiO_2 unit (Table 3), and hence, F substitution will always be preferred. Brookite and rutile exhibit a more compact crystal structure, and hence, it is likely that the presence of interstitial F will be even more unfavorable and will not be considered further.

Interestingly, the presence of an oxygen vacancy close to the F-substitution center (Vac-F-close in Table 3) has a remarkable stabilizing effect in the case of rutile but leaves the ΔE almost unaltered for anatase and brookite and, as mentioned earlier on, the Vac-F-close configuration is slightly preferable to a situation where the reduced centers are further apart. To investigate the thermodynamics of this substitution reaction in more detail and thus be able to investigate a range of temperatures of more practical interest, we have calculated the corresponding Gibbs energy change of reaction 1 following the approach recently proposed by Harb et al.[66] To this end, molecular optimizations and harmonic frequency calculations for F_2 and O_2 have been performed with the code CRYSTAL09,[67,68] to obtain entropic and enthalpic contributions at various temperatures and pressures. From these data, the phase diagrams in Figure 7

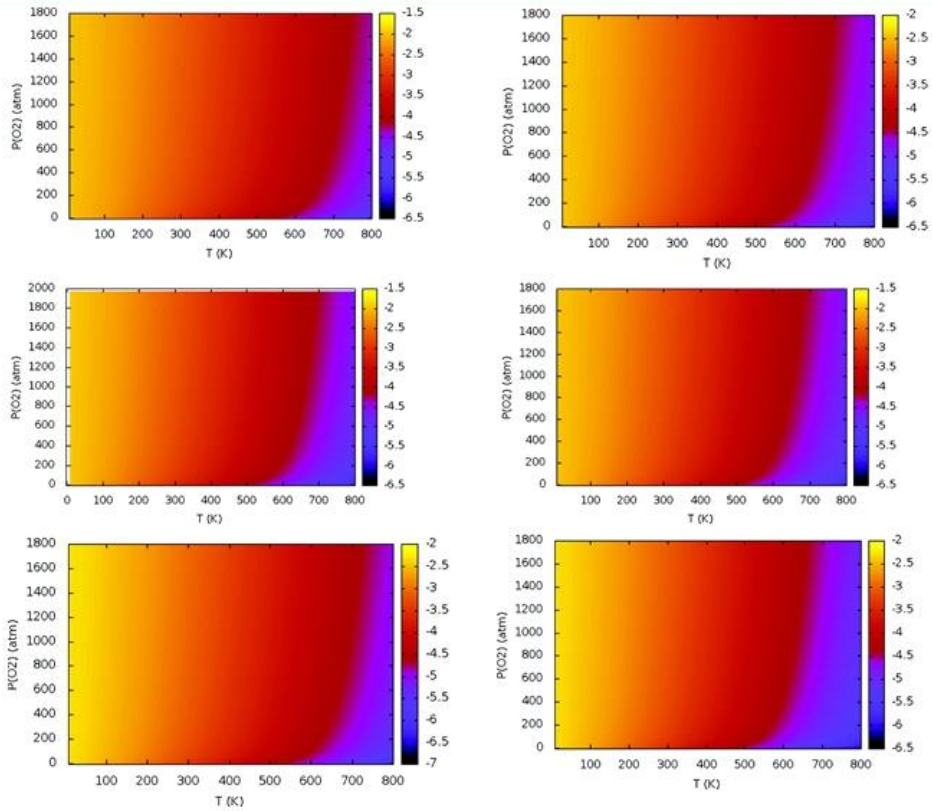

Figure 7. Calculated Gibbs energy change (ΔG in kJ/mol) for the substitution reaction (see eq 1 in the text) as a function of temperature and O_2 partial pressure for rutile (top), anatase (middle), and brookite (bottom). Both F-doped stoichiometric (left panels) and F-doped reduced (right panels) are considered.

have been obtained assuming a constant partial pressure of 10 atm for F. These diagrams show that high temperatures, together with a reducing atmosphere (low partial pressure of oxygen), make the reaction more favorable with negative ΔG at 800 K that might reach 7 kJ/mol per formula unit in the case of brookite and 6.5 kJ/mol in the case of anatase and rutile. Consequently, F-doping appears as feasible, although from the three investigated polymorphs only in the case of anatase it appears to have a hypothetical beneficial effect regarding its use in photocatalysis.

CONCLUSIONS

The electronic structure of stoichiometric, reduced, F-doped stoichiometric, and F-doped reduced rutile, anatase, and brookite polymorphs of TiO_2 has been investigated by means of periodic density functional theory based calculations. For the stoichiometric materials, a series of exchange-correlation functionals have been used including GGA, GGA+*U*, and hybrid type functionals. All functionals lead to rather accurate values of the structural parameters; however, not unexpectedly, the GGA approaches grossly underestimate the electronic band gap, and hybrid functionals provide a rather accurate description. GGA+*U* also provides an accurate prediction of the band gap, but this follows simply from the adequate (empiric) choice of the *U* parameter which, in the present work, has applied to the Ti(3d) and O(2p) bands. Nevertheless, the cost effectiveness of this approach makes it especially well suited to study F-doping in either stoichiometric or reduced samples.

The effect of F-doping on the stoichiometric and on the reduced rutile, anatase, and bookite polymorphs of titania has been studied using sufficiently large supercells which guarantee a defect concentration of ~1%. These models systems have been investigated using the PBE+*U* functional. The calculations show that F-doping of all polymorphs is thermodynamically favorable, especially at high temperatures and in the presence of a reducing atmosphere. Regarding the electronic structure of the doped titania polymorphs, the presence of substitutional F results, in all cases, in the appearance of well-localized Ti^{3+} gap states. Interestingly enough, the position of the impurity state relative to the bottom of the conduction band strongly depends on the particular crystal structure of each polymorph. Thus, anatase F-doping leads to states roughly in the middle of the band gap which are interesting in terms of potential photocatalytic activity under sunlight irradiation. However, for F-doped rutile and brookite, the states are very close in energy to the top of the valence band and are, hence, unlikely to produce a remarkable shrink in the electronic excitation energy. These results contribute to explain the success of F-doped anatase nanoparticles in promoting photocatalytic reactions. In any case, comparison with former computational works on F-doped anatase evidences that the precise location of the gap state depends not negligibly on the adopted exchange-correlation functional which calls for more accurate methods.

Finally, in terms of thermodynamic stability, F-doping of reduced rutile, anatase, and brookite appears to be slightly more favorable than doping of the stoichiometric materials, although the states induced by the presence of the oxygen vacancy are found to be always located below those induced by F doping and thus are not relevant to photocatalysis.

AUTHOR INFORMATION

Corresponding Author

*E-mail: francesc.illas@ub.edu.

Notes

The authors declare no competing financial interest.

ACKNOWLEDGMENTS

This research has been supported by Spanish MICINN through Program INNPACTO Project CASCADA IPT-120000-2010-19 and research grant FIS2008-02238. The authors are also grateful to *Generalitat de Catalunya* for partial support through grants 2009SGR1041 and XRQTC. Finally, FI acknowledges additional support through 2009 ICREA Academia award for excellence in research.

REFERENCES

(1) Hashimoto, K.; Irie, H.; Fujishima, A. *Jpn. J. Appl. Phys.* **2005**, *44*, 8269−8285.
(2) Fujishima, A.; Zhang, X.; Tryk, D. A. *Surf. Sci. Rep.* **2008**, *63*, 515−582.
(3) Chen, X.; Mao, S. S. *Chem. Rev.* **2007**, *107*, 2891−2895.
(4) Henderson, M. A. *Surf. Sci. Rep.* **2011**, *66*, 185−297.
(5) Kudo, A.; Miseki, Y. *Chem. Soc. Rev.* **2009**, *38*, 253−278.
(6) Osterloh, F. E. *Chem. Mater.* **2008**, *20*, 35−54.
(7) Yu, J. C.; Yu, J.; Ho, W.; Jiang, Z.; Zhang, L. *Chem. Mater.* **2002**, *14*, 3808−3816.
(8) Li, D.; Haneda, H.; Labhsetwar, N.; Hishita, S.; Ohashi, N. *Chem. Phys. Lett.* **2005**, *401*, 579−584.
(9) Yu, J. C.; Yu, J. G.; Ho, W. K.; Zhang, L. Z. *Chem. Commun.* **2001**, 1942−1943.
(10) Luo, H. M.; Takata, T.; Lee, Y. G.; Zhao, J. F.; Domen, K.; Yan, Y. S. *Chem. Mater.* **2004**, *16*, 846−849.
(11) Luo, H. M.; Wang, C.; Yan, Y. S *Chem. Mater.* **2003**, *15*, 3841−3846.
(12) Yu, J. G.; Xiong, J. F.; Cheng, B.; Liu, S. W. *Appl. Catal., B* **2005**, *60*, 211−221.
(13) Yu, J. G.; Yu, J. C.; Leung, M. K. P.; Ho, W. K.; Cheng, B.; Zhao, X. J.; Zhao, J. C. *J. Catal.* **2003**, *217*, 69−78.
(14) Hu, S. Z.; Li, F. Y.; Fan, Z. P. *Asian J. Chem.* **2012**, *24*, 1135−1144.
(15) Yang, H. G.; Sun, C. H.; Qiao, S. Z.; Zou, J.; Liu, G.; Smith, S. C.; Cheng, H. M.; Lu, G. Q. *Nature* **2008**, *453*, 638−641.
(16) D'Arienzo, M.; Carbajo, J.; Bahamonde, A.; Crippa, M.; Polizzi, S.; Scotti, R.; Wahba, L.; Morazzoni, F. *J. Am. Chem. Soc.* **2011**, *133*, 17652−17661.
(17) Czoska, A. M.; Livraghi, S.; Chiesa, M.; Giamello, E.; Agnoli, S.; Granozzi, G.; Finazzi, E.; Di Valentin, C.; Pacchioni, G. *J. Phys. Chem. C* **2008**, *112*, 8951−8956.
(18) Di Valentin, C.; Finazzi, E.; Pacchioni, G.; Selloni, A.; Livraghi, S.; Czoska, A. M.; Paganini, M. C.; Giamello, E. *Chem. Mater.* **2008**, *20*, 3706−3714.
(19) Di Valentin, C.; Pacchioni, G.; Selloni, A. *J. Phys. Chem. C* **2009**, *113*, 20543−20552.
(20) Sun, C.; Selloni, A.; Du, A.; Smith, S. C. *J. Phys. Chem. C* **2011**, *115*, 17092−17096.
(21) Chen, Q. L.; Tang, C. Q. *Acta Phys. Chim. Sin.* **2009**, *25*, 915−920.
(22) Shu, Y.; Yamaki, H.; Zhang, Q. W.; Komatsu, M.; Wang, J. S.; Qing, T.; Saito, F.; Sato, T. *Solid State Ionics* **2004**, *172*, 205−209.
(23) Vosko, S. H.; Wilk, L.; Nusair, M. *Can. J. Phys.* **1980**, *58*, 1200−1211.
(24) Perdew, J. P.; Zunger, A. *Phys Rev. B* **1981**, *23*, 5048−5079.
(25) Perdew, J. P.; Chevary, J. A.; Vosko, S. H.; Jackson, K. A.; Pederson, M. R.; Singh, D. J.; Fiolhais, C. *Phys. Rev. B* **1992**, *46*, 6671−6687.
(26) Dagotto, E. *Rev. Mod. Phys.* **1994**, *66*, 763−840.

(27) Moreira, I.; de, P. R.; Illas, F.; Martin, R. L. *Phys. Rev. B* **2002**, *65*, 155102.
(28) Rivero, P.; Moreira, I.; de, P. R.; Illas, F. *Phys. Rev. B* **2010**, *81*, 205123.
(29) Becke, A. D. *J. Chem. Phys.* **1993**, *98*, 5648−5652.
(30) Lee, C.; Yang, W.; Parr, R. G. *Phys. Rev. B* **1988**, *37*, 785−789.
(31) Adamo, C.; Barone, V. *J. Chem. Phys.* **1999**, *110*, 6158−6170.
(32) Ernzerhof, M.; Scuseria, G. E. *J. Chem. Phys.* **1999**, *110*, 5029−5036.
(33) Vydrov, O. A.; Scuseria, G. E. *J. Chem. Phys.* **2006**, *125*, 234109.
(34) Heyd, J.; Scuseria, G. E.; Ernzernhof, M. *J. Chem. Phys.* **2003**, *518*, 8207−8215; *ibid.* **2006**, *124*, 219906(E).
(35) Heyd, J.; Scuseria, G. E. *J. Chem. Phys.* **2004**, *120*, 7274−7280.
(36) Heyd, J.; Scuseria, G. E. *J. Chem. Phys.* **2004**, *121*, 1187−1192.
(37) Heyd, J.; Peralta, J. E.; Scuseria, G. E.; Martin, R. L. *J. Chem. Phys.* **2005**, *123*, 174101.
(38) Peralta, J. E.; Heyd, J.; Scuseria, G. E.; Martin, R. L. *Phys. Rev. B* **2006**, *74*, 073101.
(39) Hay, P. J.; Martin, R. L.; Uddin, J.; Scuseria, G. E. *J. Chem. Phys.* **2006**, *125*, 034712.
(40) Rivero, P.; Moreira, I.; de, P. R.; Scuseria, G. E.; Illas, F. *Phys. Rev. B* **2009**, *79*, 245129.
(41) Feng, X. B.; Harrison, N. M. *Phys. Rev. B* **2004**, *69*, 035114.
(42) Muñoz, D.; Harrison, N. M.; Illas, F. *Phys. Rev. B* **2004**, *69*, 085115.
(43) Perry, J. K.; Tahir-Kheli, J.; Goddard, W. A. *Phys. Rev. B* **2001**, *63*, 144510.
(44) Feng, X. B.; Harrison, N. M. *Phys. Rev. B* **2004**, *70*, 092402.
(45) Moreira, I.; de, P. R.; Dovesi, R. *Int. J. Quantum Chem.* **2004**, *99*, 805−823.
(46) Tran, F.; Blaha, P. *Phys. Rev. Lett.* **2009**, *102*, 226401.
(47) Anisimov, V. I.; Zaanen, J.; Andersen, O. K. *Phys. Rev. B: Condens. Matter Mater. Phys.* **1991**, *44*, 943.
(48) Dudarev, S. L.; Botton, G. A.; Savrasov, S. Y.; Humphreys, C. J.; Sutton, A. P. *Phys. Rev. B: Condens. Matter Mater. Phys.* **1998**, *57*, 1505.
(49) Moreira, I.; de, P. R.; Rivero, P.; Illas, F. *J. Chem. Phys.* **2011**, *134*, 074709.
(50) Park, S. G.; Magyari-Köpe, B.; Nishi, Y. *Phys. Rev. B* **2010**, *2*, 115109.
(51) Plata, J. J.; Márquez, A. M.; Sanz, J. F. *J. Chem. Phys.* **2012**, *136*, 041101.
(52) Hedin, L. *Phys. Rev. A* **1965**, *139*, 796−823.
(53) Shiskin, M.; Kresse, G. *Phys. Rev. B* **2007**, *75*, 235102.
(54) Kresse, G.; Furthmüller, J. *J. Comput. Mater. Sci.* **1996**, *6*, 15−50.
(55) Perdew, J. P.; Burke, K.; Ernzerhof, M. *Phys. Rev. Lett.* **1996**, *77*, 3865.
(56) Blöchl, P. *Phys. Rev. B* **1994**, *50*, 17953.
(57) Kresse, G.; Joubert, J. *Phys. Rev. B* **1999**, *59*, 1758.
(58) Djerdj, I.; Tonejc, A. M. *J. Alloys Compd.* **2006**, *413*, 159−174.
(59) Bokhimi, X.; Morales, A.; Pedraza, F. *J. Solid State Chem.* **2002**, *169*, 176−181.
(60) Štengl, V.; Králová, D. *Mater. Chem. Phys.* **2011**, *129*, 794−801.
(61) Monkhorst, H. J.; Pack, J. D. *Phys. Rev. B* **1976**, *13*, 5188.
(62) Lazzeri, M.; Vittadini, A.; Selloni, A. *Phys. Rev. B* **2001**, *63*, 155409.
(63) Zhang, Y.; Lin, W.; Ding, K.; Li, J. *J. Phys. Chem. B* **2005**, *109*, 19270−19277.
(64) Toroker, M. C.; Kanan, D. K.; Alidoust, N.; Isseroff, L. Y.; Liao, P.; Carter, E. A. *Phys. Chem. Chem. Phys.* **2011**, *13*, 16644−16654.
(65) Yang, H. M.; Zhang, X. C. *J. Mater. Chem.* **2009**, *19*, 6907−6914.
(66) Harb, M.; Sautet, P.; Raybaud, P. *J. Phys. Chem. C* **2011**, *115*, 19394−19404.
(67) Dovesi, R.; Orlando, R.; Civalleri, B.; Roetti, C.; Saunders, V. R.; Zicovich-Wilson, C. M. *Z. Kristallogr.* **2005**, *220*, 571−573.
(68) Dovesi, R.; Saunders, V. R.; Roetti, C.; Orlando, R.; Zicovich-Wilson, C. M.; Pascale, F.; Civalleri, B.; Doll, K.; Harrison, N. M.; Bush, I. J.; et al. *CRYSTAL09 User's Manual*; University of Torino: Torino, Italy, 2009.

3.1.1.2 Performance of a modified hybrid functional in the simultaneous description of stoichiometric and reduced TiO_2 polymorphs

PCCP

PAPER

View Article Online
View Journal | View Issue

Cite this: *Phys. Chem. Chem. Phys.*, 2016, 18, 12357

Performance of a modified hybrid functional in the simultaneous description of stoichiometric and reduced TiO_2 polymorphs†

Kyoung Chul Ko,[ab] Oriol Lamiel-García,[a] Jin Yong Lee*[b] and Francesc Illas*[a]

Conventional density functionals with either the local density approximation (LDA) or the generalized gradient approximation (GGA) form of the exchange–correlation potential fail to describe the electronic structure of a large number of metal oxides. Both the LDA and the GGA grossly underestimate the band gaps of these materials which severely affect the description of oxygen vacancy point defect states in reduced samples. To find a pragmatic approach to simultaneously and accurately describe the atomic and electronic structures of the most common TiO_2 polymorphs, we explore the effect of the percentage of exact, non-local, Fock exchange on the electronic structure of stoichiometric rutile and anatase. From these results, a modified hybrid functional is proposed to properly describe the atomic structures, formation enthalpies and electronic structures of rutile and anatase and, at the same time, the results of reduced samples are also in good agreement with the available experimental results. The present approach can be safely used to accurately describe numerous TiO_2 based materials containing defects or realistic nanoparticles for which the required large unit cells or system sizes hinder the use of GW related techniques.

Received 9th February 2016,
Accepted 1st April 2016

DOI: 10.1039/c6cp00912c

www.rsc.org/pccp

1. Introduction

Titanium dioxide (TiO_2) has attracted much attention due to its numerous applications such as in photocatalysis,[1] solar cells[2] and energy and environment.[3,4] In particular, the discovery of Fujishima and Honda that irradiation of TiO_2 with light in the ultraviolet region triggers water splitting[5] has resulted in enormous efforts in the search for efficient TiO_2 based photocatalysts,[4] and the possibility to prepare photocatalysts with activity under sun light has become a crucial issue. Several recent studies reveal that the presence of point defects in TiO_2 greatly influences the electrical,[6,7] optical[8,9] and photocatalytic properties[10–13] of this material. Among the different types of point defects in TiO_2 and related materials, oxygen vacancies (O_V) are known to play a key role in catalytic reactions as both adsorption and active sites.[14] The O_V defect is one kind of native defect, and also is easily formed during the preparation of TiO_2 materials.[15] In this regard, the electronic structure of the O_V defect state in TiO_2 systems is intimately connected to their catalytic and photocatalytic performance. Therefore, understanding and controlling the O_V defect in TiO_2 materials could be the fundamental step for designing an efficient photocatalyst.

In spite of the importance of O_V in TiO_2 materials already mentioned, several serious problems exist in the theoretical description of the electronic structure of these systems. In fact, periodic models are needed to properly describe these materials implying the use of methods based on density functional theory (DFT).[16] However, DFT based methods necessarily make use of an approximate form of the exchange and correlation potential and, because of the common way to compute the Coulomb in the Kohn–Sham implementation of DFT, the calculated results would inherently contain the so-called self-interaction error.[17] In addition, the conventional local density approximation (LDA) and generalized gradient approximation (GGA) functionals tend to predict highly underestimated band gaps.[16] This is a general trend usually referred to as the band gap problem in DFT based calculations. This shortcoming of standard LDA and DFT methods results in an incorrect description of mid gap states introduced by oxygen vacancies in TiO_2[18–20] and other reducible oxides.[21] For TiO_2, theoretical studies based on LDA and GGA approaches found that, as a consequence of the severe underestimation of

[a] Departament de Química Física & Institut de Química Teòrica i Computacional (IQTCUB), Universitat de Barcelona, c/Martí i Franquès 1, 08028 Barcelona, Spain. E-mail: francesc.illas@ub.edu; Fax: +34-93-402-1231; Tel: +34-93-402-1229
[b] Department of Chemistry, Sungkyunkwan University, Suwon 16419, Korea. E-mail: jinylee@skku.edu; Fax: +82-31-290-7075; Tel: +82-31-299-4560

† Electronic supplementary information (ESI) available: Computational details of formation enthalpy calculations, a summary of calculated band gaps and oxygen vacancy defect states reported in previous literature reports, calculated band gaps as a function of the amount of Hartree–Fock exchange, initial/final geometry, calculated energy, spin density distributions, DOS and pDOS for reduced rutile and anatase TiO_2 systems. See DOI: 10.1039/c6cp00912c

the band gap,[18–20] the O_V defect induced energy level was not even located within the band gap region. In addition to the failure in properly describing the position of the defect induced energy levels, the LDA and the GGA provided a qualitatively incorrect description of the electronic structure of the reduced systems. The creation of O_V results in the creation of Ti^{3+} centers which are clearly seen in the most recent electronic paramagnetic resonance (EPR) experiments[22,23] with the assignment confirmed by previous theoretical calculations.[24] Therefore the extra electrons left in the solid upon oxygen removal are well localized in these Ti^{3+} centers. The results obtained from the LDA and the GGA were inconsistent with the experimental observation from diverse spectroscopic techniques based on rutile samples, where the O_V defect induced energy level appeared 0.7–1.0 eV below the conduction band minimum (CBM),[25–28] and also failed to describe the localized nature of the trapped electrons.

To resolve the problem of abnormal strong delocalization effect on reduced TiO_2 systems it is necessary to go beyond the LDA and GGA schemes. In this sense, the DFT+*U* method and a variety of hybrid functionals have been employed to correct, at least in part, the self-interaction error inherent to the LDA and the GGA in describing the electronic structure of TiO_2 systems.[29–36] A comprehensive review has been reported recently by Di Valentin and Pacchioni.[37] In the DFT+*U* methods, the *U* parameter represents the screened on-site Coulomb interaction of Ti(3d) electrons although a second *U* parameter added to O(2p) further improves the results.[30,38] In the hybrid methods, a fraction of non-local Fock exchange is added which, even if applies to all electrons in the system, constitutes an external parameter (for further details, see the reviews in ref. 16 and 37). The amount of Fock exchange to be used constitutes an open issue and it has also been suggested to fix it based on the dielectric constant of the materials.[39] This approach has been recently used to investigate TiO_2 and other semiconducting oxides,[40] at first sight, it may seem to be a suitable *ab initio* alternative but one must realize that it also introduces information not included in the first principles Hamiltonian.

Actually, a number of DFT+*U* and hybrid functional calculations successfully predicted the position of the O_V energy levels as summarized in the ESI† (Table S1). In the DFT+*U* method, the results obviously depend on the value of the *U* parameter which is usually in the 2.0–4.0 eV range. This choice leads to O_V energy levels between 0.1 and 1.6 eV below the CBM, which seems to be qualitatively correct. However, the calculated band gaps were markedly underestimated over 10–34% (see Table S1, ESI†), and reproducing the experimental band gaps by adding just one *U* term for the Ti(3d) states has not been possible.[41] In fact, a large *U* parameter value of 6 eV on Ti(3p) and O(2p) is required to accurately reproduce the band gap of anatase, rutile and brookite[42–44] but in this case the states corresponding to O_V are too deep in the gap and close to the top of the valence band.[45] On the other hand, the hybrid functional normally gives an overestimated band gap for TiO_2 polymorphs. In fact, conventional hybrid functionals such as the popular B3LYP[46] containing 20% of Fock exchange (%Fock) overestimate the band gap of insulating oxides by 11–23%.[47] The PBE0 hybrid functional,[48,49] 25% of Fock exchange added to the standard PBE form[50] of the GGA functionals, leads to an even larger overestimation. A more accurate description of the band gap of rutile (3.05 eV) is reached[35] by means of the so-called screened hybrid functional. This functional, usually referred to as HSE (or HSE06),[51,52] is a modification of PBE0 and hence contains 25% of Fock exchange but introduces a second (screening) parameter. Nevertheless, one must note that subsequent HSE calculations by Déak *et al.* using the same code and the same supercell report a rather larger value for the band gap of rutile (3.37 eV).[36] The difference between the two HSE calculations can be attributed to the different amounts of Fock exchange used; Janotti *et al.*[35] used HSE with a reduced value of 20% of Fock exchange whereas Déak *et al.*[36] used the standard 25% value proposed in the original work of Heyd *et al.*[51,52] In any case, different hybrid functionals resulted in the O_V energy levels between 0.5 and 1.35 eV below the CBM (see Table S1, ESI†). Hence, due to the overestimations of the band gap most hybrid functionals predict O_V defect state levels too deep in the gap. Many-body approaches based on the so-called GW methods have been suggested to overcome the problems exhibited by the DFT methods. However, these methods are computationally expensive and geometry optimization, required to properly describe the structure relaxation induced by the presence of O_V becomes unfeasible. Consequently, GW calculations are usually carried out on DFT+*U* or hybrid optimized structures.[53]

From the above discussion it is clear that DFT+*U* and standard hybrid functionals fail to simultaneously reproduce the magnitude of the band gap and the position of O_V induced energy levels in TiO_2 polymorphs. The difference in the calculated band gap values in the HSE calculations of Janotti *et al.*[35] and Déak *et al.*[36] clearly shows that the amount of Fock exchange is a key parameter and may be system dependent. This is in full agreement with previous work showing that 35% of Fock exchange is required to properly describe the atomic and magnetic structures of NiO.[54] This work strongly suggests tuning the amount of Fock exchange so as to reproduce the known observables, as followed by Alkauskas *et al.*[55] In this study, we follow this strategy to explore whether a modified hybrid functional is able to simultaneously and correctly describe the crystal and electronic structures of stoichiometric and reduced (O_V containing) TiO_2 polymorphs overcoming those drawbacks of the DFT method. In order to achieve this goal, firstly we tried to find the optimal value of %Fock in the PBE0 functional to estimate the band gaps of bulk rutile and anatase from the Kohn–Sham band structure. One must point out that this is not rigorous since many-body effects in the quasi particles are lacking even when using hybrid functionals. However, this is a broadly used approach when GW type calculations are unaffordable. By tuning the %Fock, Moreira *et al.*[54] were able to successfully describe the electronic and magnetic structures of NiO. Very recently, Gerosa *et al.*[40] tuned the %Fock for TiO_2 using information from the dielectric constant and found good agreement between the calculated Kohn–Sham gap, GW results and experimental values. In a second step, the newly defined functional containing the optimal %Fock has been used to calculate the band gap of brookite (not used at the tuning step) and the electronic structures

and physical properties for pristine and reduced TiO_2 rutile and anatase. The accuracy and benefit of the modified functional of the present approach will be established by comparing the calculated results to those obtained with the standard PBE functional as well as to available experimental data. We expect that the rationally proposed modification of the PBE0 functional will be helpful in the study of photocatalysts based on TiO_2 nanoparticles containing hundreds or thousands of atoms.

2. Material models and computational details

Periodic density functional calculations using the standard PBE functional and a modified hybrid with various amounts of Fock exchange have been carried out for stoichiometric and reduced rutile and anatase polymorphs of TiO_2. In the first step, experimental values were used to define the primitive cell parameters of stoichiometric rutile and anatase, and single point calculations were carried out to obtain the band gap as a function of the amount of Fock exchange. The unit cell for bulk rutile and anatase contained 6 and 12 atoms, respectively. In the second step, geometry optimization for the bulk was carried out using the fraction of Fock exchange which reproduces the band gap of rutile and anatase at the experimental structure. The convergence criteria for geometry relaxations were set to 10^{-3} eV Å^{-1}.

The same modified hybrid functional, hereafter denoted PBE*x*, was used to study the atomic and electronic structures of reduced rutile and anatase; *i.e.* supercells containing one oxygen vacancy (O_V). To this end, the bulk unit cells were conveniently enlarged to avoid an excessive concentration of oxygen vacancies as described in detail in Section 3.3.

The periodic density functional calculations were carried out including all electrons in the systems with the overall density described by means of a numeric atom-centered orbital. For stoichiometric systems, a tight grid and a tier-2 basis set were employed with scalar-relativistic effects treated at the scaled ZORA level.[56] Integration in the reciprocal space was carried out using $7 \times 7 \times 7$ and $8 \times 8 \times 8$ gamma centered *k*-point meshes. The same *k*-point meshes were used to compute the band structure of each polymorph which, in turn, was used to extract the band gap. For larger supercells containing O_V and the concomitant polaronic distortion, we adopted a light grid and a tier-1 basis set. For stoichiometric systems, results obtained from this computational setup do not significantly differ from those obtained using more accurate settings, as described in detail in the next section. For reduced systems, the supercells are large enough so that calculations at the Γ-point converge the total energy to within a tolerance of 10^{-2} eV Å^{-1}.

The formation enthalpy (ΔH_f) of pristine TiO_2 polymorphs has been computed as

$$\Delta H_f(Ti_nO_{2n}) = H(Ti_nO_{2n}) - nH(Ti) - nH(O_2) \quad (1)$$

Herein, H denotes the enthalpy for each component. For solids, the contributions for pressure (P) and volume (V) are very small and can be neglected. Thus, we assume that the internal energy of each solid state is almost equivalent to its enthalpy. Eqn (1) can be changed as

$$\Delta H_f(Ti_nO_{2n}) = U(Ti_nO_{2n}) - nU(Ti) - nH(O_2) \quad (2)$$

The value of $U(Ti_nO_{2n})$ is simply used as the calculated energy for pristine TiO_2 polymorphs whereas U(Ti) is the calculated atomic energy for hcp bulk Ti which was obtained employing the experimentally obtained crystal structure for Ti solids.[57] Hence, the lattice parameters were fixed accordingly and atomic positions in the unit cell were relaxed using the appropriate functional (PBE or PBE*x*) with $7 \times 7 \times 7$ gamma centered *k*-point meshes. For the O_2 molecule, the enthalpy contribution is obtained as in eqn (3) based on standard ideal gas, rigid-rotor, and harmonic oscillator approximations.

$$H(T) - H(0\,K) = \int_0^T C_p(T')dT' = k_B T\left(\frac{7}{2} + \frac{\Theta_\nu}{T}\frac{1}{e^{\frac{\Theta}{T}} - 1}\right) \quad (3)$$

where T is the absolute temperature and Θ_ν is the vibrational temperature. The factor 7/2 results from ideal gas and rigid-rotor approximations for a homonuclear diatomic molecule. And Θ_ν is defined as

$$\Theta_\nu = \frac{\hbar\nu}{k_B} \quad (4)$$

where ν denotes vibrational frequency, and $\hbar$ and k_B are Planck's and Boltzmann's constants, respectively. The optimization and vibrational frequency calculations for an oxygen molecule were carried out to obtain this enthalpy contribution using the appropriate functional. Calculations related to formation enthalpy used a more stringent convergence criteria of 10^{-3} eV Å^{-1} for geometrical relaxations. The zero-point energy correction for oxygen was also considered. It should be noted that our calculated enthalpy formation energies are obtained by using the temperature values of standard conditions (T = 298.15 K).

All calculations were carried out using the FHI-aims code[58,59] running on the MareNostrum supercomputer of the Barcelona Supercomputing Center. It is worth pointing out that the calculations performed using the hybrid functionals (PBE0 or suitable modifications of this functional) are time consuming and required using systematically 512 cores in the case of the primitive cells and 1024 for the largest supercell.

3. Results and discussion

3.1. Defining the PBE*x* functional

In a preliminary step, the effect of Fock exchange on the quantitative prediction of the band gap of TiO_2 systems was investigated and, in order not to mix different effects, the experimental crystal structure[60,61] for rutile and anatase TiO_2 bulk polymorphs was employed. Starting with the PBE0 potential having 25% of Fock exchange, this parameter was varied from 0% to 60% to calculate the band gaps of these materials. We must point out again that the band gap estimated from the Kohn–Sham band structure is not fully justified by theory but it constitutes a useful and pragmatic approach and is the one chosen here.

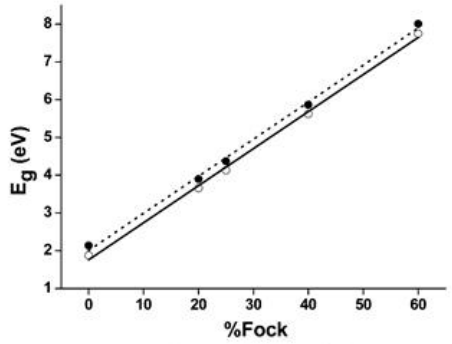

Fig. 1 Calculated band gaps (E_g in eV) of rutile (○) and anatase (●) TiO_2 as a function of %Fock. A proper linear fit leads to $E_g = 0.098 \times$ %Fock + 1.762 and $E_g = 0.098 \times$ %Fock + 2.009 for rutile and anatase, respectively, and with $r^2 = 0.997$ in both cases.

As seen in Fig. 1 and ESI† (Table S2) the calculated band gap increases with %Fock. However, the trend follows an apparent linear relationship for both rutile and anatase polymorphs with a slope of 0.098 for both polymorphs. This implies that a 10% increase in %Fock increases the calculated PBE band gap by almost 1 eV. Hence, the hybrid PBE0 functional, which has 25% of Fock exchange, predicts band gaps of 4.1 eV and 4.4 eV for rutile and anatase, respectively, which are substantially larger than the well-known experimental values of 3.03 eV and 3.20 eV for rutile and anatase,[62–64] although temperature effects cannot be disregarded.[65] Fig. 1 also explains why the band gaps predicted by the PW1PW and B3LYP hybrid functionals, which contain 20% of Fock exchange, for TiO_2 polymorphs are around 0.5 eV smaller than those predicted by the PBE0 functional (Table S1, ESI†).

Based on the linear fitting in Fig. 1, it is clear that one can tune the %Fock parameter in the PBE0 functional so as to reproduce the experimental band gap values. It appears that %Fock values of 12.1% and 12.9% reproduce the band gap of rutile and anatase, respectively. These values are sufficiently close to adopt a 12.5% value for %Fock, which is an average value for both systems. It should be noted that this value is very close to 13% of Fock exchange for the hybrid functional, as previously proposed for rutile TiO_2 by Zhang *et al.*[66] These authors used the exchange and correlation contributions of the LDA proposed by Moreira *et al.*[54] in their study of electronic and magnetic structures of NiO and then examined the performance of their modified functional in describing the electronic properties of pristine bulk rutile TiO_2 and the stoichiometric and reduced TiO_2(110) surfaces. The resulting functional with 12.5% of Fock exchange will be referred to as PBE*x* to distinguish from the standard hybrid PBE0 functional. Note that 12.5% of Fock exchange corresponds exactly to half the value in the PBE0. To further prove that PBE*x* is able to properly describe the electronic structure of TiO_2 based materials, we have considered the band gap of brookite, another well-known TiO_2 polymorph. At the experimental crystal structure,[67] the PBE*x* calculated band gap is 3.37 eV which is in good agreement with experimental values in the 3.1–3.4 eV range.[68] In order to investigate whether PBE*x* is able to properly describe the main features of TiO_2, several properties are computed for stoichiometric and reduced models of rutile and anatase.

3.2. Validation of PBE*x* on bulk TiO_2 properties

The amount of Fock exchange defining the PBE*x* functional has been empirically derived to reproduce the band gaps of rutile and anatase at the experimental crystal structure. In order to further validate this approach, the lattice parameters, band gaps and formation enthalpies of primitive cells predicted by the hybrid PBE*x* functional are discussed and compared to experiments and also to those predicted by the standard PBE functional.

The calculated lattice parameters using both PBE and PBE*x* together for errors with respect to experiment are listed in Table 1. For both rutile and anatase, PBE and PBE*x* approaches tend to overestimate both a/b and c; for the PBE case, this overestimation is in line with previous theoretical results.[53,69,70] Considering the absolute deviation from the experimental data, it can be concluded that PBE*x* provides highly improved unit cell parameters consistent with experimental values. In addition, the formation enthalpies (ΔH_f) for rutile and anatase predicted by PBE*x* are closer to experiment than those obtained with the PBE functional;[61,62,71,72] the maximum errors on the calculated ΔH_f significantly decreased from 6.3% (PBE) to 3.6% (PBE*x*) for rutile, and from 4.9% (PBE) to 2.0% (PBE*x*) for anatase, respectively.

Table 1 Experimental (Expt.) and calculated (PBE and PBE*x*) structural parameters ($a = b$, c), band gaps (E_g), and formation enthalpies (ΔH_f) for rutile and anatase using tight grid/tier-2 basis set and light grid/tier-1 basis set levels, respectively; relative deviations with respect to experimental data are given in parenthesis. Distances are in Å and energies in eV

		Rutile			Anatase		
Computational level		Expt.	PBE	PBE*x*	Expt.	PBE	PBE*x*
Tight grid/tier-2 basis set	a, b	4.592[a]	4.650 (1.3%)	4.609 (0.4%)	3.785[b]	3.799 (0.4%)	3.792 (0.2%)
	c	2.957[a]	2.975 (0.6%)	2.957 (0.0%)	9.514[b]	9.702 (2.0%)	9.578 (0.7%)
	E_g	3.03[c]	2.07 (31.7%)	2.97 (2.0%)	3.20[d]	2.14 (33.1%)	3.22 (0.6%)
	ΔH_f	−9.74[e]	−9.12 (6.3%)	−9.39 (3.6%)	−9.69[f]	−9.22 (4.9%)	−9.60 (2.0%)
Light grid/tier-1 basis set	E_g	3.03[c]	2.04 (32.7%)	2.91 (4.0%)	3.20[d]	2.12 (33.8%)	3.19 (0.3%)
	ΔH_f	−9.74[e]	−9.19 (5.7%)	−9.47 (2.8%)	−9.69[f]	−9.25 (4.5%)	−9.52 (1.7%)

[a] Ref. 62. [b] Ref. 63. [c] Ref. 64. [d] Ref. 65. [e] Ref. 75. [f] Ref. 76.

The calculated unit cell parameters and physical properties listed in Table 1 validate the reliability of the PBE*x* functional to describe the geometrical descriptions as well as the electronic structures of stoichiometric bulk systems. Though the structural results are similar to those obtained with other hybrid functionals, the electronic structure obtained by PBE*x* is now comparable to experiment, while both B3LYP and PBE0 significantly overestimate the band gaps of both polymorphs.[47] In the next section we will show that the PBE*x* functional adequately described reduced TiO_2 models as well.

3.3. PBE*x* description of the electronic structure of oxygen vacancies in rutile and anatase

The calculations for the O_V containing large supercells involve a somehow less stringent basis set, as mentioned above. The results in Table 1 indicate that the effect on the calculated values is sufficiently small. Calculations show that to obtain PBE*x* converged calculated O_V formation energies for rutile, supercell sizes larger than $2 \times 2 \times 2$ are required and a $2 \times 2 \times 4$ (95 atoms) supercell has been selected. In a similar way, a $2\sqrt{2} \times 2\sqrt{2} \times 1$ (95 atoms) supercell is chosen for anatase. Note that both supercells contain the same number of atoms and hence provide the same concentration of O_V (1.56%) which allows for a meaningful comparison. In both cases, the supercells are constructed from the primitive unit cell parameter already optimized for the bulk using either the PBE or PBE*x* functional as reported in Table 1; the resulting supercells are displayed in Fig. 2 (see also Fig. S1 and S2 in the ESI†).

From a chemical point of view, the removal of one neutral oxygen atom from TiO_2 bulk means that three five-fold Ti atoms are formed and two extra electrons are left in the system; these electrons are responsible for the formal reduction of Ti^{4+} cations to Ti^{3+}. The existence of Ti^{3+} ions in reduced TiO_2 systems was firmly confirmed by many experimental observations, such as color centers,[8] core level binding energy shifts,[73–75] and electron paramagnetic resonance (EPR).[76] Thus, inducing oxygen vacancy can be one kind of n-type doping of TiO_2 samples. From a theoretical point of view, the description of Ti^{3+} centers in TiO_2 systems is not straightforward since PBE predicts physically meaningless fully delocalized solutions whereas hybrid functionals predict a variety of near degenerate solutions with different degrees of localization as described in the literature.[33]

At the PBE level, removal of one oxygen atom from rutile resulted in a rather delocalized solution whereas PBE*x* correctly predicted a solution with two unpaired electrons (coupled high spin) localized in two different Ti^{3+} centers (Fig. 3). For PBE*x*, substantial spin density is located at symmetry related Ti_4 and $Ti_{4'}$ atoms, which are slightly away from the O_V site, instead of Ti_{1-3} atoms which are the nearest to the O_V site. This spin density distribution is in line with recent scanning tunneling microscopy (STM) measurements on the rutile (110) surface reported by Setvin *et al.*,[77] and with the recent theoretical work on reduced rutile using a $2 \times 2 \times 3$ supercell and a similar hybrid functional.[78] In spite of the different characteristics of the electronic solutions (delocalized *versus* localized) both PBE and PBE*x* predict similar optimized geometries for the O_V containing supercell. In fact, compared to the stoichiometric structure, the atomic distance between Ti_1 and Ti_2 atoms, hereafter denoted $l(Ti_1–Ti_2)$, increases by 0.38 Å for PBE and 0.37 Å for PBE*x*. In a similar way, $l(Ti_1–Ti_4)$ and $l(Ti_2–Ti_{4'})$ decrease by 0.08 Å and 0.06 Å for PBE and PBE*x*, respectively (Fig. 3).

In the case of reduced anatase, the PBE functional predicted the spin density of the two unpaired electrons fully distributed with high spin over all Ti atoms in the supercell (Fig. S3, ESI†). In contrast, the PBE*x* hybrid functional predicted almost degenerate spin states with localized unpaired electrons. A similar behavior has been reported by Finazzi *et al.* using the B3LYP functional and a rather limited basis set of localized GTO functions. In the present case, three different solutions were found using PBE*x*. In the first one (I), the spin density arising from the two unpaired electrons is localized over the three Ti atoms (Ti_{1-3}) directly adjacent to the O_V site and is similar to the previously reported solution for the antiferromagnetic singlet state obtained by Deák *et al.*[36] In the second solution (II), one electron is localized on Ti_1 atoms and the remaining spin density is delocalized (II). Finally, a fully delocalized solution similar to that obtained with PBE is also found (III). Surprisingly, III is the ground state with II and I

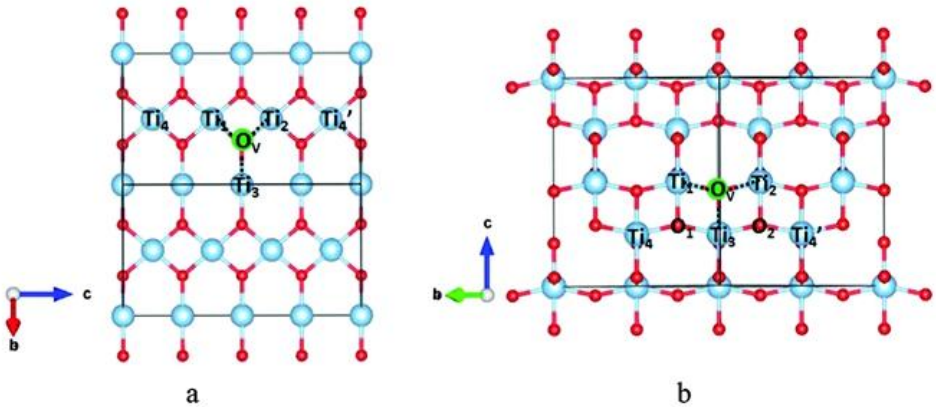

Fig. 2 Initial geometries for rutile (a) and anatase (b) containing one oxygen vacancy (O_V, denoted by green color). Relevant Ti and O atoms are labeled.

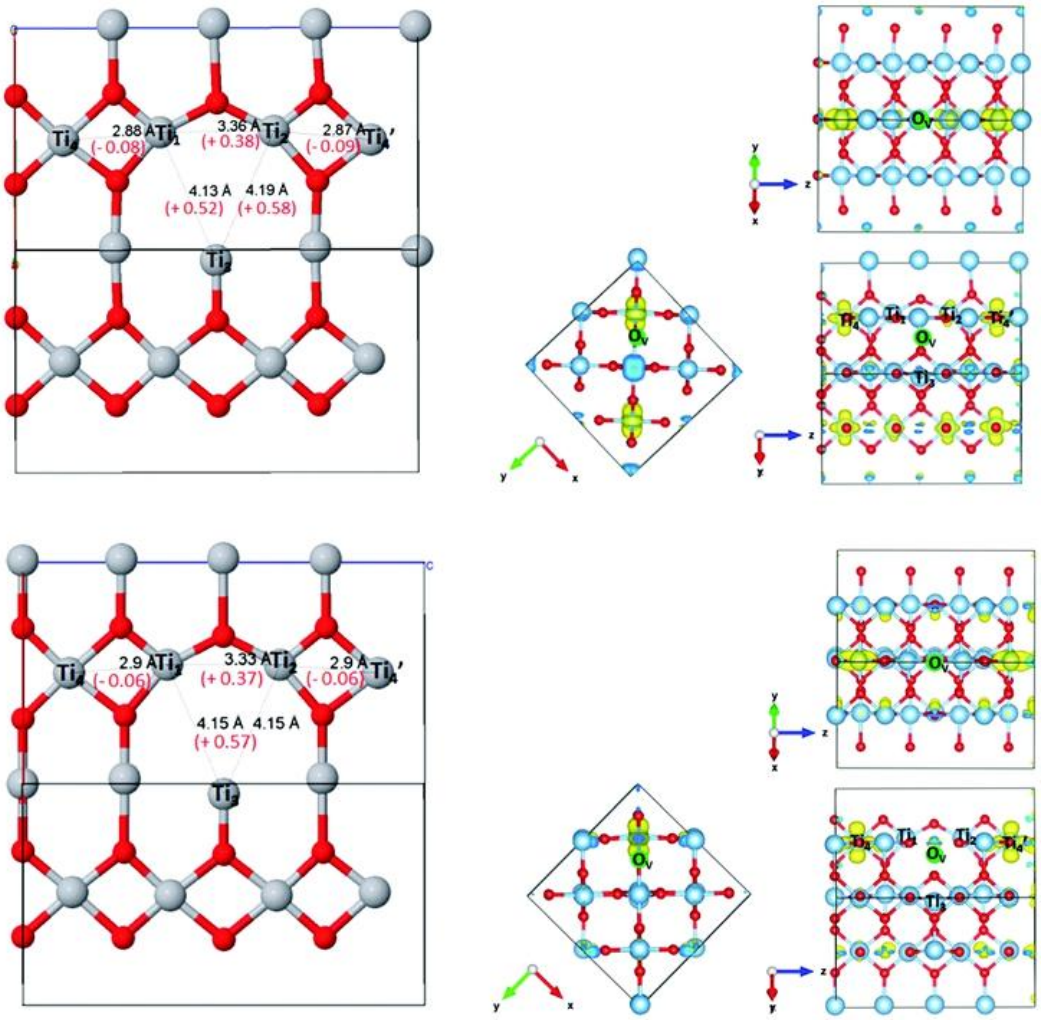

Fig. 3 PBE (top panel) and PBE*x* (bottom panel) optimized geometry and spin density plots for O_V in rutile. Representative optimized bond lengths (in Å) and their changes, before and after one oxygen vacancy involved, noted in parentheses (red color).

being 0.36 and 0.44 eV higher in energy. Solutions (II) and (III) can be obtained starting from I by gradually increasing the bond distance of $l(Ti_{4'}–O_2)$ to induce symmetry breaking. Unfortunately, all attempts to find a solution with two electrons localized on Ti_1 and $Ti_{4'}$ (IV) failed which was reported as the most stable solution (0.08 eV lower than II) for reduced anatase, as reported by Finazzi *et al.*[33] In order to analyze the origin of the difference, a single point PBE*x* calculation was carried out for the optimized structure by Finazzi *et al.*[33] that was made available to us by these authors. This PBE*x* single point calculation converged properly to a solution with two electrons localized (see IV in Fig. S3, ESI†). This result clearly indicates that PBE*x* is able to locate the solution with two electrons localized and strongly suggests that the difference comes from a different structure for the supercell with the O_V. In fact, subsequent geometry optimization with the PBE*x* functional starting from this structure led to a slightly different structure where the two electron localization eventually disappeared. It is worth pointing out that solution IV as reported by Finazzi *et al.*[33] was found for a primitive unit cell with lattice parameters a, b = 3.776 Å and c = 9.866 Å that have much larger deviation from the experimental crystal structure (a, b = 3.785 Å and c = 9.514 Å) than those predicted by PBE*x*, especially for the parameter c. Clearly, the existence of IV depends strongly on the use of a given crystal structure and much less on the amount of Fock exchange in the hybrid functional. This result also shows the delicate balance between atomic and electronic structures.

3.4. Oxygen vacancy formation energy in rutile and anatase

To further analyze the performance of the PBE*x* functional for reduced TiO_2 polymorphs, we calculated the oxygen vacancy formation energy (E_f^O) as

$$E_f^O = E(Ti_nO_{2n-1}) + \frac{1}{2}E_{O_2} - E(Ti_nO_{2n}) \quad (5)$$

Table 2 Calculated (PBE and PBE*x*) oxygen vacancy formation energies (E_f^O in eV) for rutile and anatase and the position of the corresponding defect states relative to the bottom of the conduction band as obtained from pDOS analysis. In the case of anatase, different spin polarized solutions analyzed are noted in parenthesis. All energy values are in eV

	Rutile		Anatase	
	E_f^O	O_V defect state	E_f^O	O_V defect state
PBE	4.33	−0.01	3.68	0.10
PBE*x*	4.44	0.89	4.65 (I)	0.49 (I)
			4.57 (II)	0.41 (II)
			4.21 (III)	0.09, 0.48 (III)
				0.41, 0.64 (IV)[a]

[a] Single point calculation at the structure reported by Finazzi *et al.*[3,3]

where $E(Ti_nO_{2n-1})$ and $E(Ti_nO_{2n})$ represent the total energies of the reduced and pristine TiO_2 with fully relaxed supercells, respectively. In the case of pristine TiO_2 both unit cell parameters and fractional coordinates of atoms were fully relaxed. In the case of the O_V containing a unit cell, the lattice parameters for the stoichiometric material were used and the fractional coordinates were fully relaxed. In eqn (5), E_{O_2} stands for the ground state energy of the oxygen molecule with triplet multiplicity. Herein, a positive value for E_f^O indicates that the O_V formation is an endothermic reaction. The oxygen vacancy formation energies thus obtained are listed in Table 2. For reduced rutile, the calculated E_f^O values are 4.33 eV and 4.44 eV for PBE and PBE*x*, respectively. The PBE*x* calculated value is very close to previously reported values from GGA+*U* (*U* = 3–4 eV) approaches, as summarized in Table S1 (ESI†). More importantly, the present PBE*x* calculated E_f^O value is close to the experimental value of 4.55 eV reported,[79] which was used as an appropriate reference in previous theoretical studies.[32,33]

Anatase is more complicated because of the variety of nearly degenerate solutions commented in the previous sections. In the following, we discuss each solution separately but it is important to keep in mind that, for each of them, the atomic structure is different since it corresponds to the fully relaxed geometry. For anatase, the PBE E_f^O value is 3.69 eV, where the PBE*x* E_f^O values are in the 4.21 (III)–4.65 (I) eV range. Here, depending on spin density distribution, the differences in E_f^O are relatively larger than for rutile. The smaller E_f^O value predicted from PBE calculations arises from the splitting of spin density in various centers which artificially reduces the coulomb repulsion. Nevertheless, the PBE*x* values for E_f^O in anatase are close to those obtained for rutile and are also close to the previously B3LYP reported E_f^O values of 4.78 eV and 4.84 for anatase (solutions IV and II, respectively).[3,3] Clearly, the PBE*x* functional predicts E_f^O values intermediate between those obtained from PBE (0% of Fock exchange) and B3LYP (20% of Fock exchange) approaches. It is also interesting to note that the range of calculated E_f^O of PBE*x* is almost identical to that of PBE+*U* approaches with commonly used *U* values in the 2–4 eV range (Table S1, ESI†).

From the preceding discussion one can safely affirm that the PBE*x* calculated E_f^O values are in the range of values reported in the literature. Note, however, that these values are referred to as half the energy of the oxygen molecule. Consequently, a more direct comparison to experiment is difficult.

3.5. Density of states in oxygen vacancy containing rutile and anatase

The formation of O_V is accompanied by a shift of the Fermi level towards the bottom of the conduction band (conduction band minimum or CBM) due to the excess electrons. Nevertheless, to properly define the Fermi level a proper alignment with respect to the vacuum is required.[64] In the present work we simply aligned all calculated DOSs by taking the valence band maximum (VBM) as origin. From experiment it is known that, in the case of rutile, the new state, originated by O_V, appears at around 0.7–1.0 eV below the CBM[25–28] although most of the available values correspond to measurements of the rutile TiO_2(110) surface. For anatase, resonant photoemission and X-ray absorption spectroscopy experiments observed the O_V defect state around 1.0 eV below the CBM.[80]

The density of states of reduced titania is one of the key features of these materials since it can be directly compared to

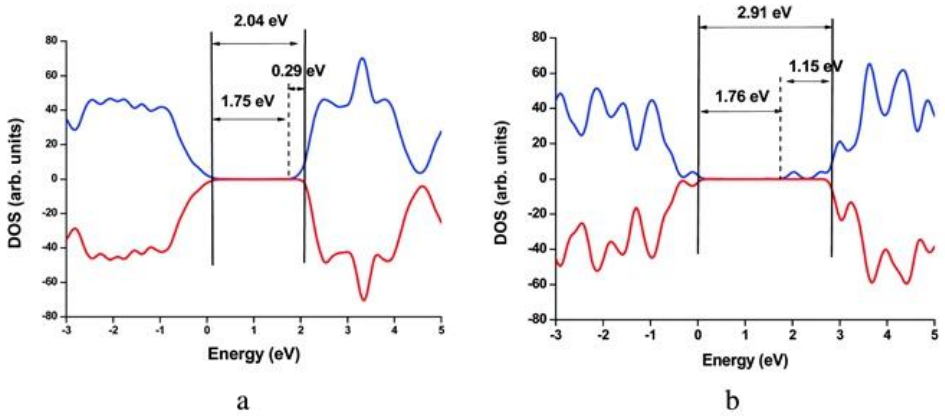

Fig. 4 PBE (left) and PBE*x* (right) total density of states (DOS) for oxygen vacancies (O_V) in rutile. The blue and red lines represent spin-up and spin-down states, respectively.

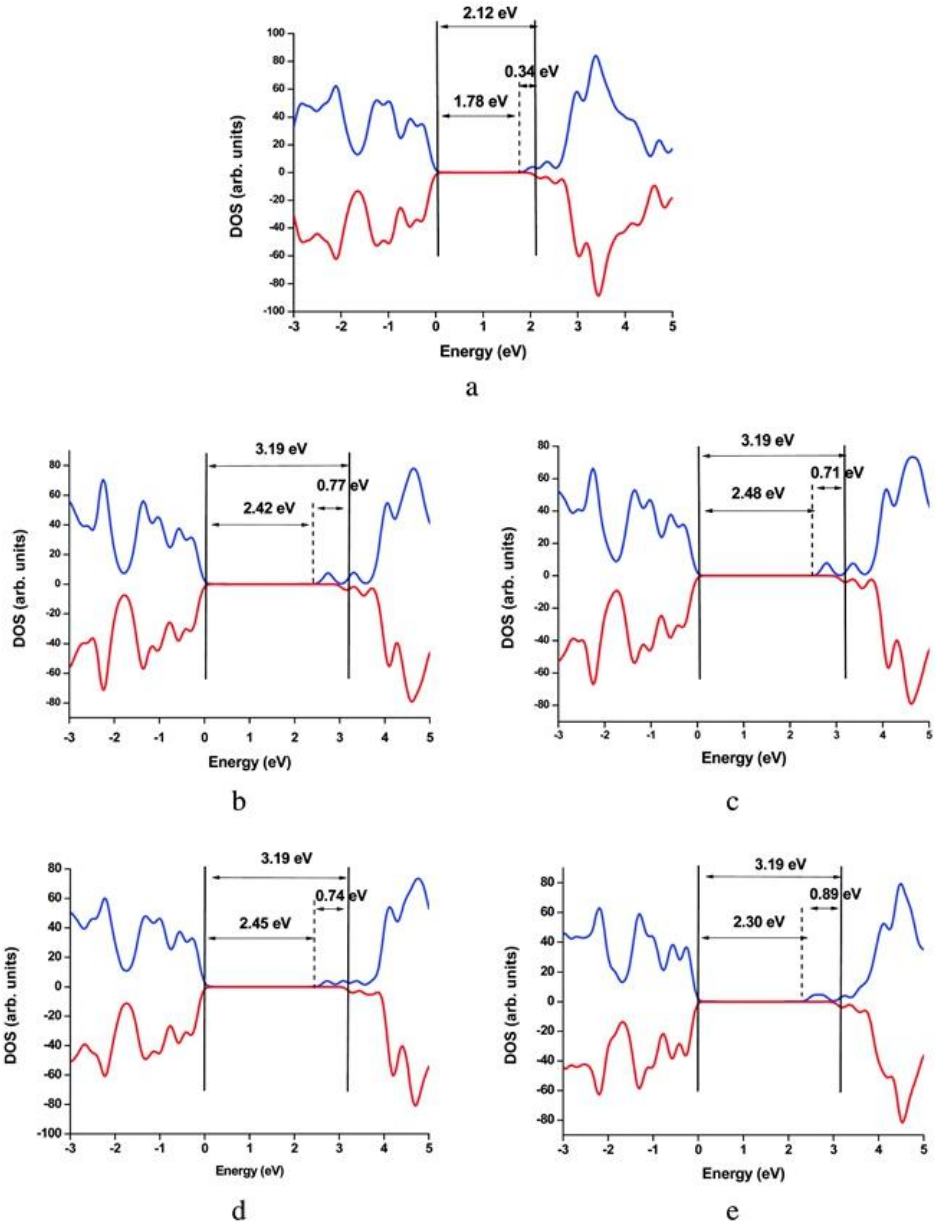

Fig. 5 PBE (a) and PBE*x* (b–e for solutions I–IV, respectively) total density of states (DOS) for oxygen vacancies (O_V) in rutile. The blue and red lines represent spin-up and spin-down states, respectively.

experiment. Here, we further analyzed the performance of the PBE*x* functional for reduced TiO_2 polymorphs by discussing the calculated total density of states (DOS) for O_V in TiO_2 polymorphs. Let us now discuss the PBE results for the O_V in the case of rutile and anatase. Fig. 4a and 5a clearly show that PBE predicts that the onset of the defect state appears at 0.3 eV below the CBM but merging with the conduction band which is an artifact that originated from the excessive delocalization of the spin density by PBE and the underestimation of the band gap. It must be noted that this problem is somehow solved by DFT+*U* approaches although the O_V defect state often appears too deep and close to the valence band maximum; the relevant information is summarized in Table S1 (ESI†). Contrary to PBE, PBE*x* properly places the O_V state: 1.15 eV below the CBM for rutile and 0.71 (II)–0.77 (I) eV below the CBM for different spin polarized solutions investigated for reduced anatase. Interestingly, I–III solutions for the fully optimized geometry have similar onsets for the O_V defect state, regardless of the degree of localization for the spin density. For solution IV, as seen in Fig. 5e, the O_V defect state appears ~0.9 eV below the CBM which is consistent

with the B3LYP results of Finazzi *et al.*[33] and also with the present results for solutions I–III. Therefore, the position of the O_V related state does not strongly depend on the type of solution and PBE*x* appears to produce a balanced description for reduced TiO_2 as well.

In order to obtain a more accurate estimate of the energy peak in the DOS related to the O_V defect state, we analyzed the atom-projected and angular-momentum resolved partial density of states (pDOS) focusing especially on Ti_{1-4} atoms where most of the excess electron density is localized in the Ti(3d) orbitals, especially for PBE*x*. The peak maxima in the pDOS for specific atoms are listed in Table 2. At the PBE level, the O_V peak maximum appears at −0.01 eV and 0.1 eV below the CBM for rutile and anatase, respectively. However, from pDOSs related to Ti_4 and $Ti_{4'}$ atoms, the PBE*x* predicts the O_V defect state in rutile 0.89 eV below the CBM in agreement with previous studies using DFT+*U* or hybrid functionals,[34–36,40] and with experiment.[27,28] On the other hand, for anatase, the PBE*x* calculated O_V defect states depend on the type of solution found. For solutions I and II involving a rather large degree of localization of the excess electron density, the O_V peaks appear at 0.49 and 0.41 eV below the CBM, respectively. In the case of solution III, exhibiting a large degree of delocalized character, two features at 0.09 and 0.48 eV below the CBM are clearly visible (Fig. S4, ESI†). Finally, in the case of IV, obtained using the unit cell parameters and fractional coordinates from Finazzi *et al.*,[33] two features at 0.41 and 0.64 eV below the CBM are found. Therefore, in spite of the differences related to different solutions, all physically meaningful results consistently predict the O_V state in anatase at ∼0.5 eV below the CBM which, as commented below, is consistent with recent findings.[78] From the above comparison it is clear that the present PBE*x* approach correctly describes the O_V state for rutile whereas for anatase the agreement seems not to be as good since the experimental feature also appears at ∼1.0 eV below the CBM, as in the case of rutile.[80] At this point it is worth pointing out that a direct comparison to experiment is not straightforward. In fact, Gerosa *et al.*[78] argue that this feature may be related to the +1 charged O_V where upon O removal only one electron is left in the material.

4. Conclusions

Using periodic models and an all-electron description with accurate numerical basis sets, a new, property tailored, modified hybrid functional has been proposed as a pragmatic approach to properly describe the atomic and electronic structures of bulk rutile and anatase TiO_2 polymorphs and those of reduced samples containing one oxygen vacancy. In this approach, the amount of Fock exchange entering into the hybrid functional has been determined based on the existing linear correlation between %Fock and the (Kohn–Sham) calculated band gap for both rutile and anatase at the experimental structure. Hence, it is found that modifying the PBE0 functional so as to contain 12.5% of Fock exchange (PBE*x*) reproduces the experimental band gaps whereas, at the same Kohn–Sham level, the commonly used B3LYP and PBE0 hybrid functionals significantly overestimate them. The resulting PBE*x* approach also leads to an accurate description of lattice parameters, fractional coordinates for the primitive unit cells as well as for formation enthalpies.

The PBE*x* functional is also found to properly describe the properties of the oxygen vacancy defect in rutile and anatase TiO_2 bulk systems. For rutile, the defect state exhibits a physically meaningful localized character and appears ∼1.0 eV below the CBM, in agreement with previous work[34–36,40] and experiment.[27,28] For anatase the calculated total density of states (DOS) and atom-projected and angular-momentum resolved partial density of states (pDOS) predict the O_V defect state at ∼0.5 eV below the CBM. This is in qualitative agreement with experiment although it appears that this value is too close to the CBM; here experiments also point out an O_V related feature at ∼1.0 eV below the CBM.[80] However, it has also been suggested that this feature can be attributed to +1 charged O_V defects rather than to the neutral O_V modeled in the present work.

Finally, it is worth pointing out that the amount of Fock exchange empirically determined in this work to be suitable to describe TiO_2 systems is in agreement with the values used by Gerosa *et al.*[78] based on arguments related to screening of the electron density and the dielectric constant of these materials. These authors determine the fraction of Fock exchange self-consistently with the static electronic dielectric constant. In such a way, the resulting approach has also an empirical flavor because it makes use of a parameter external to the electronic Hamiltonian. They found that the optimal %Fock parameters are 15.2% for rutile and 18.4% for anatase from a dielectric-dependent hybrid method.[40] The positive part, however, is that the amount of Fock exchange chosen on the basis of the experimental band gap or on the basis of the dielectric constant is very similar and smaller than the values used in standard B3LYP or PBE0. Therefore, the present approach may provide a sufficiently accurate way to study the electronic structure of large TiO_2 nanoparticles containing hundreds or thousands of atoms where GW techniques are unaffordable and this is being currently analyzed in our computational laboratory.

Acknowledgements

The authors are indebted to Prof. Volker Blum, Dr Björn Lange, and Dr Sergey Levchenko for their kind advice regarding the calculations with the FHI-aims code and to Dr Sergio Tosoni for preliminary calculations with the CRYSTAL code regarding the dependence of the band gap on the amount of Fock exchange. The authors also wish to thank Prof. Gianfranco Pacchioni and Dr Cristiana di Valentin for making their structure of the O vacancy available to us. This research was supported by Basic Science Research Program through the National Research Foundation of Korea (NRF) funded by the Ministry of Education (NRF-2014R1A6A3A03056449), by the Spanish MINECO grant CTQ2015-64618-R and, in part, by *Generalitat de Catalunya* grants 2014SGR97 and XRQTC and from the NOMAD Center of Excellence project; this project received funding from the European Union's Horizon 2020 research and innovation programme under grant

agreement No. 676580. J. Y. L. acknowledges the financial support by Ministry of Science, ICT and Future Planning, subjected project to the project EDISON (Education-research Integration through Simulation On the Net, Grant No. 2012M3C1A6035359). O. L. G. is grateful to the *Universitat de Barcelona* for a predoctoral grant, and FI acknowledges additional support from the 2015 ICREA Academia Award for Excellence in University Research. Computational time at the MareNostrum supercomputer has been provided by the Barcelona Supercomputing Centre through grants from *Red Española de Supercomputación* and the COMPHOTOCAT project 2014112608 of the Partnership for Advanced Computing in Europe (PRACE).

References

1 A. Mills, N. Elliott, G. Hill, D. Fallis, J. R. Durrant and R. L. Willis, *Photochem. Photobiol. Sci.*, 2003, **2**, 591.
2 B. O'Regan and M. Gratzel, *Nature*, 1991, **353**, 737.
3 T. L. Thompson and J. T. Yates, Jr., *Chem. Rev.*, 2006, **106**, 4428.
4 X. Chen and S. S. Mao, *Chem. Rev.*, 2007, **107**, 2891.
5 A. Fujishima and K. Honda, *Nature*, 1972, **238**, 37.
6 L. Forro, O. Chauvet, D. Emin, L. Zuppiroli, H. Berger and F. Lévy, *J. Appl. Phys.*, 1994, **75**, 633.
7 M. K. Nowotny, T. Bak and J. Nowotny, *J. Phys. Chem. B*, 2006, **110**, 16270.
8 M. V. Khomenko, K. Langer, H. Rager and A. Fett, *Phys. Chem. Miner.*, 1998, **25**, 338.
9 R. L. Kurtz, S. W. Robey, R. L. Stockbauer, D. Mueller, A. Shih and L. Toth, *Phys. Rev. B: Condens. Matter Mater. Phys.*, 1989, **39**, 4768.
10 J. Nowotny, T. Bak, M. Nowotny and L. Sheppard, *Int. J. Hydrogen Energy*, 2007, **32**, 2609.
11 J. Nowotny, T. Bak, M. Nowotny and L. Sheppard, *Int. J. Hydrogen Energy*, 2007, **32**, 2630.
12 C. Di Valentin and G. Pacchioni, *Acc. Chem. Res.*, 2014, **47**, 3233.
13 F. Spadavecchia, G. Cappelletti, S. Ardizzone, C. L. Bianchi, S. Cappelli, C. Oliva, P. Scardi, M. Leoni and P. Fermo, *Appl. Catal., B*, 2010, **96**, 314.
14 S. Polarz, J. Strunk, V. Ischenko, M. W. van den Berg, O. Hinrichsen, M. Muhler and M. Driess, *Angew. Chem., Int. Ed.*, 2006, **4**, 2965.
15 X. Pan, M.-Q. Yang, X. Fu, N. Zhang and Y.-J. Xu, *Nanoscale*, 2013, **5**, 3601.
16 C. Sousa, S. Tosoni and F. Illas, *Chem. Rev.*, 2013, **113**, 4456.
17 A. J. Cohen, P. Mori-Sanchez and W. Yang, *Chem. Rev.*, 2012, **112**, 289.
18 J. M. Sullivan and S. C. Erwin, *Phys. Rev. B: Condens. Matter Mater. Phys.*, 2003, **67**, 144415.
19 E. Cho, S. Han, H.-S. Ahn, K.-R. Lee, S. K. Kim and C. S. Hwang, *Phys. Rev. B: Condens. Matter Mater. Phys.*, 2006, **73**, 193202.
20 S. Na-Phattalung, M. F. Smith, K. Kim, M.-H. Du, S.-H. Wei, S. Zhang and S. Limpijumnong, *Phys. Rev. B: Condens. Matter Mater. Phys.*, 2006, **73**, 125205.
21 M. V. Ganduglia-Pirovano, A. Hofmann and J. Sauer, *Surf. Sci. Rep.*, 2007, **62**, 219.
22 S. Livraghi, M. Chiesa, M. C. Paganini and E. Giamello, *J. Phys. Chem. C*, 2011, **115**, 25413.
23 M. Chiesa, M. C. Paganini, S. Livraghi and E. Giamello, *Phys. Chem. Chem. Phys.*, 2013, **15**, 9435.
24 C. Di Valentin, G. Pacchioni and A. Selloni, *J. Phys. Chem. C*, 2009, **113**, 20543.
25 R. L. Kurtz, R. Stock-Bauer, T. E. Msdey, E. Román and J. De Segovia, *Surf. Sci.*, 1989, **218**, 178.
26 V. E. Henrich, G. Dresselhaus and H. J. Zeiger, *Phys. Rev. Lett.*, 1976, **36**, 1335.
27 M. Nolan, S. D. Elliott, J. S. Mulley, R. A. Bennett, M. Basham and P. Mulheran, *Phys. Rev. B: Condens. Matter Mater. Phys.*, 2008, **77**, 235424.
28 M. A. Henderson, W. S. Epling, C. H. F. Peden and C. L. Perkins, *J. Phys. Chem. B*, 2003, **107**, 534.
29 G. Mattioli, F. Filippone, P. Alippi and A. Amore Bonapasta, *Phys. Rev. B: Condens. Matter Mater. Phys.*, 2008, **78**, 241201.
30 B. J. Morgan and G. W. Watson, *J. Phys. Chem. C*, 2010, **114**, 2321.
31 J. Stausholm-Møller, H. H. Kristoffersen, B. Hinnemann, G. K. H. Madsen and B. Hammer, *J. Chem. Phys.*, 2010, **133**, 144708.
32 G. Mattioli, P. Alippi, F. Filippone, R. Caminiti and A. Amore Bonapasta, *J. Phys. Chem. C*, 2010, **114**, 21694.
33 E. Finazzi, C. Di Valentin, G. Pacchioni and A. Selloni, *J. Chem. Phys.*, 2008, **129**, 154113.
34 M. M. Islam, T. Bredow and A. Gerson, *Phys. Rev. B: Condens. Matter Mater. Phys.*, 2007, **76**, 045217.
35 A. Janotti, J. B. Varley, P. Rinke, N. Umezawa, G. Kresse and C. G. Van de Walle, *Phys. Rev. B: Condens. Matter Mater. Phys.*, 2010, **81**, 085212.
36 P. Deák, B. Aradi and T. Frauenheim, *Phys. Rev. B: Condens. Matter Mater. Phys.*, 2012, **86**, 195206.
37 C. Di Valentin and G. Pacchioni, *Acc. Chem. Res.*, 2014, **47**, 3233.
38 S. G. Park, B. Magyari-Köpe and Y. Nishi, *Phys. Rev. B: Condens. Matter Mater. Phys.*, 2010, **2**, 115109.
39 J. H. Skone, M. Govoni and G. Galli, *Phys. Rev. B: Condens. Matter Mater. Phys.*, 2014, **89**, 195112.
40 M. Gerosa, C. E. Bottani, L. Caramella, G. Onida, C. Di Valentin and G. Pacchioni, *Phys. Rev. B: Condens. Matter Mater. Phys.*, 2015, **91**, 155201.
41 Z. Hu and H. Metiu, *J. Phys. Chem. C*, 2011, **115**, 5841.
42 S. Tosoni, O. Lamiel-Garcia, D. Fernandez Hevia, J. M. Doña and F. Illas, *J. Phys. Chem. C*, 2012, **116**, 12738.
43 S. Tosoni, O. Lamiel-Garcia, D. Fernandez Hevia and F. Illas, *J. Phys. Chem. C*, 2013, **117**, 5855.
44 Y. Ortega, O. Lamiel-Garcia, D. F. Hevia, S. Tosoni, J. Oviedo, M. A. San-Miguel and F. Illas, *Surf. Sci.*, 2013, **618**, 154.
45 S. Tosoni, D. Fernandez Hevia, Ó. González Díaz and F. Illas, *J. Phys. Chem. Lett.*, 2012, **3**, 2269.
46 A. D. Becke, *J. Chem. Phys.*, 1993, **98**, 5648.
47 J. Muscat, A. Wander and N. M. Harrison, *Chem. Phys. Lett.*, 2001, **342**, 397.
48 C. Adamo and V. Barone, *J. Chem. Phys.*, 1999, **110**, 6158.

49 J. P. Perdew, M. Ernzerhof and K. Burke, *J. Chem. Phys.*, 1996, **105**, 9982.
50 J. P. Perdew, K. Burke and M. Ernzerhof, *Phys. Rev. Lett.*, 1996, **77**, 3865.
51 J. Heyd, G. E. Scuseria and M. Ernzerhof, *J. Chem. Phys.*, 2003, **118**, 8207.
52 A. V. Krukau, O. A. Vydrov, A. F. Izmaylov and G. E. Scuseria, *J. Chem. Phys.*, 2006, **125**, 224106.
53 A. Malashevich, M. Jain and S. G. Louie, *Phys. Rev. B: Condens. Matter Mater. Phys.*, 2014, **89**, 075205.
54 I. de P. R. Moreira, F. Illas and R. L. Martin, *Phys. Rev. B: Condens. Matter Mater. Phys.*, 2002, **65**, 155102.
55 A. Alkauskas, P. Broqvist, F. Devynck and A. Pasquarello, *Phys. Rev. Lett.*, 2008, **101**, 106802.
56 E. van Lenthe, E. J. Baerends and J. G. Snijders, *J. Chem. Phys.*, 1994, **101**, 9783.
57 R. W. G. Wyckoff, *Crystal structures*, Interscience Publishers, New York, 2nd edn, 1963, pp. 7–83.
58 V. Havu, V. Blum, P. Havu and M. Scheffler, *J. Comput. Phys.*, 2009, **228**, 8367.
59 V. Blum, R. Gehrke, F. Hanke, P. Havu, V. Havu, X. Ren, K. Reuter and M. Scheffler, *Comput. Phys. Commun.*, 2009, **180**, 2175.
60 R. J. Swope, J. R. Smyth and A. C. Larson, *Am. Mineral.*, 1995, **80**, 448.
61 C. J. Howard, T. M. Sabine and F. Dickson, *Acta Crystallogr., Sect. B: Struct. Sci.*, 1991, **47**, 462.
62 A. Amtout and R. Leonelli, *Phys. Rev. B: Condens. Matter Mater. Phys.*, 1995, **51**, 6842.
63 S. P. Kowalczyk, F. R. McFeely, L. Ley, V. T. Gritsyna and D. A. Shirley, *Solid State Commun.*, 1977, **23**, 161.
64 D. O. Scanlon, C. W. Dunnill, J. Buckeridge, S. A. Shevlin, A. J. Logsdail, S. M. Woodley, C. R. A. Catlow, M. J. Powell, R. G. Palgrave and I. P. Parkin, *Nat. Mater.*, 2013, **12**, 798.
65 H. Tang, F. Levy, H. Berger and P. E. Schmid, *Phys. Rev. B: Condens. Matter Mater. Phys.*, 1995, **52**, 7771.
66 Y.-f. Zhang, W. Lin, Y. Li, K.-n. Ding and J.-q. Li, *J. Phys. Chem. B*, 2005, **109**, 19270.
67 E. Meagher and G. A. Lager, *Can. Mineral.*, 1979, **17**, 77.
68 A. Di Paola, M. Bellardita and L. Palmisano, *Catalysts*, 2013, **3**, 36.
69 M. Lazzeri, A. Vittadini and A. Selloni, *Phys. Rev. B: Condens. Matter Mater. Phys.*, 2001, **63**, 155409.
70 F. Labat, P. Baranek, C. Domain, C. Minot and C. Adamo, *J. Chem. Phys.*, 2007, **126**, 154703.
71 G. V. Samsonov, *The Oxide Handbook*, IFI/Plenum, New York, 2nd edn, 1982.
72 M. W. Chase and National Institute of Standards and Technology (U.S.), *NIST-JANAF thermochemical tables*, American Chemical Society; American Institute of Physics for the National Institute of Standards and Technology, Washington, DC, New York, 4th edn, 1998.
73 E. Serwicka, M. Schlierkamp and R. Schindler, *Zeitschrift für Naturforschung A*, 1981, **36**, 226.
74 T. Sekiya, T. Yagisawa, N. Kamiya, D. Das Mulmi, S. Kurita, Y. Murakami and T. Kodaira, *J. Phys. Soc. Jpn.*, 2004, **73**, 703.
75 P. F. Chester, *J. Appl. Phys.*, 1961, **32**, 2233.
76 J. Nerlov, S. V. Christensen, S. Weichel, E. H. Pedersen and P. J. Møller, *Surf. Sci.*, 1997, **371**, 321.
77 M. Setvin, C. Franchini, X. Hao, M. Schmid, A. Janotti, M. Kaltak, C. G. Van de Walle, G. Kresse and U. Diebold, *Phys. Rev. Lett.*, 2014, **113**, 086402.
78 M. Gerosa, C. E. Bottani, L. Caramella, G. Onida, C. Di Valentin and G. Pacchioni, *J. Chem. Phys.*, 2015, **143**, 134702.
79 P. Kofstad, *Nonstoichiometry, diffusion, and electrical conductivity in binary metal oxides*, Wiley-Interscience, New York, 1972, ch. 8.
80 A. G. Thomas, W. R. Flavell, A. K. Mallick, A. R. Kumarasinghe, D. Tsoutsou, N. Khan, C. Chatwin, S. Rayner, G. C. Smith, R. L. Stockbauer, S. Warren, T. K. Johal, S. Patel, D. Holland, A. Taleb and F. Wiame, *Phys. Rev. B: Condens. Matter Mater. Phys.*, 2007, **75**, 035105.

3.1.1.3 Systematic study of the effect of HSE functional internal parameters on the electronic structure and band gap of a representative set of metal oxides.

Journal of COMPUTATIONAL CHEMISTRY WWW.C-CHEM.ORG FULL PAPER

Systematic Study of the Effect of HSE Functional Internal Parameters on the Electronic Structure and Band Gap of a Representative Set of Metal Oxides

Francesc Viñes,[a] Oriol Lamiel-García,[a] Kyoung Chul Ko,*[a,b] Jin Yong Lee,[b] and Francesc Illas*[a]

The effect of the amount of Hartree–Fock mixing parameter (α) and of the screening parameter (w) defining the range separated HSE type hybrid functional is systematically studied for a series of seven metal oxides: TiO_2, ZrO_2, CuO_2, ZnO, MgO, SnO_2, and $SrTiO_3$. First, reliable band gap values were determined by comparing the optimal α reproducing the experiment with the inverse of the experimental dielectric constant. Then, the effect of the w in the HSE functional on the calculated band gap was explored in detail. Results evidence the existence of a virtually infinite number of combinations of the two parameters which are able to reproduce the experimental band gap, without a unique pair able to describe the full studied set of materials. Nevertheless, the results point out the possibility of describing the electronic structure of these materials through a functional including a screened HF exchange and an appropriate correlation contribution. © 2017 Wiley Periodicals, Inc.

DOI: 10.1002/jcc.24744

Introduction

Metal oxides constitute the most abundant materials on Earth crust[1] and are attracting widespread interest in various scientific fields, from electronics to heterogeneous catalysis, passing through the fascinating, yet not fully understood, phenomenon of high critical temperature superconductivity discovered back in 1986 by Bednorz and Müller.[2] Applications involving metal oxides cover the broad ranges on thin-film transistors, solar cells, diodes, memories, and photocatalysts.[3–5] The properties of metal oxides are highly dependent on their electronic structure; for instance, the band gap plays a key role in optoelectronic properties and is also crucial in applications such as photocatalysis. In this context, band gap engineering becomes one of the important issues for the application of metal oxides in light energy harvesting for energy/environment sciences and technologies.[6]

The band gap of these materials is often described in the framework of band structure theory and most often numerical predictions rely on different implementations of conventional density functional theory (DFT). However, the exchange-correlation potentials derived from the commonly used local density approximation (LDA) or generalized gradient approximation GGA based functionals tend to deliver severely underestimated band gaps for metal oxides to the point that calculations may incorrectly predict a metallic behavior for experimentally confirmed semiconductors.[7,8] This wrong behavior of LDA- and GGA-based methods is usually referred to as the band gap problem.[9]

Basically, the band gap problem arises from the usage of grossly approximated potentials under the Kohn-Sham implementation, and so, suffer from the self-interaction error (SIE)[10,11] which is intrinsic to the way the Coulomb contribution is accounted for. Thus, the LDA and GGA calculated results are intrinsically affected by the SIE. To reduce SIE, which is exactly cancelled in Hartree–Fock (HF) method, mixing of LDA or GGA exchange potentials with HF non-local exact exchange term has been proposed. This choice leads to the so-called hybrid functionals, first proposed by Becke.[12] In hybrid functionals normally a certain percentage of semilocal exchange, ranging from 0.1 to 0.5 (10 to 50%), is replaced by exact HF exchange, while the pure semilocal correlation potential is maintained. Some of the most widely used hybrid functionals, such as B3LYP[12] and PBE0,[13,14] containing 20 and 25% of HF exchange, respectively, have been found to be

[a] F. Viñes, O. Lamiel-García, K. C. Ko, F. Illas
Departament de Ciència de Materials i Química Física & Institut de Química Teòrica i Computacional (IQTCUB), Universitat de Barcelona, c/ Martí i Franquès 1, Barcelona, 08028, Spain
E-mail: francesc.illas@ub.edu, E-mail: kcko1982@gmail.com
[b] K. C. Ko, J. Y. Lee
Department of Chemistry, Sungkyunkwan University, Suwon, 16419, Korea
Contract grant sponsors: Spanish MINECO/FEDER CTQ2015-64618-R, Universitat de Barcelona for a predoctoral (to O.L.G.), 2015 ICREA Academia Award for Excellence in University Research (to F.I.), Red Española de Supercomputación and the COMPHOTOCAT project 2014112608 of the Partnership for Advanced Computing in Europe (PRACE), European Union's Horizon 2020 Research and Innovation Programme under grant agreement No 676580 (the NOMAD Center of Excellence project); Contract grant sponsor: MINECO for a postdoctoral Ramón y Cajal (RyC) research contract (to F.V.); Contract grant number: RYC-2012-10129; Contract grant sponsor: Generalitat de Catalunya; Contract grant numbers: 2014SGR97 and XRQTC; Contract grant sponsors: Ministry of Science, ICT and Future Planning, subjected project to the project EDISON (Education-research Integration through Simulation On the Net, to J.Y.L.); Contract grant number: 2012M3C1A6035359; Contract grant sponsor: Basic Science Research Program through the National Research Foundation of Korea (NRF) funded by the Ministry of Education (to K.C.K.); Contract grant number: NRF-2014R1A6A3A03056449

successful in accurately describing the geometrical and thermodynamic properties for a wide range of molecular systems.[11] However, in solids, the non-local nature of the Coulomb operator in the HF exchange of hybrid functionals leads to technical difficulties regarding slow convergence[15] as well as highly expensive computational cost, especially when using a plane waves basis set although with excellent performance.[16]

Nevertheless, using a standard Gaussian type orbitals basis set, hybrid functionals have been successfully used to predict band gaps of transition metal oxides[17–19] and of more complicated systems such as antiferromagnetic NiO.[20] Hybrid functionals using a plane wave basis sets have also been successfully applied to magnetic systems such as MnO[21] and to stoichiometric and reduced CeO_2.[22] However, the latter study uses a range separated exchange-correlation functional[23] which has been introduced to overcome the convergence drawbacks of hybrid functional above mentioned. In addition to the amount of Fock exchange, the range separated functionals introduce a second parameter aimed to define the short-range or long-range domains as described in more detail in the next section. The presence of this second parameter in the exchange-correlation potential results in a rather accurate description of the structural and thermochemical properties of both molecules and solids, including energy band gaps of solids[23–30] but at the same time introducing an additional degree of empiricism which may, in addition, introduce biases or artifacts in the calculated results. Previous studies focused on the average error introduced from different choices of these parameters.[31] Here, we provide an alternative point of view by systematically exploring the combinations of the parameters reproducing experimental properties. In particular, we will show that for certain observables, such as the band gap, there is a multitude of combinations of both parameters matching the experimental result. The consequences of this behavior are also described in the forthcoming sections.

Brief description of the HSE range separated hybrid functional

The HSE functional grounds on Perdew–Burke–Ernzerhof (PBE)[32] flavor of the GGA family of functionals, where the exchange-correlation energy is separated into exchange and correlation parts:

$$E_{xc}^{PBE} = E_x^{PBE} + E_c^{PBE} \quad (1)$$

Mixing the PBE exchange potential with a given fraction of the non-local exact HF exchange, generates the PBE0 hybrid functional.[13] Here one has

$$E_{xc}^{PBE0} = \alpha E_x^{HF} + (1-\alpha)E_x^{PBE} + E_c^{PBE} \quad (2)$$

where α indicates the HF mixing parameter. The PBE0 functional uses α as 1/4, a non-empirical coefficient justified from perturbation theory.[13,33] Nevertheless, this choice is not appropriate to describe NiO[20] or the different polymorphs of stoichiometric and reduced titania (TiO_2),[34] where higher and smaller amounts of Fock exchange are required to reproduce experimental values of electronic structure dependent properties, respectively.

To avoid the cumbersome convergence of hybrid functionals in some periodic approaches, mainly due to the problematic long-range HF exchange, the HSE functional introduces a screened Coulomb potential, which only affects the exchange part of the exchange correlation potential.[23,27] Thus, the exchange part of the electron-electron Coulomb interaction is arbitrarily decomposed into short range (SR) and long range (LR) contributions, and screened using the error function erf(r) as in eq. (3)

$$\frac{1}{r} = \mathrm{SR} + \mathrm{LR} = \frac{\mathrm{erfc}(wr)}{r} + \frac{\mathrm{erf}(wr)}{r} \quad (3)$$

where $\mathrm{erfc}(wr) = 1 - \mathrm{erf}(wr)$ and w is the screen parameter.[35] Henceforth, the HSE screened hybrid functional takes the form as in eq. (4)[36]

$$E_{xc}^{HSE} = \alpha E_x^{HF,SR}(w) + (1-\alpha)E_x^{PBE,SR}(w) + E_x^{PBE,LR}(w) + E_c^{PBE} \quad (4)$$

Thus, the HSE functional contains two parameters: the HF mixing parameter α and the screen parameter w. Note also that HF exchange mixing involves the SR part of the exchange potential only. In the limiting case of $w = 0$, the HSE functional becomes PBE0, whereas for $w \to \infty$ it becomes PBE. For the standard HSE functional, usually referred to also as HSE06, α and w values were empirically defined as 0.25 and 0.21 $Å^{-1}$ (0.11 $Bohr^{-1}$), respectively, chosen by considering both accuracy of results and computational efficiency, as suggested by Scuseria and coworkers.[24,27]

Coming back to the band gap problem, it is known that while LDA and GGA significantly underestimate the band gap of oxides and related materials, the increasing of HF exchange [α in eq. (4)] increases the calculated band gap.[37] Previous studies suggested that the optimal α for NiO was ~ 0.35,[20] whereas a smaller value of 0.125 is necessary to reproduce the band gap of anatase and rutile polymorphs of TiO_2.[24] Recently, a modification of the two parameters was also tried to adjust the calculated band gap of TiO_2 materials.[30] In a similar way, Ha et al. used $\alpha = 0.25$ and $w = \sim 0.378$ $Å^{-1}$ (0.200 $Bohr^{-1}$) to reproduce the band gap of TiO_2 anatase, whereas Janotti et al. used $\alpha = 0.20$ and $w = 0.200$ $Å^{-1}$ (0.106 $Bohr^{-1}$) for rutile TiO_2.[39] In this context, it is clear that different choices of the α and w parameters are possible, and this may be a convenient way to accurately predict the band gap of metal oxides. The role of the two parameters in the HSE functional was studied in detail by Moussa et al.[31] These authors studied the effect of the two parameters in a total of 33 solids, including metals, semiconductors, and insulators but only one metal oxide. The main focus of this work was in the error trends regarding several physical properties arising from different choices of the amount of Fock exchange and screening parameters. Afterwards, Koller et al. kept w fixed at 0.312 $Å^{-1}$ while optimized α for several solids including 5 metal

oxides.[40] More recently, a non-empirical way to define the optimal parameters in range separated hybrid functionals was carried out by Galli and coworkers,[41] yet the full space of w and α combinations was not fully explored.

Despite the many studies above mentioned addressing the two parameters in HSE, studies on practical combinations for different values of α and w parameters targeting the experimental band gaps are rare, with most of the focus aimed at showing the least mean absolute error for each set of parameters. Moreover, in many studies some parameters were fixed to a certain value sparsely. Furthermore, a limited number of metal oxides was investigated, whereas the electronic structure of these materials is known to be specially challenging.[9] For this reason, we here make as a further step paying attention to disclose the effect of choice of two parameters by systematically analyzing the overall α and w combinations reproducing reliable experimental band gaps for seven metal oxides, using scalar relativistic all electron density functional calculations. Our study would help to answer the question of how a set of optimal parameters is distributed, and whether a universal parameter exists among the investigated metal oxides. These results aid at understanding the effect of the HSE functional internal parameters on calculated band gaps of metal oxides. In addition, the rational procedure to gain these combinations can, by extension, be easily applied to other solid systems within HSE formalism.

Material Models and Computational Details

To investigate the existence of an optimal combination of Hartree–Fock mixing and screening parameters, α and w, respectively, up to seven metal oxides systems were considered in this study. These are TiO_2 (anatase), $SrTiO_3$ (cubic), Cu_2O (cubic), SnO_2 (rutile), ZrO_2 (monoclinic), ZnO (wurzite), and MgO (cubic). These metal oxides were selected from previous studies reporting their electronic structure description, the choice of α in hybrid functionals following arguments based on the dielectric constant (ε_∞),[31,40–43] or their interest for the photocatalytic water splitting.[44]

To eliminate the structural effect on the calculated band gaps, we used the experimentally obtained structures taken from the inorganic crystal structure database (ICSD),[45] through the Materials Project webpage,[46] see Table S1 in Supporting Information. It is notable that effect of α parameter is large on the electronic structure and, hence the band gap but much smaller in change of atomic structure, as reported for TiO_2 cases.[34] Single point calculations were carried out using $7 \times 7 \times 7$ Monkhorst-Pack mesh of special **k**-points except for MgO where a $17 \times 17 \times 17$ **k**-points Monkhorst-Pack mesh was used just to further check convergence of the electronic structure with respect to integration in the reciprocal space. All periodic density functional calculations were performed using the FHI-aims electronic structure code.[47,48] Present calculations explicitly include all electrons and the electron density is described by means of numerical atom-centered orbitals.[49] The light grid in combination with the Tier-1 basis set was chosen for its accuracy similar to or higher than that obtained with 6-311G* and just below of TZVP quality. The accuracy of the basis set can be inspected by just focusing on the total energy as, according to the variational theorem, the lower the total energy the more complete the basis set is and the total energy closer to the exact variational solution. For instance, for the O_2 molecule in its ground triplet state at a distance of 1.156 Å, the light Tier-1 total energy for non-relativistic at the unrestricted HF (UHF) level is −4072.582 eV, significantly lower than the corresponding value of −4072.456 eV obtained with the 6-311G*. This is also the case for the TiO_2 molecule in its singlet ground state at a given geometry (with Ti-O distance of 1.5977 Å and O-Ti-O angle of 115.96°) for which HF non-relativistic total energy with light Tier-1 is −27160.764 eV and the corresponding non-relativistic HF value for the 6-311G* basis set is −27159.604 eV. For the Ti atom in the triplet state the light Tier-1 basis set leads to an UHF total energy of −23085.533 eV meanwhile with the 6-311G* basis set the total UHF energy is −23084.972 eV. With this, the TiO_2 energy formation starting from Ti and O_2 is −2.649 eV for the light Tier-1 basis set and −2.176 eV for the 6-311G*, 0.473 eV smaller than the value obtained from the light Tier-1 basis set. Note also that, except for these calculations for the O_2 and TiO_2 molecules aimed at providing information about the quality of the NOA basis sets used, all calculations described in the present work include scalar relativistic effects through the ZORA method,[50] omitted in previous works or included through a pseudopotential.[31]

To search for a possible optimal combination of α and w that can best reproduce the experimental band gap value of these oxides, we systematically screened the two parameters. Thus, w values of 0.0, 0.2, 0.4, 0.6, 0.8, and 1.2 $Å^{-1}$ were considered, and for each of them α was varied from 0 to 1 with 0.25 intervals. Moreover, additional calculations were carried out to refine some points corresponding to w parameters of 0.6 $Å^{-1}$ or 0.9 $Å^{-1}$ to find the optimal α:w curve trend. This curve corresponds, for each oxide, to the combination of α and w values which reproduce the experimental band gap. Here, a caveat is necessary as one has to regard that the band gap is computed from the band structure obtained from the Kohn-Sham orbital energies in the reciprocal space rather than from using the theoretically more grounded many-body quasi particle-based GW formalism. Nevertheless, the bang gap is usually estimated from band structure calculations at the DFT level when calculations with GW methods are not affordable. Moreover, the success of hybrid and range separated hybrid functionals in predicting the band gap is precisely based on the assumption that this property can be extracted from the band structure.

Results and Discussion

In agreement with our previous study on bulk TiO_2 rutile and anatase structures,[34] we found that α and the calculated band gap exhibit a linear relationship good enough to use linear inter/extrapolation to find, for a certain fixed value of w, the α value matching the experimental band gap (see Figure S1 in Supporting Information). In the following, we refer to

this α value as optimal. Conversely, for a fixed α, the screen parameter w and the calculated band gap are roughly in inverse proportion to each other, but without displaying a linear relationship, especially for cases of high α values where an exponential decay trend is observed. Thus, in this study, we decided to use the relationship between the α parameter and the calculated band gap to find the optimal combination of α and w also with respect to the experimental band gap. In the following, we discuss several relationships regarding the mixing parameter α, the dielectric constant (ε_∞), the band gap, and the optimal combinations of α and w.

Defining the Optimal Mixing Parameter without Screening Effect

First of all, we discuss the results obtained by varying the α parameter while keeping $w = 0$ and compare to the experimental band gaps as reported in Table 1—with ranges given in parenthesis. It should be noted except for Cu_2O, the experimental value used to obtain the optimal α is the lowest value in the experimental range in Table 1.

For Cu_2O, we estimated the experimental band gap value with consideration of the energy correction for the forbidden transition as discussed in more detail below. The present calculations predict direct band gaps for Cu_2O, SnO_2, ZnO, and MgO, and indirect band gaps for TiO_2, $SrTiO_3$, and ZrO_2, respectively; in agreement with experiments (see references in Table 1). Using the experimental band gap values in Table 1 allows one to obtain the α value leading to calculated values consistent with experiments, which we recall as optimal. Not surprisingly the optimal values for each one of the oxides studied in the present work are different (Table 1).

To properly discuss the results in Table 1, it is necessary to caution that comparing theoretical band gaps with experimental data is not free of controversy.[71–74] As indicated in the previous section, the presently calculated band gaps are computed as the energy difference between the valence band maximum (VBM) and the conduction band minimum (CBM) obtained by self-consistently solving the one electronic Kohn-Sham equations and thus neglecting many-body effects in the quasi particle excitations. Conversely, all selected experimental band gaps were measured by different techniques: Ultraviolet-visible (UV) spectroscopy in the cases of Cu_2O, TiO_2, SnO_2, and ZnO_2, electron-energy-loss spectroscopy (EELS) for $SrTiO_2$ and ZrO_2, and reflectance spectroscopy for MgO. In these experiments, the electron and hole pair, called exciton, could be generated from incident light or an electron collision; there are several kinds of EELS (transmission, reflection, aloof and high-resolution EELSs, and so on).[75–77] Herein we only discussed the cases for the energy loss occurring from the surface inter-band transitions. Thus, additional contributions for electron-hole pair electrostatic interaction have to be taken into account, when one wishes a more accurate comparison between the experimental and theoretical band gaps.[77] HSE calculations based on generalized Kohn-Sham scheme would give the calculated band gap excluding electron-hole pair binding energy. Thus, HSE band gap might be more near to the fundamental band gap. However, as a practical matter, HSE band gap also should be understood as a reasonable estimate of the experimental optical gap. This is justified because the optical and fundamental gaps in semiconductors are very close, as argued by Scuseria et al.[78] In this sense, it is understandable that the calculated results below show that the present theoretical estimates of band gaps are accurate enough.

Table 1. Experimental band gap values (Δ, in eV), calculated optimal mixing parameter α with screening parameter $w = 0$ Å^{-1}, experimental dielectric constant (ε_∞) and inverse dielectric constant ($1/\varepsilon_\infty$) for the seven metal oxides considered in the present work.

	Δ	α	ε_∞	$1/\varepsilon_\infty$	w
Cu_2O	1.57[a] (1.70–2.40)[51–54]	0.119	6.46[55]	0.155	1.21
TiO_2	3.20[b] (3.20–3.42)[56,57]	0.134	5.62[58]	0.178	1.29
$SrTiO_3$	3.25 (3.25–3.75)[59]	0.154	5.18[60]	0.193	1.14
ZrO_2	5.30 (5.30–7.09)[61,62]	0.181	4.54[c]	0.220	0.94
SnO_2	3.30[63] (3.30–4.00)[63]	0.207	4.00[64]	0.250	0.94
ZnO	3.37[65] (3.37–3.44)[65–67]	0.254	3.74[68]	0.267	0.88
MgO	7.67 (7.67 −7.83)[69,70]	0.293	2.96[70]	0.338	0.72

[a] Estimated value considering the energy correction around 0.13 eV from the experimental band gap 1.7 eV. [b] Consensus value. [c] Simply calculated from well-known refractive index value 2.13, using the relation $\varepsilon_0 = n^2$. The rightmost column reports the optimal (matching the experimental band gap) screening parameter w (Å^{-1}) for $\alpha = 1$.

Relationship between the optimal HF mixing parameter and experimental dielectric constant. From results in Table 1, it is clear that, with w parameter 0 Å^{-1}, the optimal α values range from 0.119 to 0.293, indicating that a universal hybrid functional able to reproduce the experimental band gaps is not achievable. To explain the need of using different values of α to reproduce the band gap of different materials, Fiorentini and Baldereschi,[79] suggested that α is related to the inverse of the static dielectric constant ($1/\varepsilon_\infty$) of the material.[80] Experimental dielectric constant values and of its inverse ($1/\varepsilon_\infty$) are reported in Table 1. Herein, it is noted that the average values of static dielectric constants were used, when there are several experimental data reported for optically anisotropic oxides. The relationship between calculated optimal α and experimental $1/\varepsilon_\infty$ is plotted in Figure 1. Indeed, the relationship is almost linear and a proper fit leads to $\alpha = 0.958 \times (1/\varepsilon_\infty) + 0.045$ with $R^2 = 0.965$. This finding supports the present estimate of the band gaps and reinforces the interpretation of Marques et al.,[80] although it leaves the role of the w parameter open.

The case of Cu_2O deserves, however, a separate discussion since when we plotted the graph of Figure 1, we realized that previously reported band gaps measured by optical transition considerably deviated from the trend in Figure 1. Interestingly, the reported experimental band gap has been decreasing from the earlier measurements: 2.17 eV in 1966,[53] 2.02 eV in

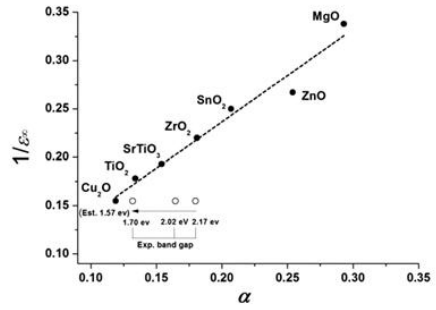

Figure 1. Correlation between the optimal mixing parameter α and the inverse of the experimental dielectric constants ($1/\varepsilon_\infty$) for metal oxides under scrutiny.

1970,[52] and 1.70 eV in 1994.[54] The different values are marked as open circles in Figure 1. The differences in the reported experimental values of the band gap of Cu_2O might be due to difficulties in growing stoichiometric and clean Cu_2O samples,[81] and to fact that the band gap of this material has the character of optically forbidden-direct transition because of the state symmetries of VBM and CBM having Cu 3*d*- and Cu 4*s*-like characters, respectively.[82] The most recent and carefully done UV experiments for a Cu_2O thin film supported on MgO(100) reported a value of 1.70 eV. However, it is expected that this optical band gap would be wider than the ideal band gap of Cu_2O, because optical transitions between the band-edge states are also forbidden. Thus, we decided to get an estimate from this minimum value of 1.70 eV by considering the reported correction energy, calculated as the difference between the forbidden transition energy and the first allowed transition energy, sized to be around 0.13 eV.[82] Interestingly, our estimated value of minimum band gap 1.57 eV (1.70 eV minus 0.13 eV) lines up the optimal α value, showing the remarkable nice fit to the plot in Figure 1.

Optimal α:*w* trends of HSE hybrid functional reproducing experimental band gap value. The above discussion highlighted a clear relationship between the band gap and α parameter, excluding the screening effect. Moreover, by comparing the optimal α parameters with the inverse experimental dielectric constant values, indirectly one can state that present selection of experimental band gap values seems to be reasonable. This setting might become an important first step to precisely explore the space for α and *w* parameters of HSE functional. Here, one must point out that range separated functionals such as HSE introduce a physically meaningful additional parameter (*w*) controlling the range where Fock exchange needs to switched off. To investigate more in detail the combined effect of α and *w* and to find a possible combination working for all the materials studied in the present work we carried out a series of calculations to find the optimal α for different values of *w*, results summarized in Figure 2 and the complete set of data points included in Table S2 of Supporting Information.

The curves in Figure 2 correspond to α:*w* pairs which, for each material, exactly reproduce the experimental ban gap, as collected in Table 1. Otherwise, on the basis of each line, the calculated band gap values on the up-left are underestimated, and overestimated on the bottom-right. On two dimensional space composed of α and *w* axes, the point for $\alpha = 0.25$ and $w = 0$ Å^{-1} formally is corresponding to the PBE0 functional. Interestingly, PBE0 correctly describes the band gap of ZnO as reported in previous studies,[42,83] yet underestimates the band gap of TiO_2, $SrTiO_3$, Cu_2O, SnO_2, and ZrO_2, while overestimates that of MgO. Let us now focus on the values with $\alpha = 0.25$ and $w = 0.21$ Å^{-1}, which correspond to the so-called HSE06 functional. This functional properly describes the band gap of ZrO_2 as described in previous studies,[42,84] but underestimates the band gap of TiO_2, $SrTiO_3$, Cu_2O oxides, while overestimating that of SnO_2, ZnO, and MgO. From Figure 2, it appears that the success of HSE06 in describing band gaps, either fundamental of optical, for various semiconductors,[35] precisely is due to the fact that it lies on the central part of the curve rainbow.

Conversely, for a given α value, such as 0.25 chosen for PBE0, it appears that different amounts of screening parameters are required to reproduce band gaps for the different metal oxides: around 0.4 Å^{-1} for Cu_2O and TiO_2, around 0.3 Å^{-1} for $SrTiO_3$, 0.2 Å^{-1} for ZrO_2, and around 0.1 Å^{-1} for SnO_2, respectively. This is not surprising as the screening needs to be also related to the electric response of the material. Hence, one could argue that it is more appropriate to stay with a particular amount of Fock exchange but tuning *w* instead. However, it is noticeable that for MgO using any values of screening parameter (*w*) with a given α value as 0.25 would not solve the band gap problem of underestimation. This is in agreement with the failure of HSE functional using $\alpha = 0.25$ for large-gap insulators.[80] In fact, Figure 2 shows that $\alpha > 0.3$ is

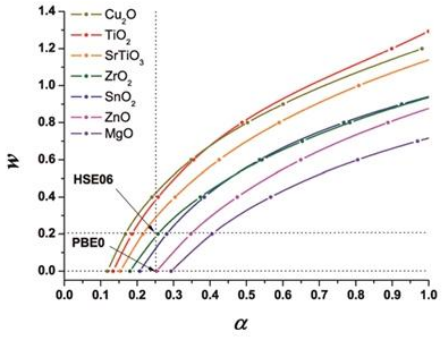

Figure 2. Optimal α:*w* trend of HSE hybrid functional reproducing the experimental band gap for seven metal oxides. [Color figure can be viewed at wileyonlinelibrary.com]

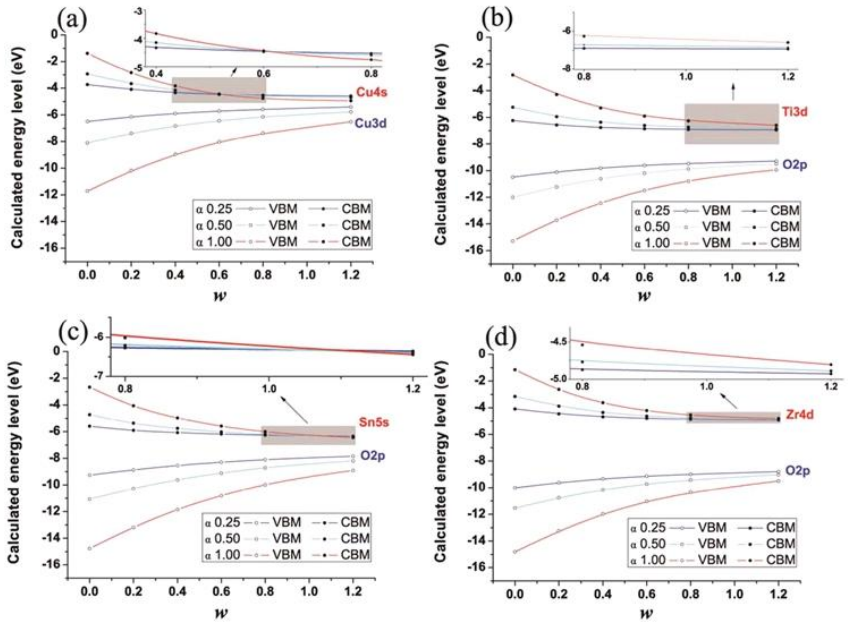

Figure 3. VBM and CBM (in eV) for Cu_2O a), TiO_2 b), SnO_2 c), and ZrO_2 d), as a function of w for three values of α and screen parameter w. [Color figure can be viewed at wileyonlinelibrary.com]

necessary to reproduce the band gap of MgO within HSE formalism. This is also in line with the previously suggested HSE12 and HSE12s functionals, having $\alpha = 0.313$ and $\alpha = 0.425$, respectively, with different w parameters to minimize overall error for diverse physical properties of broad range of solids, including MgO.[31]

As stated, from Figure 2 it is clear that there is an infinite number of α:w pairs reproducing the experimental band gap of a given oxide, but it is worth to highlight that the overestimation by applying a large α value is counteracted by increasing the w screening. Following this rule, each metal oxide tends to exhibit a particular curvature of the α:w plot compatible with the experimental band gap value. Figure 2 also shows that, unfortunately, there is no single α:w pair describing all materials, although this seems possible for pairs of metal oxides. Indeed, cross points are found at the combination of ($\alpha = 0.4$: $w = 0.68$ Å^{-1}) and ($\alpha = 0.47$: $w = 0.52$ Å^{-1}) for Cu_2O-TiO_2 and ZrO_2-SnO_2, respectively. In this regard, these particular setups of the range separated HSE functional could be used to describe these binary metal oxide systems regarding the band gap. To shed light on the underlying reason for the existence of the crossing points for Cu_2O-TiO_2 and ZrO_2-SnO_2 couples, we analyze the changes of energy levels for VBM and CBM of these oxides induced by w for fixed values of α. Figure 3 shows these trends for Cu_2O, TiO_2, ZrO_2, and SnO_2.

Most notable feature of Figure 3 is that, for α values of 0.25, 0.50, and 1.00, the effect of w on the CBM lowering is different for the different metal oxides. Comparing TiO_2 to Cu_2O, the CBM lines cross around $w = 0.6$ Å^{-1} for the three α values. This cross point is also found for SnO_2 at around $w = 1.1$ Å^{-1} (see inset in Fig. 3), whereas for TiO_2 and ZrO_2 the cross point occurs beyond $w = 1.2$ Å^{-1}. Interestingly, for Cu_2O and SnO_2 the CBM is composed of Cu 4*s* and Sn 5*s* states,[85,86] whereas for TiO_2 and ZrO_2 the CBM is dominated by Ti 5*d* and Zr 4*d* states.[34,87] This seems to indicate that, not surprisingly, the screening affects *s* and *d* bands differently. Supporting Information Figure S2 shows the CBM cross points for ZnO_2 and MgO possessing both a CBM of *s*-like character.[88,89] Conversely, no cross point is found for $SrTiO_3$ with a CBM of 3*d* character. Consequently, the band energy levels are influenced by α and w but also by the orbital character of the involved energy states. Thus, the difference of orbital character for energy state is likely to be behind the matching points of Cu_2O-TiO_2 and ZrO_2-SnO_2 pairs. It should be mentioned that this is not likely to be the sole reason, or a general feature, since other crossing points should be observed and validated in future works.

Finally, it is interesting to note that starting from pure Hartree–Fock ($\alpha = 1.0$) it would be possible to reproduce the band gap of the oxides using the appropriate screening factor, implying that SR is only described by HF exchange and LR

only by PBE exchange while adding the appropriate correlation functional. From eq. (4), the form can be derived as

$$E_{xc}^{sX-PBE} = E_x^{HF,SR}(w) + E_x^{PBE,LR}(w) + E_c^{PBE} \quad (5)$$

This is similar to the sX-LDA, proposed to yield improved band gaps by including screened exchange.[7] Basically, exchange and correlation have an unambiguous definition when using wave functions.[90] It retakes the meaning of exchange and correlation used in wave function-based methods where Hartree–Fock is a well-defined method and electron correlation has the meaning of instantaneous electron-electron interactions beyond the mean (self-consistent) field approximation. Generally, increasing the Fock exchange can reduce the spurious self-interaction but then it misses electronic correlation effects leading to an overestimation of the band gap. Thus, the lack of correlation in pure Hartree–Fock exchange makes the gap too large and the physics needed to reduce the gap is simply to add the electron correlation contribution. This is more or less taken with the different functionals incorporating the proper screening length. This is a reason why it may be appealing to compensate the error of the band gap by the balance between the correlation and screened Hartree–Fock with appropriate screening parameters reflecting the cancellation of the long-range correlation and exchange energies. Figure 2 indicates that the proper screening parameters on those points have material dependence as like a proper HF mixing parameter with no screening effect. Note that the expected proper screening parameters at $\alpha = 1.0$ depicted in Figure 2 is highly related to Thomas-Fermi (TF) screening parameters (in $Å^{-1}$) of sX-LDA functional comprehensively studied by Clark and coworkers.[91–95] The only difference between HSE scheme and sX-LDA is the replacement of the LDA form for correlation and long-range exchange with the PBE form, as discussed by Chelikowsky and coworkers.[31] Within a simply screened Hartree–Fock exchange plus correlation logic, TiO_2 appears to need the highest value of the screening parameter to properly predict the band gap whereas MgO will need the smallest one. However, the underlying reason of this tendency and the description for the defect systems still remains to be fully understood.

Conclusions

The effect of the internal parameters (α and w) of the range separated HSE hybrid functional incorporating scalar relativistic effects in the description of the electronic structure mainly through the optical band gap neglecting possible excitonic effects, has been studied in detail for a set of seven metal oxides including transition metals with incomplete *d*-shells transition metals (Ti, Zr), with complete *d*-shells (Cu, Zn), and also considering non-transition metals (Mg and Sn). In this study, we mainly investigated the effect of two parameters on band gaps. This is because the band gap is the most sensitive property to different settings of HSE functional. In fact, calculations for anatase, TiO_2 (see Tables S3 and S4 in Supporting Information) evidence that the effect of the two parameters on lattice parameters and formation enthalpy does not exceed 3%. It is worth pointing out that our investigation of the effect of two parameters is in line with recent work of Garza and Scuseria precisely on the band gap of oxides.[94]

Neglecting the range separation, that is, for pure hybrid functionals, the calculated band gap is linearly correlated with the amount of Fock exchange included in the exchange part of the exchange-correlation potential, thus generalizing previous observations.[73] This finding suggest that the screening parameter w may not be needed, at least as far as the prediction of the band gap is concerned for metal oxides, although introducing this parameter facilitates convergence of the required calculations. In these cases, it appears that the amount of optimal Fock exchange corresponding to the selected experimental band gap linearly correlates with the inverse of the experimental dielectric constant of the material, again in agreement with previous works.[79,80] From this step, we can confirm that our selection about the experimental band gap values, specifically optical gap values, are uniformly reasonable for the studied metal oxides.

The introduction of the screening parameter has an effect which is contrary to that of the amount of Fock exchange in such a way that increasing the value of the screening parameter reduces the calculated band gap value, this is one of the reasons why HSE06 represent an improvement over PBE0 for the calculation of band gaps, where a possible overestimation of the bandgap cannot be counteracted. However, compared to Fock exchange, the correlation between screening parameters and the calculated band gap tends to be changed from inverse proportional to exponential decay as the percentage of Fock exchange increases. Thus, only using the linear relationship between the Fock exchange and the calculated band gap would be a straightforward way to find the optimal set of two parameters via linear inter/extrapolation method.

At last, it is found that there is an infinite number of α:w combinations which, for a given metal oxide, reproduce its experimental band gap. This makes it difficult to define a unique range separated HSE-like functional able to properly describe the band gap of a given family of oxides, even though matching points for Cu_2O-TiO_2 and ZrO_2-SnO_2 pairs are expected to exist. From the energy state analysis regarding these, it is shown that the subtle curvature difference on α:w curves between oxides might be related with the orbital characteristic of the involved energy states. Consequently, our results provide an evidence that the band energy levels for oxides are influenced by α and w but also by the orbital character within HSE functional formalism. However, the details of the electric response for the electron density according to orbital character should be explored depending on the two parameters of HSE functional. Additionally, the present systematic study shows that it is possible to reproduce the band gap of oxides starting from the Hartree–Fock approximation, and adding correlation through the appropriate functional, provided the SR part of the Fock exchange is properly screened. This will put the difference in the material rather than on the method, which seems physically appealing. These conclusions are presented for metal oxides, it is sensible to think that

conclusions would remain valid for other semiconductors and isolators, such as sulfides and selenides.

Keywords: metal oxides · band gap · density functional theory · Hartree–Fock exchange · screen parameter · HSE functional

How to cite this article: F. Viñes, O. Lamiel-García, K. Chul Ko, J. Yong Lee, F. Illas. *J. Comput. Chem.* **2017**, DOI: 10.1002/jcc.24744

Additional Supporting Information may be found in the online version of this article.

[1] G. Koster, *Epitaxial Growth of Complex Metal Oxides*; Elsevier: Boston, MA, **2015**.
[2] J. Bednorz, K. Müller, *Z. Phys. B* **1986**, *64*, 189.
[3] M. Imada, A. Fujimori, Y. Tokura, *Rev. Mod. Phys.* **1998**, *70*, 1039.
[4] X. Yu, T. J. Marks, A. Facchetti, *Nat. Mater.* **2016**, *15*, 383.
[5] T. Grewe, M. Meggouh, H. Tüysüz, *Chem.-Asian J.* **2016**, *11*, 22.
[6] L. Yuan, C. Han, M. Q. Yang, Y. J. Xu, *Int. Rev. Phys. Chem.* **2016**, *35*, 1.
[7] D. M. Bylander, L. Kleinman, *Phys. Rev. B* **1990**, *41*, 7868.
[8] V. N. Staroverov, G. E. Scuseria, J. Tao, J. P. Perdew, *Phys. Rev. B* **2004**, *69*, 075102.
[9] C. Sousa, S. Tosoni, F. Illas, *Chem. Rev.* **2013**, *113*, 4456.
[10] J. P. Perdew, A. Zunger, *Phys. Rev. B* **1981**, *23*, 5048.
[11] A. J. Cohen, P. Mori-Sanchez, W. Yang, *Chem. Rev.* **2012**, *112*, 289.
[12] A. D. Becke, *J. Chem. Phys.* **1993**, *98*, 5648.
[13] P. Perdew, M. Ernzerhof, K. Burke, *J. Chem. Phys.* **1996**, *105*, 9982.
[14] C. Adamo, V. Barone, *J. Chem. Phys.* **1999**, *110*, 6158.
[15] S. V. Levchenko, X. Ren, J. Wieferink, R. Johanni, P. Rinke, V. Blum, M. Scheffler, *Comput. Phys. Commun.* **2015**, *192*, 60.
[16] J. Paier, R. Hirschl, M. Marsman, G. Kresse, *J. Chem. Phys.* **2005**, *122*, 234102.
[17] T. Bredow, A. R. Gerson, *Phys. Rev. B* **2000**, *61*, 5194.
[18] J. Muscat, A. Wander, N. M. Harrison, *Chem. Phys. Lett.* **2001**, *342*, 397.
[19] K. N. Kudin, G. E. Scuseria, R. L. Martin, *Phys. Rev. Lett.* **2002**, *89*, 266402.
[20] I. de P. R. Moreira, F. Illas, R. L. Martin, *Phys. Rev. B* **2002**, *65*, 155102.
[21] C. Franchini, V. Bayer, R. Podloucky, J. Paier, G. Kresse, *Phys. Rev. B* **2005**, *72*, 045132.
[22] J. L. F. Da Silva, M. V. Ganduglia-Pirovano, J. Sauer, V. Bayer, G. Kresse, *Phys. Rev. B* **2007**, *75*,
[23] J. Heyd, G. E. Scuseria, M. Ernzerhof, *J. Chem. Phys.* **2003**, *118*, 8207.
[24] J. Heyd, G. E. Scuseria, M. Ernzerhof, *J. Chem. Phys.* **2006**, *124*, 219906(E).
[25] J. Heyd, G. E. Scuseria, *J. Chem. Phys.* **2004**, *120*, 7274.
[26] J. Heyd, G. E. Scuseria, *J. Chem. Phys.* **2004**, *121*, 1187.
[27] A. V. Krukau, O. A. Vydrov, A. F. Izmaylov, G. E. Scuseria, *J. Chem. Phys.* **2006**, *125*, 224106.
[28] J. Heyd, J. E. Peralta, G. E. Scuseria, R. L. Martin, *J. Chem. Phys.* **2005**, *123*, 174101.
[29] J. E. Peralta, J. Heyd, G. E. Scuseria, R. L. Martin, *Phys. Rev. B* **2006**, *74*, 073101.
[30] I. D. Prodan, G. E. Scuseria, R. L. Martin, *Phys. Rev. B* **2006**, *73*, 045104.
[31] J. E. Moussa, P. A. Schultz, J. R. Chelikowsky, *J. Chem. Phys.* **2012**, *136*, 204117.
[32] J. P. Perdew, K. Burke, M. Ernzerhof, *Phys. Rev. Lett.* **1996**, *77*, 3865.
[33] M. Ernzerhof, G. E. Scuseria, *J. Chem. Phys.* **1999**, *110*, 5029.
[34] K. C. Ko, O. Lamiel-García, J. Y. Lee, F. Illas, *Phys. Chem. Chem. Phys.* **2016**, *18*, 12357.
[35] B. G. Janesko, T. M. Henderson, G. E. Scuseria, *Phys. Chem. Chem. Phys.* **2009**, *11*, 443.
[36] E. N. Brothers, A. F. Izmaylov, J. O. Normand, V. Barone, G. E. Scuseria, *J. Chem. Phys.* **2008**, *129*, 011102.
[37] Y. F. Zhang, W. Lin, Y. Li, K. N. Ding, J. Q. Li, *J. Phys. Chem. B* **2005**, *109*, 19270.
[38] M. A. Haa, A. N. Alexandrova, *J. Chem. Theory Comput.* **2016**, *12*, 2889.
[39] A. Janotti, J. Varley, P. Rinke, N. Umezawa, G. Kresse, C. Van de Walle, *Phys. Rev. B* **2010**, *81*, 085212.
[40] D. Koller, P. Blaha, F. Tran, *J. Phys.: Condens. Matter* **2013**, *25*, 435503.
[41] J. H. Skone, M. Govoni, G. Galli, *Phys. Rev. B* **2016**, *93*, 235106.
[42] M. Gerosa, C. E. Bottani, L. Caramella, G. Onida, C. Di Valentin, G. Pacchioni, *Phys. Rev. B* **2015**, *91*, 155201.
[43] S. Lany, *Phys. Rev. B* **2013**, *87*, 085112.
[44] V. Stevanovic, S. Lany, D. S. Ginley, W. Tumas, A. Zunger, *Phys. Chem. Chem. Phys.* **2014**, *16*, 3706.
[45] Available at: www.icsd.ill.fr/icsd/index.php
[46] Available at: www.materialsproject.org
[47] V. Blum, R. Gehrke, F. Hanke, P. Havu, V. Havu, X. Ren, K. Reuter, M. Scheffler, *Comput. Phys. Commun.* **2009**, *180*, 2175.
[48] V. Havu, V. Blum, P. Havu, M. Scheffler, *J. Comput. Phys.* **2009**, *228*, 8367.
[49] I. Y. Zhang, X. G. Ren, P. Rinke, V. Blum, M. Scheffler, *New J. Phys.* **2013**, *15*, 123033.
[50] E. van Lenthe, E. J. Baerends, J. G. Snijders, *J. Chem. Phys.* **1994**, *101*, 9783.
[51] S. B. Ogale, P. G. Bilurkar, N. Mate, S. M. Kanetkar, N. Parikh, B. Patnaik, *J. Appl. Phys.* **1992**, *72*, 3765.
[52] S. P. Tandon, J. P. Gupta, *Phys. Status Solidi B* **1970**, *37*, 43.
[53] S. Brahms, S. Nikitine, J. P. Dahl, *Phys. Lett.* **1966**, *22*, 31.
[54] I. Grozdanov, *Mater. Lett.* **1994**, *19*, 281.
[55] M. O'Keeffe, *J. Chem. Phys.* **1963**, *39*, 1789.
[56] D. O. Scanlon, C. W. Dunnill, J. Buckeridge, S. A. Shevlin, A. J. Logsdail, S. M. Woodley, C. R. A. Catlow, M. J. Powell, R. G. Palgrave, I. P. Parkin, *Nat. Mater.* **2013**, *12*, 798.
[57] H. Tang, F. Lévy, H. Berger, P. E. Schmid, *Phys. Rev. B* **1995**, *52*, 7771.
[58] S. Wemple, *J. Chem. Phys.* **1977**, *67*, 2151.
[59] A. Benrekia, N. Benkhettou, A. Nassour, M. Driz, M. Sahnoun, S. Lebègue, *Physica B* **2012**, *407*, 2632.
[60] W. Zhong, R. D. King-Smith, D. Vanderbilt, *Phys. Rev. Lett.* **1994**, *72*, 3618.
[61] L. K. Dash, N. Vast, P. Baranek, M. C. Cheynet, L. Reining, *Phys. Rev. B* **2004**, *70*, 245116.
[62] H. French, S. J. Glass, F. S. Ohuchi, Y. N. Xu, W. Y. Ching, *Phys. Rev. B* **1994**, *49*, 5133.
[63] O. Madelung, *Semiconductors—Basic Data*; Springer Science & Business Media: Berlin, **2012**.
[64] M. Dou, C. Persson, *J. Appl. Phys.* **2013**, *113*, 083703.
[65] K. H. Hellwege; O. Madelung, *Numerical Data and Functional Relationships in Science and Technology, Landolt-Börnstein, New Series, Group III*, Vol. *17*, Part A; Springer: Berlin, **1982**.
[66] W. Y. Liang, A. D. Yoffe, *Phys. Rev. Lett.* **1968**, *20*, 59.
[67] D. C. Reynolds, D. C. Look, B. Jogai, C. W. Litton, G. Cantwell, W. C. Harsch, *Phys. Rev. B* **1999**, *60*, 2340.
[68] N. Ashkenov, B. N. Mbenkum, C. Bundesmann, V. Riede, M. Lorenz, D. Spemann, E. M. Kaidashev, A. Kasic, M. Schubert, M. Grundmann, G. Wagner, H. Neumann, V. Darakchieva, H. Arwin, B. Monemar, *J. Appl. Phys.* **2003**, *93*, 126.
[69] R. C. Whited, C. J. Flaten, W. C. Walker, *Solid State Commun.* **1973**, *13*, 1903.
[70] D. R. Lide, *CRC Handbook of Chemistry and Physics*; CRC press: New York, **2004**.
[71] H. Jiang, R. I. Gomez-Abal, P. Rinke, M. Scheffler, *Phys. Rev. B* **2010**, *81*, 085119.
[72] J. L. Bredas, *Mater. Horiz.* **2014**, *1*, 17.
[73] D. Cho, K. C. Ko, O. Lamiel-García, S. T. Bromley, J. Y. Lee, F. Illas, *J. Chem. Theory Comput.* **2016**, *12*, 3751.
[74] L. Kronik, T. Stein, S. Refaely-Abramson, R. Baer, *J. Chem. Theory Comput.* **2012**, *8*, 1515.
[75] R. F. Egerton, *Rep. Prog. Phys.* **2009**, *72*, 016502.
[76] B. Reed, M. Sarikaya, *Ultramicroscopy* **2002**, *93*, 25.
[77] G. Bracco, B. Holst, *Surface Science Techniques*; Springer Science & Business Media: Berlin, **2013**.
[78] T. M. Henderson, J. Paier, G. E. Scuseria, *Phys. Status Solidi B* **2011**, *248*, 767.

[79] V. Fiorentini, A. Baldereschi, *Phys. Rev. B* **1995**, *51*, 17196.
[80] M. A. L. Marques, J. Vidal, M. J. T. Oliveira, L. Reining, S. Botti, *Phys. Rev. B* **2011**, *83*, 035119.
[81] D. Tahir, S. Tougaard, *J. Phys.: Condens. Matter* **2012**, *24*, 175002.
[82] D. C. Reynolds, *Excitons: Their Properties and Uses;* Elsevier: New York, **2012**.
[83] D. Gryaznov, E. Blokhin, A. Sorokine, E. A. Kotomin, R. A. Evarestov, A. Bussmann-Holder, J. Maier, *J. Phys. Chem. C* **2013**, *117*, 13776.
[84] A. Sinhamahapatra, J. P. Jeon, J. Kang, B. Han, J. S. Yu, *Sci. Rep.* **2016**, *6*, 27218.
[85] B. K. Meyer, A. Polity, D. Reppin, M. Becker, P. Hering, P. J. Klar, T. Sander, C. Reindl, J. Benz, M. Eickhoff, C. Heiliger, M. Heinemann, J. Bläsing, A. Krost, S. Shokovets, C. Müller, C. Ronning, *Phys. Status Solidi B* **2012**, *249*, 1487.
[86] M. Batzill, U. Diebold, *Prog. Surf. Sci.* **2005**, *79*, 47.
[87] C. Ricca, A. Ringuedé, M. Cassir, C. Adamo, F. Labat, *J. Comput. Chem.* **2015**, *36*, 9.
[88] A. S. Alshammari, L. Chi, X. Chen, A. Bagabas, D. Kramer, A. Alromaeh, Z. Jiang, *RSC Adv.* **2015**, *5*, 27690.
[89] R. A. Evarestov, *Theoretical Modeling of Inorganic Nanostructures: Symmetry and Ab-Initio Calculations of Nanolayers, Nanotubes and Nanowires;* Springer: Berlin, **2015**.
[90] G. C. Lie, E. Clementi, *J. Chem. Phys.* **1974**, *60*, 1275.
[91] S. J. Clark, J. Robertson, *Phys. Rev. B* **2010**, *82*, 085208.
[92] S. J. Clark, J. Robertson, *Phys. Status Solidi B* **2011**, *248*, 537.
[93] G. Yuzheng, R. John, J. C. Stewart, *J. Phys.: Condens. Matter* **2015**, *27*, 025501.
[94] A. J. Garza, G. E. Scuseria, *J. Phys. Chem. Lett.* **2016**, *7*, 4165.

Received: 15 November 2016
Revised: 22 December 2016
Accepted: 10 January 2017
Published online on 00 Month 2017

Overview

The aim of the work presented in this chapter was to find a computational model able to describe the energetic and electronic features of the most stable polymorphs of TiO_2 in order to elucidate the key role they play to the photocatalytic activity of this material.

The first work presented shows a systematic study of the performance of different DFT functionals in the description of TiO_2. We find in all cases that all functionals (GGA, GGA+U and hybrid functionals) described quite well the structural features (e.g. cell parameters). The GGA functionals provide a good description of the energetics and geometric features but underestimating the band gap of the material. The DFT+U, setting a U = 6 eV for both Ti(3d) and O(2p), improved the description of the electronic structure with an affordable computational cost. The hybrid functionals tested (PBE0, B3LYP and HSE06) give a better description of the electronic structure than GGA but slightly overestimate the band gap for TiO_2 polymorphs and have a considerably larger computational cost. The same trends regarding the description of the electronic structure was found when studying the electronic states derived from the fluorine doping of TiO_2.

Motivated by these results we decided to study more deeply the performance of modified hybrid functionals with respect to the description of the electronic structure of TiO_2. In this work, different amounts of Fock exchange have been tested. We found that the band gap value is almost linearly dependent on the percentage of Fock exchange used in the functional. These results allowed us to find the amount of Fock exchange needed to have an accurate description of the electronic structure features of our bulk anatase and rutile. With a 12.5% of Fock exchange in the PBE0 functional we were able to reproduce the experimental results previously reported in the literature.

With the finding of this direct relation between the band gap and the amount of Fock exchange used in a hybrid functional for Anatase and Rutile. Extending this idea, we decided to study the HSE functional in a similar way, while also analysing the effect of the screening parameter, for the description of the electronic structure of other metal oxides: ZrO_2,CuO_2, ZnO, MgO, SnO_2, and $SrTiO_3$. As for our previous study, in each case the band gap value increases with the amount of Fock exchange included in the functional. On the other hand the screening parameter value works in the opposite way, leading to a reduction of the band gap as the screening parameter increases. We could

not find a unique combination for the Fock exchange and screening parameter that led to an accurate description of all semiconductors at same time. This work shows that by modifying these two parameters, one can reach an accurate level of description of the band gap and electronic properties of a range of metal oxides separately. These first results form the basis of the methodology used in the work presented in the forthcoming chapters of the thesis.

3.1.2. Effect of Fluorine in the electronic structure of bulk and surfaces of TiO_2: relevance to photocatalytic activity.

In recent years several experimental studies showed that doping TiO_2 with certain atom types could lead to more active photocatalysts.[62–66] This effect is due to the appearance of electronic states that reduce the band gap of the material shifting of the wavelength absorbed by the photocatalysist and subsequently increasing its efficiency. In addition, it was recently discovered that the use of compounds containing fluorine (as fluorhidric acid or fluoroacetic acid) during the synthesis of the TiO_2 nanoparticles led to a change in their morphology. This change represents an increase of the (001) surface area exposed by the nanoparticles against a reduction of the (101) surface area, which is known to be the most stable. This is a very interesting achievement since the (001) surface has been proved to present more activity in the photocatalytic processes.[67] Motivated by these experimental discoveries, and with the computational methodology validated in previous works with the pure TiO_2 bulk systems, we decided to study the interaction of fluorine atoms and fluorhidric acid with TiO_2.

We performed three studies presented in this chapter. The first one consists of the study of the diffusion of fluorine atoms through the lattice of the different TiO_2 polymorphs: rutile, anatase and brookite. We analysed the energetic profile of pathways with different directions, with special interest in the directions perpendicular to the most stable and most reactive (101) and (001) surfaces, respectively. This study was aimed at elucidating how insertion of fluorine in the bulk structure of TiO_2 procedes.

The second work presented in this block regards the order of stability of the anatase (101) and (001) surfaces. The (101) surface has been shown to be the most stable surface for anatase TiO_2, followed by the (001) surface which seem to present different electronic properties which has been related to its high photocatalytic activity. We thus performed a systematic study of the energetic stabilities of the two surfaces in the presence of fluorine and how this affects the electronic structure of the bare surfaces. To reach to a more realistic description of the effect of the fluorine adsorption on the energetic stability of both surfaces, *ab-initio* thermodynamic models were used. Specifically, this work was aimed at understanding the different (101)/(001) ratios presented by TiO_2 nanoparticles when fluorine is involved in the synthesis process.

Continuing with the effect of fluorine on the stability of(001) surfaces we focused another problem. The synthesis of TiO_2 nanoparticles with abundant (001) surfaces often involves hydrothermal processes with hydrofluoric acid (HF) as a fluorine source. The presence of fluorine has been shown to increase the surface free energy of the most stable (101) facet and decrease the surface free energy of the initially less stable (001) as it has been explained in the previous article.[68] The problem with the use of HF is its high toxicity, high reactivity and corrosive behavior. Motivated by the experimental results by the group of Caballero et al. were prove that trifluoroacetic acid (TFAA) is also efficient in obtaining TiO_2 with a large amount of (001) surfaces.[69] We decided to perform a theoretical study of the adsorption properties of the trifluoroacetic acid on the (001) and (101) surfaces to better understand of the role of this molecule on the stability and electronic structure of these surfaces.

3.1.2.1 Theoretical study of atomic Fluorine diffusion through TiO_2 bulk polymorphs

THE JOURNAL OF PHYSICAL CHEMISTRY C

Article

pubs.acs.org/JPCC

Theoretical Study of Atomic Fluorine Diffusion through Bulk TiO_2 Polymorphs

Sergio Tosoni,[†,‡] Oriol Lamiel-Garcia,[†] Daniel Fernandez Hevia,[‡,§] and Francesc Illas*[,†]

[†]Departament de Química Física & Institut de Química Teòrica i Computacional (IQTCUB), Universitat de Barcelona, C/Martí i Franquès 1, E-08028 Barcelona, Spain

[‡]Departamento de Química, Universidad de Las Palmas de Gran Canaria, Campus Universitario de Tafira, 35017 Las Palmas de Gran Canaria, Spain

[§]INAEL Electrical Systems S.A., C/Jarama 5, 45007 Toledo, Spain

ABSTRACT: Diffusion of F through the anatase, brookite, and rutile polymorphs has been studied by periodic density-functional-theory-based calculations and large supercells. Different crystallographic directions for F diffusion have been explicitly considered. F diffusion has been found to be kinetically favored in the case of anatase and rutile, although in the latter the process is thermodynamically disfavored. Diffusion along each direction involves channels between the TiO_2 octahedral units in each crystal with different size. However, the analysis of the structures near the minimum and maximum energy values along each diffusion pathway before and after substrate relaxation indicates that considering the size of the channels does not allow one to make accurate predictions because the main effect concerns the different degree of flexibility of each polymorph, which may facilitate or hinder the formation of interstitial complexes.

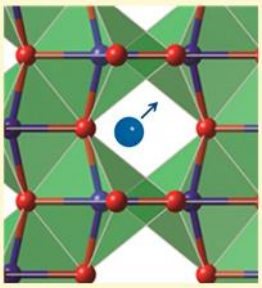

INTRODUCTION

Photocatalysis aims at accelerating and controlling chemical reactions between species adsorbed at surfaces through interaction with electrons and holes created under irradiation by light.[1] Photocatalytic materials are usually semiconducting oxides among which titanium dioxide (TiO_2), commonly referred to as titania, is focusing increasing attention due to the countless possible applications in green chemistry, catalysis, photovoltaic processes, fine chemicals fabrication, and hydrogen production[2−8] The properties of titania under UV irradiation have been known for many years and have been reviewed in depth.[9−12] However, the detailed microscopic chemical mechanisms involving several excited states are still to be unveiled.[13] From a practical point of view, however, the workhorse concerns the possible photocatalytic activity under visible light, which is hindered by the large band gap (∼3 eV) of commonly encountered rutile and anatase TiO_2 polymorphs. Hence, a main objective of scientific research involves investigating possible and suitable modifications of titania toward a substantial reduction of its rather large band gap to the 1 to 1.5 eV energy range.[9,14] Several strategies have been recently proposed to shrink the TiO_2 band gap, in particular, doping with nonmetallic elements such as nitrogen[15] or fluorine.[16−18] The latter has additional advantages because treating TiO_2 anatase nanoparticles with F largely stabilizes the reactive (001) facets.[19]

Notwithstanding the foreseeable practical applications of doped titania, understanding and characterizing the electronic structure of these systems remains challenging for both theory and experiment. This is evidenced by the case of N doping, which has been broadly studied. In fact, the experiments of Chambers et al.[20,21] on N-doped rutile reveal a substantial reduction of the band gap with N doping, which is also reproduced by linear response (LR), real-time (RT) time-dependent density functional theory (TD-DFT) and high-level active space equation-of-motion coupled cluster (EOMCC) calculations on pure and N-doped rutile.[22] However, band gap reduction does not seem to be sufficient because DFT-based calculations of the N-doped rutile TiO_2(101) surface carried out using the PW91 form of the generalized gradient approach (GGA) exchange-correlation potential found that it is not likely that N-doping will improve the photocatalytic behavior of this polymorph.[23,24] A key question here concerns whether N-doping triggers the appearance of localized Ti^{3+} species, which may be then involved in electronic excitation and redox processes. The previous GGA-type calculations for models for N-doped anatase and rutile, carried out using the PBE exchange-correlation functional, did not find evidence of localized Ti^{3+} centers.[25] However, a subsequent study including electron paramagnetic resonance (EPR) experiments unambiguously showed that N-doping induces the presence of paramagnetic Ti^{3+} centers, and this is well-reproduced by DFT-based calculations using hybrid or DFT+U functionals.[26−29] A similar situation is also encountered for F-doped anatase[30,31] and also for the F-doped rutile and brookite polymorphs.[32] The problem in describing the electronic state

Received: January 15, 2013
Revised: February 27, 2013
Published: February 27, 2013

dx.doi.org/10.1021/jp400474y | J. Phys. Chem. C 2013, 117, 5855−5860

related to Ti^{3+} comes from the fact that they are also very close in energy or even degenerate with partially or highly delocalized solutions, where the extra charge is distributed over several Ti ions. The location in the band gap of the defect states corresponding to these different solutions is obviously an important issue because it has implications on the conductivity mechanism in reduced or n-type-doped titania. Recently, optical properties of N-doped anatase from simulated UV and visible absorption spectra have been reported using the imaginary part of the frequency-dependent dielectric function, showing that the $TiO_{(2-3x)}N_{2x}$ diamagnetic system exhibits an enhanced optical absorption under visible-light irradiation, which is due to a band gap narrowing of 0.6 eV induced by delocalized impurity states located at the top of the valence band of TiO_2.[29]

Similarly to N-doping, also in the case of F-doping, the main open issues concern the nature of the defect states and the location of the corresponding energy levels in the band gap. Using a PBE+U approach chosen to reproduce the band gap of the three titania polymorphs and a strategy similar to that used by Harb et al.[29] we simulated the optical spectra of F-doped anatase, rutile, and brookite. This allowed us to identify a new optical feature in the gap due to the presence of Ti^{3+} center, especially in anatase and to a lesser extent in brookite.[33] However, the position of the corresponding state appears to be too low in the gap, indicating the difficulty to simultaneously predict the band gap and the position of the Ti^{3+} levels. Here it is important to point out that the PBE+U calculations show that whereas interstitial F in anatase is possible F-doping in these three polymorphs preferably involves the substitution of an oxygen atom of the titania lattice. This opens an interesting question because the substitution of O by F is only possible if the latter can diffuse through the bulk structure without too large of an energy cost. Experiments on photocatalytic properties of F-doped titania are normally carried on TiO_2 nanoparticles impregnated with a fluorine-containing solution.[16,17,34,35] Whereas the presence of fluorine in the doped samples is evidenced by XPS experiments, far less is known about the distribution of fluorine in the surface of the nanoparticles and about the energy barrier that the dopant encounters while diffusing through the structure. Indeed, the diffusion of the dopant in TiO_2 nanoparticles is also a relevant issue in photocatalysis because the distribution and the space separation between defects are both related to the kinetics of recombination between photoelectrons and photoholes.[12] Also, the electronic structure of the defective material is influenced by the defects distribution because the cumulative overlap between nearby-lying defects may change the curvature of the populated bands in the gap, thus altering the excitation energy. The main aim of the present paper is precisely to go beyond the description of the electronic structure of F-doped titania polymorphs at the equilibrium geometry, providing a realistic model for fluorine diffusion in these bulk phases. The knowledge of the energy barriers for F diffusion thus obtained will allow carrying out simulations on the dopant distribution that can provide useful hints to tailor new materials with specific desired properties by tuning the synthesis' conditions.

■ MODEL STRUCTURES AND COMPUTATIONAL DETAILS

Rutile and anatase exhibit a tetragonal primitive cell, whereas brookite exhibits an orthorhombic crystal structure. Fluorine diffusion through these polymorphs is studied by using supercell models large enough to simulate F at very low concentration. For anatase, a $3 \times 2 \times 2$ supercell is adopted, corresponding to a $Ti_{48}O_{96}$ repeated unit. For rutile, a $3 \times 3 \times 3$ supercell ($Ti_{54}O_{108}$) is used, whereas the one corresponding to brookite is $1 \times 2 \times 3$ supercell, leading to a $Ti_{48}O_{96}$ unit cell formula; the coincidence of the number atoms in the anatase and brookite unit cells is fortuitous.

In the present work, the Ti(3p,4s,3d), O(2s,2p), and F(2s,2p) electrons are treated explicitly. The corresponding valence states are expanded in a plane-wave basis set within a cutoff of 400 eV for the kinetic energy. The effect of the core electrons in the valence electron density is described through the projector-augmented wave (PAW) method.[36,37] The parameters of the primitive cell obtained via X-ray diffractions[38−40] have been used as an initial guess, but all structures have been relaxed using a cutoff of 900 eV and a Monkhorst-Pack[41] grid of $8 \times 8 \times 4$ K points for anatase, $6 \times 6 \times 8$ for rutile, and $8 \times 8 \times 4$ for brookite, respectively. The structures have been relaxed within a gradient threshold of 0.005 eV/Å. The resulting relaxed structures are then used to build the larger supercells employed to study F-diffusion, and the corresponding calculations have been carried out using the same computational setup except for the *k*-points mesh, which has been reduced to $2 \times 2 \times 2$. The standard DFT part of the calculations has been carried adopting the PBE form of the GGA exchange-correlation functional.[12] The effective U potential has been added to Ti(3d) and O(2p) levels within the scheme suggested by Dudarev,[43] and the U value has been chosen by comparing to experiment but constraining U(3d) and U(2p) to be the same to thus avoid an excessive parametrization. In the case of rutile (anatase), we varied U between 2 and 6 eV, and the band gap thus predicted varies between 1.96 and 2.69 eV (2.54 and 2.95). Therefore, $U = 6$ eV for both Ti(3d) and O(2p) bands has been found to provide the best possible comparison to experiment. The DFT-based calculations reported in the present work have been carried out with the 5.2 version of the VASP package.[44] Manipulation and editing of the structures have been performed with the code MOLDRAW.[45] Figures have been realized with PovRay and VESTA.[46]

To determine the barriers for F diffusion, we carried out 1-D scans were with single-point calculations, letting a fluorine atom diffuse along the principal crystallographic directions of anatase, brookite, and rutile. These are identified by the corresponding Miller indices [*j*,*k*,*l*], according to the standard crystallographic notation. The effect of structure relaxation was taken into account by optimizing the TiO_2 frameworks in the structures corresponding to the minimum and highest energy points in the potential energy scan and maintaining the position of the fluorine atom fixed to avoid it jumping to nearby channels, which leads to discontinuities in the potential energy surface.

■ RESULTS AND DISCUSSION

To identify the most likely directions of fluorine diffusion in titania, it is useful to look at the structures of anatase (Figure 1), brookite (Figure 2), and rutile (Figure 3), including the octahedral coordination spheres of Ti^{4+} ions. Inspections of Figures 1−3 readily show the existence of channels separating the octahedra along a given crystallographic directions. For anatase, the structure looks compact along the [001] direction. However, void channels symmetrically appear along both [010] and [100] directions. A different situation appears for brookite, where this type of channel exists only along [001]. Finally, in

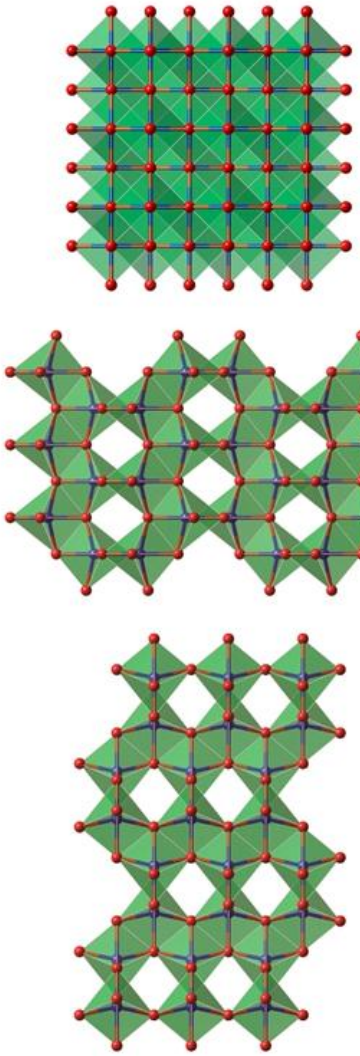

Figure 1. Schematic view of anatase aligned along the [001] (top), [010] (middle), and [100] (bottom) directions. The semitransparent octahedra evidence the coordination sphere of the Ti^{4+} ions.

the case of rutile, it is possible to observe some porosity along the [001] and [110] directions.

The calculated energy barriers for fluorine diffusion along the aforementioned directions are reported in Table 1. In a first step, single-point calculations have been carried out, moving a fluorine atom along the aforementioned directions but maintaining the TiO_2 framework fixed. We define ΔE_{un} in Table 1 as the energy difference between the most and least favorable structures encountered in the scan. The same energy difference but now taking into account the relaxation of the TiO_2 framework around the fluorine atom defines ΔE_{rel}. Finally, ΔE_{ext} measures the thermodynamic stability of the energy minimum for the relaxed F-TiO_2 complex with respect to the perfect TiO_2 and one-half of the energy of the gas-phase F_2 molecule.

Inspection of the results concerning anatase in Table 1 and the energy profile in Figure 4 reveals that there is a huge

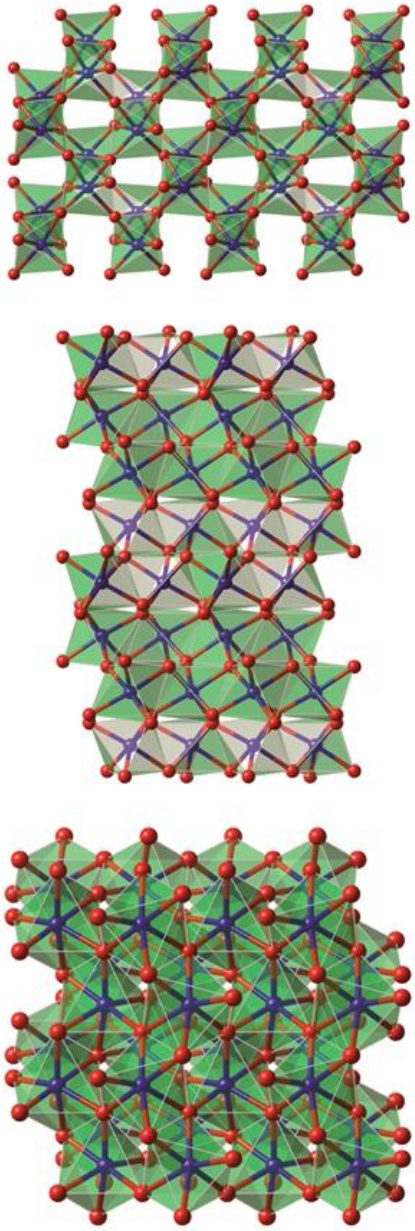

Figure 2. Schematic view of brookite aligned along the [001] (top), [010] (middle), and [100] (bottom) directions. The semitransparent octahedron evidences the coordination sphere of the Ti^{4+} ions.

difference between calculated energy barriers and relative stability for F diffusion through the [001] direction and the corresponding values for the [100] and [010] directions. Note also that the two last directions are symmetry-related in the orthorhombic lattice of anatase. The more compact structure of anatase along the [001] direction causes a rather high diffusion barrier of 8.3 eV, as predicted from the calculations with the fixed TiO_2 framework. Allowing structural relaxation of the anatase through F diffusion implies a rather large rearrangement of the octahedral units, which remarkably reduces the

dx.doi.org/10.1021/jp400474y | J. Phys. Chem. C 2013, 117, 5855−5860

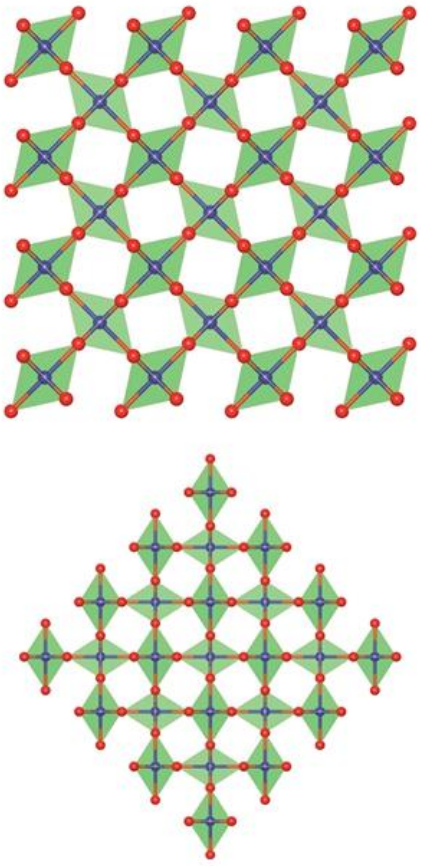

Figure 3. Schematic view of rutile aligned along the [001] (top) and [110] (bottom) directions. The semitransparent octahedron evidences the coordination sphere of the Ti^{4+} ions.

Table 1. Energy Barriers for Diffusion of Fluorine through Anatase, Brookite, and Rutile[a]

structure	direction	ΔE_{un}	ΔE_{rel}	ΔE_{ext}
anatase	[001]	8.30	2.46	3.82
	[100]	0.49	0.00	0.08
brookite	[001]	1.59	0.73	1.66
rutile	[001]	1.21	0.00	1.15
	[110]	4.05	0.00	1.16

[a] ΔE_{un} and ΔE_{rel} correspond to diffusion through the fixed and relaxed TiO_2 framework, respectively. ΔE_{ext} stands for the relative stability with respect to the TiO_2 crystal and a half the energy of the gas-phase F_2 molecule. All energy values are in electronvolts.

diffusion barrier to 2.5 eV. However, even the most favorable F-TiO_2 structure generated by moving the fluorine atom along the [001] direction is almost 4 eV unstable with respect to the isolated components, indicating that diffusion along this direction is highly hindered both thermodynamically and kinetically.

The situation is very different for the channel along the [100] direction, which appears to be rather permeable to fluorine diffusion; the calculated energy barrier maintaining the anatase network fixed is of 0.5 eV only. Allowing the structure to relax in response to the presence of the guest F atom, the energy

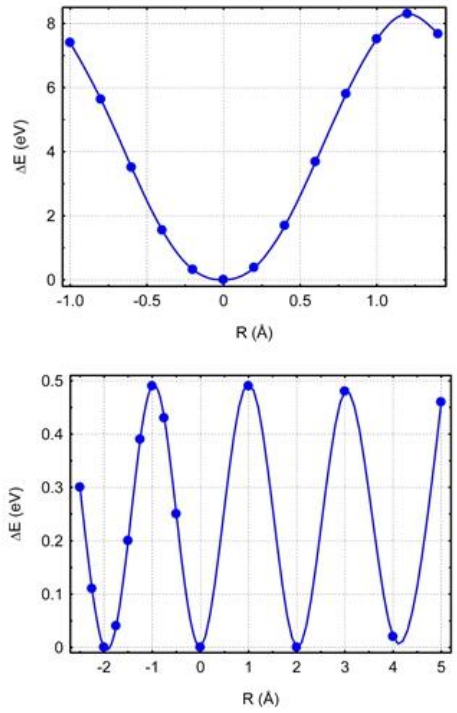

Figure 4. Energy profile of the diffusion of fluorine in anatase along the [001] (above) and [100] (below) direction. The TiO_2 structure is fixed to better illustrate the differences along each direction. Values corresponding to the relaxed structure are given in Table 1.

barrier vanishes. Moreover, the resulting structures are only 0.08 eV unstable with respect to the isolated, separated, components. This is in agreement with our previous work, where it has been found that F can create stable interstitial complexes in anatase provided that the structure is fully relaxed; that is, fluorine atom position is also optimized.[32]

For brookite, we concentrate on the only suitable direction, which corresponds to the [001] channel. From the results in Table 1 and the potential energy profile in Figure 5, it is clear that F diffusion through this polymorph is rather hindered. The calculated energy barrier predicted by maintaining the TiO_2 fixed, ΔE_{un} in Table 1, is as large as 1.6 eV. Substrate relaxation

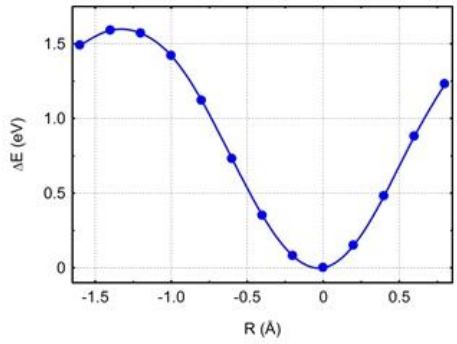

Figure 5. Energy profile of the diffusion of fluorine through a fixed brookite structure along the [001] direction.

dx.doi.org/10.1021/jp400474y | J. Phys. Chem. C 2013, 117, 5855−5860

reduces partially the barrier for diffusion ΔE_{rel}, which becomes 0.7 eV. The magnitude of the barrier is not so large and could be surmounted at a moderate temperature. However, the resulting interstitial complex is 1.7 eV less stable than the separated components. Hence, F diffusion is hindered thermodynamically and, to a smaller extent, also kinetically.

Finally, we consider the case of rutile for which the potential energy profiles corresponding to the fixed framework are reported in Figure 6. In this case, there are two possible

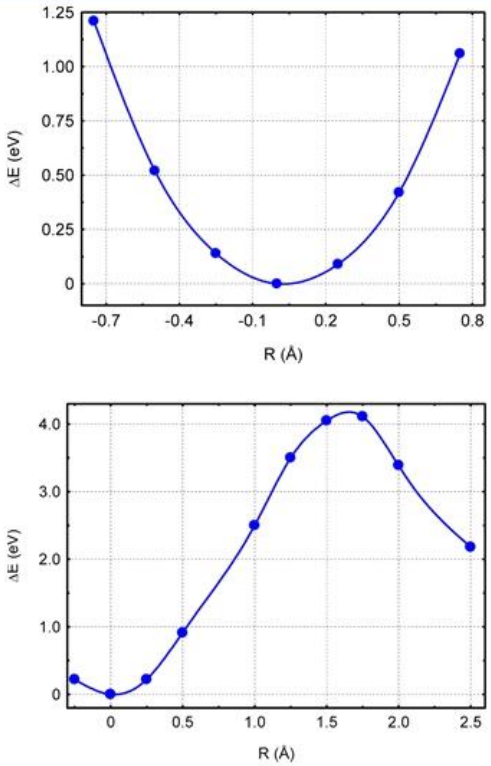

Figure 6. Energy profile of the diffusion of fluorine through a fixed rutile network along the [001] (above) and [110] (below) directions.

directions for F diffusion, [001] and [110]. Here the ΔE_{un} values are rather large: 1.2 eV for [001] and above 4 eV for [110]. However, allowing for substrate relaxation causes the energy barriers to almost vanish for both directions. Interestingly, the resulting interstitial complexes are both more stable than in the case of brookite but less stable than anatase with ΔE_{ext} close to 1.2 eV in both cases.

The differences found for F diffusion in the different polymorphs can be interpreted in a simple way. Analyzing the crystal structures in some details reveals that the size of the channels is rather different. Thus, in anatase, the channel along [001] is quadrangular with a size of 1.9 × 1.9 Å, whereas the channel along [100] is a 3.9 × 3.3 Å parallelogram. In the case of brookite, the [001] channel is remarkably smaller, measuring 1.5 × 2.6 Å, whereas the rutile [001] and [110] channels measure both 2.8 × 2.8 Å. It is then interesting to look into some more detail at the chemical environment of the structures corresponding to minima and maxima of the potential energy curve before and after relaxation. In the case of anatase [100], the unrelaxed structures are reported in the left panel of Figure 7. It is clear that in the minimum position the fluorine atom lies

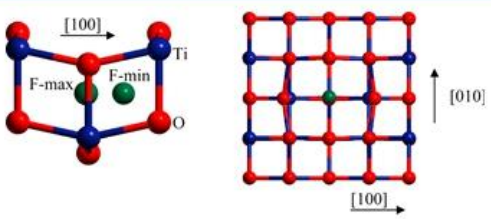

Figure 7. Detail of fluorine diffusion along anatase [100]. Unrelaxed structure (left) and relaxed structure (right). F-min and F-max stand for the positions of minimum and maximum energy of Fluorine in the channel, respectively.

in a middle of a cage, whereas in the maximum energy position it interferes closely with a Ti_2O_4 ring. However, the relaxation of the TiO_2 framework leads to a displacement of the nearby oxygen atoms and consequently to a stable interstitial structure, which is clearly seen on the right panel of Figure 7. Similar arguments hold for the other polymorphs. The existence of an energy barrier is mainly due to steric effects. However, what differentiates the three structures goes well beyond the size of the channels and concerns the different degree of flexibility of each polymorph, which may facilitate or hinder the formation of interstitial complexes.

The analysis of the electron and spin density of the F-TiO_2 complexes studied in the present work offers some additional insight into the main features of their electronic structure. In all three polymorphs, the incorporated fluorine atom has a predominant anionic character, thus further confirming that the encountered differences in the diffusion barriers have to be attributed to structural features. Moreover, the spin density is, in all cases, localized on a neighboring oxygen atom that exhibits the largest displacement from its lattice position. Therefore, the diffusion of fluorine induces a polaronic type distortion in the titania structure. The polaron follows the path of the F^- anion thus formed with a concomitant localized hole on a neighboring O center of the TiO_2 lattice. Clearly, the anionic character of interstitial fluorine arises from its larger electronegativity compared with oxygen, an elementary concept of chemistry, which is well-reproduced by all density functional methods. Nevertheless, the degree of localization of the corresponding electron−hole pair in the lattice is not a simple issue because it strongly depends on the exchange-correlation potential. In particular, compared with a standard GGA density functional, the PBE+U scheme adopted in the present article favors a localized solution. A thorough discussion on these aspects can be found in the article from Czoska.[30]

■ CONCLUSIONS

Diffusion through the crystal structure is a key step in the process of doping TiO_2 samples. In the present work, diffusion of F through the anatase, brookite, and rutile polymorphs has been studied by periodic density functional theory-based calculations using sufficiently large supercells. For each polymorph, different crystallographic directions are possible for F diffusion, which have been all considered explicitly. Diffusion along each direction exhibits particular features with energy barriers, which are initially determined by the size of the channels between the TiO_2 octahedral units in each crystal.

However, relaxation of the substrate in response to the presence of the dopant turns out to be the main physical effect, which in the case of F diffusion in anatase along the [100] direction appears to be barrierless and almost thermodynamically favored. The present calculations also predict that F diffusion through brookite is both kinetically and thermodynamically disfavored. The case of rutile is intermediate with a vanishing barrier through the [110] direction but with the F-TiO_2 complex being thermodynamically disfavored with respect to the separated systems.

The analysis of the structures near the minimum and maximum energy values along each diffusion pathways before and after substrate relaxation indicates that considering the size of the channels does not allow one to make accurate predictions because the main effect concerns the different degree of flexibility of each polymorph, which may facilitate or hinder the formation of interstitial complexes.

Finally, one must realize that diffusion of F through the bulk of the three TiO_2 polymorphs must necessarily start by incorporation from the gas phase. This can be either from atoms adequately dosed or, more likely, by dissociative chemisorption of F_2 at the corresponding surface. Preliminary results reveal that at least in the case of the anatase (001) surface the initial barrier for F penetration is of 0.2 eV, provided the surface is fully relaxed. This is one order of magnitude less than the corresponding value for diffusion in the anatase bulk along the [001] direction, strongly suggesting that incorporation from the gas phase is not the rate-limiting step. The rational for this energy barrier decrease comes from the fact that for a given diffusion direction relaxation of a few surface layers will always cost less than relaxation of the bulk structure. Nevertheless, a more definite answer requires a more systematic study that is now being carried out in our group.

AUTHOR INFORMATION

Notes

The authors declare no competing financial interest.

ACKNOWLEDGMENTS

This research has been supported by Spanish MICINN through Program INNPACTO Project CASCADA IPT-120000-2010-19 and Spanish MINECO through FIS2008-02238 and CTQ2012-30751 research grants. We are also grateful to *Generalitat de Catalunya* for partial support through grants 2009SGR1041 and XRQTC. F.I. acknowledges additional support through 2009 ICREA Academia award for excellence in research. Finally, we appreciate the collaboration of Gianfranco Ulian, Università di Bologna, in preparing the figures.

REFERENCES

(1) Herrmann, J. M. *Appl. Catal. B, Environ.* **2010**, *99*, 461−468.
(2) Hoffmann, M. R.; Martin, S. T.; Choi, W.; Bahnemann, D. W. *Chem. Rev.* **1995**, *95*, 69−96.
(3) Mill, A.; Davies, R. H.; Worsley, D. *Chem. Soc. Rev.* **1993**, *22*, 417−425.
(4) Fox, M. A.; Dulay, M. T. *Chem. Rev.* **1993**, *93*, 341−357.
(5) Ravelli, D.; Dondi, D.; Fagnoni, M.; Albini, A. *Chem. Soc. Rev.* **2009**, *38*, 1999−2011.
(6) Akihiko, K.; Yugo, M. *Chem. Soc. Rev.* **2009**, *38*, 253−278.
(7) Yuliati, L.; Yoshida, H. *Chem. Soc. Rev.* **2008**, *37*, 1592−1602.
(8) Chen, X. B.; Shen, S. H.; Guo, L. J.; Mao, S. S. *Chem. Rev.* **2010**, *110*, 6503−6570.
(9) Hashimoto, K.; Irie, H.; Fujishima, A. *Jpn. J. Appl. Phys.* **2005**, *44*, 8269−8285.
(10) Fujishima, A.; Zhang, X.; Tryk, D. A. *Surf. Sci. Rep.* **2008**, *63*, 515−582.
(11) Chen, X.; Mao, S. S. *Chem. Rev.* **2007**, *107*, 2891−2959.
(12) Henderson, M. A. *Surf. Sci. Rep.* **2011**, *66*, 185−297.
(13) Sousa, C.; Tosoni, S.; Illas, F. *Chem. Rev.* **2013**, DOI: 10.1021/cr300228z.
(14) Kudo, A.; Miseki, Y. *Chem. Soc. Rev.* **2009**, *38*, 253−278.
(15) Asahi, R.; Morikawa, T.; Ohwaki, T.; Aoki, K.; Taga, Y. *Science* **2001**, *293*, 269−271.
(16) Yu, J. C.; Yu, J.; Ho, W.; Jiang, Z.; Zhang, L. *Chem. Mater.* **2002**, *14*, 3808−3816.
(17) Li, D.; Haneda, H.; Labhsetwar, N.; Hishita, S.; Ohashi, N. *Chem. Phys. Lett.* **2005**, *401*, 579−584.
(18) Yu, J. G.; Xiong, J. F.; Cheng, B.; Liu, S. W. *Appl. Catal., B* **2005**, *60*, 211−221.
(19) Yang, H. G.; Sun, C. H.; Qiao, S. Z.; Zou, J.; Liu, G.; Smith, S. C.; Cheng, H. M.; Lu, G. Q. *Nature* **2008**, *453*, 638−641.
(20) Chambers, S. A.; Cheung, S. H.; Shutthanandan, V.; Thevuthasan, S.; Bowman, M. K.; Joly, A. G. *Chem. Phys.* **2007**, *339*, 27−35.
(21) Cheung, S. H.; Nachimuthu, P.; Joly, A. G.; Engelhard, M. H.; Bowman, M. K.; Chambers, S. A. *Surf. Sci.* **2007**, *601*, 1754−1762.
(22) Govind, N.; Lopata, K.; Rousseau, R.; Andersen, A.; Kowalski, K. *J. Phys. Chem. Lett.* **2011**, *2*, 2696−2701.
(23) Nambu, A.; Graciani, J.; Rodriguez, J. A.; Wu, Q.; Fujita, E.; Sanz, J. F. *J. Chem. Phys.* **2006**, *125*, 094706.
(24) Graciani, J.; Alvarez, L. J.; Rodriguez, J. A.; Sanz, J. F. *J. Phys. Chem. C* **2008**, *112*, 2624−2631.
(25) Di Valentin, C.; Pacchioni, G.; Selloni, A. *Phys. Rev. B* **2004**, *70*, 085116.
(26) Di Valentin, C.; Pacchioni, G.; Selloni, A.; Livraghi, S.; Giamello, E. *J. Phys. Chem. B* **2005**, *109*, 11414−11419.
(27) Livraghi, S.; Paganini, M. C.; Giamello, E.; Selloni, A.; Di Valentin, C.; Pacchioni, G. *J. Am. Chem. Soc.* **2006**, *128*, 15666−15671.
(28) Di Valentin, C.; Finazzi, E.; Pacchioni, G.; Selloni, A.; Livraghi, S.; Paganini, M. C.; Giamello, E. *Chem. Phys.* **2007**, *339*, 44−56.
(29) Harb, M.; Sautet, P.; Raybaud, P. *J. Phys. Chem. C* **2011**, *115*, 19394−19404.
(30) Czoska, A. M.; Livraghi, S.; Chiesa, M.; Giamello, E.; Agnoli, S.; Granozzi, G.; Finazzi, E.; Di Valentin, C.; Pacchioni, G. *J. Phys. Chem. C* **2008**, *112*, 8951−8956.
(31) Di Valentin, C.; Pacchioni, G.; Selloni, A. *J. Phys. Chem. C* **2009**, *113*, 20543−20552.
(32) Tosoni, S.; Lamiel-Garcia, O.; Fernandez Hevia, D.; Doña, J. M.; Illas, F. *J. Phys. Chem. C* **2012**, *116*, 12738−12746.
(33) Tosoni, S.; Fernandez Hevia, D.; González Díaz, O.; Illas, F. *J. Phys. Chem. Lett.* **2012**, *3*, 2269−2274.
(34) Senna, M.; Špelák, V.; Shi, J.; Bauer, B.; Feldhoff, A.; Laporte, V.; Becker, K. D. *J. Solid State Chem.* **2012**, *187*, 51−60.
(35) Wu, Q.; Liu, M.; Wu, Z.; Li, Y.; Piao, L. *J. Phys. Chem. C* **2012**, *116*, 26800−26804.
(36) Blöchl, P. *Phys. Rev. B* **1994**, *50*, 17953.
(37) Kresse, G.; Joubert, J. *Phys. Rev. B* **1999**, *59*, 1758.
(38) Djerdj, I.; Tonejc, A. M. *J. Alloys Compd.* **2006**, *413*, 159−174.
(39) Bokhimi, X.; Morales, A.; Pedraza, F. *J. Solid State Chem.* **2002**, *169*, 176−181.
(40) Štengl, V.; Králová, D. *Mater. Chem. Phys.* **2011**, *129*, 794−801.
(41) Monkhorst, H. J.; Pack, J. D. *Phys. Rev. B* **1976**, *13*, 5188.
(42) Perdew, J. P.; Burke, K.; Emzerhof, M. *Phys. Rev. Lett.* **1996**, *77*, 3865.
(43) Dudarev, S. L.; Botton, G. A.; Savrasov, S. Y.; Humphreys, C. J.; Sutton, A. P. *Phys. Rev. B: Condens. Matter Mater. Phys.* **1998**, *57*, 1505−1509.
(44) Kresse, G.; Furthmüller, J. *J. Comput. Mater. Sci.* **1996**, *6*, 15.
(45) Ugliengo, P.; Viterbo, D.; Chiari, G. *Z. Kristallogr.* **1993**, *208*, 383−383.
(46) Momma, K.; Izumi, F. *J. Appl. Crystallogr.* **2008**, *41*, 653−658.

3.1.2.2 Relative Stability of F-Covered TiO_2 Anatase (101) and (001) Surfaces from Periodic DFT Calculations and ab Initio Atomistic Thermodynamics

THE JOURNAL OF PHYSICAL CHEMISTRY C

Article

pubs.acs.org/JPCC

Relative Stability of F-Covered TiO_2 Anatase (101) and (001) Surfaces from Periodic DFT Calculations and ab Initio Atomistic Thermodynamics

Oriol Lamiel-Garcia, Sergio Tosoni, and Francesc Illas*

Departament de Química Física &Institut de Química Teòrica i Computacional (IQTCUB), Universitat de Barcelona, C/Martí i Franquès 1, E-08028 Barcelona, Spain

ABSTRACT: A density functional theory based computational study is presented of fluorine adsorption on anatase TiO_2(101) and TiO_2(001) surfaces. A variety of surface coverage situations ranging from 10 to 100% have been considered, and the effect on the electronic structure of the material has been analyzed. The adsorption of F atoms on these surfaces directly affects the band structure with new features in the band gap due to the presence of partially oxidized anions. The effect of F coverage on the relative stability of both surfaces has been studied by applying the ab initio thermodynamic formalism. Interestingly, the effect of fluorine on the surface free energy at 298.15 K and 1 bar of F_2 pressure is to stabilize the (001) surface and destabilize the (101), which nicely explains the experimental observation that the presence of F allows growing TiO_2 anatase nanoparticles with a higher percentage of the more reactive 001 surface with enhanced photocatalytic activity.

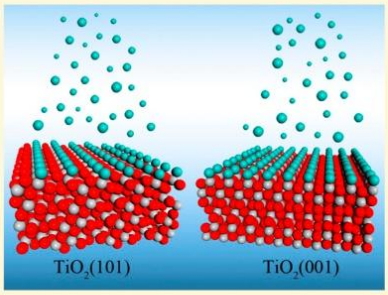

INTRODUCTION

Titanium dioxide (titania) nanoparticles constitute no doubt a reference material for applications in photocatalysis.[1−4] However, because of the quite large band gap (of ∼3 eV) exhibited by the common rutile, anatase, or brookite polymorphs of titania, their resulting photocatalytic activity is restricted to the UV region of the electromagnetic spectra. Indeed, the ∼3 eV band gap of titania polymorphs implies that only 10% of the incoming photons from sunlight are adsorbed and hence can participate in the photocatalytic process. This feature seriously hinders the possible efficiency of this clean and environmental friendly process and represents a serious constraint for practical uses such as water splitting to produce hydrogen or as its capability to remove organic pollutants from either air; additional interesting applications of titania and related semiconducting, photocatalytically active materials can be found in various recent review articles.[5−11]

To improve the photocatalytic activity of titania, a significant amount of recent work has been devoted to devise suitable strategies to reduce the band gap down to 1−1.5 eV which would allow photocatalytic activity of titania upon visible light irradiation.[1,12] Among the different strategies used to optimize the absorption of sunlight photons for photocatalytic processes, doping with nonmetallic elements (n-doping) has attracted considerable attention.[3] Nevertheless, the situation is not that simple, since several factors influence the performance of the resulting photocatalytic system; parameters such as the position of the edge of the valence and conduction bands have to be taken into account, and these should fit with redox potential of the reaction substrate.[13] Also, kinetic effects concerning the recombination of photogenerated holes and free electrons are relevant and are likely to play a significant role.[4] Last but not least, shape and size of the titania nanoparticles also play an important role. Precisely, fluorine is one of the elements proposed to dope titania which, in addition to introduce states in the gap and hence potentially increasing photon absorption in the visible, has been shown to stabilize the reactive (001) surface of anatase in detriment of the most stable and abundant but less active (101) surface.[14] This interesting finding triggered a number of studies aimed at modifying the shape and size of the TiO_2 anatase nanoparticles to increase (001) surface.[15−17] A similar strategy has been recently applied to obtain high-quality porous TiO_2 films with tunable orientation of rutile using an electrochemical route.[18] These authors show also that the fraction of exposed rutile (101) facets can be adjusted by modifying the orientation of rutile using HCl or HF additives without altering polymorph composition and surface area. In the case of using HF additives, F is found to contaminate the surface, and it is suggested that this can further improve the photocatalytic performance.

The experiments discussed above have triggered a series of theoretical studies aimed at understanding the modifications introduced in the electronic structure of bulk TiO_2 or the energetic requirements to introduce F in the crystal substituting O anions, diffusion through anatase, or implanting F at anatase surfaces.[19−22] The theoretical studies provide evidence that F-

Received: April 2, 2014
Revised: May 30, 2014
Published: June 2, 2014

doping is thermodynamically stable for all TiO_2 polymorphs and, in addition, that Ti^{3+} gap states arising from doping well located in the middle of the band gap appear in the case of anatase but not for rutile and brookite.[19] These features are not significantly affected by the presence of oxygen vacancies, the electronic properties of F-substituted TiO_2 remain for reduced titania, and the resulting system is even slightly stabilized.[19,20] These studies refer mainly to the effect of F on bulk titania but doping at or near the surface layer has also been considered. Periodic density functional theory based calculations using different forms of the exchange-correlation functional reveal that predict F implantation at anatase (101) and (001) surfaces is more favorable at surface sites than at subsurface ones.[22] Clearly, to complete the picture concerning the effect of F in the electronic structure of anatase it is also necessary to consider the cases where F is adsorbed at the surface rather than doping the material through O substitution. This need is further evidenced by the recent paper by Su et al.,[18] providing evidence that F at surfaces of rutile enhances its photocatalytic activity. Hence, the present study focuses on the adsorption properties of atomic F on the anatase (101) and (001) surfaces and on their relative thermodynamic stability.

■ COMPUTATIONAL DETAILS

The interaction of atomic fluorine with the (101) and (001) surfaces of anatase has been carried out using periodic density functional theory (DFT) based calculations within the repeated slab model. In order to properly study the effect of F coverage, a large enough supercell has been employed. In the case of more stable TiO_2(101)-anatase surface, a 1 × 3 × 4 supercell model with dimension of 11.4 × 11.4 Å in the surface plane and 27.5 Å in perpendicular direction has been used as in a previous study dealing with F implantation.[22] This supercell contains 48 TiO_2 units or a total of 144 substrate atoms and up to 6 F atoms covering the 1/6 to 1 coverage range where coverage is here defined as the number of F atoms relative to the number of possible Ti surface sites. In the case of the TiO_2(001)-anatase surface, the supercell used is 3 × 3 × 9 with 60 TiO_2 units or 180 atoms and up to 9 F atoms covering the 1/9 to 1 coverage range. This supercell is similar but slightly thicker than the one used to study F implantation.[22] In both cases a minimum of 10 Å of vacuum is added to guarantee there is no interaction between the periodic replicas in the direction perpendicular to the surface. A schematic representation of the surface supercell models used in this work is presented in Figure 1.

All the calculations in this study were performed with the periodic plane wave based code VASP[23−25] using the PBE[26] exchange-correlation potential with an added effective U potential to Ti(3d) and O(2p) levels. The resulting DFT+U formalism follows the scheme proposed by Dudarev et al.,[27] and a value of U = 6 eV has been chosen because it reproduces correctly the experimental band gap for the TiO_2 bulk anatase, rutile, and brookite even if with this choice gap states in reduced titania appear to be too distant from the conduction band leading to too high electronic transitions. Smaller U values predict gap states closer to the conduction band but fail to predict the band gap of the bulk materials. Nevertheless, to avoid artifacts arising from the choice of the density functional, single point energy calculations have been carried out using the standard GGA type PBE functional and the hybrid HSE06. Hybrid functionals provide a better estimate of the band gap in oxides in general[28] and of titania in particular[29] although the amount of Fock exchange to be included seems to be material dependent and remains an unsolved issue.[30,31]

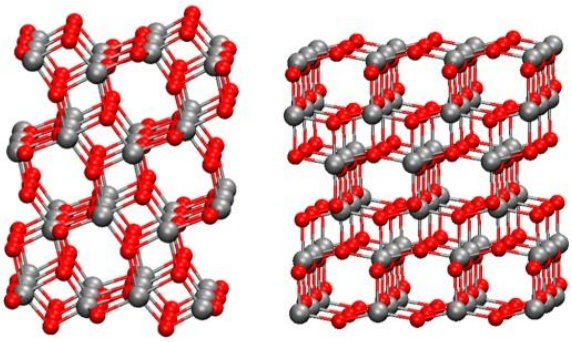

a b

Figure 1. Supercell slab models used to represent anatase (101) and (001) surfaces, left and right panels, respectively. Ti and O atoms are represented by gray and red spheres, respectively.

The valence electrons (3p, 4s, 3d for Ti; 2s, 2p for O and 2s, 2p) are expanded in a plane-wave basis set within a cutoff of 400 eV; meanwhile, to describe the effect of the core electrons in the valence electron density is described through the projector-augmented wave (PAW) method of Blochl.[32] Gamma centered k-point meshes of 2 × 2 × 1 were used to sample the electronic density in the reciprocal space. All structures were relaxed until the forces acting over each atom were smaller than 0.005 eV/Å.

The adsorption energy of fluorine has been calculated in two different ways. First, we use the standard definition

$$E_{ads,nF} = \frac{1}{n}[E_{nF\text{-}ads} - (E_{slab} + nE_F)] \quad (1)$$

where $E_{ads,nF}$ is the adsorption energy per F atoms relative to the energy of the clean surface (E_{slab}) and to one-half of the energy of the F_2 molecule (E_F); $E_{nF\text{-}ads}$ is the energy of the surface covered by n fluorine atoms. The values obtained from eq 1 provide information about the affinity of the surface toward F atoms but do not allow discriminating the influence of preadsorbed F atoms. To this end, we define the incremental adsorption energy ($\Delta E_{ads,nF}$) as in eq 2 which provides the adsorption energy of a F atom on a surface already containing ($n - 1$) F atoms:

$$\Delta E_{ads,nF} = E_{nF\text{-}ads} - (E_{(n-1)F\text{-}ads} + E_F) \quad (2)$$

Most of symbols in eq 2 are as in eq 1, and $E_{(n-1)F\text{-}ads}$ is the energy of the surface covered by ($n - 1$) F atoms. The energy of the F_2 molecule was obtained from a calculation in a sufficiently large box considering the gamma point and the same 400 eV cutoff for the kinetic energy of the plane waves and until forces acting between atoms are below 0.005 eV/Å as in the supercell calculations for F adsorption.

Fluorine Adsorption at the Anatase TiO_2(101) Surface. The different coverage situations have been studied using the same unit cell (Figure 1a) and increasing the number of F atoms at the surface but always directly interacting with the 5-fold coordinated Ti (Ti_{5f}) surface cations. In all cases, a spin-polarized solution is found with as many unpaired electrons as F atoms in the surface. This is because the F atoms, having the largest electronegativity, can oxidize O anions of anatase. The oxidized anion becomes formally O^- instead of $O^{2-}$and F

becomes formally F^-. In all cases, the unpaired electron corresponds to the O atoms closest to the adsorbed F which displays a magnetization of 0.78, independently of the number of adsorbed F atoms. The open shell nature of the O atom near the adsorbed F is clearly seen in the spin density contour plots of Figure 2 for the cases of 1 (left panel) and 6 (right panel)

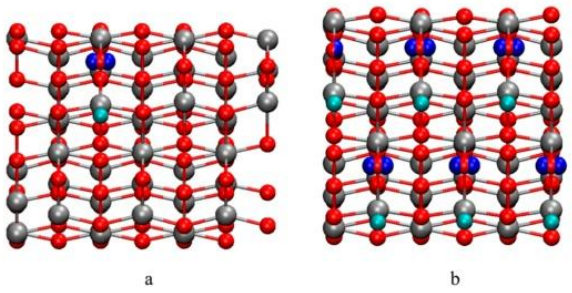

Figure 2. Top view of the spin isodensity contour plots (0.5) for the electronic ground state of F on TiO_2(101) at 17% (1F) and 100% (6F) coverage left and right panels, respectively. Ti, O, and F atoms are represented by gray, red, and light green spheres, respectively.

adsorbed F atoms. The electronic ground state always corresponds to the maximum multiplicity. Note, however, that near degenerate states exist where the unpaired electrons are antiferromagnetically, rather than ferromagnetically, coupled or even randomly coupled which is the most likely situation at finite temperatures. Note also that for each O atom the open shell can be located at each of the different 2p orbitals although the most stable solution correspond to have singly occupied the orbitals in the (101) planes.

For each of the coverage values, all different possible situations in the surface unit cell have been considered. Not surprisingly, the most stable distribution corresponds to the F atoms as separated from each other as possible to decrease the electrostatic repulsion arising from the negative charge in the adsorbates (see below) but with similar Ti−F distances of 1.82 Å. First, we note that the $E_{ads,nF}$ values obtained from eq 1follow a monotonic trend from 1.86 eV for the adsorption of a single F atom to 1.77 eV per F atom when all the Ti_{5f} sites are covered by F. The decrease in the $E_{ads,nF}$ values with coverage is to be expected from repulsive interactions between the negatively charged F adatoms. Nevertheless, it is clear that the $E_{ads,nF}$ values provide an average estimate of the adsorption energy only. In order to investigate the effect of preadsorbed F, let us now discuss the calculated $\Delta E_{ads,nF}$ values as defined as in eq 2. Starting from the clean surface one has $\Delta E_{ads,1F}$ which exothermic by 1.87 eV, this is the calculated value also for $\Delta E_{ads,2F}$ as expected from the large distance between the adsorbates. The interaction is somewhat smaller for $\Delta E_{ads,3F}$, 1.79 eV, and monotonically decreases with increasing coverage with values of 1.77, 1.71, and 1.63 eV for $\Delta E_{ads,4F}$, $\Delta E_{ads,5F}$, and $\Delta E_{ads,6F}$, respectively.

Note that it is possible to increase the F coverage but with the adsorbate directly interacting with surface O atoms. These situations have also been considered, and the calculated $E_{ads,7F}$ to $E_{ads,12F}$ values are in the 1.6−1.3 eV per F range, the corresponding per $\Delta E_{ads,7F}$ to $\Delta E_{ads,12F}$ being in the 0.86−0.76 eV range. Both, $E_{ads,nF}$ and $\Delta E_{ads,nF}$ are significantly smaller than the equivalent values for F atoms interacting directly with Ti_{5f} cations but still correspond to an exothermic process. Therefore, having the surface completely covered with F atoms becomes thermodynamically stable. The difference in interaction energy at Ti_{5f} and surface O sites is large enough to be detected by thermal programmed desorption experiments although it is likely that at room temperature only Ti sites are covered by F.

The presence of F atoms at the surface with the concomitant oxidation of oxygen anions has consequences in the electronic structure of the system. This is clearly observed in the total density of states in Figure 3 which displays a characteristic peak

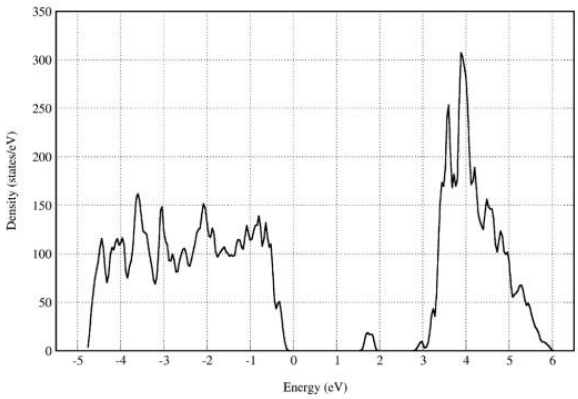

Figure 3. Total density of states of a TiO_2(101) with all Ti_{5f} cations covered by F atoms.

in the region of the gap at 1 eV below the conduction band. This peaks does not appear in the density of states of the clean surface which display a band gap of ∼3.2 eV, which is in excellent agreement with experiment for bulk anatase but because the U value in Ti(3d) and O(2p) levels has been chosen precisely to reproduce this experimental features.[19−21] Nevertheless, the fact that the band gap for this surface is very close to that calculated for the bulk using the same method[19] is not unexpected since this is the most stable surface. A more detailed analysis shows that the feature in the gap induced by the presence of F at the surface is mainly due to O atoms as expected from the discussion above.

Fluorine Adsorption at the Anatase TiO_2 (001) Surface. For this surface, different coverage situations have also been studied although, in the view of the results for the (101) surface, only the direct interaction with the 5-fold coordinated Ti (Ti_{5f}) surface cations has been considered. Note also that, with the unit cell in Figure 1b, it is possible to accommodate up to 9 F atoms. Moreover, except in the case of 1 and 9 F atoms, several configurations exist for the different coverage situations which largely complicate the situation. Let us take the case with 2 F atoms as an example. Here one can have three different configurations, and for each one it would be necessary to consider five different cases or 15 situations in total; even if one consider cases equivalent by symmetry, the number of possible configurations becomes exceedingly large. Therefore, we have decided to sample the surface and consider the most stable situations only. The calculated $E_{ads,nF}$ values are considerable larger than those corresponding to the more stable TiO_2(101) surface, as expected, ranging from 3.1 eV for $E_{ads,1F}$ to 2.2 eV per F atom for $E_{ads,9F}$. The corresponding $\Delta E_{ads,nF}$ values range from 3.1 to 1.9 eV, indicating that the capability to adsorb F decreases significantly with coverage which is not

surprising due to the large negative charge of the adsorbed F atoms and, compared to the case of $TiO_2(101)$, the shorter distance between the adatoms.

The negative charge on F atoms implies oxidation of the underlying substrate, and as discussed in the previous section for F on $TiO_2(101)$, the net result is appearance of formally O^- species. This is clearly seen in the spin density plots reported in Figure 4 for the cases with one and nine F atoms corresponding

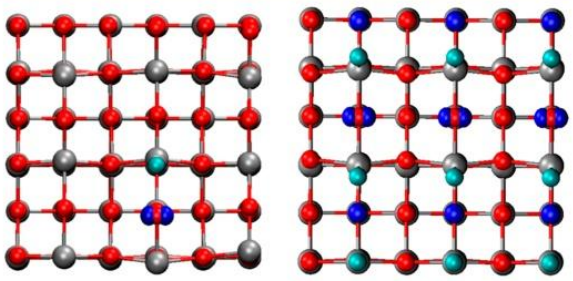

Figure 4. Top view of the spin isodensity contour plots (0.5) for the electronic ground state of F on $TiO_2(001)$ at 11% (1F) and 100% (9F) coverage left and right panels, respectively. Ti, O, and F atoms are represented by gray, red, and light green spheres, respectively.

to 11% (Figure 4a) and 100% (Figure 4b) coverage, respectively. The left panel of Figure 4 clearly evidences the existence of an unpaired electron localized in one of the oxygen atoms of the TiO_2 surface; note also that the oxygen atom carrying the spin density is the one closest to the F adatom. A similar situation is encountered when analyzing Figure 4b. Here, nine O atoms have been oxidized and display a concomitant spin density. Figure 4a also shows a particular spin ordering with one row of O atoms with the spin density localized on the 2p orbital perpendicular to the surface and the neighboring rows with the spin density localized on a 2p orbital in the surface plane and in the direction parallel to the row with the 2p spin density perpendicular to the surface. Nevertheless, one must advert that many nearly degenerate solutions exist with different spin order. The important point here is not the particular spin order but the existence of spin density localized in the O atoms caused by the presence of the adsorbed F atoms.

The picture of the electronic structure arising from the spin density plots in Figure 4 can be complemented by the analysis of the density of states for the same physical situations. To this end, Figure 5 reports the total density of states for the case where the Ti_{5f} atoms of the $TiO_2(001)$ are all covered by one F atom. Similar to the case of the $TiO_2(101)$ surface discussed in the previous section, the presence of F atoms at the $TiO_2(001)$ surfaces results in the appearance of new peaks in the gap which correspond precisely to the oxidized O atoms. Here, the density of states corresponding to these atoms exhibits a broader structure which is due to the presence of different types of O atoms at the surface. A similar situation is observed when the F coverage is smaller, the only difference being a less intense peak in the calculated density of states. Finally, it is worth to point out that the states near the bottom of the conduction band are also present in the corresponding density of states of the clean surface. Therefore, as compared to bulk anatase or to the $TiO_2(101)$ surface, the apparent lower band gap in Figure 5 is

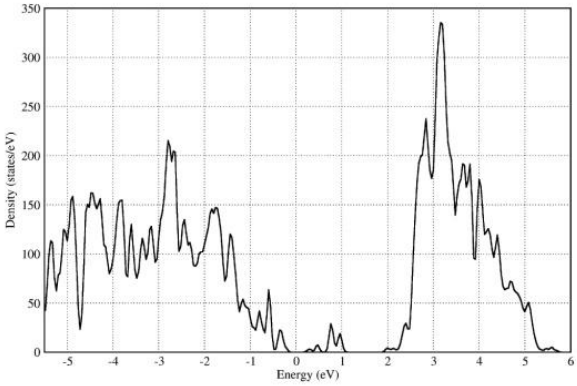

Figure 5. Total density of states of a TiO_2 (001) with all Ti_{5f} cations covered by F atoms.

not due to the presence of F but just due to the presence of this surface. Further studies are needed to relate this particular decrease of the band gap of the anatase $TiO_2(001)$ surface to its enhanced photocatalytic activity. Calculations using more accurate functionals, and quasiparticle GW calculations are currently being carried out in our laboratory.

We close this discussion about the electronic structure of the F-covered $TiO_2(001)$ surface by mentioning that the features in the gap seen in the density of states in Figure 5 appear for smaller coverage values as well and are fully visible for a 30% value.

Relative Stability of F-Covered Anatase $TiO_2(101)$ and $TiO_2(001)$ Surfaces. The adsorption energy values reported in the previous sections strongly indicate that the presence of F is largely exothermic and, thus, stabilizes the corresponding surfaces. Moreover, the fact that the interaction energy does only moderately decrease with coverage suggests that F-covered surfaces are rather stable. Interestingly, the interaction of F with the less stable $TiO_2(001)$ surface is much stronger, pointing toward a differential effect on the two surfaces. Note, however, that the values of the adsorption energy being taken with respect to half the energy of the diatomic F_2 molecule cannot be directly compared to experiment and hardly can provide information about the real thermodynamic stability.

The arguments above are in agreement with the experimental and theoretical findings of Yang et al.[14] that the presence of F stabilizes the $TiO_2(001)$ surface. In their computational study (see Supporting Information of ref 14), these authors provide a rough estimate of the surface free energy of the clean and F-covered $TiO_2(001)$ surface and conclude that the latter is much more stable. However, their approach, essentially relying on a measure of the surface energy, rather than on the surface free energy, does not allow comparing the relative stability of the two surfaces, the main reason being that the two surfaces are represented by different unit cell having different number of atoms and different structure. A possible way to circumvent the problem is to estimate the surface free energy following the ab initio atomistic thermodynamics formalism of Reuter and Scheffler,[33,34] which in addition allows one to take pressure, temperature, and coverage effects into account.

Here, we use the formalism of ab initio thermodynamics to obtain a reliable estimate of the surface free energy of both $TiO_2(101)$ and $TiO_2(001)$ for different coverage situations. To illustrate the adopted procedure, we start by defining the Gibbs energy (G) of a system of surface area at a given temperature

(T) in contact with a gas (F_2 in our case) at pressure (P) that can be adsorbed on the surface. In a similar way we can define the Gibbs energy of the clean surface and of the gas. We define the surface free energy (γ) as the difference, normalized per surface area, in Gibbs free energy between the surface−adsorbate system and its separated components, namely the clean surface and the gas-phase fluorine. Note that with this formalism it is possible to compare the stability of different surfaces just by the γ value. In practice, the surface free energy is estimated as in eq 3

$$\gamma = -\frac{1}{A}(G_{\text{surf+F}} - G_{\text{surf}} - G_{\text{F}}) = -\frac{1}{A}(E_{\text{surf+F}} - E_{\text{surf}} - N_{\text{F}}\mu_{0_{\text{F}_2}}) \quad (3)$$

where we assume that for the clean and covered surface the vibrational and entropic contributions to the energy are negligible in comparison with the other terms so, in practice, G is represented by the total energy E, either of surface plus F ($E_{\text{surf+F}}$) or clean surface (E_{surf}), as calculated by the density functional theory based method. On the contrary, the Gibbs energy for the gas takes into account all thermodynamics contributions and is derived from the chemical potential of the F_2 which leads to

$$\gamma = -\frac{1}{A}\left[(E_{\text{surf+F}} - E_{\text{surf}} - N_{\text{F}}\left(\frac{E_{\text{F}_2}}{2} + \frac{E_{\text{ZPE}}}{2} + \Delta\mu_{0_{\text{F}_2}} + kT\ln\left(\frac{P}{P_0}\right)\right)\right] \quad (4)$$

where E_{F_2} is the energy of the diatomic F_2 molecule, E_{ZPE} is the zero point energy, and $\Delta\mu_{0_{\text{F}_2}}$ can be obtained from thermodynamic tables or can be also calculated from appropriate ab initio calculations assuming the partition functions of an ideal gas. In the present case, the values have been obtained from DFT-based calculations with the same PBE functional.. Hence, one finally gets

$$\Delta\mu_0 = -\frac{1}{2}kT\ln Q_{\text{tot}} \quad (5)$$

where k is the Boltzmann constant and Q_{tot} is the sum of the translational, vibrational, rotational, and electronic partition functions of the F_2 molecule.

The surface free energy values obtained from the density functional theory calculations for the clean, F-covered, and gas phase F_2 molecule are summarized in Table 1. These values have been obtained considering room temperature (298.15 K) and 1 bar of F_2 total pressure and can be easily transformed to other conditions if required. Negative values of surface free energy indicates that the fluorine-covered surface is stable at the given (T, P) conditions with respect to the clean surface and the free F_2 molecules. First of all, note that, in absence of F_2 on the surface, the $TiO_2(101)$ surface is predicted to be more stable than $TiO_2(001)$, in agreement with the results reported by Yang et al.[14]

Moreover, the surface free energy values in Table 1 already show that the two surfaces are differently affected when in contact with a F_2 gas reservoir. An immediate consequence of results in Table 1 is that the presence of F_2 stabilizes the $TiO_2(001)$ surface, as already predicted by the calculations of Yang et al.[14] This result is also in agreement with the very recent work of Selçuk and Selloni[35] which uses ab initio atomistic thermodynamics to show that the $TiO_2(001)$ surface free energy decreases in the presence of HF. However, an important additional outcome of the present results is that they do also show that the $TiO_2(101)$ surface is destabilized by the presence of F. This is a new an important result not reported in previous work. In fact, showing that one of the surfaces is stabilized by the presence of F does not imply that the other surface is stabilized, too. However, the calculated surface free energy values in Table 1 indicate that this is indeed the case. Moreover, the fact that the surface free energy values for the $TiO_2(001)$ surface become negative indicates that, under these specific conditions, the surface will be spontaneously covered by F, at least as far as thermodynamic arguments is concerned. On the contrary, in the case of the $TiO_2(101)$ surface, the surface free energy is initially negative, indicating that this surface will be in thermodynamic equilibrium, but under the presence of F the values become positive which indicated that this surface will tend to avoid being covered by F.

Table 1. Surface Free Energy of the $TiO_2(101)$ and $TiO_2(001)$ Surfaces as a Function of F Coverage[a]

$TiO_2(101)$		$TiO_2(001)$	
coverage (%)	γ (eV/A^2)	coverage (%)	γ (eV/A^2)
0	−0.015	0	0.026
17	−0.004	11	0.006
33	0.007	22	−0.014
50	0.018	33	−0.033
67	0.028	44	−0.055
83	0.038	56	−0.074
100	0.047	67	−0.095
		78	−0.115
		89	−0.136
		100	−0.155

[a]The calculated values correspond to 298.15 K and 1 bar.

To better illustrate the above argument, Figure 6 displays the calculated surface free energy of the two TiO_2 surfaces as a function of F coverage. Clearly, for small coverage values the F-covered $TiO_2(101)$ surface is less stable than the clean one but still thermodynamically favorable, but the situation rapidly

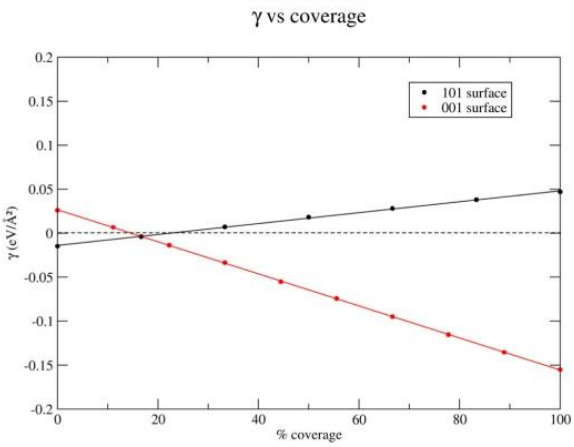

Figure 6. Calculated surface free energy of the TiO_2 (101) and TiO_2 (001) surfaces as a function of F coverage. The values have been obtained assuming T = 298.15 K and P = 1 bar.

changes upon increasing F coverage. On the contrary, the F-covered $TiO_2(001)$ surface is always more stable than the clean one, which nicely fits with the experimental observation that the presence of F largely stabilizes the reactive $TiO_2(001)$ facets.

To end up the discussion, it is convenient to link the surface free energy values to the adsorption energy ones reported in previous sections. It is important to point out that, as usual, adsorption energy values are reported with respect to one-half of the energy of the F_2 molecule and hence contain half the dissociation energy. The experimental value of the dissociation energy is of 2.75 eV; the adsorption energies reported in previous section are of the order of 1.8 eV for $TiO_2(101)$ and 3.1 eV for $TiO_2(001)$ per F atom, meaning that, in the first case, the energy gain upon adsorption is not enough to compensate for the cost to dissociate F_2 (2.75/2 eV per F atom) whereas in the second case the energy balance is favorable.

The discussion above follows from model calculations on the perfect stoichiometric surfaces, and one may wonder whether the conclusions will be valid on more realistic samples containing O vacancies. To answer this question, one needs to realize that, in any case, the concentration of the O vacancies will be small enough so that their effect on the calculated surface free energy values will be also small enough so as to preserve the main trends. Note also that under the presence of F the O vacancies will be rapidly healed since even substitution of O by F at the stoichiometric surfaces is thermodynamically favored. In any case, the number of F atoms at the surface will also be too small to change the trends arising from the calculation in the perfect surfaces.

A final aspect to consider is the diffusion of fluorine from the surface to the bulk, which would reduce the effective F loading on the surface, influencing also the thermodynamic stability of the slab. This is especially relevant for the (001) surface, which, as shown in the present work, is the most stable in a F-rich environment. Following an approach analogous to the one presented in our recent work on F diffusion in bulk titania,[21] we simulated the diffusion of an F atom from the vacuum above the slab into the first layer of anatase, by first rigidly displacing the F atom along the [001] direction (i.e., perpendicular to the surface) and next allowing the substrate to fully relax. As expected, the neglect of TiO_2 relaxation implies a very high repulsion barrier of 13.2 eV. This is even higher that the barrier encountered by a F atom moving along the [001] direction in a rigid anatase crystal (8.30 eV).[21] We explain this as an effect of the crystal truncation, which induces a shortening of the Ti−O bonds at the surface and a local increase of the density at the surface. However, a dramatic reduction of the diffusion barrier to 0.2 eV is observed upon full relaxation of the slab model. This is at variance from what is observed in the bulk, where a larger residual barrier of 2.5 eV remains after relaxation of the TiO_2 lattice. This can be rationalized as an effect of the higher mobility of the ions belonging to the topmost layer of a slab compared to those in the bulk, which facilitates the penetration of a F atom compared to the resistance encountered when moving along an equivalent direction in the bulk. We have also considered diffusion parallel to the surface, i.e., along the symmetry-related [100] and [010] directions in the different layers of the slab. In the bulk, we found that these directions are extremely prone to F diffusion, displaying a rigid-lattice barrier of 0.49 eV only, which completely disappears after lattice relaxation. In the channel of the topmost layer, the encountered rigid-lattice barrier is 0.56 eV, which reduces to the bulk-limit value of 0.49 eV in the second layer already. Nevertheless, the fact that a small but noticeable barrier still remains implies that the TiO_2 surface will be covered before F starts to diffuse to the bulk, thus reinforcing the conclusions of the present work.

■ CONCLUSIONS

Periodic density functional theory based calculations with the GGA+U exchange-correlation functional and realistic supercell surface models have been carried out to study the interaction of fluorine with the anatase $TiO_2(101)$ and $TiO_2(001)$ surface as a function of coverage.

The interaction of F with the two surfaces is exothermic and is accompanied by oxidation of the substrate. The analysis of the spin density reveals that, in all cases, the charge transfer to the F adatoms occurs from one of the O atoms nearby. This results in the appearance of new features in the density of states which are located in the band gap of the surface.

Regarding the adsorption energy, the effect of coverage is moderate, leading to a general decrease of the calculated value which is to be expected from the negative charge of the adsorbate. Not unexpectedly, the interaction is stronger for the less stable $TiO_2(001)$ surface although from the adsorption values it is not possible to differentiate the relative stability of the two surfaces.

The analysis of surface free energy values corresponding to 298.15 K and 1 bar of F_2 pressure, obtained following the ab initio thermodynamics formalism, reveals that the clean $TiO_2(101)$ is more stable than $TiO_2(001)$, as expected and in agreement with previous work. However, the order of stability is reversed when the F coverage overcomes a critical value to the point that the F-covered $TiO_2(001)$ becomes thermodynamically favored and the opposite occurs for the F-covered $TiO_2(101)$, providing rigorous additional interpretation of the results reported by Yang et al.[14] and offering a way to easily screen the effect of other adsorbates which can be used to obtain active photocatalysts with less aggressive chemical agents.

■ AUTHOR INFORMATION

Corresponding Author

*E-mail: francesc.illas@ub.edu (F.I.).

Notes

The authors declare no competing financial interest.

■ ACKNOWLEDGMENTS

This work has been supported by the Spanish MINECO grant CTQ2012-30751 grant and, in part, by Generalitat de Catalunya grant XRQTC. O.L.G. is grateful to the Universitat de Barcelona for a predoctoral grant, and F.I. acknowledges additional support through the ICREA Academia award for excellence in research. Computational time at the MARENOSTRUM supercomputer has been provided by the Barcelona Supercomputing Centre through a grant from Red Española de Supercomputación.

■ REFERENCES

(1) Hashimoto, K.; Irie, H.; Fujishima, A. TiO_2 Photocatalysis: A Historical Overview and Future Prospects. *Jpn. J. Appl. Phys.* **2005**, *44*, 8269−8285.

(2) Fujishima, A.; Zhang, X.; Tryk, D. A. TiO_2 Photocatalysis and Related Surface Phenomena. *Surf. Sci. Rep.* **2008**, *63*, 515−582.

(3) Chen, X.; Mao, S. S. Titanium Dioxide Nanomaterials: Synthesis, Properties Modifications and Applications. *Chem. Rev.* **2007**, *107*, 2891−2959.
(4) Henderson, M. A. A Surface Science Perspective on TiO_2 Photocatalysis. *Surf. Sci. Rep.* **2011**, *66*, 185−297.
(5) Hoffmann, M. R.; Martin, S. T.; Choi, W.; Bahnemann, D. W. Environmental Applications of Semiconductor Photocatalysis. *Chem. Rev.* **1995**, *95*, 69−96.
(6) Mill, A.; Davies, R. H.; Worsley, D. Water-Purification by Semiconductor Photocatalysis. *Chem. Soc. Rev.* **1993**, *22*, 417−425.
(7) Fox, M. A.; Dulay, M. T. Heterogeneous Photocatalysis. *Chem. Rev.* **1993**, *93*, 341−357.
(8) Ravelli, D.; Dondi, D.; Fagnoni, M.; Albini, A. Photocatalyisis. A Multi-Faceted Concept for Green Chemistry. *Chem. Soc. Rev.* **2009**, *38*, 1999−2011.
(9) Akihiko, K.; Yugo, M. Heterogeneous Photocatalyst Materials for Water Splitting. *Chem. Soc. Rev.* **2009**, *38*, 253−278.
(10) Yuliati, L.; Yoshida, H. Photocatalytic Conversion of Methane. *Chem. Soc. Rev.* **2008**, *37*, 1592−1602.
(11) Chen, X. B.; Shen, S. H.; Guo, L. J.; Mao, S. S. Semiconductor-Based Photocatalytic Hydrogen Generation. *Chem. Rev.* **2010**, *110*, 6503−6570.
(12) Kudo, A.; Miseki, Y. Heterogeneous Photocatalyst Materials for Water Splitting. *Chem. Soc. Rev.* **2009**, *38*, 253−278.
(13) Osterloh, F. E. Inorganic Materials as Catalysts for Photochemical Splitting of Water. *Chem. Mater.* **2008**, *20*, 35−54.
(14) Yang, H. G.; Sun, C. H.; Qiao, S. Z.; Zou, J.; Liu, G.; Smith, S. C.; Cheng, H. M.; Lu, G. Q. Anatase TiO_2 Single Crystals With a Large Percentage of Reactive Facets. *Nature* **2008**, *453*, 638−641.
(15) Peng, X.; Wang, J.; Thomas, D. F.; Chen, A. Tunable Growth of TiO_2 Nanostructures on Ti Substrates. *Nanotechnology* **2005**, *16*, 2389−2395.
(16) Shein, I. R.; Zhukov, V. P.; Zainullina, V. M. Electronic Band Structure, Optical Absorption and Photocatalytic Activity of Anatase Doped with Bismuth or Carbon. *J. Alloys Compd.* **2013**, *548*, 46−51.
(17) Dozzi, M. V.; Andrea, C. D.; Ohtani, B.; Valentini, G.; Selli, E. Fluorine-Doped TiO_2 Materials: Photocatalytic Activity vs Time-Resolved Photoluminescence. *J. Phys. Chem. C* **2013**, *117*, 25586−25595.
(18) Su, R.; Christensen, M.; Shen, Y.; Kibsgaard, Y.; Elgh, B.; Vang, R. T.; Bechstein, R.; Wendt, S.; Palmqvist, A.; Iversen, B. B.; Besenbacher, B. Rapid Synthesis of Porous, Mixed Phase Titania Films with Tailored Orientation of Rutile for Enhanced Photocatalytic Performance. *J. Phys. Chem. C* **2013**, *117*, 27039−27046.
(19) Tosoni, S.; Lamiel-Garcia, O.; Hevia, D. F.; Miguel, J.; Illas, F. Electronic Structure of F-Doped Bulk Rutile, Anatase, and Brookite Polymorphs of TiO_2. *J. Phys. Chem. C* **2012**, *116*, 12738−12746.
(20) Tosoni, S.; Fernandez Hevia, D.; González Díaz, O.; Illas, F. Origin of Optical Excitations in Fluorine-Doped Titania from Response Function Theory: Relevance to Photocatalysis. *J. Phys. Chem. Lett.* **2012**, *3*, 2269−2274.
(21) Tosoni, S.; Lamiel-Garcia, O.; Fernandez Hevia, D.; Illas, F. Theoretical Study of Atomic Fluorine Diffusion through Bulk TiO_2 Polymorphs. *J. Phys. Chem. C* **2013**, *117*, 5855−5860.
(22) Ortega, Y.; Lamiel-Garcia, O.; Fernandez Hevia, D.; Tosoni, S.; Oviedo, J.; San-Miguel, M. A.; Illas, F. Theoretical Study of the F Doped Anatase Surfaces. *Surf. Sci.* **2013**, *618*, 154−158.
(23) Kresse, G. Efficient Iterative Schemes for Ab Initio Total-Energy Calculations Using a Plane-Wave Basis Set. *Phys. Rev. B* **1996**, *54*, 11169−11186.
(24) Kresse, G.; Hafner, J. Ab Initio Molecular-Dynamics Simulation of the Liquid-Metal−Amorphous-Semiconductor Transition in Germanium. *Phys. Rev. B* **1994**, *49*, 14251−14269.
(25) Kresse, G.; Hafner, J. Ab Initio Molecular Dynamics for Liquid Metals. *Phys. Rev. B* **1993**, *47*, 558−561.
(26) Perdew, J. P.; Ernzerhof, M.; Burke, K. Generalized Gradient Approximation Made Simple. *Phys. Rev. Lett.* **1996**, *77*, 3865−3868.
(27) Dudarev, S.; Botton, G.; Savrasov, S.; Humphreys, C.; Sutton, A. Electron-Energy-Loss Spectra and the Structural Stability of Nickel Oxide: An LSDA+ U Study. *Phys. Rev. B* **1998**, *57*, 1505−1509.
(28) Muscat, J.; Wander, A.; Harrison, N. M. On the Prediction of Band Gaps from Hybrid Functional Theory. *Chem. Phys. Lett.* **2001**, *342*, 397−401.
(29) di Valentin, C.; Pacchioni, G.; Selloni, A. Reduced and n-Type Doped TiO_2: Nature of Ti^{3+} Species. *J. Phys. Chem. C* **2009**, *113*, 20543−20552.
(30) Moreira, I. de P.R.; Illas, F.; Martin, R. L. Effect of Fock Exchange on the Electronic Structure and Magnetic Coupling in NiO. *Phys. Rev. B* **2002**, *65*, 155102.
(31) Pacchioni, G. Modeling Doped and Defective Oxides in Catalysis with Density Functional Theory Methods: Room for Improvements. *J. Chem. Phys.* **2008**, *128*, 182505.
(32) Blöchl, P. E. Projector Augmented-Wave Method. *Phys. Rev. B* **1994**, *50*, 17953−17979.
(33) Reuter, K.; Scheffler, M. Composition, Structure, and Stability of RuO_2(110) as a Function of Oxygen Pressure. *Phys. Rev. B* **2002**, *65*, 035406.
(34) Reuter, K.; Scheffler, M. First-Principles Atomistic Thermodynamics for Oxidation Catalysis: Surface Phase Diagrams and Catalytically Interesting Regions. *Phys. Rev. Lett.* **2003**, *90*, 046103.
(35) Selçuk, S.; Selloni, A. Surface Structure and Reactivity of Anatase TiO_2 Crystals with Dominant {001} Facets. *J. Phys. Chem. C* **2013**, *117*, 6358−6362.

3.1.2.3 Adsorption properties of trifluoroacetic acid on anatase (101) and (001) surfaces: a density functional theory study

PCCP

PAPER

View Article Online
View Journal | View Issue

Cite this: *Phys. Chem. Chem. Phys.*, 2015, **17**, 23627

Adsorption properties of trifluoroacetic acid on anatase (101) and (001) surfaces: a density functional theory study

Oriol Lamiel-Garcia,[a] Daniel Fernandez-Hevia,[bc] Amador C. Caballero[d] and Francesc Illas*[a]

Received 30th June 2015,
Accepted 10th August 2015

DOI: 10.1039/c5cp03780h

www.rsc.org/pccp

The interaction of trifluoroacetic acid with anatase TiO_2(101) and TiO_2(001) surfaces has been studied by means of periodic density functional theory based calculations. On the former, the interaction is weak with the adsorbed molecules in a configuration almost indistinguishable from the gas phase structure. On the latter, the interaction is very strong; the molecule adsorbs as trifluoroacetate and releases a proton that binds an oxygen surface atom with a significant distortion of the substrate. The difference in adsorption the mode and strength can be understood from the different structural features of both surfaces and provides arguments to the role of trifluoroacetic as a morphological control agent in the solvothermal synthesis of TiO_2 nanoparticles with predominant (001) facets. This, in turn, has a very significant impact on industrial production strategies of value-added TiO_2 for photocatalytic applications. Analysis of calculated core level binding energies for F(1s) confirms the experimental assignment to F at the surface as F^- at Ti surface sites and to F in $-CF_3$ groups of the adsorbed molecule.

Introduction

Photocatalysis constitutes a very active field of research due to its implications in environmental chemistry,[1,2] hydrogen production,[3,4] self-cleaning surfaces,[5] self-sterilizing surfaces[6] and water cleaning technologies.[7] Among the different materials scrutinized as possible photocatalysts, titanium dioxide (TiO_2) continues to be one of the main key players.[2,4,7–9] TiO_2 exhibits three stable polymorphs namely anatase, rutile and brookite among which anatase exhibits the highest activity and is present in most of the existing photocatalysts based on this material. This is the case of the well-known commercial Degussa P25 (Evonik) catalyst often used as a standard even if its exact composition remains a matter of controversy.[10] Nevertheless, the excessively large bandgap of the bulk forms of TiO_2 (rutile $\approx$ 3 eV and anatase $\approx$ 3.2 eV) severely limits its efficient use for photocatalysis under visible light. Several strategies have been proposed to decrease the bandgap of anatase involving new synthetic processes aimed at introducing doping either with non-metals, metals or simply introducing defects.[11,12] The case of doping with nitrogen is very illustrative as it raised enormous expectation; over 5000 citations have followed its publications in 2001 by Asahi *et al.*[13] However, in spite of initial evidence, the photocatalytic reaction rates are still low. More importantly, the detailed origin of photocatalysis over visible-light-activated N-doped TiO_2 is still a matter of considerable controversy.[14,15] Nevertheless, in spite of all these efforts, photocatalysts working under visible sunlight with activity higher than TiO_2 powders under ultraviolet light have not been yet developed.[16]

A different approach to enhance the photocatalytic activity of TiO_2 under the visible light consists of controlling the morphology and size of the nanoparticles constituting the TiO_2 based powders such as the above mentioned Degussa P25 (Evonik). In this respect, the seminal work of Yang *et al.*[17] showing that adsorbed F stabilizes the reactive (001) surface of TiO_2 anatase to the detriment of the most stable and abundant but less active (101) surface represents a major breakthrough. TiO_2 anatase single crystal mesoparticles with controlled size, well-defined polyhedral facets,[18,19] and high-level photocatalytic activities have been synthetized in the past few years. The enormous degree of experimental control achieved in the synthesis of tailored TiO_2 nanoparticles with either anatase or rutile crystal structure is well-described in the recent review by Liu *et al.*[20] Nevertheless, it is worth pointing out that a clear cut relationship with particle morphology and photocatalytic activity does not so far exist. Yet, this understanding is critical in order to promote the development of

[a] *Departament de Química Física & Institut de Química Teòrica i Computacional (IQTCUB), Universitat de Barcelona, C/ Martí i Franquès 1, E-08028 Barcelona, Spain. E-mail: francesc.illas@ub.edu; Tel: +34 934 021 229*
[b] *INAEL Electrical Systems S.A., C/ Jarama 5, 45007 Toledo, Spain*
[c] *Departamento de Química, Universidad de Las Palmas de Gran Canaria, Campus Universitario de Tafira, 35017 Las Palmas de Gran Canaria, Spain*
[d] *Department of Electroceramics, Instituto de Cerámica y Vidrio (CSIC), Kelsen 5, 28049, Madrid, Spain*

large-scale production facilities that can produce a low-cost/high-efficiency TiO_2-based material and create a competitive advantage in the industry by leveraging the nanoscale morphology control. Note, for instance, that high photocatalytic activity has also been reported as well for TiO_2 nanoparticles with dominant (111) facets.[21]

The synthesis of TiO_2 nanoparticles with abundant (001) surfaces often involves hydrothermal processes with hydrofluoric acid (HF) as a fluorine source. The presence of fluorine increases the surface free energy of the most stable (101) facet and decreases the surface free energy of the initially less stable (001).[22] The problem with the use of HF is its high toxicity, high reactivity and corrosive behavior. Recently, trifluoroacetic acid (TFAA) has proven to be efficient in obtaining TiO_2 with a large amount of (001) surfaces and resulted in samples with enhanced photoactivity.[23] Moreover, the use of TFAA enormously reduces the presence of water in the reaction medium allowing for a better control. The experiments of Calatayud *et al.* suggest that TFAA acts as a fluorine source. Moreover, analysis of X-ray photoemission spectra (XPS) of the F(1s) core suggests that F is simultaneously present as a direct adsorbate (Ti–F) and also as part of the CF_3COO moiety (C–F). Infrared and Raman spectra suggest that TFAA species are adsorbed through the O atoms in a bidentate mode, either by bridging or chelating. The stabilization of the (001) facets may be attributed to the presence of adsorbed atomic F released under the semi-solvothermal reaction or to the presence of the carboxylic group which is also known to stabilize the (001) facet.[24]

In order to further understand the interactions between TFAA and the TiO_2 surfaces and to shed light on the role of TFAA in stabilizing the reactive (001) facets, a series of systematic periodic density functional theory based calculations have been carried out aimed at disclosing the preferential adsorption mode at each surface and to further confirm the assignment of XPS peaks corresponding to the F(1s) core level binding energies. The present results fully confirm the experimental assignment and suggest that the simultaneous presence of TFAA and atomic F at the surface acts in a synergic way with the result of a preferential stabilization of the (001) facets.

Computational details

Periodic density functional theory (DFT) based calculations were performed for suitable surface slab models of the clean TiO_2(001) and TiO_2(101) surfaces as well as for various adsorption modes of the TFAA molecule. Details regarding the surface models and adsorption modes are described in the next section.

In the present DFT calculations the valence electrons are described with a plane wave basis set with a kinetic energy cutoff of 400 eV for the plane waves, enough to obtain total energies converged up to 1 meV per atom. The effect of the inner cores on the valence electron density is taken into account by means of the projector augmented wave (PAW) method,[25,26] and this may be regarded as an all electron approach in which the cores are frozen as in the reference system used to extract the corresponding PAW. The 3p, 3d and 4s electrons (12 electrons) of Ti and 2s and 2p electrons of C, O and F (4, 6 and 7 electrons, respectively) are explicitly included in the calculation. Numerical integration in the reciprocal space has been carried out by sampling the Brillouin zone using the Monkhorst–Pack method;[27] in particular a $2 \times 2 \times 1$ grid of special k-points has been used. The same number of k-points was used for the electronic analysis and for the optimization process. Calculations on the isolated TFAA molecule were carried out at the Γ point. All calculations involve closed shell species and non-magnetic material. Accordingly, the non-spin polarized implementation of the periodic Kohn–Sham formalism was always used. Geometry optimizations regarding relaxation of the surface models without or with TFAA were carried out using analytical gradients and a convergence was achieved when forces on the relaxed atoms (see below) are less than 5×10^{-3} eV Å^{-1}. The same criterion has been used to optimize the geometry of the isolated TFAA molecule which has been carried out by placing the molecule in a large enough cubic box (15 Å per side).

The generalized gradient approximation (GGA) in the Perdew–Burke–Ernzerhof (PBE) formulation was used for the electron exchange and correlation contribution to the total energy.[28,29] This type of approach is known to considerably underestimate the band gap of oxides in general and of TiO_2 in particular and is especially problematic in the description of reduced titania.[30] A better description is obtained using either PBE+U or hybrid functionals.[31,32] Nevertheless, one must caution that the choice of hybrid functional (amount of Fock exchange) is an open issue[33,34] and that the nature of electronic states of reduced anatase is a matter of discussion.[35,36] However, since only stoichiometric models are considered here and the main purpose of the present work is to investigate the adsorption properties of TFAA on TiO_2 surfaces, one may consider that the choice of standard PBE is adequate enough. This also implies that dispersion terms are not taken into account. In the forthcoming discussion we will show that this does not represent a limitation and does not affect the main conclusions.

All calculations were carried out using the VASP code.[37–39]

Surface models and bonding modes

The TiO_2(001) and (101) surfaces have been represented within the repeated slab model using large enough supercells built from lattice parameters optimized consistently using the density functional theory (DFT) based method. The lattice parameters calculated using the computational setup described in the previous section are $a = b = 3.806$ Å and $c = 9.734$ Å which compare rather well with the experimental values ($a = b = 3.78$ Å and $c = 9.50$ Å)[40] and are similar to values reported in previous work dealing with F adsorption[22] and implantation.[41] These studies have shown that these models provide converged results with respect to the slab thickness and the vacuum width between the periodically repeated slabs although the presence of TFAA requires some adjustment as explained in detail below.

The anatase TiO_2(001) surface has been represented by a 3 × 3 × 9 supercell with dimensions 11.419 × 11.419 × 33.877 Å including a vacuum width in the direction perpendicular to the surface plane larger than 10 Å between the interleaved slabs. The overall surface model contains 72 TiO_2 units. The position of the atoms in the upper layers was fully relaxed whereas those lying 5 Å below the surface plane were fixed to reproduce the bulk structure. In the case of the anatase TiO_2(101) surface the supercell dimensions are 10.448 × 11.419 × 31.528 Å and also include the vacuum width between the interleaved slabs. The slightly different dimensions in the (101) plane arise from the tilted nature of the slab model and do not introduce any spurious effect. The resulting model contains 60 TiO_2 and the position of the atoms in the outermost layers was fully relaxed whereas atoms below 5 Å were fixed at the bulk structure as in the case of the TiO_2(001) surface model. Here it is worth pointing out that the anatase TiO_2(001) surface is known to exhibit reconstruction under ultra-high-vacuum conditions[42] and several models have been proposed.[43] These effects are likely to be suppressed under the solvothermal conditions at which the synthesis takes place. Hence, unreconstructed models are used.

The slab models above described are similar but larger than those used in previous studies regarding F adsorption[22] and implantation.[41] The main difference concerns the number of atomic layers, which is larger here, and the dimension of the cell in the *c* direction, which is also larger due to the need for accommodating the TFAA adsorbed molecule while maintaining a large enough vacuum width between the periodically repeated models. A graphical representation of both surface models is reported in Fig. 1. To investigate the adsorption mode and adsorption coordination of TFAA on the two surface models several initial geometries have been tested in a systematic way, some representative examples are shown in Fig. 2 for the case of the TiO_2(001) surface and further discussed in the next section.

It is worth noting that under the conditions of the semi-solvothermal synthesis,[23] TFAA may be hydrated with several water molecules even if the presence of water was minimal. Several isomers of hydrated TFAA have been described from the experiment[44] or from theoretical calculations.[45,46] However, to better understand the type of interaction of TFFA with the TiO_2 surfaces of interest we considered the isolated molecule without solvating water molecules. We will show that TFAA adsorbs strongly on TiO_2(001) and weakly on TiO_2(101), and the energy difference is so large that the conclusions will not be affected when considering the hydrated molecule, in one case the interaction will be still weak and in the other case the interaction with the surface will displace the solvating water molecules. One may also wonder whether the strong acidic character of TFAA results in dissociative adsorption and whether the resulting structure resembles that of formic or acetic acid adsorbed on these surfaces.[47–49] We will show that the strong acidic character of TFAA leads to adsorption modes that do not resemble those of formic or acetic acid. In addition, the strong acidic character favors dissociative adsorption and this is the final optimized geometry even if the initial geometry always concerns molecular adsorption.

For the final optimized configurations the adsorption energy (E_{ads}) has been calculated as usual as

$$E_{ads} = E_{(surf+TFAA)} - (E_{surf} + E_{TFAA})$$

where $E_{(surf+TFAA)}$ stands for the energy of the slab model plus TFAA in the final optimized geometry, E_{surf} stands for the energy of the relaxed naked surface and, finally, E_{TFAA} corresponds to the energy of the isolated TFAA molecules obtained as indicated in the previous sections.

In order to further gain insight into the electronic structure of TFAA adsorbed on the TiO_2 surface of interest, core level binding energy for F(1s) electrons in different environments was estimated within the initial state approximation and hence estimated directly from the Kohn–Sham (KS) eigenvalues (ε_{KS}) of a particular core state with respect to the Fermi energy. The values thus obtained are generally too small compared to the experiment and imply meaningless positive relaxation energy

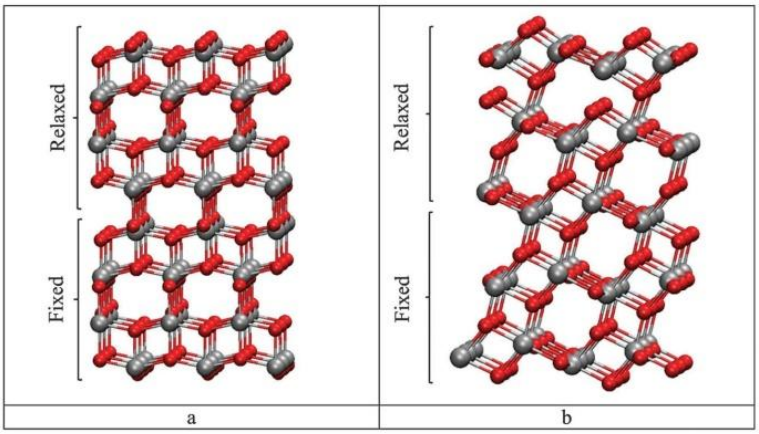

Fig. 1 Slab models used to represent the anatase TiO_2(001) and TiO_2(101) surfaces; left and right panels, respectively. Ti atoms are in grey and O atoms in red. The atomic layers relaxed or fixed in the study of TFAA adsorption are also indicated.

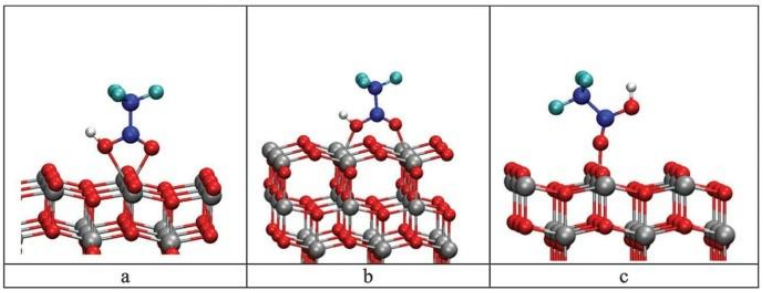

Fig. 2 Illustrative examples of chelating (a), bridging (b) and top (c) bonding modes of TFAA above the anatase TiO_2(001) surface.

values; the change in the total energy is due to the change in electronic density of the core state in response to the core hole. Nevertheless, it has been recently shown that while ε_{KS} cannot be compared to absolute values of the core level binding energy, the differences with respect to a common reference (core level binding energy shifts or $\Delta\varepsilon_{KS}$) are physically meaningful,[50,51] thus justifying a common practice (see *e.g.* ref. 52 and 53).

Results and discussion

Adsorption structure and energy

In order to assess the effect of the TiO_2 surface on the structure of TFAA it is convenient to analyze first the structure of the isolated molecule. This would also allow us to evaluate the accuracy of the present computational approach, at least for structural parameters. There are very few studies reporting the structure of the gas phase TFAA molecule and the only experimental information corresponds to the data obtained from electron diffraction.[54] From the computational point of view, the structure has been studied in the context of accurate pK_a determination at various theoretical levels.[55] Table 1 reports results for structural parameters obtained in the present work and compares them with those reported at the B3LYP/6-311+G(d,p) and MP2(full)/6-311+G(d,p) level and levels of theory by Namazian *et al.*[55] The analysis of results collected in Table 1 indicates that, not surprisingly, the PBE results for distances and angles agree with those obtained using the more sophisticated B3LYP and MP2 approaches and with experiment. In fact, the distances all agree within 0.01 Å and the angles by less than 1 degree.

Table 1 Structural parameters of the isolated TFAA molecule as predicted from the present PBE calculations; the results from previous work are included for comparison. The last row reports the result for TFAA adsorbed on the TiO_2(001) surface in the most stable configuration. Distances are in Å and the F–C–F bond angle in degrees

	C–F	C–F[b]	O–H	C–O	C=O	F–C–F[c]
Gas phase TFAA						
B3LYP/6-311+G(d,p)[55]	1.34	1.33	0.97	1.34	1.20	108
MP2(full)/6-311+G(d,p)[55]	1.34	1.33	0.97	1.34	1.21	108
PBE present work	1.34	1.37	0.98	1.35	1.20	109
Experimental[54]	1.32	1.32	0.96	1.35	1.19	109
Adsorbed TFAA						
PBE present work	1.35	1.36	0.98[a]	1.29	1.25	108

[a] Note that TFAA chemisorbs dissociatively, this value corresponds to the distance between H and the O atom of the surface to which it is bonded. [b] F atom located at the COOH plane. [c] Angle involving two symmetrically equivalent F atoms.

Let us now consider the case of the adsorbed molecule on the most stable TiO_2(101) surface. The geometry optimization procedure was started from almost all possible coordination modes and orientations of the TFAA molecule to the surface. Thus, orientations with the molecule parallel or perpendicular to the surface were considered and in each case initial geometries were tried with the molecule being placed above different surface sites. The parallel initial geometry always evolves to a perpendicular one with the O atoms pointing towards the surface. For the perpendicular orientation, the bridge, chelate, and monodentate bonding modes were considered; the orientation with the CF_3-moiety pointing towards the surface is found to be repulsive. In the bridge, chelate, and monodentate bonding modes the O atoms point towards the surface directly interacting with the Ti surface atoms. Except for the latter, the final geometry corresponds to a non-dissociative adsorption with a very weak interaction. Fig. 3 displays two of the final geometries, in one case the H atom of the TFAA molecule interacts with an O atom of the surface (O_{surf}) whereas in the other case the contact involves the O atom of the TFAA molecules not attached to H and one Ti atom (Ti_{surf}). In both cases, the structure of the adsorbed molecule is almost indistinguishable from that of the gas phase TFAA. This is a clear indication that, in theTiO_2(101) surface, the molecule is physisorbed. This conclusion is reinforced by the calculated values of the adsorption energy since, in spite of the difference in coordination mode, the adsorption energy values are almost identical ($E_{ads} \sim 0.35$ eV). There are several other similar structures with different coordinations but all of them have even lower E_{ads} values. This is characteristic of physisorbed species where the interaction is not directional and the molecular structure is preserved. One can properly argue that the calculated E_{ads} values are too small since the present computational approach does not include dispersion forces. However, while the inclusion of dispersion forces can easily double the E_{ads} calculated value,[56,57] it is very unlikely that dispersion forces will change the bonding mechanism and qualitative picture, the TFAA molecule will be predicted to be molecularly adsorbed.

Interestingly, a completely different picture emerges from the calculations when considering the more reactive anatase

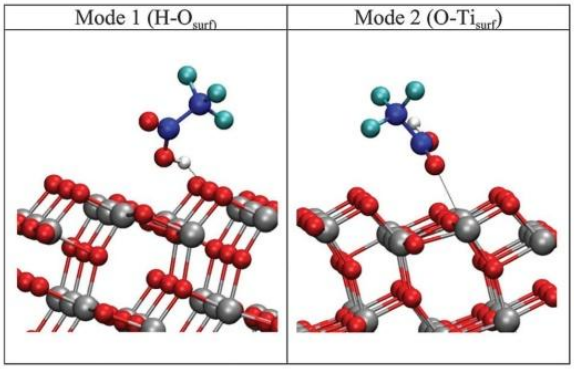

Fig. 3 Structure of the two most stable bonding modes and TFAA adsorbed on anatase TiO_2(101). Note that the TFAA molecule is adsorbed in a non-dissociative way.

TiO_2(001) surface. Here, geometry optimization was also carried out starting from different bonding modes and orientations of the TFAA molecule with respect to the surface. Overall, 15 possible adsorption configurations have been considered which can be mainly divided into three groups according to the bonding modes displayed in Fig. 2. Following the strategy used for the TiO_2(101) commented above, different bonding modes were tested, considering different orientations, with the molecule perpendicular to the surface or slightly tilted. Initial geometries where the TFAA molecule was parallel to the surface were also checked and the bonding modes where the fluorine atoms were the main contact of the molecule with the surface were also considered. However, in all cases, the most stable configuration corresponds to a situation in which the OH bond dissociates, and the H atom binds to one of the O_{surf} atoms which is considerably displaced from the equilibrium position towards the vacuum and the trifluoroacetate moiety is bonded to the surface directly through two O–Ti_{surf} bonds (Fig. 4). For this trifluoroacetate adsorbed structure, the C–O distances are almost equal (Table 1) as expected from symmetry arguments and verified by the gas phase calculations of Namazian *et al.*[55] The corresponding adsorption energy is very large (E_{ads} = 3.36 eV)

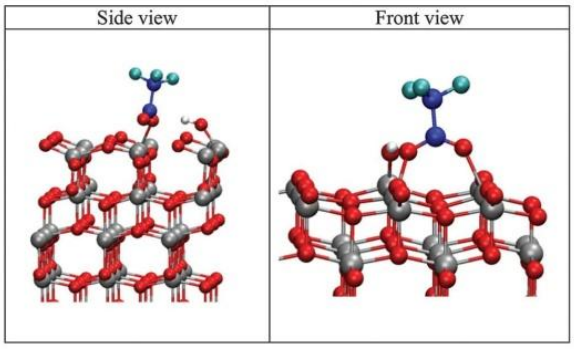

Fig. 4 Structure of the most stable bonding modes and TFAA adsorbed on anatase TiO_2(001). Note that here the TFAA molecule is adsorbed in a dissociative way.

indicating a very strong interaction. This is remarkable since this bonding mode involves the deformation of the surface. Note that the cost corresponding to the dissociation of the O–H bond will be largely compensated by the formation of the H–O_{surf} bond. Interestingly, the resulting bridging adsorption mode is in agreement with the suggestion from analysis of the infrared spectra of TFAA on TiO_2 anatase nanoparticles.[23] The particular bonding geometry of the trifluoroacetate moiety on TiO_2(001) explains why a similar structure cannot be stabilized on the TiO_2(101), in the latter surface the O atoms of the TFAA molecule cannot directly interact with the Ti_{surf} atoms which are located slightly below the surface plane. It is worth pointing out that a second rather stable structure is found with E_{ads} = 2.80 eV involving also a bridging type configuration. However, in the second adsorption mode the OH moiety of TFAA is preserved, the second O atom of TFAA binds a Ti_{surf} atom forming a first C–O–Ti_{surf} and the bridging mode is completed by pulling one of the O_{surf} atoms so as to build the second C–O_{surf}–Ti_{surf} pillar of the bridge. This type of configuration is, however, less stable and unlikely to be found under ultra-high-vacuum conditions. Nevertheless, this can play a role in the semisolvo-thermal synthesis conditions used by Calatayud *et al.*[23] and may be the reason why a too high temperature results in nanoparticles with less well-defined facets.

Interpretation of XPS experiments

To complete the discussion we will now focus on the interpretation of the XPS experiments reported by Calatayud *et al.*[23] These authors found two well separated contributions corresponding to the F(1s) core level binding energies. The first peak appears at 684 eV and is attributed to F species adsorbed above Ti_{surf} sites, and the second peak exhibits larger intensity, appears at a rather higher binding energy of 688 eV and is attributed to F atoms on the $-CF_3$ moiety of the TFAA molecule. Both features are relative to C(1s) at 284.6 which was used for calibration. From chemical intuition and as confirmed by previous theoretical calculations, F species at the surface are negatively charged with almost 1e transferred from the substrate.[22] Therefore, charge transfer arguments suggest to assign the peak at lower binding to F^- species above Ti_{surf} sites and the peak at higher binding energy to F atoms in the $-CF_3$ group. This assignment is fully confirmed by the present DFT based calculations predicting also two main XPS peaks at 655.0 and 657.5 eV, respectively. The peak at lower binding energy corresponds to F atoms at the surface precisely above Ti_{surf} sites and the one at higher binding energy corresponds to the F atoms in the $-CF_3$ group. For comparison we have also obtained the F(1s) binding energy corresponding to the F_2 molecule where the F atoms are necessarily neutral. The calculated F(1s) binding energy is much higher, $\sim$664 eV, as expected.

At this point, the reader would have noticed that the trends in the calculated core level binding energies commented above agree well with the experimental ones but also that the absolute values are quite different thus severely questioning the validity of the present theoretical predictions. There are several reasons for the discrepancy between experimental and calculated absolute values of the F(1s) binding energies. Some reasons are purely

technical and some other have a more fundamental origin.[58,59] Regarding the former, one needs to realize that experimental values are relative to C(1s) centered at 284.6 eV. This is usual convention but note that the experiments for the gas phase TFAA molecule report C(1s) binding energies of 296.5 and 299.3 for the C atom in the –COO and $-CF_3$ groups, respectively.[60] Within the present approach, the calculated values for the gas phase TFAA molecule are 273.9 and 276.8, the trend is the same as in the experiment with a difference between the two C(1s) binding energies of 2.8 eV in the experiment and 2.9 eV in the calculated values. However, the absolute values are too small and this brings us to the more fundamental reasons for quantitative disagreement. The calculated values correspond to the so-called initial state estimate and here are approximated from the Kohn–Sham orbital energies. This is a common practice, fully justified by the Hartree–Fock level of theory[58,59] through Koopman's theorem and assumed to be valid in DFT based calculations, with the latter hypothesis being often justified from practical observation.[52,53] We already mentioned that as has been recently shown that Kohn–Sham orbital energies do not provide an estimate of core level binding energies,[50,51] the values thus obtained are too small implying a negative contribution of final state effects, and the energy gain due to the relaxation of the electron density in response to the core hole must be necessarily negative. Interestingly, Kohn–Sham orbital energies with respect to a given reference follow the experimental trend, as shown in recent work[50,51] and illustrated here with the example of C(1s) for the TFAA molecule above, and this is the origin of the success of many theoretical studies. To further illustrate this let us compare the F(1s) binding energies relative to C(1s) in both the experiment and calculations. From the data reported above it is clear that the two F(1s) peaks in the experiments of Calatayud *et al.* appear at 399.4 and 403.4 eV relative to C(1s), respectively. Taking the average of the two calculated C(1s) values for the adsorbed trifluoroacetate (270.3 eV) as an origin one would find the F(1s) features at 384.7 and 387.2 eV. The agreement now is semiquantitative and the difference between experimental and calculated values can be safely ascribed to final state effects. To conclude, the present theoretical calculations fully confirm the experimental assignment. The present discussion also validates and reinforces previous conclusions regarding the validity of Kohn–Sham orbital energies to predict relative values of core level binding energies.

Conclusions

Periodic density functional theory based calculations, with the PBE flavor for the exchange correlation functional, have been carried out to investigate the adsorption of TFAA on the anatase TiO_2(101) and TiO_2(001) surfaces. The analysis of the bonding modes and the results regarding the strength of the interaction reveal that TFAA adsorbs molecularly on the TiO_2(101) surface, the structure of the adsorbed molecule largely resembles that of the gas phase species and the small calculated value of the adsorption energy points towards a weak interaction. The opposite holds for the interaction of the TFAA molecule with the TiO_2(001) surface, the molecule dissociates into trifluoroacetate and a proton, the trifluoroacetate moiety strongly binds to the surface in a bridging configuration and the proton binds to a nearby surface oxygen atom that is considerably displaced towards the vacuum. The bonding mode is in agreement with suggestions from experiments regarding the TFAA mediated solvothermal synthesis of TiO_2 nanoparticles although these were unable to distinguish between the two surfaces. The present results fully justify the fact that TFAA stabilizes the more reactive TiO_2(001) surfaces. This comes simply from the much larger adsorption energy of TFAA on TiO_2(001). Therefore, once a small surface area is available for adsorption, TFAA will strongly adsorb thus hindering the growth of the most thermodynamically favored TiO_2(101). For the case of TFAA on the TiO_2(001) surface, analysis of the F(1s) core level binding energy confirms the experimental assignment of the low energy peak to F adsorbed at the surface as F^- and of the high energy peak to the F atoms in the $-CF_3$ group. Overall, the present paper contributes to understand the role of TFAA in directing the growth of TiO_2 particles with abundant (001) facets.

Acknowledgements

This work has been supported by the Spanish MINECO grant CTQ2012-30751 and, in part, by *Generalitat de Catalunya* grants 2014SGR97 and XRQTC. O.L.G is grateful to the *Universitat de Barcelona* for a predoctoral grant. Computational time at the MARENOSTRUM supercomputer has been provided by the Barcelona Supercomputing Centre through grants from *Red Española de Supercomputación* and the DSUNCAT project of the Partnership for Advanced Computing in Europe (PRACE).

References

1 M. R. Bahnemann, S. T. Hoffmann, W. Y. Martin and D. W. Choi, *Chem. Rev.*, 1995, **95**, 69.
2 X. Chen and S. S. Mao, *Chem. Rev.*, 2007, **107**, 2891.
3 X. Chen, S. Shen, L. Guo and S. S. Mao, *Chem. Rev.*, 2010, **110**, 6503.
4 M. Ni, M. K. H. Leung, D. Y. C. Leung and K. Sumathy, *Renewable Sustainable Energy Rev.*, 2007, **11**, 401.
5 Y. Paz, Z. Luo, L. Rabenberg and A. Heller, *J. Mater. Res.*, 1995, **10**, 2842.
6 K. P. Kuhn, I. F. Chaberny, K. Massholder, M. Stickler, V. W. Benz, H. G. Sonntag and L. Erdinger, *Chemosphere*, 2003, **53**, 71.
7 H. Chen, C. E. Nanayakkara and V. H. Grassian, *Chem. Rev.*, 2012, **112**, 5919.
8 A. Fujishima, X. Zhang and D. A. Tryk, *Surf. Sci. Rep.*, 2008, **63**, 515.
9 K. Hashimoto, H. Irie and A. Fujishima, *Jpn. J. Appl. Phys.*, 2005, **44**, 8269.
10 B. Ohtani, O. O. Prieto-Mahaney, D. Li and R. Abe, *J. Photochem. Photobiol., A*, 2010, **216**, 179.
11 C. di Valentin and G. Pacchioni, *Catal. Today*, 2013, **206**, 12.

12 L. Li, J. Yan, T. Wang, Z. Zhao, J. Zhang, J. Gong and N. Guan, *Nat. Commun.*, 2015, **6**, 5881.
13 R. Asahi, T. Morikawa, T. Ohwaki, K. Aoki and Y. Taga, *Science*, 2001, **293**, 269.
14 C. di Valentin and G. Pacchioni, *Acc. Chem. Res.*, 2014, 3233–3241.
15 R. Asahi, T. Morikawa, H. Irie and T. Ohwaki, *Chem. Rev.*, 2014, **114**, 9824.
16 B. Ohtani, *Phys. Chem. Chem. Phys.*, 2014, **16**, 1788.
17 H. G. Yang, C. H. Sun, S. Z. Qiao, J. Zou, G. Liu, S. C. Smith, H. M. Cheng and G. Q Lu, *Nature*, 2008, **453**, 638.
18 F. Amano, T. Yasumoto, O. O. Prieto-Mahaney, S. Uchida, T. Shibayama and B. Ohtani, *Chem. Commun.*, 2009, 2311.
19 F. Amano, T. Yasumoto, O. O. Prieto-Mahaney, S. Uchida, T. Shibayama, Y. Terada and B. Ohtani, *Top. Catal.*, 2010, **53**, 455.
20 G. Liu, H. G. Yang, J. Pan, Y. Q. Yang, G. Q. (Max) Lu and H. M. Cheng, *Chem. Rev.*, 2014, **114**, 9559.
21 J. Zhang, L. Qian, L. Yang, X. Tao, K. Su, H. Wang, J. Xi and Z. Ji, *Appl. Surf. Sci.*, 2014, **311**, 521.
22 O. Lamiel-Garcia, S. Tosoni and F. Illas, *J. Phys. Chem. C*, 2014, **118**, 13667.
23 D. G. Calatayud, T. Jardiel, M. Peiteado, C. Fernández Rodríguez, M. R. Espino Estévez, J. M. Doña Rodríguez, F. J. Palomares, F. Rubio, D. Fernández-Hevia and A. C. Caballero, *J. Mater. Chem. A*, 2013, **1**, 14358.
24 D. G. Calatayud, T. Jardiel, M. Rodríguez, M. Peiteado, D. Fernández-Hevia and A. C. Caballero, *Ceram. Int.*, 2013, **39**, 1195.
25 P. E. Blöchl, *Phys. Rev. B: Condens. Matter Mater. Phys.*, 1994, **50**, 17953.
26 G. Kresse and J. Joubert, *Phys. Rev. B: Condens. Matter Mater. Phys.*, 1999, **59**, 1758.
27 H. I. Monkhorst and J. D. Pack, *Phys. Rev. B: Solid State*, 1976, **13**, 5188.
28 J. P. Perdew, J. A. Chevary, S. H. Vosko, K. A. Jackson, M. R. Pederson, D. J. Singh and C. Fiolhais, *Phys. Rev. B: Condens. Matter Mater. Phys.*, 1992, **46**, 6671.
29 J. P. Perdew, K. Burke and M. Ernzerhof, *Phys. Rev. Lett.*, 1996, **77**, 3865.
30 C. Sousa, S. Tosoni and F. Illas, *Chem. Rev.*, 2013, **113**, 4456.
31 H. Y. Lee, S. J. Clark and J. Robertson, *Phys. Rev. B: Condens. Matter Mater. Phys.*, 2012, **86**, 075209.
32 C. di Valentin and G. Pacchioni, *Catal. Today*, 2013, **206**, 12.
33 I. de P. R. Moreira, F. Illas and R. L. Martin, *Phys. Rev. B: Condens. Matter Mater. Phys.*, 2002, **65**, 155102.
34 G. Pacchioni, *J. Chem. Phys.*, 2008, **128**, 182505.
35 E. Finazzi, C. di Valentin, G. Pacchioni and A. Selloni, *J. Chem. Phys.*, 2008, **129**, 154113.
36 A. Janotti, J. B. Varley, P. Rinke, N. Umezawa, G. Kresse and C. G. Van de Walle, *Phys. Rev. B: Condens. Matter Mater. Phys.*, 2010, **81**, 085212.
37 G. Kresse and J. Hafner, *Phys. Rev. B: Condens. Matter Mater. Phys.*, 1993, **47**, 558.
38 G. Kresse and J. Furthmuller, *Comput. Mater. Sci.*, 1996, **6**, 15.
39 G. Kresse and J. Furthmuller, *Phys. Rev. B: Condens. Matter Mater. Phys.*, 1996, **54**, 11169.
40 J. K. Burdett, T. Hughbanks, G. J. Miller Jr., J. W. Richardson and J. V. Smith, *J. Am. Chem. Soc.*, 1987, **109**, 3639.
41 Y. Ortega, O. Lamiel-Garcia, D. Fernandez Hevia, S. Tosoni, J. Oviedo, M. A. San-Miguel and F. Illas, *Surf. Sci.*, 2013, **618**, 154.
42 Y. Liang, S. Gan, S. A. Chambers and E. I. Altman, *Phys. Rev. B: Condens. Matter Mater. Phys.*, 2001, **63**, 235402.
43 Y. Wang, H. Sun, S. Tan, H. Feng, Z. Cheng, J. Zhao, A. Zhao, B. Wang, Y. Luo, J. Yang and J. G. Hou, *Nat. Commun.*, 2013, **4**, 2214.
44 F. Ito, *Chem. Phys.*, 2011, **382**, 52–57.
45 F. Ito, *Comput. Theor. Chem.*, 2013, **1016**, 48.
46 P. Krishnakumar and D. K. Maity, *J. Phys. Chem. A*, 2014, **118**, 5443.
47 W. Kun Li, X. Qing Gong, G. Lu and A. Selloni, *J. Phys. Chem. C*, 2008, **112**, 6594.
48 K. L. Miller, J. L. Falconer and J. W. Medlin, *J. Catal.*, 2011, **278**, 321.
49 C. di Valentin and D. Fittipaldi, *J. Phys. Chem. Lett.*, 2013, **4**, 1901.
50 N. Pueyo Bellafont, F. Illas and P. S. Bagus, *Phys. Chem. Chem. Phys.*, 2015, **17**, 4015.
51 N. Pueyo Bellafont, P. S. Bagus and F. Illas, *J. Chem. Phys.*, 2015, **142**, 214102.
52 L. Köhler and G. Kresse, *Phys. Rev. B: Condens. Matter Mater. Phys.*, 2004, **70**, 165405.
53 M. Happel, N. Luckas, F. Viñes, M. Sobota, M. Laurin, A. Görling and J. Libuda, *J. Phys. Chem. C*, 2011, **115**, 479.
54 *Handbook of Chemistry and Physics*, ed. D. R. Lide, CRC, Boca Raton, 84th edn, 2003, pp. 9–40.
55 M. Namazian, M. Zakery, M. R. Noorbala and M. L. Coote, *Chem. Phys. Lett.*, 2008, **451**, 163.
56 J. P. Prates Ramalho and F. Illas, *Chem. Phys. Lett.*, 2012, **545**, 60.
57 J. P. Prates Ramalho, J. R. B. Gomes and F. Illas, *RSC Adv.*, 2013, **3**, 13085.
58 P. S. Bagus, F. Illas, G. Pacchioni and F. Parmigiani, *J. Electron Spectrosc. Relat. Phenom.*, 1999, **100**, 215.
59 P. S. Bagus, E. S. Ilton and C. J. Nelin, *Surf. Sci. Rep.*, 2013, **68**, 273.
60 A. A. Bakke, H. W. Chen and W. L. Jolly, *J. Electron Spectrosc. Relat. Phenom.*, 1980, **20**, 333.

Overview:

From these works we can extract several conclusions. Firstly the diffusion of fluorine along each direction of the TiO_2 structures exhibits particular features with different energy barriers. This behavior is determined by the size of the channels between the TiO_2 octahedral units in each crystal and on the capability of the structure to relax. In the case of the [001] direction of the anatase polymorph the diffusion process is thermodynamically barrierless and thermodynamically favorable. On the other hand the diffusion of F atoms through the brookite channels proved to be unfavorable both thermodynamically and kinetically. For rutile two options can be found. Through the [110] direction, the F diffusion presents a very small barrier, but on the other hand the stability of the doped system is much higher than the separated systems. This indicates to that although fluorine could go through the channels in the [110] direction, it probably will not enter in the rutile structure. To these conclusions we must add the fact that the size of the channel is not a clear indicator of the viability of the F-diffusion and that the flexibility of the crystal of the TiO_2 polymorph is much more determining. It is also interesting to point out that the process to incorporate the fluorine requires one order of magnitude less energy than that needed to overcome the diffusion barrier which indicates that the incorporation seems not to be the determining step of the process.

Moving now to the conclusions obtained from the study of the fluorine adsorption on the (101) and (001) surfaces we highlight that for both surfaces the adsorption process of F is exothermic and leads to an oxidation of the substrate. The analysis of the spin density reveals that, in all cases, there is a charge transfer to the F atoms from the nearby O atoms. This results in the appearance of new features in the density of states which are located in the band gap of the surface. This effect can may contribute to the higher activity of the nanoparticles synthesized in presence of fluorine due to the reduction of the band gap, and the resulting shifting the wavelength of light absorbed by the material. In terms of energetic stability the fluorine-titania interaction is stronger for the most reactive (001) surface, as it was expected. However, the difference between the fluorine interaction strength with both surfaces is not enough to explain the different ratios of both type of surfaces when fluorine is present. By applying the *ab initio* thermodynamic formalism we observed that as expected the (101) clean surface presents a higher stability than the (001) surface. But this stability order turns around

when a certain fluorine coverage is reached. From this point until full coverage the stability of the (001) surface increases and meanwhile decreases for the (101) surface, confirming the experimental results that motivated the study.

Following the same line, the study of the adsorption of TFAA on the two different TiO_2 surfaces highlighted that the TFAA is adsorbed on the (101) surface with almost no distortion from the equilibrium gas phase geometry and presents a very low adsorption energy. However, the interaction of TFAA with the (001) surface is much stronger and dissociative. This lead to the TFAA molecule being strongly adsorbed to the surface by a bridge configuration plus a proton that is captured by one of the nearest oxygen atoms that is pulled away from the surface. These results can explain the strong stabilization of the (001) surface that can be achieved by using of TFAA in the synthesis. This is explained by the big difference between the adsorption energy observed for both surfaces. Therefore, when the (001) surface is exposed to TFAA during the synthesis It is rapidly covered by the TFAA molecules. This inhibits the growth of the nanoparticle in that direction assisting the exposure of a higher area of the (001) surface.

From all these works we can conclude that the interaction of fluorine with TiO_2 systems can be very useful to tune their electronic properties and increase their efficiency. This can be related to the different effects mentioned before: the ease of F atoms to go through the crystalline structure, the charge transfer effect that occur when F is adsorbed on the surface and the subsequent reduction of the material. And last but not least the effect on the growth control; due to the unique capacity of F species to increase the proportion of a more reactive surface during the process of nanoparticles synthesis.

3.1.3 Results for TiO_2 clusters and nanoparticles

All the work previously presented in this thesis has involved *ab initio* periodic calculations and was focused on the description of the geometry stability and electronic properties of TiO_2 bulk or surfaces and their interactions with doping atoms. In all these extended systems the periodic modeling has proved to be solid and reliable. In industry and especially for photocatalysis purposes TiO_2 is mainly used in form of nanoparticles with properties not always directly relatable to the ones shown by the extended periodic systems. This fact is due to the small size of the nanoclusters and nanoparticles that introduce new surface defects and enhance quantum confinement effects.

Nanostructuring can also lead to different morphologies that can potentially increase the photocatalytic activity of the material as have been commented in previous sections. For these reasons the study of the nanometric TiO_2 systems is of great importance therefore the results obtained may be different from the ones obtained for the extended systems and also can more easily be correlated with the experimental results obtained from the industrial TiO_2 powders. This fact motivated several theoretical studies carried out during the latter years of the thesis for non-periodic systems covering the range from a few atoms (that we will call nanoclusters) to over one thousand atoms (nanoparticles).

In this thesis the results will be exposed and ordered starting from the smaller nanoclusters to the larger nanoparticles. For both cases the methodology used to predict and model the geometries will be introduced below.

The first paper shows the study of the ground states and excited states of small TiO_2nanoclusters and small nanoparticles constructed following the Wulff methodology. As mentioned above this method consists in modeling the nanoparticles by taking into account stability of the different surfaces to create a nanoparticle with the shape that exposes the energetically lowest combination of surfaces. The geometries of the smaller clusters have been obtained by applying global optimization techniques and data mining from structures reported previously in the literature, obtaining in this way a reliable set of ground states candidates. The electronic structure of the ground state and excited states of the above-mentioned structures has been calculated with and without presence of solvent by using DFT and TDDFT methodologies.

The second article presented in this chapter reports on studies concerning the stability of TiO_2 nanoclusters and nanocrystals. One main difference between both is the crystallinity that these structures present. Nanoclusters show low or almost no crystallinity or resemblance with the atomic ordering of the bulk system, meanwhile the nanocrystals show the same ordering as the bulk system. The aim of this work is to find the point where the most stable candidates change to from the nanocluster structures to the nanocrystals, which is important to be able to predict the behavior of this photocatalyst and its properties depending on the size of the particles.

The last paper continues with the study of the TiO_2 nanocrystals and how they energetic and electronic properties evolve with size and shape in order to try to elucidate the size of the nanoparticles where they electronic features become close to the bulk properties.

The full work presented in this chapter encompasses the study of a large set of the different TiO_2 stable structures from a few atoms to more than 1000, paying special attention to the evolution of the energetic and electronic properties with the increasing size of the system and the different morphologies they exhibit.

3.1.3.1 Effect of Size and Structure on the Ground-State and Excited-State Electronic Structure of TiO_2 Nanoparticles.

JCTC Journal of Chemical Theory and Computation — Article
pubs.acs.org/JCTC

Effect of Size and Structure on the Ground-State and Excited-State Electronic Structure of TiO_2 Nanoparticles

Daeheum Cho,[†] Kyoung Chul Ko,[†,‡] Oriol Lamiel-García,[‡] Stefan T. Bromley,[‡,§] Jin Yong Lee,*[,†] and Francesc Illas*[,‡]

[†]Department of Chemistry, Sungkyunkwan University, Suwon 16419, Korea

[‡]Departament de Ciència de Materials i Química Física & Institut de Química Teòrica i Computacional (IQTCUB), Universitat de Barcelona, c/Martí i Franquès 1, 08028 Barcelona, Spain

[§]Institució Catalana de Recerca i Estudis Avançats (ICREA), 08010 Barcelona, Spain

S *Supporting Information*

ABSTRACT: We investigated the influence of size and structure on the electronic structure of TiO_2 nanoparticles 0.5−3.2 nm in diameter, in both vacuum and water, using density functional theory (DFT) calculations. Specifically, we tracked the optical and electronic energy gap of a set of $(TiO_2)_n$ nanoparticles ranging from small non-bulklike clusters with n = 4, 8, and 16, to larger nanoparticles derived from the anatase bulk crystal with n = 35 and 84. As the difference between these two energy gaps (the exciton binding energy) becomes negligible in the bulk, this magnitude provides an indicator of the bulklike character of the electronic structure of the nanoparticles under study. Extrapolating our results to larger sizes, we obtain a rough estimate of the nanoparticle size at which the electronic structure will begin to be effectively bulklike. Our results generally confirmed that the electronic structure of the nanoparticle ground state and excited state has a more pronounced structure dependency than size dependency within a size range of 0.5−1.5 nm. We also showed that the thermodynamic preference for the photocatalytic species is the first S_1 exciton. This S_1 exciton is stable under vacuum but may evolve to free charge carriers upon structural relaxation in an aqueous environment for particles 0.5−1.5 nm in size studied in the present article. An analysis of ionization potentials and electron affinities, relative to the standard reduction potential for the water splitting half-reactions, revealed the importance of considering the structural relaxation in the excited states and the presence of water for assessing the thermodynamic conditions for photocatalytic water splitting.

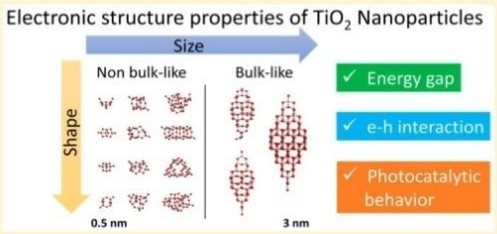

1. INTRODUCTION

Titanium dioxide (TiO_2), also referenced as titania, is widely studied by theory[1] and experiment,[2,3] both with respect to its fundamental properties[2,3] and from a more applied perspective.[4] The latter interest in this material originates from the broad range of industrial applications ranging through solar cells,[5,6] environmental cleanup,[7,8] and photocatalysis.[9−12] The applications of TiO_2 in photocatalysis constitute a particularly active field of research, because of the possibility of generating H_2 from water splitting under light irradiation.[13,14] Because of the rather large band gap (>3.0 eV)[15] of the most common polymorphs of titania (anatase and rutile), photocatalytic water splitting using these materials requires ultraviolet (UV) radiation. This feature inhibits their practical use under sunlight as only ∼10% of the sunlight incoming photons have enough energy to be absorbed and, hence, participate in the photocatalytic process.

Many different strategies have been used to modify the band gap of TiO_2 in order to increase its viable use with sunlight. Doping by different types of chemical elements, in particular with atomic nitrogen, has attracted much interest[16,17] However, some theoretical studies have shown that reducing the band gap to the visible range by introducing doping-induced defect states does not guarantee better catalytic performance.[18] For instance, heavily fluorine-doped anatase exhibits a clear blue color, which electron paramagnetic resonance (EPR) measurements unambiguously attributes to Ti^{3+} centers.[19] However, despite these improved electronic properties, the photocatalytic activity of F-doped anatase in the visible remains quite modest. This example clearly highlights the difficulties encountered in the search for water splitting photocatalysts with sufficient activity in the visible region.[19]

Nanostructuring has also been used to modify the photocatalytic activity of TiO_2. Of particular relevance to the present study, techniques have been developed for a control of the shape and size of titania nanoparticles in order to optimize them for photoactivity.[20] However, in such experiments, it is

Received: May 20, 2016
Published: July 5, 2016

DOI: 10.1021/acs.jctc.6b00519
J. Chem. Theory Comput. 2016, 12, 3751−3763

difficult to discern between the different effects of size and shape and those introduced by the synthetic conditions. Lu et al.[21] have shown, for example, that F-doping largely stabilizes the (001) reactive facets of anatase, which is a feature that has been explained by *ab initio* thermodynamic arguments based on density functional theory (DFT) calculations.[22] However, as mentioned above,[19] F-doping also introduces Ti^{3+} centers. The intertwined influences of F-doping thus make it difficult to assign any resulting change in reactivity to either the presence of the particular enhanced structural feature or the new chemistry of the resulting nanomaterial.

The difficulties encountered by experiments to separate complex factors are not present when employing theoretical models in which one can represent different morphologies for a given composition or vary the composition for a given morphology. However, modeling the structure of TiO_2 nanoparticles of an experimentally relevant size using first-principles electronic structure methods is still a huge challenge, and even more so, if the goal is to determine excited states and their properties. To overcome this difficulty, a large amount of work has used extended models for TiO_2 bulk polymorphs[18,23−30] and several surfaces,[31−33] where the computational cost is significantly reduced by imposing periodic boundary conditions. The use of these models has provided a large amount of useful information but effects arising from the finite size and shape of the TiO_2 nanoparticles are largely missing. To help close the gap between such periodic models and small nanocluster models, Barnard et al.[34] developed a self-consistent tight-binding (SCTB) model that was found to be able to mimic the results obtained from DFT calculations of a moderately sized $(TiO_2)_{35}$ nanoparticle. This approach was then subsequently employed to investigate the stability and atomic structure of $(TiO_2)_n$ particles with n having a value up to 455 (i.e., 1365 atoms), with different realistic bulk-cut morphologies. Nevertheless, a more accurate description of the electronic structure properties of these large nanoparticles has yet to be attempted. Auvinen et al.[35] carried out DFT and time-dependent density functional theory (TD-DFT) calculations for $(TiO_2)_n$ particles with selected sizes in the range of n = 8−38. They showed that the electronic structure of the studied TiO_2 nanoparticles is strongly dependent on the atomic structure and also that constraining small nanoparticles to possess a bulklike atomic structure is very likely to yield metastable structures, with respect to the most stable structural ground states, which are typically non-bulklike. In other reported studies that specifically searched for low-energy $(TiO_2)_n$ clusters, those with sizes up to n = 16 are indeed found to not display the anatase crystal structure.[36−39] Instead, small to moderately large $(TiO_2)_n$ nanoclusters typically exhibit a significant number of non-bulklike energetically low-lying isomers. Since this implies that experimental measurements may provide information over an ensemble of particles rather than on the most stable structural ground state, it is necessary to investigate the properties of different isomers of TiO_2 nanoparticles. This is analogous to the bulk case of TiO_2 polymorph engineering, where similarly energetically stable yet distinct crystal structures lead to different modifications of band edges and, hence, band gaps due to varying local coordination.[40] The ground state and excited electronic structure of specific low-energy $(TiO_2)_n$ non-bulklike clusters in the size range of n = 1−15 have been studied in detail,[41,42] but information regarding larger particles is almost nonexistent. Therefore, the objective of the present work is to provide a bridge between these two ranges through a unified consistent theoretical examination of how the ground state and excited electronic structure evolves from non-bulklike clusters to bulk-structured nanoparticles considering several different isomers of the smaller clusters.

Using DFT and TD-DFT methods, we have explored the electronic structure properties of the ground and excited states of $(TiO_2)_n$ with n = 4, 8, 16, 35, and 84 resulting in nanoparticles containing up to 252 atoms and reaching ∼3 nm in diameter. We show that, while energetic stability has a tendency to increase monotonically with size, the corresponding electronic structure can vary significantly, depending on the structure and shape of the nanoparticle. To investigate the size-dependent change in electronic structure, we focus on the optical and electronic energy gaps. In particular, we use the difference between these two energy gaps (i.e., the exciton binding energy) as a measure of how bulklike a cluster of a certain size is, with respect to its electronic structure. For the range of nanoparticles studied, we will also show that, under vacuum, the exciton state is always more stable than free charge carriers and that this holds for both vertical and adiabatic time scales, whereas solvation may reverse this order. Finally, we present a thermodynamic analysis, with respect to the necessary, but not sufficient, conditions for spontaneous water splitting triggered by photoexcited TiO_2 nanoparticles under vacuum and in water.

2. ELECTRONIC STRUCTURE PROPERTIES

The band gap of TiO_2 materials is one of the key properties enabling their technological applications either in photocatalysis or in solar cells. Hence, it is important to recall that there are two well-defined ways to determine the band gap of a material; these are often referenced as the electronic (or fundamental) gap and the optical band gap, respectively.[43] The electronic (or fundamental) band gap is measured by (direct and inverse) photoemission experiments and therefore involves charged states either of cationic (free extra hole, h^+) or anionic (free extra electron, e^-) character. On the other hand, the optical band gap is obtained by photoexcitation process that generates an excited electron−hole (e^-−h^+) pair (a so-called "exciton pair"). In the case of relatively small finite systems, the optical band gap is lower than the electronic band gap, because of the electrostatic stabilization of the electron−hole pair interaction in the exciton state. However, for large systems including bulk or extended surfaces, the difference between electronic and optical gaps typically becomes negligible, since the addition/removal of one electron to/from fully delocalized states in the infinite solid will not significantly affect its electronic structure. A difference can be found when, because of the specific electronic structure features, the excess electron and/or hole involve localized states, forming a well-defined exciton. In fact, small exciton-like excitations have been found in rutile and anatase but the corresponding excitation energies are of the order of a few meV.[44−46]

Since the concept of a band for a finite system is ill-defined, we will hereafter use the term "energy gap" for TiO_2 nanoparticles, which corresponds to the "band gap" for surface or bulk. We denote the electronic energy gap as "E_{gap}" and the optical energy gap as "O_{gap}" in order to distinguish the two different types of energy gaps. A rough estimate of the E_{gap} can often be obtained from the difference between the orbital (Hartree−Fock or Kohn−Sham) energy of the highest occupied molecular orbital (HOMO) and that of the lowest

DOI: 10.1021/acs.jctc.6b00519
J. Chem. Theory Comput. 2016, 12, 3751−3763

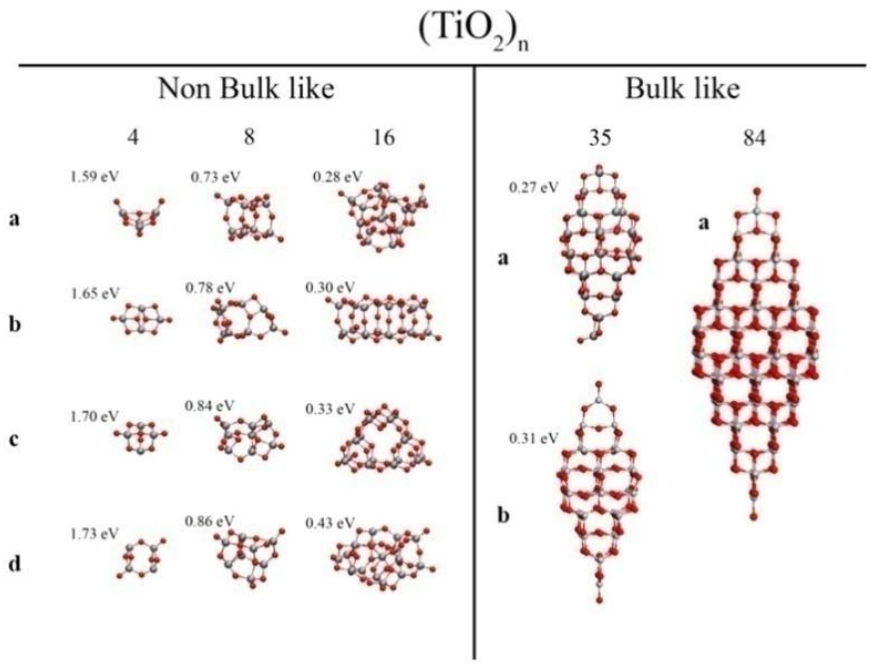

Figure 1. Optimized structures of the four isomers of $(TiO_2)_4$, $(TiO_2)_8$, and $(TiO_2)_{16}$ studied (left) and the bulk-cut structures for $(TiO_2)_{35}$ and $(TiO_2)_{84}$ (right). Relative total energies per TiO_2 unit are given relative to that of the $(TiO_2)_{84}$ nanoparticle.

unoccupied molecular orbital (LUMO); hereafter, this quantity will be denoted as $\Delta E_{H\text{-}L} = E(\text{LUMO}) - E(\text{HOMO})$. These values show a strong dependence on the choice of the exchange-correlation functional, because they are solely dependent on the ground-state one-electron Kohn−Sham eigenvalues. A more reliable method to estimate E_{gap} consists of using the energy difference between the vertical ionization potential (IP_v) and electron affinity (EA_v) (see eqs 2, 4, and 5 presented later in this paper).

The O_{gap} is obtained from the S_0 ground to S_1 excited state $(S_0 \rightarrow S_1)_v$ vertical excitation which involves the creation of an exciton in the S_1 state (see eq 3). We note that, in some cases, the lowest triplet T_1 state is used instead of S_1 to define the optical gap. In the present work, we will focus mainly on the $(S_0 \rightarrow S_1)_v$ electronic transition (similar results are found for the $(S_0 \rightarrow T_1)_v$ excitation, as shown in the Supporting Information (Tables S1 and S2).

Another important quantity is the so-called exciton binding energy (ΔE_{ex}), which is defined as

$$\Delta E_{ex} = E_{gap} - O_{gap} \tag{1}$$

,This term provides an estimate of e^-−h^+ pair interaction energy in the S_1 exciton state, compared to free charged particles. In the following, we will use the notation introduced earlier by Guiglion et al.,[47] which has also been employed in subsequent works by some of these authors.[48,49] Thus, for a particle P, we will use $E(P)$ to denote the energy of the ground state S_0 at the optimized geometry and $E(P^*)$, $E(P^+)$, and $E(P^-)$ to denote the energies of the S_1, cationic, and anionic states at the S_0 optimized geometry, respectively. One then has

$$E_{gap} = IP_v - EA_v \tag{2}$$

$$O_{gap} = (S_0 \rightarrow S_1)_v = E(P^*)_v - E(P) \tag{3}$$

$$IP_v = E(P^+)_v - E(P), \quad IP_{ad} = E(P^+)_{ad} - E(P) \tag{4}$$

$$EA_v = E(P) - E(P^-)_v, \quad EA_{ad} = E(P) - E(P^-)_{ad} \tag{5}$$

,where the subscripts "v" and "ad" hereafter denote vertical (using S_0 geometry only) and adiabatic (using the relaxed geometry of each species at each electronic state) quantities, respectively. Accordingly, one can define vertical and adiabatic exciton binding energy values, which takes the form

$$\Delta E_{ex,v} = [E(P^+)_v + E(P^-)_v] - [E(P^*)_v + E(P)] \tag{6}$$

$$\Delta E_{ex,ad} = [E(P^+)_{ad} + E(P^-)_{ad}] - [E(P^*)_{ad} + E(P)] \tag{6'}$$

which formally corresponds to the energy change associated with the hypothetical process:

$$P + P^* \rightarrow P^- + P^+ \tag{7}$$

Therefore, $\Delta E_{ex,v}$ and $\Delta E_{ex,ad}$ provide a measure of the stability of the exciton relative to free charge carriers in vertical and adiabatic time scales, respectively. With the definitions given in eqs 6 and 6′, a positive value of ΔE_{ex} indicates that the exciton is more stable than free charge carriers.

3. SELECTED TiO_2 NANOPARTICLES AND COMPUTATIONAL DETAILS

The primary goal of the present manuscript is to reveal how the ground-state and excited-state electronic structure and derived properties vary with the size and the shape of TiO_2 nanoparticles. We also studied the photocatalytic requirements in a thermodynamic sense and estimated the excited-state lifetimes of these nanoparticles. A set of $(TiO_2)_n$ nanoparticles

DOI: 10.1021/acs.jctc.6b00519
J. Chem. Theory Comput. 2016, 12, 3751−3763

with n = 4, 8, 16, 35, and 84 was selected, encompassing systems containing up to 252 atoms (~3 nm in diameter). For the selection of the smaller particles, we have been inspired in the recent works of Zwijnenburg and co-workers,[42,47,48] whereas, for the larger TiO_2 nanoparticles, we rely on the previous work of Barnard et al.[34]

Regarding the selection of the small nanoparticles, we know from previous work that the excitation (or photoemission) energy of $(TiO_2)_n$ with n = 2, 5, 10 calculated by the B3LYP functional shows serious deviation from values obtained with the CAM-B3LYP functional.[38,42,48] Hence, we selected non-bulklike $(TiO_2)_n$ clusters with n = 4, 8, 16, where CAM-B3LYP and B3LYP yielded qualitatively similar results; we also added structures of several lowest isomers that are well-studied. The particles with n = 4, 8, and 16 thus chosen have structures with little resemblance to bulk anatase and thus correspond to the so-called "nonscalable" (i.e., not having properties that can be simply scaled from bulk values) regime (see Figure 1, left). In contrast, the larger particles with n = 35 and 84 exhibit clear bulklike structure and can be taken as representative examples of particles in the scalable regime (see Figure 1, right). For the particles with n = 4−16, the structural effect of these nanoparticles on the electronic structure was also investigated by choosing four different isomers (isomers a−d in Figure 1) for each selected n value, since exploring all stable isomers for relatively large TiO_2 nanoparticles is effectively intractable. Electronic structures of ground and excited states in the $(TiO_2)_4$ and $(TiO_2)_8$ were studied by many authors and it is known that, for these nanoparticles, DFT and TD-DFT approaches with hybrid functionals work well. On the other hand, it is known that theoretical calculations employing the pure Generalized Gradient Approximation (GGA) to the exchange-correlation potential have difficulties in describing the electronic structure of oxides and other strongly correlated materials.[1,18] Thus, we employed B3LYP[50] and CAM-B3LYP[51] hybrid functionals, which incorporate a certain fraction of Hartree−Fock exchange. The corresponding calculations for ground-state and excited-state electronic structure properties have been carried out using a 6-31G(d) basis sets and the Gaussian09[52] suite of programs.

The initial geometry of the structural ground state (isomer a in Figure 1) and of the three higher-energy isomers (isomers b−d in Figure 1) of the $(TiO_2)_4$ and $(TiO_2)_8$ particles were taken from Marom et al.[38] For the $(TiO_2)_{16}$ particle, the candidate ground state and the rest of the isomers were generated using Monte Carlo basin hopping[53] global optimization, using a mixed interatomic potential-based strategy that was employed in previous work.[37] In order to minimize the variance in energetic stability of our isomers for each size n, we chose low-energy isomers that were within 0.16 eV total energy per unit of the lowest-energy isomer found, calculated at a B3LYP/6-31G(d) level under vacuum. Specifically, isomers were taken within the energy ranges of +0.143, +0.130, and +0.156 eV per TiO_2 unit for sizes n = 4, 8, and 16, respectively.

The structures of bulklike particles $(TiO_2)_{35}$ and $(TiO_2)_{84}$ were selected based on bipyramidal Wulff cuts[54] from the anatase bulk crystal. We found that $(TiO_2)_{35}$ is the smallest Wulff cut nanoparticle that preserves anatase (101) facets after geometrical relaxation. For the $(TiO_2)_{35}$, two slightly different geometries were used: (i) a B3LYP/6-31G(d)/Gaussian09 optimized structure, starting from the anatase bulk-cut structure optimized using SCTB, as reported by Barnard et al.[34] ($(TiO_2)_{35a}$), and (ii) a PBE/tier-1/FHI-aims[55] optimized structure starting from the Wulff cut from experimental anatase bulk exhibiting (101) facets ($(TiO_2)_{35b}$). We note that, apart from the tilting of the apical O atoms, the two $(TiO_2)_{35}$ structures obtained from geometries (i) and (ii) are quite similar to the difference in total energy calculated at the B3LYP/6-31G(d) under vacuum, that being 1.609 eV (0.046 eV per TiO_2 unit). Finally, for the largest $(TiO_2)_{84}$ nanoparticle reaching 3 nm in size, the structure was optimized also using the FHI-aims code at the PBE/tier-1 level from an anatase bulk cut exhibiting (101) facets ($(TiO_2)_{84a}$). In the forthcoming discussion, we will refer to results for the two types of structures following the standard method//structure notation. Consequently, B3LYP/6-31G(d)//B3LYP/6-31G(d) denotes calculations at the B3LYP/6-31G(d) level of theory at the structure optimized with the same method, and B3LYP/6-31G(d)//PBE-tier1 refers to calculations at the B3LYP/6-31G(d) level of theory but using the structures obtained from geometry optimization using the PBE/tier-1 basis set.

For each of the structures, the IP, EA, E_{gap}, O_{gap}, and ΔE_{ex} values were obtained at two different level of theories—B3LYP/6-31G(d) and CAM-B3LYP/6-31G(d)—using the Gaussian09 code for comparison. The CAM-B3LYP functional was chosen because it was designed to provide relatively improved results for excitations regarding charge-transfer character.[51] For the B3LYP, the Tamm−Dancoff approximation (TDA)[56] was used to reduce the instability of excited states in the calculations involving the larger clusters. Nevertheless, test calculations for the small $(TiO_2)_n$ particles (n = 4, 8, 16) indicate that the O_{gap} values obtained at TDA-B3LYP and TD-B3LYP levels differ by <0.005 eV. For the CAM-B3LYP calculations, TDA was not found to be necessary.

In addition, we considered solvation effect of TiO_2 nanoparticles by water (dielectric constant ε = 78.3553) by using the implicit conductor-like polarizable continuum model (CPCM)[57] to estimate the thermodynamic driving force to facilitate water splitting half-reactions, i.e., hydrogen (HER) and oxygen evolution (OER) at pH 7. Several reports in the literature explicitly consider water solvent molecules and hydration/hydroxylation of TiO_2 surfaces.[42,58−60,64] This is because the defect sites of TiO_2 surfaces, such as mono-coordinated O and three-coordinated Ti atoms, are highly prone to be protonated/hydrated to stabilize the system (exothermic process) when immersed in water. It is clear that the approximate nature of the CPCM method cannot account for local (and explicit) water solvation effects and hydration of the possible defect sites, which may be especially important for the small nanoparticles studied in the present work. Nevertheless, we argue that CPCM may qualitatively capture some of the most important features of water solvation, such as dielectric screening of electrostatic interaction, which is critical to describe the e^-−h^+ interaction energy in the exciton state and spatial distributions of molecular orbitals. Indeed, significant and sensible changes in half-reaction potentials of the TiO_2 nanoparticles upon water solvation were found in the present study, which are useful to understand the effect of the solvation, at least in a qualitative way. It is also interesting to note that the ranges of the half-reaction potentials in CPCM water model in the present study well-correspond with those of rutile nanocrystals immersed in explicit water environment with hydrated surfaces.[42] However, we also note that the results obtained by CPCM model artificially affect some properties, such as localization of free electron/hole in the (unhydrated)

DOI: 10.1021/acs.jctc.6b00519
J. Chem. Theory Comput. 2016, 12, 3751−3763

structural defects, such as undercoordinated titanium/oxygen, as shown in Figures S8–S11 in the Supporting Information. This caveat applies to all the CPCM-related results and discussions presented throughout the paper.

4. RESULTS AND DISCUSSION

4.1. TiO_2 Nanoparticle Structure. From Figure 1, it is quite clear that the structure of small nanoparticles containing 4–16 TiO_2 units have many under-coordinated Ti and O atoms and little resemblance to the bulk structure, which is a feature that is well-known for small clusters of metal oxides.[61] In these cases, the size of the particle is not large enough to build a Madelung field, which is an important component defining the stability of the structure of bulk polymorphs. Small $(TiO_2)_n$ (i.e., for n = 4, 8, and 16 in our study) nanoparticles made from symmetric cuts from the bulk anatase polymorphs are expected to be highly metastable, with respect to our correspondingly sized lowest-energy clusters. Taking as an example, the $(TiO_2)_{16}$ nanoparticle derived from the anatase bulk by Persson et al.,[62] the optimized structure maintains a distorted anatase structure; however, at this size, it cannot display well-defined low-index surfaces. The total energy difference between our candidate ground state and this structural isomer is also found to be quite large (4.867 or 0.304 eV per TiO_2 unit) at a B3LYP/6-31G(d) level under vacuum, and clearly outside of our considered stability range. A different situation is encountered for our larger $(TiO_2)_{35}$ nanoparticle, which displays a relatively unperturbed anatase structure, and exhibits clear (101) facets.[34] Clearly, this nanoparticle can be regarded as a true anatase nanocrystal, although at present, we do not have good knowledge of other possible energetically competing isomers in this size range to assess its corresponding energetic stability.

Figure 2 reports the trend in stability for the different particles, taking into account the size, shape and structure as obtained from B3LYP/6-31G(d) calculations under vacuum. We note that similar trends are found for the results in water and for those obtained at the B3LYP/6-31G(d) level either under vacuum or water, as we report in the Supporting Information (Table S3). The plot in Figure 2 shows the expected monotonic decrease of the total energy per unit for the our lowest energy $(TiO_2)_n$ nanoparticles for n = 4, 8, and 16 units, and for the optimized bulk cuts with 35 and 84 units. Ideally, one would need to use the bulk value obtained with the same methods and basis set as a reference. However, since we performed our calculations with a local basis set using a DFT code developed for nonperiodic calculations, this implies several technical problems and we found it convenient to use the value for the largest particle as the reference. Figure 2 shows the steep descent in energetic stability for the smaller particles and the smoother leveling off in stability for the largest ones. The range of energy per TiO_2 unit spanned for the different isomers is indicated by a vertical shaded bar.

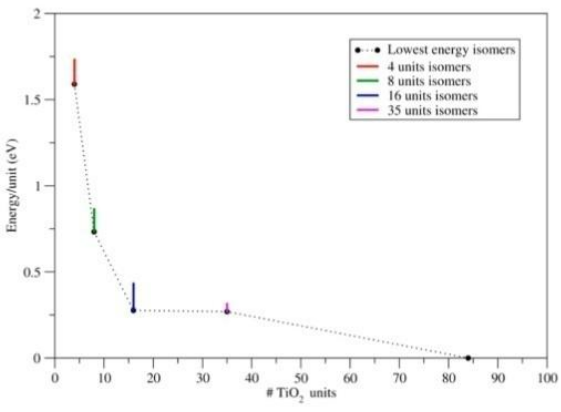

Figure 2. Energy per unit as a function of size for the lowest energy isomers of the $(TiO_2)_n$ particles with n = 4, 8, 16, 35, and 84, as predicted from B3LYP/6-31G(d) calculations. Structures are as described in Figure 1 and the vertical shaded bars for particles with n = 4, 8, and 16 indicate the energy range spanned by the different isomers studied. The total energy per TiO_2 unit of the largest particle is taken to be zero.

4.2. Electronic Structure of TiO_2 Nanoparticles under Vacuum. We first analyze the electronic structure of the small $(TiO_2)_n$ nanoparticles for n = 4, 8, and 16, as a function of shape and size under vacuum and as predicted by the B3LYP/6-31G(d)//B3LYP/6-31G(d) calculations. Qualitatively, both O_{gap} and $\Delta E_{H\text{-}L}$ follow similar trends (see Table S4 in the Supporting Information for $\Delta E_{H\text{-}L}$), with respect to their dependency on structure for each size and changes in size. Moreover, for the lowest-energy structures of the $(TiO_2)_4$ and $(TiO_2)_8$ nanoparticles, the present values for O_g are similar to those reported by Berardo et al.,[42] using also the B3LYP functional. For the $(TiO_2)_{35}$ bulk-cut nanoparticle, the O_{gap} value calculated using B3LYP/6-31G(d) is somewhat dependent on the structure that is chosen; 3.67 eV for the B3LYP/6-31G(d) optimized structure and 3.36 eV for the PBE/tier-1 optimized structure. Hence, the effect of the DFT method used to optimize the structure on the calculated O_{gap} is 0.31 eV, or ~10%. For the largest $(TiO_2)_{84}$ particles, the B3LYP/6-31G(d) value of O_{gap} employing the PBE/tier-1 optimized structure is 3.40 eV.

We note that the O_{gap} values are 0.38–1.16 eV lower than the corresponding $\Delta E_{H\text{-}L}$ ones; this is simply a result of having the LUMO singly occupied in the S_1 excited state and of the concomitant stabilization through the electron–hole pair interaction. Interestingly, the $\Delta E_{H\text{-}L}$ value for $(TiO_2)_{84}$ is 4.02 eV, which is close to the band gap of 3.92 eV computed for bulk anatase by Finazzi et al.,[27] using the B3LYP functional and a periodic model. Nevertheless, this comparison must be considered with caution, since, as shown below, convergence to bulk electronic properties involves rather larger nanoparticle sizes. Figure 3 also reveals that the O_{gap} values of the investigated TiO_2 nanoparticles exhibit a large dependence on the nanoparticle structure and a smaller one on the size. On the other hand, the E_{gap} values decrease significantly with the particle size. This is likely due to the free charge carriers (cationic and anionic nanoparticles) being relatively more stabilized through spatial delocalization of the electron (e^-) or hole (h^+) in the larger nanoparticles. Nevertheless, the dependence of E_{gap} on nanoparticle structure can be significant for the smaller cluster and is found to vary by up to 2.3 eV for both $(TiO_2)_4$ and $(TiO_2)_{16}$. In the case of $(TiO_2)_8$, however, the range of E_{gap} values spanned by the different isomers is much narrower.

At the CAM-B3LYP/6-31G(d) level of theory, the size and structure dependency of O_{gap} and E_{gap} are almost quantitatively identical to that for B3LYP/6-31G(d) discussed above, indicating that these trends are, to some extent, independent of the hybrid DFT method employed. Although the CAM-

DOI: 10.1021/acs.jctc.6b00519
J. Chem. Theory Comput. 2016, 12, 3751–3763

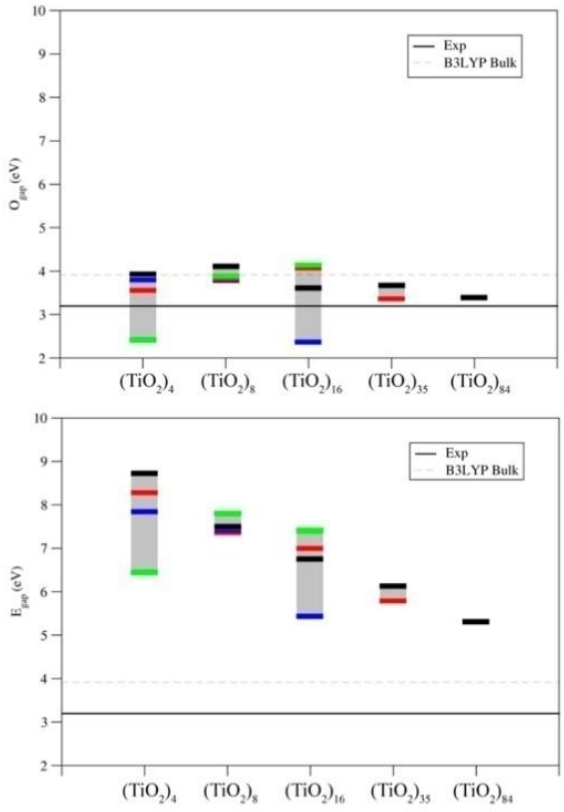

Figure 3. Optical (O_{gap}) energy gap (top panel) and electronic (E_{gap}) energy gap (bottom panel) of $(TiO_2)_4$, $(TiO_2)_8$, and $(TiO_2)_{16}$ cluster isomers (at a B3LYP/6-31G(d) level) and $(TiO_2)_{35}$, $(TiO_2)_{84}$ (at a B3LYP/6-31G(d)//PBE/tier-1 level) bulk-cut nanoparticles under vacuum. Horizontal black and dashed lines indicate the experimental and B3LYP calculated[27] band gaps of bulk anatase. For the $(TiO_2)_4$, $(TiO_2)_8$, and $(TiO_2)_{16}$ particles, the colors black, red, green, and blue correspond to results for isomers a, b, c, and d, respectively. For $(TiO_2)_{35}$, black and red correspond to isomers a and b, respectively.

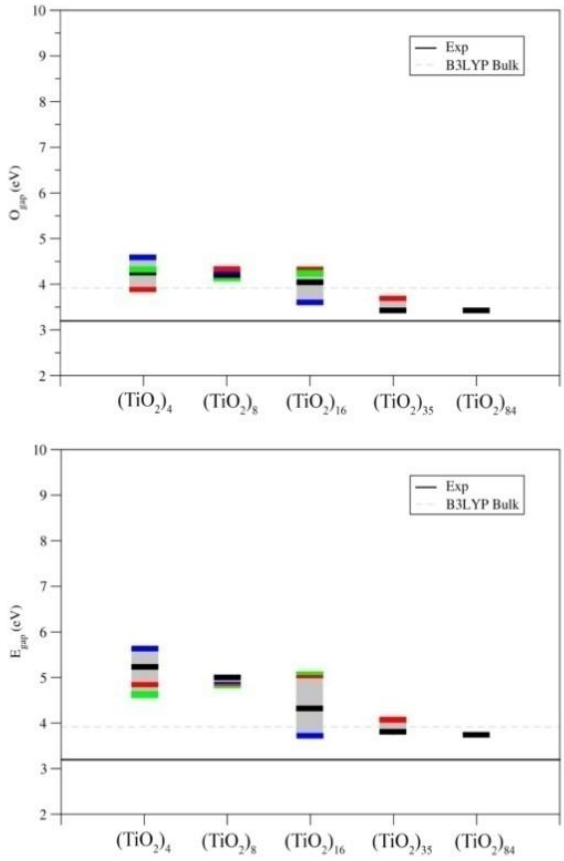

Figure 4. Optical (O_{gap}) energy gap (top panel) and electronic (E_{gap}) energy gap (bottom panel) of $(TiO_2)_4$, $(TiO_2)_8$, and $(TiO_2)_{16}$ cluster isomers (at a B3LYP/6-31G(d) level) and $(TiO_2)_{35}$, $(TiO_2)_{84}$ (at a B3LYP/6-31G(d)//PBE/tier-1 level) bulk-cut nanoparticles in water. Horizontal black and dashed lines indicates the experimental and B3LYP calculated[27] band gaps of bulk anatase. For the $(TiO_2)_4$, $(TiO_2)_8$, and $(TiO_2)_{16}$ particles, the colors black, red, green, and blue correspond to results for isomers a, b, c, and d, respectively. For $(TiO_2)_{35}$, black and red correspond to isomers a and b, respectively.

B3LYP functional only yields slightly larger values of both O_{gap} and E_{gap}, compared to B3LYP, it provides $\Delta E_{H\text{-}L}$ values that are ~3 eV higher than those from B3LYP, which is a drawback of CAM-B3LYP previously reported by several authors.[63] This difference in the $\Delta E_{H\text{-}L}$ values does not seem to represent a problem, since the physically meaningful O_{gap} values predicted by B3LYP and CAM-B3LYP under vacuum are quite similar. Note also that reported CAM-B3LYP calculated values for photoluminesence of TiO_2 nanoparticles correspond well to experimental data.[48,64]

4.3. Electronic Structure of TiO_2 Nanoparticles in Water. The effect of water as a solvent, as included using the CPCM method, leads to a dramatic change in the calculated O_{gap} values (see Figure 4). Notably, a rather large reduction in the O_{gap} dependence on cluster isomer structure, with respect to the nonsolvated calculations (see Figure 3 for comparison), is predicted from the TD-DFT calculations using both B3LYP/6-31G(d) and CAM-B3LYP/6-31G(d) methods. This phenomenon is probably due to the dielectric screening of specific charge localization patterns of extra electron and hole species on each isomer (see Figure S1 in the Supporting Information). In this context, a significant reduction in E_{gap} can also be expected and understood. Overall, the O_{gap} and E_{gap} values in water slightly decrease as the size of the TiO_2 nanoparticle increases.

4.4. Dependence of the Exciton Binding Energy on Nanoparticle Size and Shape. In section 2, we argued that the exciton binding energy (ΔE_{ex}) can be taken as a measure of electron−hole pair interaction in the excited state and of the stability of excitons relative to free charge carriers. Figure 5a shows vertical exciton binding energies $\Delta E_{ex,v}$ for all TiO_2 nanoparticles under vacuum and in water, as predicted from DFT and TD-DFT calculations using the B3LYP and CAM-B3LYP functionals, whereas Figure 5b reports the CAM-B3LYP results for the adiabatic ΔE_{ex} values for the particles containing up to 16 units. For the vertical ΔE_{ex} values, both B3LYP and CAM-B3LYP functionals provide qualitatively and quantitatively similar results, except for a slight deviation in small nanoparticles under vacuum. The adiabatic ΔE_{ex} values in Figure 5b correspond to results obtained with the CAM-B3LYP

DOI: 10.1021/acs.jctc.6b00519
J. Chem. Theory Comput. 2016, 12, 3751−3763

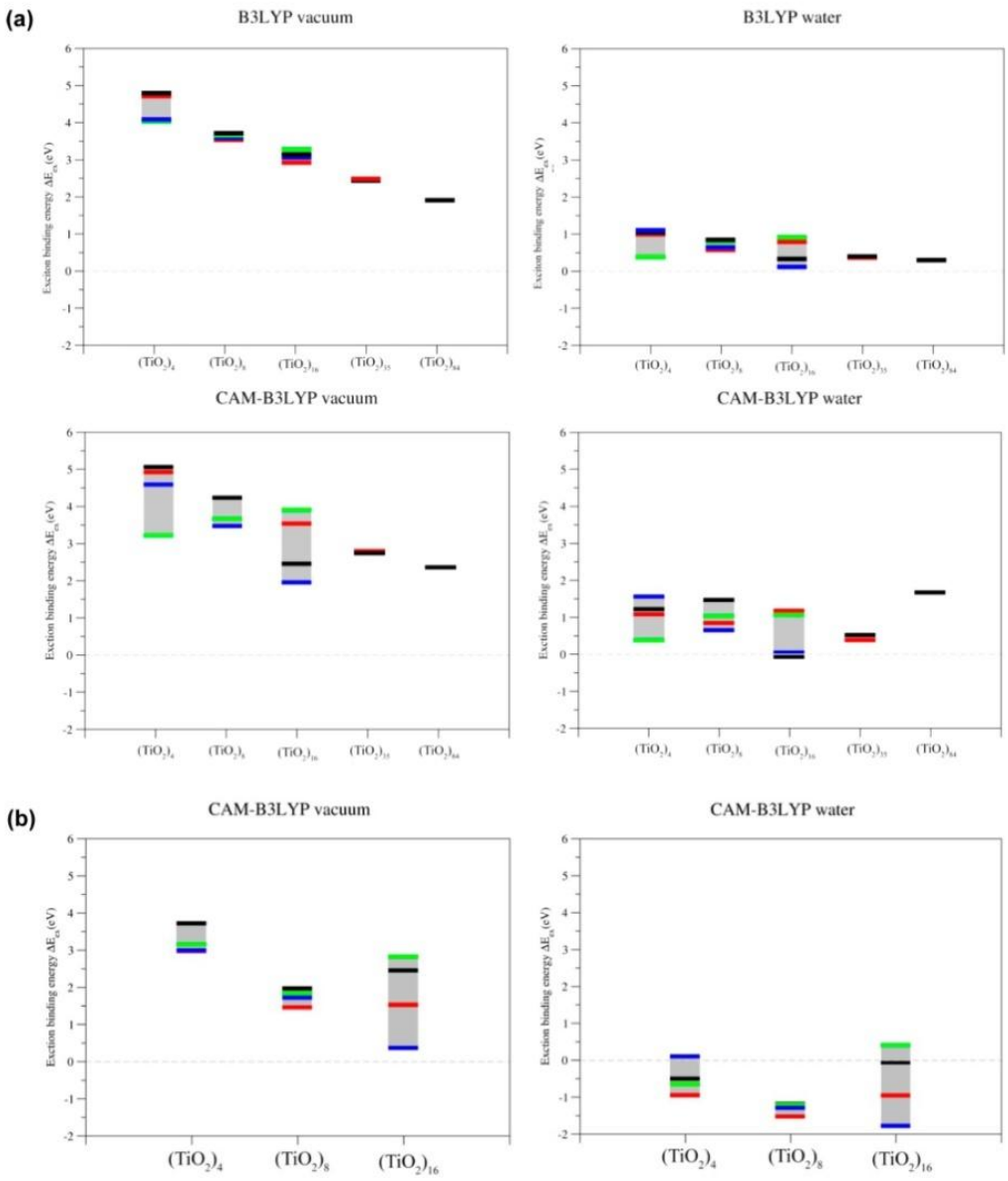

Figure 5. (a) Vertical (ΔE_{ex}) exciton binding energies, with respect to the number of TiO_2 units under vacuum and in water, calculated at the B3LYP/6-31G(d) (top panels) and CAM-B3LYP/6-31G(d) (bottom panels) levels of theory. For the $(TiO_2)_{35}$ and the $(TiO_2)_{84}$ particles, the calculation corresponds to the B3LYP/6-31G(d)//PBE/tier-1 level of theory. (b) Adiabatic (ΔE_{ex}) exciton binding energies, with respect to the number of TiO_2 units under vacuum and in water, calculated at the CAM-B3LYP/6-31G(d) level. For the $(TiO_2)_4$, $(TiO_2)_8$, and $(TiO_2)_{16}$ particles, the colors black, red, green, and blue correspond to the results for isomers a, b, c, and d, respectively. For $(TiO_2)_{35}$, the colors black and red correspond to isomers a and b, respectively.

method, since the B3LYP calculations exhibited a computational instability for geometry relaxation in the excited state with charge transfer character.[42]

4.5. Relative Stability of S_1 Excitons and Free Charge Carriers. A very important feature in Figure 5b is that the exciton binding energy of the TiO_2 nanoparticles in water becomes negative after geometry relaxation. Hence, at the CAM-B3LYP level, one gets a vertical ΔE_{ex}(water) value of >0 eV and an adiabatic E_{ex}(water) value of <0 eV. In other words, the stabilization through structural relaxation in the free charge carrier state is larger than that in the S_1 exciton state. This indicates that, under irradiation, photocatalytic species initially stable as an S_1 exciton pair may evolve to free charge carriers upon structural relaxation in a water environment. Considering that the excited-state lifetime for bulk anatase is ~10 ns,[65−67] one can safely argue that a similar time scale will apply for TiO_2 nanoparticles. This seems to be sufficient to allow for structural relaxation in the excited state, which has important

DOI: 10.1021/acs.jctc.6b00519
J. Chem. Theory Comput. 2016, 12, 3751−3763

consequences. In fact, it would be especially meaningful that free charge carriers may become abundant and do play an important role during the photocatalytic reaction in water; this is a picture that contrasts with the purely thermodynamic point of view favoring the S_1 exciton species.

To further verify that the lifetime of excited states in TiO_2 nanoparticles is long enough to allow for structural relaxation, the excited-state lifetime (τ) has been calculated. This spans a rather wide range (0.05−50 μs) of time scales, depending on the sizes and structures of the TiO_2 nanoparticles studied; details regarding the calculation of lifetimes and the corresponding values are reported in Figures S6 and S7, as well as Tables S12−S17, in the Supporting Information. Hence, structural relaxation in the S_1 exciton state may occur before electronic decay. It is also worth noting that the S_1 lifetime in water is significantly smaller than that under vacuum, because of the dielectric screening of the electron−hole interaction and transition dipole moment from S_0 to S_1. Considering that the calculated lifetime values in the present work are significantly longer than experimental reports for the bulk and surface,[65−67] nonradiative decay would be a much faster process than radiative decay, which is consistent with the report by Zwijnenburg for hydrated rutile nanocluster in water.[64] Yet, the calculated lifetime in the present work is much shorter than the prediction for the hydrated nanocluster (0.2−3 ms),[64] indicating that nonradiative decay would become dominant for these systems.

In contrast, under vacuum, the S_1 exciton state is more stable than the free charge carriers state, regardless of the structural relaxation, both vertical ΔE_{ex}(vacuum) values of >0 (for up to $(TiO_2)_{84}$) and adiabatic ΔE_{ex}(vacuum) values of >0 eV (for up to $(TiO_2)_{16}$) (see Figures 5a and 5b). These different thermodynamic preferences among free charge carrier and S_1 exciton states upon structural relaxation— $S_1 \rightarrow S_1$ under vacuum but $S_1 \rightarrow$ free charge carriers in water—in conjunction with their redox potentials, relative to water splitting half-reactions, has important implications on the determination of the photocatalytic ability of TiO_2 nanoparticles (see section 4.5).

4.6. Size and Shape Dependence of Exciton Binding Energy. Figure 5a shows that vertical ΔE_{ex} sharply decreases as the number of TiO_2 units increases, which is primarily due to the behavior of E_{gap}(vacuum) as shown in Figure 3. This indicates that the electrostatic electron−hole pair interaction energy in a large $(TiO_2)_{84}$ nanoparticle is small which is probably due to the large electron−hole distance and/or to the delocalized character of both electron and hole. The latter effect is evidenced by weak electron−hole densities for larger nanoparticles as shown in Supporting Information (Figures S8−11). The plot of $\Delta E_{ex,v}$(vacuum), as a function of the number of TiO_2 units in Figure 6a, is found to be well-fitted by an inverse power law of the form

$$\Delta E_{ex,v}(\text{vacuum}) = 7.16n^{-0.3} \qquad (R^2 = 0.99) \tag{8}$$

revealing that the initial rapid decline of ΔE_{ex} with the nanoparticle size becomes more gradual for larger nanoparticles. For example, the difference in ΔE_{ex}(vacuum) going from $(TiO_2)_4$ to $(TiO_2)_{84}$ (2.87 eV) is much larger than that between $(TiO_2)_{84}$ and $(TiO_2)_{500}$ (estimated as 0.80 eV), indicating a significant quantum confinement effect for particles with sizes below ~100 units (ca. ~3 nm size). This is likely to result from a relatively strong electrostatic electron−hole pair

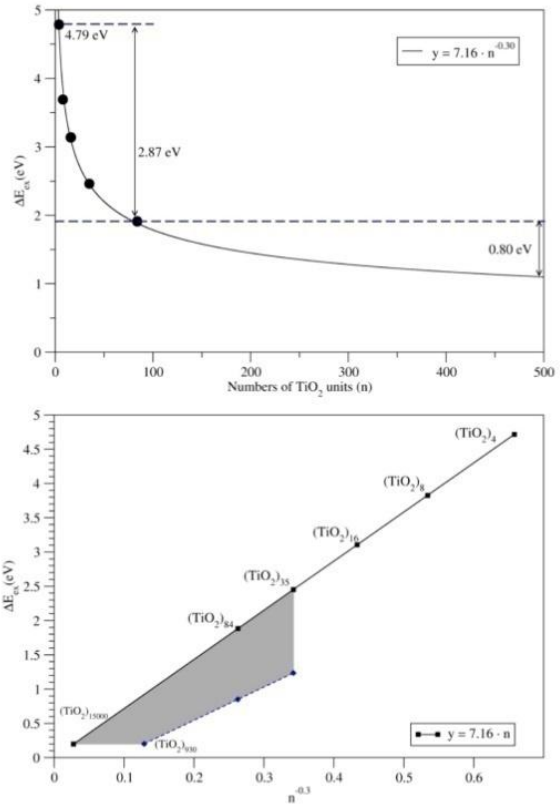

Figure 6. Variation of the vertical exciton binding energy $\Delta E_{ex,v}$(vacuum) with particle size from calculations at the B3LYP/6-31G(d) level. Top panel: $\Delta E_{ex,v}$ against size in number of TiO_2 units (n) with fit to the five data points; bottom panel: $\Delta E_{ex,v}$ against $n^{-0.3}$ with extrapolation to size for which $\Delta E_{ex,v}$(vacuum) = 0.2 eV. The blue dashed line in the bottom panel corresponds to B3LYP values scaled down by 20% to correct for the known overestimation of the optical gap (see text).

interaction in small nanoparticles. Assuming that the extrapolation of ΔE_{ex}(vacuum) holds for larger particles, one can estimate the point at which the electrostatic electron−hole pair interaction in an S_1 exciton becomes similar to that of free charge carriers. At this point, ΔE_{ex}(vacuum) ≈ 0 and one can safely argue that the electronic structure of the nanoparticle becomes practically bulklike. Taking a typical experimental error to be ~0.1 eV, when the difference in measured energy gaps is ≲0.2 eV, the optical and fundamental gaps are assumed to be effectively indistinguishable in magnitude and (both) bulklike. Therefore, we consider the size at which the exciton binding energy is 0.2 eV to be indicative of the smallest size at which a TiO_2 nanoparticle exhibits a bulklike electronic structure. Using eq 8 and plotting the exciton binding energy against $n^{-0.3}$, we can extrapolate from our data to give an estimate of this bulk onset size to be ~15 000 units (~20 nm apical diameter in an anatase bipyramidal nanoparticle); see Figure 6b. This is rather large and is actually at a size when anatase nanoparticles are predicted to become metastable to rutile nanoparticles, implying that only relatively large metastable anatase nanoparticles would display a saturated bulklike electronic structure.[68] We note, however, that this

DOI: 10.1021/acs.jctc.6b00519
J. Chem. Theory Comput. 2016, 12, 3751−3763

estimate is dependent on the functional employed. This is especially true with respect to the optical gap magnitude, which is particularly sensitive to the degree of nonlocal Fock exchange introduced in the functional.[69] In our case, the B3LYP functional is known to overestimate the band gap of bulk anatase by 23%.[27] Assuming a similar overestimate of the optical gap in our TD-DFT B3LYP calculations for our large bulklike nanoparticles, we can make an approximate correction to the extrapolated nanoparticle size at which the electronic structure becomes bulklike. In Figure 6b, we show that the corrected extrapolated size becomes $(TiO_2)_{930}$ (~6.5 nm apical diameter in an anatase bipyramidal nanoparticle). Although this value clearly relies on some assumptions, we present it at a reasonable estimation of the lower size limit at which anatase nanoparticles start to become bulklike, with respect to their electronic structure.

4.7. Relevance to Photocatalytic Water Splitting. It is interesting to relate the presence of free charge carriers and S_1 exciton states as possible driving forces for the photocatalytic water splitting reaction, at least from a thermodynamic point of view. Recently, many theoretical attempts have been made to evaluate the photocatalytic capability of semiconducting materials. Such calculations have focused on properties such as the band edge (valence band maximum and conduction band minimum) for bulk and surfaces,[40,75,76] or the IP and EA of nanoparticles and clusters.[70,71] Comparing these quantities with standard reduction potentials of water splitting half-reactions, one can obtain a rough estimate of the necessary thermodynamic conditions for the photocatalytic capability of an anatase catalyst.

The water splitting reaction driven by photoexcited TiO_2 nanoparticles involves the hydrogen evolution reaction (HER) and the oxygen evolution reaction (OER) redox processes; where TiO_2 nanoparticles in free charge carrier and/or S_1 exciton states are the source for electrons and holes, respectively. The corresponding redox reactions for hole/electron generation in TiO_2 nanoparticles from free charge carriers are defined in eqs 4 and 5. Here, we note that IP/EA of anionic/cationic TiO_2 particle were employed to simulate the redox behaviors of free electron/hole in free charge carriers by assuming negligible electron−hole interactions. Here, we define similar quantities for the S_1 exciton.

$$IP_v^* = E(P^+)_v - E(P^*)_v, \quad IP_{ad}^* = E(P^+)_{ad} - E(P^*)_{ad} \tag{9a}$$

$$EA_v^* = E(P^*)_v - E(P^-)_v, \quad EA_{ad}^* = E(P^*)_{ad} - E(P^-)_{ad} \tag{9b}$$

which correspond to the dissociation of bound electron through the electron transfer processes involving the S_1 (P^*) exciton state:

$$P^* \rightarrow P^+ + e^- \tag{10}$$

$$P^* + e^- \rightarrow P^- \tag{11}$$

We also note that $IP^* = IP - (S_0 \rightarrow S_1)$ and $EA^* = EA + (S_0 \rightarrow S_1)$.

Following previous work,[64,72] it is possible to relate the $IP^{(*)}/EA^{(*)}$ values to the experimental value for the potential of the standard hydrogen electrode (SHE) potential (4.44 eV),[73,74] by subtracting 4.44 eV from the calculated $IP^{(*)}/EA^{(*)}$ values for the free carrier and exciton states, respectively. In fact, for the photocatalytic HER and OER to occur, redox potentials of each half-reaction and photocatalytic TiO_2 reduction and oxidation should be in a suitable order. Hence, each pair of IP/EA and (or) IP*/EA* values should be well-separated from the potentials of the half-reactions, one above (i.e., more negative than) the HER and the other below (i.e., more positive than) OER standard reduction potential so that HER and OER half-reactions spontaneously receive e^- and h^+ via redox pair reactions, respectively (see Figure 7). From this

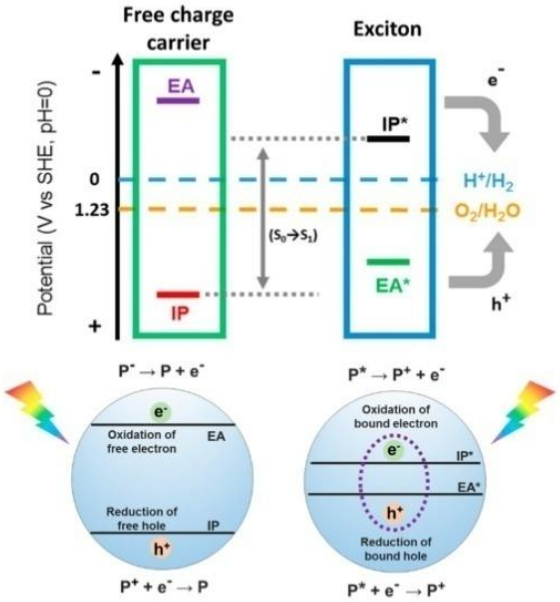

Figure 7. Schematic representation of standard reduction potentials in free charge carrier and S_1 exciton states for photocatalytic water splitting by TiO_2.

comparison, it is then possible to obtain the trends for the photocatalytic capability of free charge carrier and S_1 exciton species toward HER and OER half-reactions at pH 0 and 7 (also see refs 70 and 71 for further details on these concepts). It would be also interesting to investigate the dynamical behaviors of the photocatalytic capabilities of TiO_2 nanoparticles by comparing the standard redox potentials in the vertical and adiabatic time scales, i.e., $IP_v^{(*)}/EA_v^{(*)}$ and $IP_{ad}^{(*)}/EA_{ad}^{(*)}$, respectively. Indeed, dynamical aspects of photoexcited TiO_2 nanoparticles are of great importance, because the excited-state lifetime of TiO_2 nanoparticles and standard chemical reactions are long enough to allow the carrier relaxation in the excited state. The vertical and adiabatic $IP^{(*)}/EA^{(*)}$ potentials of the nanoparticles in water calculated by CAM-B3LYP/6-31G(d) are reported in Figure 8 (a similar trend is predicted when employing B3LYP; see Figures S2−S4 in the Supporting Information and, for full results for the standard reduction potentials calculated by CAM-B3LYP under vacuum and in water, see Tables S8− S11 in the Supporting Information). The absolute values (not relative to SHE potential) of IP_v (9.2−11.0 eV) and EA_v (1.5−3.3 eV) potentials in the TiO_2 nanoparticles under vacuum calculated by the CAM-B3LYP/6-31G(d) level are much higher and lower than the corresponding IP_v (7.82−8.30 eV) and EA_v (4.67−5.10 eV) potentials for periodic TiO_2 anatase,[40,75,76] probably because of the quantum confinement effect in the TiO_2 nanoparticles. Furthermore, direct comparison of the vertical and adiabatic $IP^{(*)}/EA^{(*)}$ potentials of our

DOI: 10.1021/acs.jctc.6b00519
J. Chem. Theory Comput. 2016, 12, 3751−3763

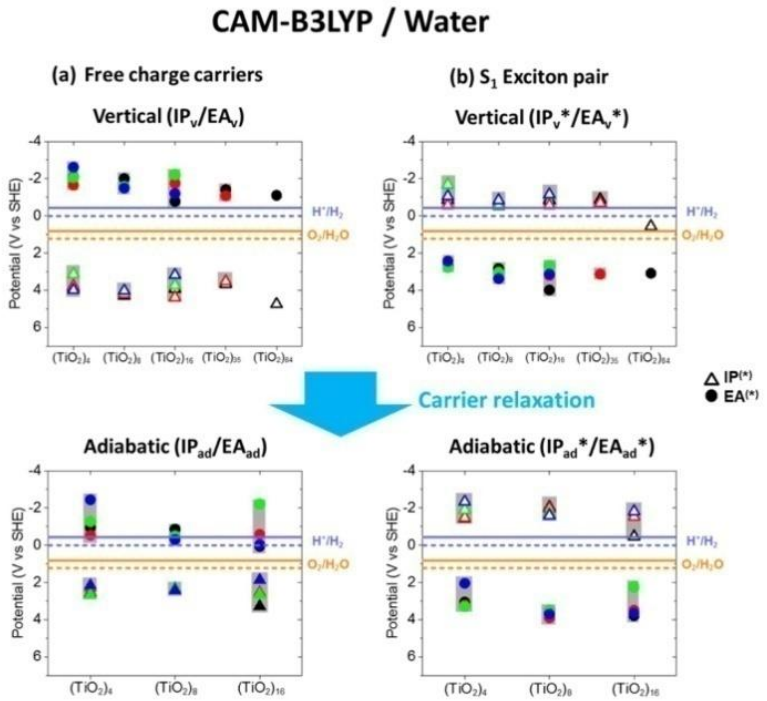

Figure 8. Calculated CAM-B3LYP/6-31G(d) vertical (top panel) and adiabatic (bottom panel) IP (triangles), EA (circles) of the TiO_2 nanoparticle free charge carrier (left) and S_1 exciton states (right) in water, relative to absolute value of the experimental SHE potential (4.44 eV). Potentials for HER (violet lines) and OER (orange lines) at pH 0 (dashed lines) and pH 7 (solid lines) are shown. The colors black, red, green, and blue correspond to results for isomers a, b, c, and d, respectively.

nanoparticles in water calculated using the CAM-B3LYP/6-31G(d) level with those of hydrated rutile nanocrystal immersed in explicit water molecules in ref 64 confirm the validity of the present results (see Table S9 in the Supporting Information).

To facilitate the discussion, we will first consider the properties of the particles under vacuum. This is just for completeness and for comparison purposes, since water splitting under vacuum is physically meaningless. In short, only free charge carriers, which is metastable species under vacuum (Figures 5a and 5b, left panels), have photocatalytic capabilities, whereas S_1 exciton has no driving force for HER, because of the EA* value being too high, i.e., low LUMO energy (see Figure S2). Hence, TiO_2 nanoparticles studied are incapable of photocatalytic water splitting under vacuum. Regarding the effect of the size and shape of the nanoparticles, one can barely see a significant trend in the potentials, except for a slight upward/downward trend of IP_v/EA_v as a function of the size (Figure S2a, top).

The presence of water, taken into account in the CPCM solvent model, significantly changes the trend noted above. Result in Figure 8a show that a water solvent leads to a lowering/lifting of IP/EA potentials of free charge carriers due to electrostatic stabilization of positive holes/negative electrons, respectively. Since IP values are found to be more affected than EA values, photocatalytic OER driven by free charge carrier becomes less exothermic. In contrast, a water solvent leads to a lifting/lowering of IP*/EA*, because the energy stabilization in the S_1 exciton is smaller than that of free charge carriers (Figure 8b). Hence, the presence of water shifts the IP*/EA* potentials to the point of enabling photocatalytic water splitting driven by the S_1 exciton. Therefore, most of the small TiO_2 nanoparticles in both free charge carrier and S_1 exciton states are expected to have photocatalytic capability for water splitting, even though some of them are incapable of the HER. Regarding the effect of the size and shape of the nanoparticles, one can only see a slight downward trend of EA_v potentials, as a function of the particle size.

According to the thermodynamic analysis of $IP^{(*)}/EA^{(*)}$ potentials and to the energetic stability between free charge carriers and the S_1 exciton, one may argue that the vertically generated S_1 exciton first facilitates the photocatalytic reaction and then free charge carriers become the main contributor to the reaction. However, it is very difficult to determine the major contributor throughout the entire reaction, because tracking time-resolved dynamics of excited-state relaxation when free charge carriers become more abundant than S_1 excitons is not at all trivial within the standard TD-DFT framework. Therefore, the dynamics regarding the excited state decay and the electron transfer processes in the course of photocatalytic water splitting of TiO_2 nanoparticles remain as key issues to be solved. Another challenge is how to modify the TiO_2 nanoparticles to lower the EA and IP* potentials in free charge carrier and S_1 exciton states, respectively, because, in practice, the thermodynamic driving force for the HER reaction will not be sufficient. Obviously, it is very important to find a trend of the half-reaction potentials of TiO_2 nanoparticles studied here, so that one would be able to predict the values of larger nanoparticles. However, unfortunately, we could not find any significant and consistent trend in those potentials as a function

DOI: 10.1021/acs.jctc.6b00519
J. Chem. Theory Comput. 2016, 12, 3751−3763

of size and/or shape. This is because the structural effect of small clusters studied here may be significant. However, we found weak size dependencies of IP_v and EA_v potentials.

To conclude this section, we note that structural relaxation in the excited state is responsible for significant change in the standard reduction potentials. It was found that stabilization energy values through structural relaxation in the S_1 exciton, free electron (anionic), and free hole (cationic) states in water are 0.3−1.0, 0.2−1.2, and 0.5−1.9 eV, respectively, at the CAM-B3LYP/6-31G(d) level, indicating that the relaxation in the free hole state is the most significant. On the other hand, the shape dependence of the TiO_2 particles on the structural relaxation was also found to be significant. Upon structural relaxation in the excited states, this leads to changes in the IP, EA, IP*, and EA* values, up to 1.9, 1.4, 1.5, and 0.7 eV, respectively, with concomitant changes in $IP_v^{(*)}/EA_v^{(*)}$ and $IP_{ad}^{(*)}/EA_{ad}^{(*)}$. The significant change in the standard reduction potentials induced by structural relaxation in the excited states highlights the importance of tracking adiabatic potential energy surface in the excited states.

5. CONCLUSIONS

We have studied the influence of the shape and size on the electronic structure of TiO_2 nanoparticles in a realistic 0.5−3.2 nm range, using DFT and TD-DFT calculations using two types of hybrid functional and including solvent effects. The present results show that the electronic structure is significantly more dependent on a nanoparticle's structure than its size. Hence, especially for the smaller nanoclusters, several different isomeric structures should be considered in order to evaluate the electronic structure and subsequently derived properties.

The calculation of relevant properties of TiO_2 nanoparticles indicates that, in the 0.5−3.2 nm range, the exciton binding energy is significant. This implies that the exciton state is favored, thermodynamically, significantly, and energetically, over free charged species both under vacuum and in water for this size range. Tentative extrapolation of our results indicate that this is likely also to be the case for relatively large nanoparticles and that bulklike electronic behavior may be expected to emerge for ∼6.5-nm-diameter TiO_2 nanoparticles. The analysis of ionization potentials and electron affinities, relative to the standard reduction potential for the HER and OER, shows that the free charge carrier state of the TiO_2 nanoparticles studied here is able to drive photocatalytic water splitting, at least from a thermodynamic point of view. However, for the more stable exciton state, water splitting is only favored when the presence of water is taken into account, although the approximate solvation model used implies that this conclusion must be taken with caution. Finally, we note that the present analysis provides necessary but not sufficient conditions for water splitting by photoexcited TiO_2 nanoparticles.

■ ASSOCIATED CONTENT

Supporting Information

The Supporting Information is available free of charge on the ACS Publications website at DOI: 10.1021/acs.jctc.6b00519.

Comparison between $(S_0 \rightarrow S_1)_v$ and $(S_0 \rightarrow T_1)_v$ excitations; energy per unit of the $(TiO_2)_n$ particles with n = 4, 8, 16, 35, and 84, as predicted from B3LYP/6-31G(d)/water; $\Delta E_{H\text{-}L}$ (in eV) obtained at different level of theories; neutralization of unique charge localization patterns of each isomer upon water solvation; water splitting capabilities of TiO_2 NPs (IP/EA and IP*/EA* diagram) obtained at CAM-B3LYP/6-31G(d) level; excited-state lifetime (τ) for vertical and relaxed S_1 excitons in vacuum and water; calculated electron and hole distributions in S_1 exciton and free charge carrier in vacuum and water obtained at the CAM-B3LYP/6-31G(d) level of theory; and optimized geometries of neutral ground state and relaxed cationic, anionic, and adiabatic S_1 exciton states of $(TiO_2)_n$ with n = 4, 8, 16, 35, and 84, under vacuum at the CAM-B3LYP/6-31G(d) level (PDF)

■ AUTHOR INFORMATION

Corresponding Authors

*E-mail: jinylee@skku.edu (J. Y. Lee).
*E-mail: francesc.illas@ub.edu (F. Illas).

Notes

The authors declare no competing financial interest.

■ ACKNOWLEDGMENTS

The authors are indebted to Prof. Peter Zapol for having made available the TD-DFT optimized structures reported in ref 34 and to Prof. Martijn Zwinenburg for many valuable comments. This research was supported by the Spanish MINECO/FEDER CTQ2015-64618-R grant and, in part, by *Generalitat de Catalunya* (Grant Nos. 2014SGR97 and XRQTC) and by the NOMAD Center of Excellence Project, which received funding from the European Union's Horizon 2020 research and innovation programme under Grant Agreement No 676580. J.Y.L. acknowledges the financial support by Ministry of Science, ICT and Future Planning, subjected project to the project EDISON (Education-research Integration through Simulation On the Net, Grant No. 2012M3C1A6035359); K.C.K. acknowledges the financial support by Basic Science Research Program through the National Research Foundation of Korea (NRF) funded by the Ministry of Education (No. NRF-2014R1A6A3A03056449); O.L.G. is grateful to the Universitat de Barcelona for a predoctoral grant; and F.I. acknowledges additional support from the 2015 ICREA Academia Award for Excellence in University Research. Computational time at the Marenostrum Supercomputer has been provided by the Barcelona Supercomputing Centre through grants from Red Española de Supercomputación and the COMPHOTOCAT Project No. 2014112608 of the Partnership for Advanced Computing in Europe (PRACE).

■ REFERENCES

(1) Sousa, C.; Tosoni, S.; Illas, F. Theoretical Approaches to Excited-State-Related Phenomena in Oxide Surfaces. *Chem. Rev.* **2013**, *113*, 4456−4495.
(2) Henderson, M. A. A Surface Science Perspective on TiO_2 Photocatalysis. *Surf. Sci. Rep.* **2011**, *66*, 185−297.
(3) Diebold, U. The Surface Science of Titanium Dioxide. *Surf. Sci. Rep.* **2003**, *48*, 53−229.
(4) Chen, X.; Mao, S. S. Titanium Dioxide Nanomaterials: Synthesis, Properties Modifications and Applications. *Chem. Rev.* **2007**, *107*, 2891−2959.
(5) Gratzel, M. Photoelectrochemical Cells. *Nature* **2001**, *414*, 338−344.
(6) Hagfeldt, A.; Boschloo, G.; Sun, L.; Kloo, L.; Pettersson, H. Dye-Sensitized Solar Cells. *Chem. Rev.* **2010**, *110*, 6595−6663.

DOI: 10.1021/acs.jctc.6b00519
J. Chem. Theory Comput. 2016, 12, 3751−3763

(7) Hoffmann, M. R.; Martin, S. T.; Choi, W.; Bahnemann, D. W. Environmental Applications of Semiconductor Photocatalysis. *Chem. Rev.* **1995**, *95*, 69−96.
(8) Mills, A.; Davies, R. H.; Worsley, D. Water-Purification by Semiconductor Photocatalysis. *Chem. Soc. Rev.* **1993**, *22*, 417−425.
(9) Fox, M. A.; Dulay, M. T. Heterogeneous Photocatalysis. *Chem. Rev.* **1993**, *93*, 341−357.
(10) Xu, H.; Ouyang, S.; Liu, L.; Reunchan, P.; Umezawa, N.; Ye, J. Recent Advances in TiO_2-based Photocatalysis. *J. Mater. Chem. A* **2014**, *2*, 12642−12661.
(11) Hashimoto, K.; Irie, H.; Fujishima, A. TiO_2 Photocatalysis: A Historical Overview and Future Prospects. *Jpn. J. Appl. Phys.* **2005**, *44*, 8269−8285.
(12) Fujishima, A.; Zhang, X.; Tryk, D. A. TiO_2 Photocatalysis and Related Surface Phenomena. *Surf. Sci. Rep.* **2008**, *63*, 515−582.
(13) Chen, X. B.; Shen, S. H.; Guo, L. J.; Mao, S. S. Semiconductor-Based Photocatalytic Hydrogen Generation. *Chem. Rev.* **2010**, *110*, 6503−6570.
(14) Kudo, A.; Miseki, Y. Heterogeneous Photocatalyst Materials for Water Splitting. *Chem. Soc. Rev.* **2009**, *38*, 253−278.
(15) Kavan, L.; Gratzel, M.; Gilbert, S. E.; Klemenz, C.; Scheel, H. J. Electrochemical and Photoelectrochemical Investigation of Single-Crystal Anatase. *J. Am. Chem. Soc.* **1996**, *118*, 6716−6723.
(16) Asahi, R.; Morikawa, T.; Ohwaki, T.; Aoki, K.; Taga, Y. Visible-light Photocatalysis in Nitrogen-Doped Titanium Oxides. *Science* **2001**, *293*, 269−271.
(17) Asahi, R.; Morikawa, T.; Irie, H.; Ohwaki, T. Nitrogen-Doped Titanium Dioxide as Visible-Light-Sensitive Photocatalyst: Designs, Developments, and Prospects. *Chem. Rev.* **2014**, *114*, 9824−9852.
(18) Di Valentin, C.; Pacchioni, G. Spectroscopic Properties of Doped and Defective Semiconducting Oxides from Hybrid Density Functional Calculations. *Acc. Chem. Res.* **2014**, *47*, 3233−3241.
(19) Calatayud, D.; Jardiel, T.; Peiteado, M.; Illas, F.; Giamello, E.; Palomares, F.; Fernández Hevia, D.; Caballero, A. Synthesis and characterization of blue faceted anatase nanoparticles through extensive fluorine lattice doping. *J. Phys. Chem. C* **2015**, *119*, 21243−21250.
(20) Liu, G.; Yang, H. G.; Pan, J.; Yang, Y. Q.; Lu, G. Q.; Cheng, H. M. Titanium Dioxide Crystals with Tailored Facets. *Chem. Rev.* **2014**, *114*, 9559−9612.
(21) Yang, H. G.; Sun, C. H.; Qiao, S. Z.; Zou, J.; Liu, G.; Smith, S. C.; Cheng, H. M.; Lu, G. Q. Anatase TiO_2 single crystals with a large percentage of reactive facets. *Nature* **2008**, *453*, 638−641.
(22) Lamiel-Garcia, O.; Tosoni, S.; Illas, F. Relative stability of F covered TiO_2 anatase (101) and (001) surfaces from periodic DFT calculations and *ab initio* atomistic thermodynamics. *J. Phys. Chem. C* **2014**, *118*, 13667−13673.
(23) Mattioli, G.; Filippone, F.; Alippi, P.; Amore Bonapasta, A. *Ab Initio* Study of the Electronic States Induced by Oxygen Vacancies in Rutile and Anatase TiO_2. *Phys. Rev. B: Condens. Matter Mater. Phys.* **2008**, *78*, 241201.
(24) Morgan, B. J.; Watson, G. W. Intrinsic n-type Defect Formation in TiO_2: A Comparison of Rutile and Anatase from GGA+U Calculations. *J. Phys. Chem. C* **2010**, *114*, 2321−2328.
(25) Stausholm-Møller, J.; Kristoffersen, H. H.; Hinnemann, B.; Madsen, G. K. H.; Hammer, B. DFT+U Study of Defects in Bulk Rutile TiO_2. *J. Chem. Phys.* **2010**, *133*, 144708.
(26) Mattioli, G.; Alippi, P.; Filippone, F.; Caminiti, R.; Amore Bonapasta, A. Deep versus Shallow Behavior of Intrinsic Defects in Rutile and Anatase TiO_2 Polymorphs. *J. Phys. Chem. C* **2010**, *114*, 21694−21704.
(27) Finazzi, E.; Di Valentin, C.; Pacchioni, G.; Selloni, A. Excess electron states in reduced bulk anatase TiO_2: Comparison of standard GGA, GGA+U, and hybrid DFT calculations. *J. Chem. Phys.* **2008**, *129*, 154113.
(28) Islam, M. M.; Bredow, T.; Gerson, A. Electronic properties of oxygen-deficient and aluminum-doped rutile TiO_2 from first principles. *Phys. Rev. B: Condens. Matter Mater. Phys.* **2007**, *76*, 045217.
(29) Janotti, A.; Varley, J. B.; Rinke, P.; Umezawa, N.; Kresse, G.; Van de Walle, C. G. Hybrid Functional Studies of the Oxygen vacancy in TiO_2. *Phys. Rev. B: Condens. Matter Mater. Phys.* **2010**, *81*, 085212.
(30) Deák, P.; Aradi, B.; Frauenheim, T. Quantitative Theory of the Oxygen Vacancy and Carrier Self-Trapping in Bulk TiO_2. *Phys. Rev. B: Condens. Matter Mater. Phys.* **2012**, *86*, 195206.
(31) Lazzeri, M.; Vittadini, A.; Selloni, A. Structure and energetics of stoichiometric TiO_2 anatase surfaces. *Phys. Rev. B: Condens. Matter Mater. Phys.* **2001**, *63*, 155409.
(32) Gong, X. Q.; Selloni, A. Reactivity of anatase TiO_2 nanoparticles: The role of the minority (001) surface. *J. Phys. Chem. B* **2005**, *109*, 19560−19562.
(33) Morgan, B. J.; Watson, G. W. A DFT+U description of oxygen vacancies at the TiO_2 rutile (110) surface. *Surf. Sci.* **2007**, *601*, 5034−5041.
(34) Barnard, A. S.; Erdin, S.; Lin, Y.; Zapol, P.; Halley, J. W. Modeling the Structure and Electronic Properties of TiO_2 Nanoparticles. *Phys. Rev. B: Condens. Matter Mater. Phys.* **2006**, *73*, 205405.
(35) Auvinen, S.; Alatalo, M.; Haario, H.; Jalava, J. P.; Lamminmäki, R. J. Size and Shape Dependence of the Electronic and Spectral Properties in TiO_2 Nanoparticles. *J. Phys. Chem. C* **2011**, *115*, 8484−8493.
(36) Hamad, S.; Catlow, C. R.A; Woodley, S. M.; Lago, S.; Mejias, J. A. Structure and stability of small TiO_2 nanoparticles. *J. Phys. Chem. B* **2005**, *109*, 15741−15748.
(37) Syzgantseva, O. A.; Gonzalez-Navarrete, P.; Calatayud, M.; Bromley, S.; Minot, C. Theoretical Investigation of the Hydrogenation of $(TiO_2)_n$ Clusters (n= 1−10). *J. Phys. Chem. C* **2011**, *115*, 15890−15899.
(38) Marom, N.; Kim, M.; Chelikowsky, J. R. Structure Selection Based on High Vertical Electron Affinity for TiO_2 Clusters. *Phys. Rev. Lett.* **2012**, *108*, 106801.
(39) Chen, M. Y.; Dixon, D. A. Tree Growth-Hybrid Genetic Algorithm for Predicting the Structure of Small $(TiO_2)_n$, n = 2−13, Nanoclusters. *J. Chem. Theory Comput.* **2013**, *9*, 3189−3200.
(40) Buckeridge, J.; Butler, K. T.; Catlow, C. R. A.; Logsdail, A. J.; Scanlon, D. O.; Shevlin, S. A.; Woodley, S. M.; Sokol, A. A.; Walsh, A. Polymorph Engineering of TiO_2: Demonstrating How Absolute Reference Potentials Are Determined by Local Coordination. *Chem. Mater.* **2015**, *27*, 3844−3851.
(41) Shevlin, S. A.; Woodley, S. M. Electronic and Optical Properties of Doped and Undoped $(TiO_2)_n$ Nanoparticles. *J. Phys. Chem. C* **2010**, *114*, 17333−17343.
(42) Berardo, E.; Hu, H. S.; Shevlin, S. A.; Woodley, S. M.; Kowalski, K.; Zwijnenburg, M. A. Modeling Excited States in TiO_2 Nanoparticles: On the Accuracy of a TD-DFT Based Description. *J. Chem. Theory Comput.* **2014**, *10*, 1189−1199.
(43) Bredas, J. L. Mind the gap! *Mater. Horiz.* **2014**, *1*, 17−19.
(44) Pascual, J.; Camassel, J.; Mathieu, H. Fine Structure in the Intrinsic Absorption Edge of TiO_2. *Phys. Rev. B: Condens. Matter Mater. Phys.* **1978**, *18*, 5606−5614.
(45) Tang, H.; Levy, F.; Berger, H.; Schmid, P. E. Urbach tail of anatase TiO_2. *Phys. Rev. B: Condens. Matter Mater. Phys.* **1995**, *52*, 7771−7774.
(46) Kang, W.; Hybertsen, M. S. Quasiparticle and Optical Properties of Rutile and Anatase TiO_2. *Phys. Rev. B: Condens. Matter Mater. Phys.* **2010**, *82*, 085203.
(47) Guiglion, P.; Butchosa, C.; Zwijnenburg, M. Polymeric watersplitting photocatalysts; A computational perspective on the water oxidation conundrum. *J. Mater. Chem. A* **2014**, *2*, 11996−12004.
(48) Berardo, E.; Hu, H. S.; van Dam, H. J. J.; Shevlin, S. A.; Woodley, S. M.; Kowalski, K.; Zwijnenburg, M. A. Describing excited state relaxation and localization in TiO_2 nanoparticles using TD-DFT. *J. Chem. Theory Comput.* **2014**, *10*, 5538−5548.
(49) Guiglion, P.; Berardo, E.; Butchosa, C.; Wobbe, M. C. C.; Zwijnenburg, M. A. Modelling materials for solar fuel synthesis by artificial photosynthesis; Predicting the optical, electronic and redox properties of photocatalysts. *J. Phys.: Condens. Matter* **2016**, *28*, 074001.

DOI: 10.1021/acs.jctc.6b00519
J. Chem. Theory Comput. 2016, 12, 3751−3763

(50) Becke, A. D. Density-Functional Thermochemistry. III. The Role of Exact Exchange. *J. Chem. Phys.* **1993**, *98*, 5648.
(51) Yanai, T.; Tew, D. P.; Handy, N. C. A New Hybrid Exchange−Correlation Functional Using the Coulomb-Attenuating Method (CAM-B3LYP). *Chem. Phys. Lett.* **2004**, *393*, 51−57.
(52) Frisch, M. J.; Trucks, G. W.; Schlegel, H. B.; Scuseria, G. E.; Robb, M. A.; Cheeseman, J. R.; Scalmani, G.; Barone, V.; Mennucci, B.; Petersson, G. A.; Nakatsuji, H.; Caricato, M.; Li, X.; Hratchian, H. P.; Izmaylov, A. F.; Bloino, J.; Zheng, G.; Sonnenberg, J. L.; Hada, M.; Ehara, M.; Toyota, K.; Fukuda, R.; Hasegawa, J.; Ishida, M.; Nakajima, T.; Honda, Y.; Kitao, O.; Nakai, H.; Vreven, T.; Montgomery, J. A., Jr.; Peralta, J. E.; Ogliaro, F.; Bearpark, M.; Heyd, J. J.; Brothers, E.; Kudin, K. N.; Staroverov, V. N.; Kobayashi, R.; Normand, J.; Raghavachari, K.; Rendell, A.; Burant, J. C.; Iyengar, S. S.; Tomasi, J.; Cossi, M.; Rega, N.; Millam, J. M.; Klene, M.; Knox, J. E.; Cross, J. B.; Bakken, V.; Adamo, C.; Jaramillo, J.; Gomperts, R.; Stratmann, R. E.; Yazyev, O.; Austin, A. J.; Cammi, R.; Pomelli, C.; Ochterski, J. W.; Martin, R. L.; Morokuma, K.; Zakrzewski, V. G.; Voth, G. A.; Salvador, P.; Dannenberg, J. J.; Dapprich, S.; Daniels, A. D.; Farkas, Ö.; Foresman, J. B.; Ortiz, J. V.; Cioslowski, J.; Fox, D. J. *Gaussian 09, Revision D.01*; Gaussian, Inc.: Wallingford, CT, 2013.
(53) Wales, D. J.; Doye, J. P. K. Global Optimization by Basin-Hopping and the Lowest Energy Structures of Lennard-Jones Clusters Containing up to 110 Atoms. *J. Phys. Chem. A* **1997**, *101*, 5111−5116.
(54) Wulff, G. On the question of speed of growth and dissolution of crystal surfaces. *Z. Kristallogr.* **1901**, *34*, 449−530.
(55) Blum, V.; Gehrke, R.; Hanke, F.; Havu, P.; Havu, V.; Ren, X.; Reuter, K.; Scheffler, M. *Ab Initio* Molecular Simulations with Numeric Atom-Centered Orbitals. *Comput. Phys. Commun.* **2009**, *180*, 2175−2196.
(56) Hirata, S.; Head-Gordon, M. Time-Dependent Density Functional Theory within the Tamm−Dancoff Approximation. *Chem. Phys. Lett.* **1999**, *314*, 291−299.
(57) Tomasi, J.; Persico, M. Molecular Interactions in Solution: An Overview of Methods Based on Continuous Distributions of the Solvent. *Chem. Rev.* **1994**, *94*, 2027−2094.
(58) Pandey, L. B.; Aikens, C. M. Theoretical Investigation of the Electrochemical Mechanism of Water Splitting on a Titanium Oxide Cluster Model. *J. Phys. Chem. A* **2012**, *116*, 526−535.
(59) De Angelis, F.; Fantacci, S.; Gebauer, R. Simulating Dye-Sensitized TiO_2 Heterointerfaces in Explicit Solvent: Absorption Spectra, Energy Levels, and Dye Desorption. *J. Phys. Chem. Lett.* **2011**, *2*, 813−817.
(60) Di Valentin, C.; Pacchioni, G.; Selloni, A. Electronic Structure of Defect States in Hydroxylated and Reduced Rutile TiO_2 (110) Surfaces. *Phys. Rev. Lett.* **2006**, *97*, 166803.
(61) Bromley, S. T.; Moreira, I. De P.R.; Neyman, K.-M.; Illas, F. Approaching nanoscale oxides: models and theoretical methods. *Chem. Soc. Rev.* **2009**, *38*, 2657−2670.
(62) Persson, P.; Gebhardt, J. C. M.; Lunell, S. The Smallest Possible Nanocrystals of Semiionic Oxides. *J. Phys. Chem. B* **2003**, *107*, 3336−3339.
(63) Manzhos, S.; Segawa, H.; Yamashita, K. Computational Dye Design by Changing the Conjugation Order: Failure of LR-TDDFT to Predict Relative Excitation Energies in Organic Dyes Differing by the Position of the Methine Unit. *Chem. Phys. Lett.* **2012**, *527*, 51−56.
(64) Berardo, E.; Zwijnenburg, M. A. Modeling the Water Splitting Activity of a TiO_2 Rutile Nanoparticle. *J. Phys. Chem. C* **2015**, *119*, 13384−13393.
(65) Xu, M.; Gao, Y.; Moreno, E. M.; Kunst, M.; Muhler, M.; Wang, Y.; Idriss, H.; Wöll, C. Photocatalytic Activity of Bulk TiO_2 Anatase and Rutile Single Crystals Using Infrared Absorption Spectroscopy. *Phys. Rev. Lett.* **2011**, *106*, 138302.
(66) Tamaki, Y.; Furube, A.; Murai, M.; Hara, K.; Katoh, R.; Tachiya, M. Dynamics of Efficient Electron-Hole Separation in TiO_2 Nanoparticles Revealed by Femtosecond Transient Absorption Spectroscopy under the Weak-Excitation Condition. *Phys. Chem. Chem. Phys.* **2007**, *9*, 1453−1460.
(67) Tamaki, Y.; Hara, K.; Katoh, R.; Tachiya, M.; Furube, A. Femtosecond Visible-to-IR Spectroscopy of TiO_2 Nanocrystalline Films: Elucidation of the Electron Mobility before Deep Trapping. *J. Phys. Chem. C* **2009**, *113*, 11741−11746.
(68) Barnard, A. S.; Zapol, P. Predicting the Energetics, Phase Stability, and Morphology Evolution of Facted and Spherical Anatase Nanocrystals. *J. Phys. Chem. B* **2004**, *108*, 18435−18440.
(69) de P. R. Moreira, I.; Illas, F.; Martin, R. L. Effect of Fock exchange on the electronic structure and magnetic coupling in NiO. *Phys. Rev. B: Condens. Matter Mater. Phys.* **2002**, *65*, 155102.
(70) Guiglion, P.; Berardo, E.; Butchosa, C.; Wobbe, M. C. C.; Zwijnenburg, M. A. Modelling Materials for Solar Fuel Synthesis by Artificial Photosynthesis; Predicting the Optical, Electronic and Redox Properties of Photocatalysts. *J. Phys.: Condens. Matter* **2016**, *28*, 074001.
(71) Guiglion, P.; Butchosa, C.; Zwijnenburg, M. A. Polymer Photocatalysts for Water Splitting: Insights from Computational Modeling. *Macromol. Chem. Phys.* **2016**, *217*, 344−353.
(72) Nunzi, F.; Agrawal, S.; Selloni, A.; De Angelis, F. Structural and Electronic Properties of Photoexcited TiO_2 Nanoparticles from First Principles. *J. Chem. Theory Comput.* **2015**, *11*, 635−645.
(73) Trasatti, S. The Absolute Electrode Potential: An Explanatory Note. *Pure Appl. Chem.* **1986**, *58*, 955−966.
(74) Trasatti, S. The Concept of Absolute Electrode Potential: An Attempt at a Calculation. *J. Electroanal. Chem.* **1974**, *52*, 313−329.
(75) Scanlon, D. O.; Dunnill, C. W.; Buckeridge, J.; Shevlin, S. A.; Logsdail, A. J.; Woodley, S. M.; Catlow, C. R. A.; Powell, M. J.; Palgrave, R. G.; Parkin, I. P.; Watson, G. W.; Keal, T. W.; Sherwood, P.; Walsh, A.; Sokol, A. A. Band Alignment of Rutile and Anatase TiO_2. *Nat. Mater.* **2013**, *12*, 798−801.
(76) Stevanovic, V.; Lany, S.; Ginley, D. S.; Tumas, W.; Zunger, A. Assessing Capability of Semiconductors to Split Water Using Ionization Potentials and Electron Affinities Only. *Phys. Chem. Chem. Phys.* **2014**, *16*, 3706−3714.

DOI: 10.1021/acs.jctc.6b00519
J. Chem. Theory Comput. 2016, 12, 3751−3763

3.1.3.2 Predicting size-dependent emergence of crystallinity in nanomaterials: titania nanoclusters versus nanocrystals

Nanoscale

PAPER

View Article Online
View Journal | View Issue

Cite this: *Nanoscale*, 2017, **9**, 1049

Predicting size-dependent emergence of crystallinity in nanomaterials: titania nanoclusters *versus* nanocrystals†

Oriol Lamiel-Garcia,[a] Andi Cuko,[a,b] Monica Calatayud,[b,c] Francesc Illas[a] and Stefan T. Bromley*[a,d]

Bottom-up and top-down derived nanoparticle structures refined by accurate *ab initio* calculations are used to investigate the size dependent emergence of crystallinity in titania from the monomer upwards. Global optimisation and data mining are used to provide a series of $(TiO_2)_N$ global minima candidates in the range $N = 1–38$, where our approach provides many new low energy structures for $N > 10$. A range of nanocrystal cuts from the anatase crystal structure are also considered up to a size of over 250 atoms. All nanocrystals considered are predicted to be metastable with respect to non-crystalline nanoclusters, which has implications with respect to the limitations of the cluster approach to modelling large titania nanosystems. Extrapolating both data sets using a generalised expansion of a top-down derived energy expression for nanoparticles, we obtain an estimate of the non-crystalline to crystalline crossover size for titania. Our results compare well with the available experimental results and imply that anatase-like crystallinity emerges in titania nanoparticles of approximately 2–3 nm diameter.

Received 22nd July 2016,
Accepted 4th October 2016

DOI: 10.1039/c6nr05788h

www.rsc.org/nanoscale

Introduction

Size reduction from the macroscopic to length scales of only a few nanometres can lead to dramatic changes in a material's properties. Further to the effects directly arising from high surface-to-bulk ratios, nano-sized particles often possess distinct atomic and electronic structures with respect to stable bulk crystals. Titania (TiO_2) is a prototypical example of a material displaying an extreme size-dependence of both structure and properties.[1] Under ambient conditions bulk titania is most thermodynamically stable with atomic ordering following the rutile crystal structure. However, upon reduction in size, titania nanoparticles with average diameters less than ~14 nm begin to exhibit the anatase crystal structure.[2] This structural transition has been thermodynamically rationalised by top-down calculations of the size-dependent enthalpies of titania nanoparticles, which highlight the roles of surface energies and surface stresses on nanoparticle stability.[2,3]

Anatase nanocrystals are found to greatly differ from their rutile counterparts in being highly photochemically active and form the basis for many nano-titania based applications (*e.g.* photocatalysts,[4] sunscreens,[5] anti-pollution building materials[6]). Often the key to enhanced photoactivity is to form composite materials containing very small (≤5 nm diameter) stable anatase nanocrystals.[7,8] As with most materials, however, further decreasing the size of anatase nanocrystals will eventually give way to a regime of nanoclusters, which generally do not display a crystalline order, thus losing much of their utility. Evidence from high resolution transmission electron microscopy has shown that isolated anatase nanocrystals can persist down to sizes as small as ~5 nm in diameter.[9] Recent experiments have further shown that the anatase crystal structure is extremely thermally persistent in 4 nm diameter nanoparticles.[10] Although this implies that anatase is still thermodynamically stable, in this latter size range it is unclear whether such nanoparticles retain a facetted nanocrystal morphology. Indirect evidence from modelling suggests that when anatase nanoparticles start to become smaller than ~5 nm, they may begin to exhibit a spherical morphology with an anatase core and an amorphous shell.[11] Although not strictly nanocrystals according to our definition, such core–shell nanoparticles should clearly be regarded as partially crystalline. For even smaller TiO_2 nanoparticles, with average

[a]*Departament de Ciència de Materials i Química Física and Institut de Química Teòrica i Computacional (IQTCUB), Universitat de Barcelona, E-08028 Barcelona, Spain*
[b]*SorbonneUniversités, UPMC Univ Paris 06, CNRS, Laboratoire de Chimie Théorique CC 137, 4, place Jussieu F. 75252, Paris Cedex 05, France*
[c]*InstitutUniversitaire de France, France*
[d]*Institució Catalana de Recerca i Estudis Avançats (ICREA), E-08010 Barcelona, Spain. E-mail: s.bromley@ub.edu*
†Electronic supplementary information (ESI) available. See DOI: 10.1039/c6nr05788h

diameters in the range 2–3 nm, fitting experimental X-ray spectroscopy data using the reverse Monte Carlo refined nanoparticle structures tend to support this feature.[12] With decreasing size, eventually the anatase core is subsumed by the amorphous shell, and the nanoparticles will not exhibit any crystallinity. We refer to the non-crystalline titania species in this ultra-small size regime as nanoclusters.

From a bottom-up perspective, increasing in size from a single TiO_2 monomer, nanoclusters need to attain a certain size before they begin to thermodynamically favour regular atomic ordering characteristic of a bulk crystal. From this perspective, this structural crossover between nanoclusters and nanocrystals can be seen as a size-dependent non-crystalline to crystalline (NC ↔ C) crossover. Herein, we provide an estimate of the NC ↔ C crossover size regime for TiO_2 using accurate quantum chemically calculated energies of relaxed atomistically detailed nanoclusters and nanocrystals derived from bottom-up and top-down approaches respectively.

In Fig. 1 we represent the generic size dependent energetic stability of both non-crystalline (red line) and nanocrystals (blue line) for an arbitrary material. We note that although herein we will use calculated energies at 0 K to demonstrate our approach, these data could equally well be free energies from experiment and/or theory. The energy difference, $\Delta E_{C\text{–}NC}(N)$, gives a measure of the metastability of crystalline particles with respect to non-crystalline clusters at relatively small sizes and *vice versa* at larger sizes. Using the plotted energies the NC ↔ C crossover size would seem to be defined as the size at which $\Delta E_{C\text{–}NC}(N)$ becomes zero. In general, however, it is not expected that this crossover will always be defined by a definite single transition size above which nanocrystals are always more energetically stable and below which non-crystalline nanoclusters are always more stable. Size dependent structural preferences are well-known in nanocluster systems (*e.g.* icosahedral shell closing) and it is quite possible that, with increasing size, crystallinity would be first energetically favoured in a set of discrete increasingly sized nanoparticles covering a crossover range (N_1, N_2, ... N_C) before being manifestly prevalent for all $N \geq N_C$. More generally, it is quite likely that for sizes close to but smaller than N_C there will be nanoclusters that exhibit partial crystallinity (*e.g.* a nanoparticle with crystalline cores and an amorphous shell). As such we define the NC size range as those nanoparticles which do not exhibit full crystallinity. In turn, we roughly define a fully crystalline nanocrystal as one which can be cut from a bulk crystal and which maintains its atomic ordering upon structural relaxation and with only minor displacement of atomic positions (*i.e.* no more than a ~20% of a bond length). We further note that the NC ↔ C crossover will not generally be to the most stable bulk crystalline phase of the material but rather to a polymorph which is metastable in the bulk. Depending on the material there will be variable number of subsequent size dependent crossovers between polymorphs until the most stable bulk crystalline phase is reached.

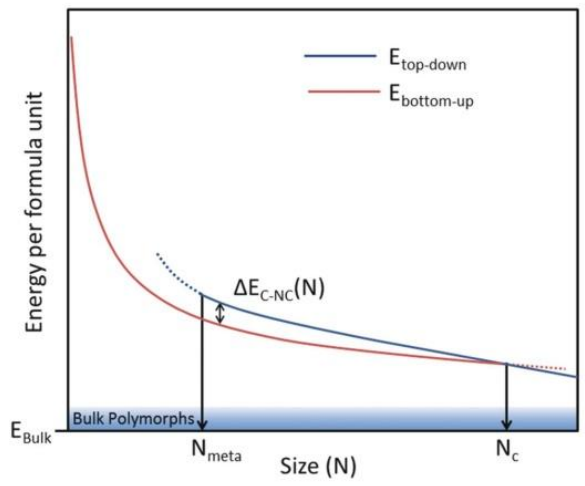

Fig. 1 Schematic representation of size-dependent energetic stability of crystalline (C) and non-crystalline (NC) nanoparticles with respect to their size. The red line indicates the stability of nanoclusters and the blue line that of nanocrystals. $\Delta E_{C\text{–}NC}(N)$ denotes the energy difference between a nanocrystal and nanocluster, both having N formula units. The blue shaded region denotes the typical energy range within which metastable bulk polymorphs can exist. N_{meta} and N_C are described in the text.

In Fig. 1 we also note another interesting crossover size, N_{meta}, indicating the smallest size that a nanocrystal can maintain an energetically metastable crystalline structure with respect to a non-crystalline nanocluster of the same size. Related to this concept, there have been important studies of nanosize dependent metastability of one crystal phase over another.[13] The metastability we refer to, however, is, in a converse way, more similar to the metastability that a non-crystalline bulk structure (*e.g.* an amorphous glass) can possess with respect to a crystalline phase. The size region around N_{meta} denotes the limit at which small nanocrystals start to become structurally unstable and spontaneously relax into non-crystalline species. We note that due to the stability of small clusters often being irregularly dependent on size, it is quite possible that close to size N_{meta} there will be a set of different cluster sizes for which the crystalline order is easier to maintain and sizes for which only non-crystalline clusters are structurally stable.

For the vast majority of materials, neither N_C nor N_{meta} crossover sizes have been determined. For highly ionic materials N_C and N_{meta} will be quite similar and small in magnitude. In other words, in such cases the strong near-isotropic electrostatic interactions between the ions drive the system towards crystalline closely packed structures even for very small sizes (*e.g.* $N < 20$ for $(NaCl)_N$,[14] $(MgO)_N$,[15] $(CeO_2)_N$ [16]). For such materials we note that small to moderately sized crystalline nanoparticles appear to be good theoretical models for calculating the properties of large nanocrystals and/or the corresponding bulk crystal.[17–20] For many materials where the tendency to establish highly ordered atomic arrangements is relatively weaker, we may expect that the N_C and N_{meta} transition sizes could be very different. For example, in such a material one may be able to construct relatively small but very

View Article Online

Nanoscale Paper

metastable nanocrystals, but where the thermodynamic NC ↔ C transition occurs at significantly larger nanoparticle sizes. Such a situation has been strongly hinted at in the IP-based studies of $(ZnO)_N$ [21] and $(Fe_2O_3)_N$ [22] nanosystems and is found to be the case in our DFT-based study of the $(TiO_2)_N$ nanosystem. In such cases, calculations using such highly metastable nanocrystal models (*i.e.* with sizes close to N_{meta}) as a means to explain experimental data involving considerably larger nanocrystals and/or bulk crystals, should be very carefully assessed.

Using a bottom-up global optimisation approach we show that, in the case of titania, such small bulk-mimicking nanocrystals are significantly metastable with respect to the most energetically stable nanoclusters of a corresponding size. Furthermore, by also considering a set of bulk-derived nanoparticles for various sizes we estimate the lower size limit at which bulk-like nanoparticles actually start to become the most energetically stable titania species. This latter estimate, corresponding to the N_C size for titania, provides a guide to the size of crystalline nanoparticles which can safely be used as natural stable structural models of larger titania nanoparticles used in the experiment. Generally, our work demonstrates how *ab initio* calculations can provide lower bound estimates for N_C. In other words, we show how the intrinsic size regimes for a material's (nano)crystalline stability can be theoretically predicted.

Methodology

In this study we compare two classes of nanotitania species: (i) nanoclusters derived from bottom-up global optimisation, and (ii) nanocrystals derived from cuts from the anatase bulk phase. As the size ranges covered by these two approaches tend to be quite different, and in order to compare their respective energetic stabilities for arbitrary N, general size dependent relationships between energy and size are required for each class. Below we describe how appropriate relationships were derived in each case. The final reported structures of all nanoclusters, nanocrystals, and the bulk anatase crystal, were fully optimised using DFT calculations with no symmetry constraints employing the PBE0 hybrid functional[23] and a Tier 1/Tight basis set of numeric atom-centred orbitals, as implemented in the all-electron code FHI-AIMS.[24] This level of theory has recently been shown to be good for accurately evaluating both relative total energies and trends in the electronic structure of a range of $(TiO_2)_N$ clusters with sizes between N = 4–20.[25]

Top-down derived $(TiO_2)_N$ nanocrystals

Nanoscale titania, due to its technological importance, is intensively studied both theoretically and experimentally. Ideally, from the computational modelling perspective one would like to employ nanoparticles possessing a realistic size and structure in order to probe their properties using efficient yet acceptably accurate descriptions of their electronic structure. Generally, this entails using calculations based on density functional theory (DFT). Titania nanoparticles used in the experiment, however, typically contain many thousands of atoms; a size that is beyond the current capacity of routine computational modelling using DFT. Efforts to model the optical and electronic properties of nanotitania have thus used a variety of models ranging from nanoclusters containing only a few atoms to nanoparticles possessing up to a few hundred TiO_2 units. Often these studies have attempted to find nanoparticles of titania which retain as much as possible the bulk crystalline and electronic structure. The smallest of these nanocrystals correspond closely to the N_{meta} crossover size below which bulk-like crystallinity cannot be maintained. Nanoparticles as small as $(TiO_2)_{15}$ for rutile[26] and $(TiO_2)_{16}$ for anatase[27] have been reported, and even employed as nanocrystal models.[28] According to our definition of a nanocrystal, we rule out the $(TiO_2)_{16}$ anatase cut as a true nanocrystal due to the large change in atomic positions and accompanying changes in the local bonding of the majority of its atoms that occurs upon relaxing its structure, as also noted in other work.[27]

Herein, we employ five nanocrystals all derived from stoichiometric cuts from the bulk anatase crystal phase with between 28–84 TiO_2 units (*i.e.* 84–252 atoms), which retain their atomic structure reasonably well with respect to the original bulk atomic ordering and positions after structural relaxation (see Fig. 2). Anatase nanocrystals are experimentally

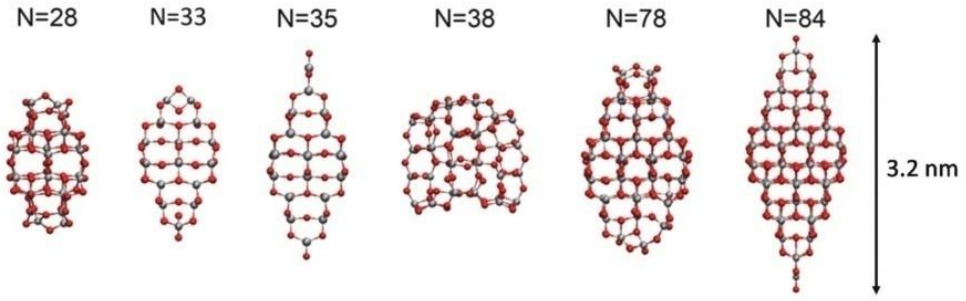

Fig. 2 Atomic structures of the top-down $(TiO_2)_N$ nanocrystals employed. Atom key: O – red, Ti – grey. Note that the scale arrow to the right strictly relates only to the size of the 252 atom $(TiO_2)_{84}$ nanocrystal – the other four nanocrystals have been scaled to show their atomic structure more clearly.

found to exhibit a {101}-faceted bipyramidal shape which typically possess some degree of {001} truncation of the apices. Such a morphology can be rationalised through by cuts of the anatase bulk crystal exposing facets whose size and shape follow their surface energies as described by the Wulff construction.[29] Our nanocrystals with N = 35 and N = 84 were cut from the parent anatase crystal so as to exhibit bipyramidal morphologies, and those with N = 33 and N = 78 units cut to have truncated bipyramidal shapes respectively. The 28 and 38 TiO_2 unit nanocrystals were taken from those studies which used a number of structural principles in order to guide the way in which they were cut from the parent anatase crystal. In particular, the structures of the N = 38 nanocrystal were fabricated according to the requirements that all atoms should have sufficient coordination to support their formal oxidation state (*i.e.* O^{2-} and Ti^{4+} for TiO_2) and that the nanocrystal should have no net dipole moment.[27,30] This procedure results in the N = 38 nanocrystal being fully-coordinated in contrast to the N = 35 and N = 84 bipyramidal nanocrystals which display two apical Ti–O terminations. In the case of the 28 unit nanocrystal a similar, albeit less formal, approach was followed whereby nanocrystals that would be as symmetric as possible in every direction were sought, while still possessing as much anatase-like structure as possible.[31] We note that for this latter $(TiO_2)_{28}$ nanocrystal the original bulk-cut yields four terminal Ti–O groups which persist even after relaxing the structure. Nevertheless, this feature does not appear to detrimentally affect the energetic stability of the nanocrystal compared to similarly sized nanocrystals considered (*i.e.* for sizes N = 33 and N = 35). Conversely, however, we also note that in ref. 31 a N = 38 bulk cut is reported which has two singly coordinated terminal oxygen atoms, which after relaxation form bonds with nearby oxygen atoms (O–O distance of 1.44 Å). This nanoparticle is not used in our study due to this very non-bulk-like feature and the fact that it is highly metastable (>5 eV) relative to the $(TiO_2)_{38}$ bulk cut we employ from ref. 27.

Under the assumption that nanoclusters grow in a perfectly spherical manner one can derive the fraction of surface atoms, $F_{surf}(N)$, to be $kN^{-\alpha}$, where $\alpha = -1/3$ and $k = 4$. Following the derivation for other cluster shapes yields different k values, while α is an unchanged general constant determined by the area-to-volume dimension of $F^{surf}(N)$. Many generic properties, $G(N)$, of simple clusters (*e.g.* total energies, ionisation energies, melting temperatures) can be approximately fitted to a scaling law of the following type:[32]

$$G(N) = G_{bulk} + a_1 N^{-1/3}, \quad (1)$$

where G_{bulk} is a characteristic constant value of the property in question for the chosen bulk phase. For small nanoclusters such fits are worse than those for larger nanoparticles due to the more extreme dependency on properties with small changes in size. This regime of small nanoclusters is often termed the size range where "every atom counts". For large facetted nanocrystals, analysing the most significant size dependent contributions to the total energy yields that it both depends on $F_{surf}(N)$ and $V_{dilate}(N)$, the volume dilation of the nanoparticle induced by surface stress.[3,33] $V_{dilate}(N)$ varies inversely with respect to the radius of the nanocrystal and thus introduces a $bN^{-1/3}$ energy dependence similar to $F_{surf}(N)$. Overall this leads to a general $E(N)$ dependence of the following form for increasingly sized large nanocrystals:[3]

$$\begin{aligned} E(N) &= E_{bulk} + a_1\left(1 - bN^{-1/3}\right)N^{-1/3} \\ &= E_{bulk} + a_1 N^{-1/3} - a_2 N^{-1/3}\cdot N^{-1/3} \\ &= E_{bulk} + a_1 N^{-1/3} - a_2 N^{-2/3}, \end{aligned} \quad (2)$$

where a_1 and a_2 are the constants when the nanocrystals are always of the same shape and crystal structure. We note that for large N, eqn (1) will increasingly become a better approximation to eqn (2) due to the relatively larger magnitude of the exponent of the last term in the latter. More generally, taking eqn (1) as representing the zeroth order dependence on N, we can see eqn (2) as the first three terms of a power series expansion of the form:

$$E(N) = a_0 + a_1 x + a_2 x^2 + a_3 x^3 + \ldots, \quad (3)$$

where $a_0 = E_{bulk}$, $x = N^{-1/3}$ and the a_n values are (possibly N dependent) constants. Eqn (2) has been used to estimate the anatase-to-rutile crossover in titania nanocrystals, with the optimisation of a_1 and a_2 for each polymorph and size considered to obtain the appropriate morphology.[3,34] In this case periodic DFT calculations of bulk titania were used to calculate the surface energies and surface stresses required to evaluate a_1 and a_2.[3] As these top-down calculated values are only strictly valid for infinite slabs, application to faceted nanocrystals was deemed acceptable to the anatase nanocrystals of a minimum size of approximately 450 TiO_2 units (corresponding to a truncated bipyramid with a B/A side length ratio of ~0.3 and side A = 2 nm).[34] Below this size it is more appropriate to perform explicit electronic structure calculations of nanocrystals.[3] In our study we use DFT calculations to directly calculate the fully relaxed structure and energetic stability of $(TiO)_N$ nanoclusters and nanocrystals with sizes $1 < N < 84$ and use these data to extrapolate to nanoparticle sizes with $N \leq 150$. Although quantities calculated for infinite surfaces should not be used in eqn (1) for this size regime, this equation still contains the essential elements to describe the stability of faceted nanocrystals, albeit with more appropriate values of a_1 and a_2.

Bottom-up derived $(TiO_2)_N$ nanoclusters

Numerous previous studies have attempted to find the lowest energy structures of small $(TiO_2)_N$ nanoclusters ($N \leq 20$) without recourse to using bulk crystalline structures.[25,26,35–42] Such a "bottom-up" approach can be attempted by hand using analogy with known nanoclusters of other materials and principles of chemical structure as in ref. 26 and 30. Such intuitive methods, however, are generally not as reliable in finding low energy structures as using global optimisation algorithms to thoroughly search the complex multidimensional potential energy surface (PES) for nanocluster isomer possibilities. The

View Article Online

Nanoscale Paper

need for efficient global optimisation tends to increase with nanocluster size as it becomes progressively more difficult to find the lowest energy structures from a bottom-up approach due to the concomitant combinatorial increase in possible atomic configurations.

Here, we employ global optimisation with classical interionic potentials (IPs) to search the PES in a computationally efficient manner, and subsequently refine the resulting low energy cluster structures using unconstrained geometry optimisations at the DFT level of theory. This general IP–DFT strategy has been employed in a number of studies[25,35,39,41,42] with various choices of IP and DFT functionals. We have found that the often-used bulk-parameterised IPs such as those reported by Matsui and Akaogi (MA)[43] are not very size-transferable for evaluating the relative stabilities and structures of small discrete $(TiO_2)_N$ species. We note, for example, that the MA IP tends to predict highly coordinated compact cluster structures to be very energetically stable,[35,42] but which are not found to be particularly low in energy compared to more open structures, when refined using DFT geometry optimizations.[39,41] In an attempt to rectify these shortcomings we have employed two strategies based on the MA IP type.

Firstly, we have taken the original MA IP parameterisation and used this together with another IP which favours the 4-coordination of oxygen ions around each cation. Specifically, we use the interaction parameters of IP by Flikkema and Bromley (FB) which was originally parameterised for $(SiO_2)_N$ nanoclusters.[44] For any particular $(TiO_2)_N$ composition we assign a percentage of the Ti cations and O anions to be treated by the FB IP and the rest by the MA IP. The is purely a formal definition within the overall mixed IP parameterisation and finally all oxygen and all titanium ions are taken to be respectively equivalent after an energy minimisation of a cluster structure. The full set of parameters for this mixed MA–FB IP approach can be found in the ESI.† The FB-treated ions energetically favour the formation of four-coordinated Ti centres largely due to the FB IP possessing a relatively higher degree of O–O repulsion. Thus, when FB-parameterised centres replace the centres originally parametrised by the MA IP (which favour 6-coordinated Ti centres) more open cluster structures are favoured. We found that replacing 30–50% of the original MA-parameterised centres by our FB-parameterised centres was optimal for improving the tendency of the mixed IP to generate low energy $(TiO_2)_N$ cluster structures. We note that this approach was employed previously in ref. 36 to generate candidate global minima for $(TiO_2)_N$ for $N = 8, 10$.

Secondly, we have re-parameterised the original MA IP to reduce its strong tendency to form highly coordinated clusters. Here, the main change was to increase the repulsion between oxygen anions for O–O separations of 1.5–2.5 Å while maintaining very similar Ti–O interaction parameters. We note that the degree of O–O repulsion in this new parameterisation is not as high as in the FB IP (see the ESI† for IP parameters). We found that, as for the mixed IP strategy, this new parameterisation of the MA IP led to low energy cluster structures with relatively less compact structures and fewer highly coordinated Ti centres.

For both the above IP-based approaches we use Monte Carlo basin hopping[45] global optimisation where we typically employ 10 runs each of typically one million steps, each one starting from a different initial structure. For the smallest sizes considered (*i.e.* $N < 15$) we note that the proposed global minima were usually obtained in runs of less than one million steps. During the run, the temperature was automatically adjusted to maintain an average acceptance ratio of new structures of between 65–80%. For the case of the mixed IP approach we also used specific oxygen–oxygen and titanium–titanium swap moves to help ensure that the best configuration of the two oxygen and two titanium types was achieved for any particular cluster structure. The lowest energy 40–50 structures resulting from the 10 runs for each cluster size were then re-optimised using FHI-AIMS with a light Tier 1 basis and the PBE[46] functional. After this refinement, the best 7–8 structures were finally optimised using our reference PBE0/tight Tier 1 settings.

In addition to attempting direct global optimisation of $(TiO_2)_N$ species, we also employed data mining[47] where we took low energy globally optimised structures of $(SiO_2)_N$[48,49] and $(CeO_2)_N$[16] and re-optimised them as corresponding $(TiO_2)_N$ nanoclusters. Specifically, we mainly tried columnar-type $(SiO_2)_N$ clusters[49] and tetrahedral $(CeO_2)_N$ fluorite-like cuts.[50] We note, for example, that in the former case low energy structures were found for sizes $N = 12$ and 18, which concurred with the results from our global optimisations. More interestingly, in the latter case, for sizes $N = 10$, 20 and 35, new candidate global minima structures were found as described below.

Results and discussion

For relatively small cluster sizes $(TiO_2)_N$ for $N = 1$–9 we could find no lower energy clusters than those reported previously in the literature indicating that global minima in this size range are reasonably well established. Specifically, our finding for $N = 1$–8 coincide with those reported in both ref. 40 and 41 where global optimisation was performed and, as in the present study, the final structures were optimised with DFT using a hybrid functional. For $N = 9$ and $N = 10$, we concur with the global minima candidate structures found in ref. 41 and 50 respectively. For $(TiO_2)_N$ nanocluster sizes with $N =$ 11–14, 16–24, 28, 35 and 38, we report new candidate global minima from our bottom-up global optimisation and data-mining approach (see Fig. 3 and 4). We note that all our reported isomers for these sizes are more energetically stable than any structures we could find in the literature (see the ESI† for a comparison between our results and those reported elsewhere). Herein, we are concerned with the structure and stability of the nanoclusters, and results pertaining to other properties (*e.g.* electronic, vibrational *etc.*) will be reported elsewhere.

In line with the assumptions made in other studies regarding the tendency for higher energetic stability and more bulk-

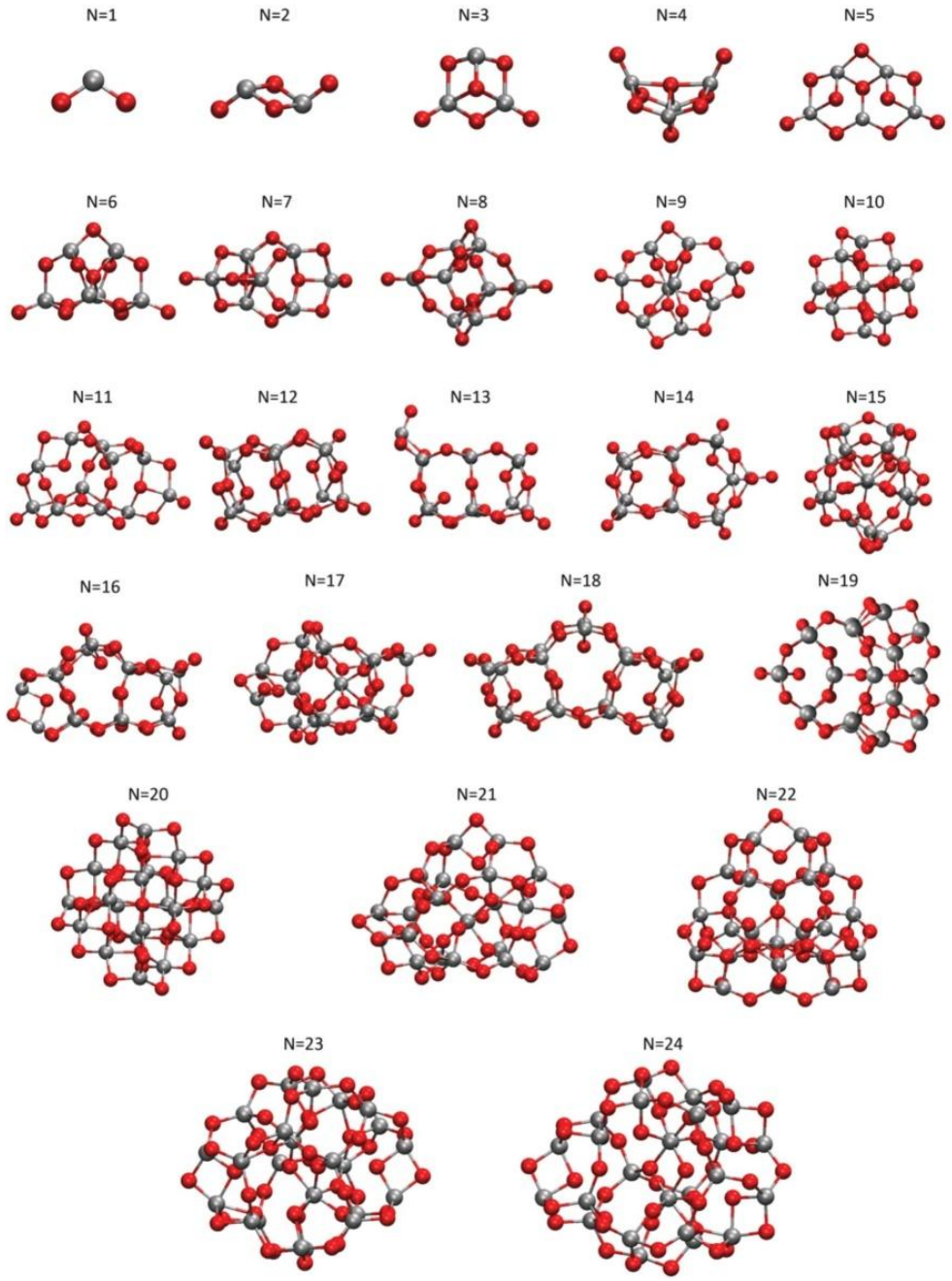

Fig. 3 Structures of the low energy bottom-up derived $(TiO_2)_N$ clusters N = 1–24 employed in this work.

like character being associated with fewer terminal dangling oxygen Ti–O defects,[26,30] our bottom-up generated set of clusters show a clear tendency to exhibit fewer such defects with increasing size. In particular all clusters we find for $N > 18$ are either fully-coordinated (*i.e.* zero terminal defects) or have at most one Ti–O defect. This tendency is also fully in line with the bottom-up studies of $(SiO_2)_N$ clusters where a similar transition to fully-coordinated clusters has been predicted to occur for sizes $N \geq 26$.[51] Generally speaking, we also see a tendency for decreasing structural symmetry in the clusters with increasing size. Although, for example, all $(TiO_2)_N$ global minima in the range N = 1–8 have some symmetry (*i.e.* greater than C_1)

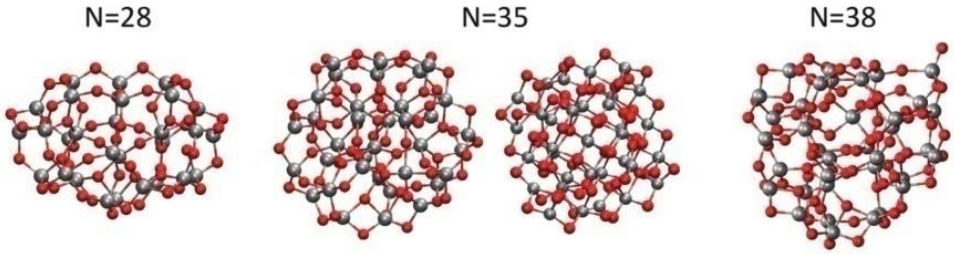

Fig. 4 Structures of low energy bottom-up derived $(TiO_2)_N$ clusters N = 28, 35 (left), 38 found in this work from global optimisation. The N = 35 (right) nanoparticle was obtained from data-mining from a tetrahedral $(CeO_2)_{35}$ nanoparticle in ref. 16 and is calculated to be marginally metastable relative to the $(TiO_2)_{35}$ nanoparticle to its left.

the propensity for our candidate global minima to be symmetric falls away to such an extent that all our lowest energy clusters for $N > 22$ are not symmetric. We note that for the size N = 35, in addition to our lowest energy NC cluster, we also find a highly symmetric and very low energy, yet non-anatase-like, cluster (see Fig. 4) which we discuss below.

Generally, our searches do not find structures which display the anatase crystal structure for N = 1–38. In particular for sizes N = 28, 35 and 38, we find NC clusters which are significantly more stable (by 7.9–9.9 eV total energy) than their correspondingly sized anatase nanocrystal counterparts (shown in Fig. 2). This clearly implies that using metastable anatase nanocrystal structures within this size range to model the behaviour of larger nanocrystals may potentially introduce significant errors, and tests are required to accurately assess the validity and consequences of such modelling approaches.

Estimating the NC ↔ C crossover size regime

Taking the DFT energies of the optimised bulk cut nanocrystals in Fig. 2 we made a fit to eqn (2) to yield a_1 and a_2 for the size range N = 1–150 (see the corresponding data points and blue fit line in Fig. 5). Strictly speaking, as the morphology of our bulk-cut nanocrystals is not always the same, a_1 and a_2 will not be the same for all of them. However, as the considered polymorph (*i.e.* anatase) is always the same and all the considered nanocrystals tend to display similar relaxed surface sites, we fit our eight data points (*i.e.* six bulk cut nanocrystals, and the limits of the infinite anatase crystal and the TiO_2 monomer) with fixed constants for all N values. We also note that by only using the Wulff-type bulk cuts (*i.e.* our bipyramids and truncated bipyramids with N = 33, 35, 78 and 84) we obtain a very similar fit.

For our low energy clusters coming from our bottom-up searches, their structures and morphologies vary immensely with size and thus a fit using eqn (2) is not justified. Instead we assume that although the basic geometric and surface stress energy components of the total energy for regular nanocrystals is captured in eqn (2), a general expansion building on this basis (see eqn (3)) would be more suitable for this diverse set. We have attempted fits using eqn (3) with polynomials from degree 3 to degree 8. We find that for degree 3 and 4 polynomial fits, the resulting extrapolated line does not cross the fit derived for the top-down nanocrystals and simply tends to zero, implying unreasonably, and against experimental evidence, that non-crystalline clusters are always more stable than anatase nanocrystals. For degree 7 and 8 polynomial fits, the extrapolated trend line is non-monotonically decreasing with increasing N, unphysically predicting a decrease in energetic stability with increasing nanoparticle size. Fits with polynomials of degree 5 and 6, however, provide almost exactly the same monotonically decreasing trend line which meets the nanocrystal fit line, which is consistent with the observations. As such, these latter expansions of eqn (3) appear to be the only ones which lead to physical consistent fits of the data. We thus used the degree 5 fit to the nanocluster data which leads to estimate a NC ↔ C crossover size of N = 125 (*i.e.* 375 atoms) as shown in Fig. 5. The fitting parameters used can be found in the ESI† along with the plots of the energetic data with respect to $N^{-1/3}$.

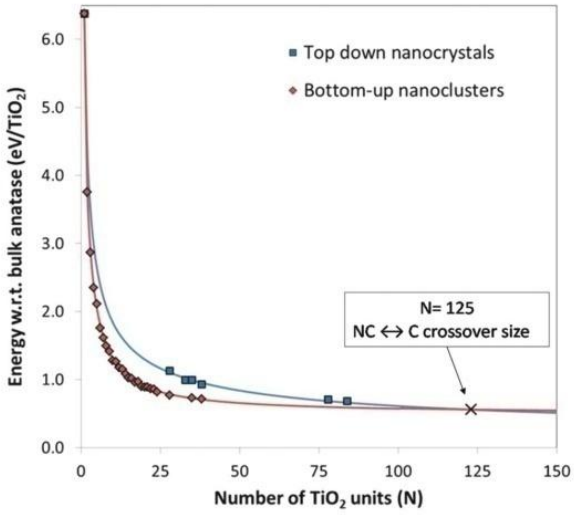

Fig. 5 Energies of bottom-up (red) generated nanoclusters and top-down (blue) generated nanocrystals with corresponding fitting lines. The NC ↔ C crossover size is indicated by a cross at 125 TiO_2 units (*i.e.* 375 atoms).

To provide an idea of the diameter of such an $N = 125$ sized nanoparticle in Fig. 6 we show a spherical semi-crystalline (*i.e.* anatase core and amorphous shell) nanoparticle of 130 TiO_2 units (~2.0 nm diameter) and a facetted anatase bulk cut of 151 TiO_2 units (~2.6 nm diameter). Accordingly, we thus predict the emergence of anatase-like crystallinity in TiO_2 nanoparticle sizes to occur in nanoparticles of approximately 2–3 nm diameter. We note that our prediction, coming purely from a theoretical basis, is fully consistent with the experimental results in ref. 12.

Crystallinity in <2–3 nm diameter non-anatase nanoparticles

Experimentally assessing the degree of crystallinity in very small nanoparticles with diameters <2 nm is clearly complicated by the fact that the concept of long range order is rather ill-defined and thus usual X-ray diffraction (XRD) methods used for larger samples are not applicable. This size regime is also where a bulk electronic structure typically starts to become significantly different from bulk samples also hindering the use of other indirect spectroscopic assessments of bulk-like structures.[52] Theoretically, we can simulate XRD patterns from arbitrarily small nanoparticles but interpreting the results of doing so are rather inconclusive with respect to comparisons with experiment. Here, for example, simulated XRD patterns from seemingly non-crystalline nanoclusters can give rise to broad peaks often taken to be indicative of bulk-like atomic ordering in experimentally measured XRD patterns.[53] To avoid complications of theoretical/experimental comparisons and the formal applicability of XRD for very small nanoparticles, we choose to assess the crystallinity of our nanoparticles through consistently calculating a single alternative measure of the atomic order for both the bulk anatase crystal and our titania nanoparticles. Specifically, we have used the atomic pair distribution function (PDF) which describes the distribution of distances between pairs of atoms in a system (*e.g.* nanoparticle, bulk material). The peaks in the PDF represent the probability to find a neighbourhood particle at the corresponding radial distance from a certain atom. In Fig. 7 we compare the PDFs of a $(TiO_2)_{35}$ top-down bulk cut nanocrystal with that of bulk anatase and the lowest energy $(TiO_2)_{35}$ nanoparticle found from our bottom-up global optimisations. Although clearly not exhibiting the detailed spectra of the perfect bulk anatase crystal, the relaxed top-down $(TiO_2)_{35}$ nanocrystal has a number of well-defined peaks of diminishing size with positions that appear to correspond to those in the bulk anatase crystal. The slight shifting of some peaks to smaller distances in the nanocrystal spectra relative to the bulk anatase spectra is likely due to the surface stress induced compression of the former. Conversely, the more energetically stable bottom-up $(TiO_2)_{35}$ nanocluster has much less well defined spectra with one main fairly broadened peak corresponding to the nearest neighbouring Ti–O bonds. Clearly, although small, the $(TiO_2)_{35}$ nanocrystal can be said to possess some crystallinity, whereas the $(TiO_2)_{35}$ nanocluster is essentially non-crystalline. In this sense, we argue that the blue and red curves, and the point at which they cross in Fig. 5, possess real meaning with respect to a NC ↔ C crossover and thus in assessing the emergence of anatase-like crystallinity with increasing nanoparticle size.

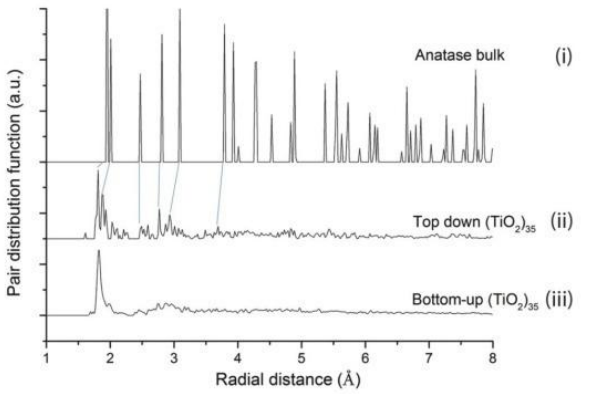

Fig. 7 Pair distribution functions calculated using the Debyer code[54] for: (i) anatase bulk-like nanocrystal, (ii) a top-down $(TiO_2)_{35}$ anatase bulk cut nanocrystal, and (iii) the lowest energy $(TiO_2)_{35}$ nanoparticle from our bottom-up global optimisations. Blue lines indicate tentative correspondence of anatase-like peaks in (i) and (ii).

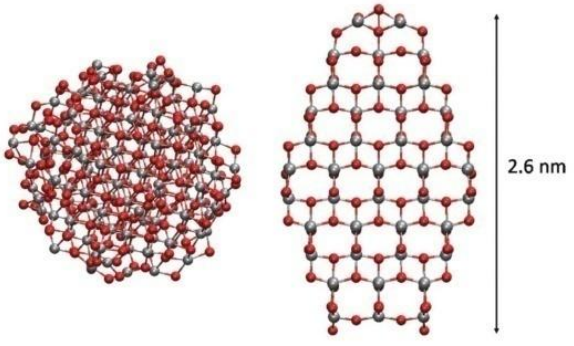

Fig. 6 Nanoparticles with sizes near to the predicted NC ↔ C crossover size. Left: A $(TiO_2)_{130}$ semi-crystalline spherical nanoparticle and right: A $(TiO_2)_{151}$ facetted bulk cut anatase nanocrystal.

Although we have predicted a NC ↔ C crossover which is consistent with experiment, and for which we clearly can define nanocrystals with anatase crystallinity that are metastable to non-crystalline nanoparticles for sizes up to $N = 125$, we also find some very low energy nanoparticles which neither appear to be anatase-like nor totally non-crystalline. Specifically, for $(TiO_2)_N$ sizes $N = 10$, 20 and 35, we obtain very energetically stable nanoclusters from data-mining from tetrahedral nanoclusters reported in ref. 16. For $N = 10$ and $N = 20$ these tetrahedral clusters are actually our best candidate global minima structures. All these nanoclusters are based on cuts from the cubic CeO_2 bulk fluorite crystal structure which has eight-coordinated Ce^{4+} ions and four-coordinated O^{2-} ions. For $(CeO_2)_N$ these bulk-cut-based nanoclusters retain the

as-cut fluorite crystal structure. However, in the case of $(TiO_2)_N$ we find that, upon relaxation, the clusters distort in a such a way as to lower the local atomic coordination of the ions (see the ESI†). This distortion is consistent with the fact that the cubic polymorphs of TiO_2 can only be stabilised at very high temperatures and pressures.[55] Relaxation from a fluorite bulk cut allowing for lowering of coordination would be consistent with a distortion to the columbite crystal structure (*i.e.* the α-PbO_2 structure, also known as the TiO_2 II phase), another known high pressure phase of TiO_2. Experimental X-ray absorption spectroscopy results report evidence for the TiO_2 II phase (*i.e.* columbite) in ~7 nm diameter titania nanoparticles[56] and geologically α-PbO_2-type TiO_2 (*i.e.* columbite) has been found naturally in nanometer sized ultrahigh-pressure inclusions.[57] Indeed, the energetically favoured prevalence for a columbite-like phase at small sizes could be consistent with the high surface stresses in such small nanoparticles which induces an effective high internal pressure. Our comparisons of the structures of the fluorite-cut-derived TiO_2 nanoparticles with the bulk columbite crystal structure, however, do not strongly support the hypothesis that the nanoparticles are simple cuts from the columbite bulk crystal. In fact, although these nanoparticles clearly possess some regular fluorite-derived atomic ordering, they do not appear to be a single phase. From some directions, for example, the clusters appear to exhibit atomic ordering reminiscent of the brookite crystal phase, predicted in some studies to be an intermediate size-dependent stable TiO_2 phase for nanoparticles with diameters between 11–35 nm.[58] The structure of the $Ti_{20}O_{40}$ fluorite-derived nanocluster and its comparison with the original data-mined structure and the brookite crystal can be found in the ESI.†

Conclusions

We present a detailed study of the size dependent energetic stability of nanoscale titania from both a bottom-up and top-down perspective. Using global optimisation and data-mining we report global minima $(TiO_2)_N$ candidates for nanoclusters in the size range N = 1–38 (*i.e.* up to 114 atoms), where in the range N = 11–38, nearly all cluster structures are new and lower in energy than those previously reported. Taking Wulff constructed bulk cuts from the anatase crystal structure and other anatase bulk cuts from the literature, we also track the energetic stability of anatase nanocrystals up to N = 84 (*i.e.* 252 atoms). From direct comparison of the two data sets we can conclude that up to N = 38 anatase nanocrystals are significantly metastable with respect to correspondingly sized non-crystalline nanoclusters. Firstly, this strongly indicates that nanocrystals in this size regime should be employed with caution when used as models of significantly larger nanocrystals and, secondly, that the crossover size at which anatase nanocrystals become more energetically stable than non-crystalline nanoclusters occurs at significantly larger sizes. Using both data sets and fitting using a generalised expansion of a top-down derived energy expression for nanoparticles, we extrapolate the fit to both data sets to predict an approximate NC ↔ C crossover size of N = 125 (*i.e.* 375 atoms). This size corresponds to a nanoparticle diameter of between 2–2.6 nm, depending on nanoparticle morphology, and corresponds well to the observed dominance of amorphous spherical titania nanoparticles of 2–3 nm diameter before facetted anatase nanocrystals tend to take over for larger sizes.[12] We hope that the approach described in this work will inspire similar studies in order to derive estimates of the fundamental NC ↔ C crossover size for a range of other important materials for which nanoscale crystallinity is a key property.

Acknowledgements

Support from Spanish MINECO/FEDER grant CTQ2015-64618-R grant and, in part, by Generalitat de Catalunya grants 2014SGR97, XRQTC is acknowledged. We also acknowledge the NOMAD Center of Excellence project (this project has received funding from the European Union's Horizon 2020 research and innovation programme under grant agreement no. 676580). Access to supercomputer resources was provided through grants from the Red Española de Supercomputación and the COMPHOTOCAT project 2014112608 of the Partnership for Advanced Computing in Europe (PRACE). We also acknowledge funding from H2020 project ITN-EJD-642294 (TCCM: Theoretical Chemistry and Computational Modelling).

References

1 H. Zhang and J. F. Banfield, *Chem. Rev.*, 2014, **114**, 9613–9644.
2 H. Zhang and J. F. Banfield, *J. Mater. Chem.*, 1998, **8**, 2073–2076.
3 A. S. Barnard and P. Zapol, *Phys. Rev. B: Condens. Matter*, 2004, **70**, 235403.
4 X. Chen and A. Selloni, *Chem. Rev.*, 2014, **114**, 9281–9282.
5 M. Kapilashrami, Y. Zhang, Y.-S. Liu, A. Hagfeldt and J. Guo, *Chem. Rev.*, 2014, **114**, 9662–9707.
6 J. Schneider, M. Matsuoka, M. Takeuchi, J. Zhang, Y. Horiuchi, M. Anpo and D. W. Bahnemann, *Chem. Rev.*, 2014, **114**, 9919–9986.
7 W. Dong, Y. Sun, C. W. Lee, W. Hua, X. Lu, Y. Shi, S. Zhang, J. Chen and D. Zhao, *J. Am. Chem. Soc.*, 2007, **129**, 13894–13904.
8 C. Jiang, K. Y. Lee, C. M. A. Parlett, M. K. Bayazit, C. C. Lau, Q. Ruan, S. J. A. Moniz, A. F. Lee and J. Tang, *Appl. Catal., A*, 2016, **521**, 133–139.
9 R. L. Penn and J. F. Banfield, *Geochim. Cosmochim. Acta*, 1999, **63**, 1549–1557.
10 S. Patra, C. Davoisne, H. Bouyanfif, D. Foix and F. Savage, *Sci. Rep.*, 2015, **5**, 10928.
11 J. F. Banfield and H. Zhang, *Mineralogical Society of America*, Washington DC, 2001, vol. 44.

12 H. Zhang, B. Chen, J. F. Banfield and G. A. Waychunas, *Phys. Rev. B: Condens. Matter*, 2008, **74**, 214106–214101.
13 K. Jacobs, J. Wickham and A. P. Alivisatos, *J. Phys. Chem. B*, 2002, **106**, 3759.
14 P. Dugourd, R. R. Hudgins and M. F. Jarrold, *Chem. Phys. Lett.*, 1997, **267**, 186–192.
15 R. Dong, X. Chen, X. Wang and W. Lu, *J. Chem. Phys.*, 2008, **129**, 044705.
16 A. Migani, K. M. Neyman and S. T. Bromley, *Chem. Commun.*, 2012, **48**, 4199–4201.
17 S. T. Bromley, I. Moreira, P. R. de, K. M. Neyman and F. Illas, *Chem. Soc. Rev.*, 2009, **38**, 2657–2670.
18 C. Chizallet, G. Costentin, M. Che, F. Delbecq and P. Sautet, *J. Am. Chem. Soc.*, 2007, **129**, 6442–6452.
19 M. C. C. Wobbe, A. Kerridge and M. A. Zwijnenburg, *Phys. Chem. Chem. Phys.*, 2014, **16**, 22052–22061.
20 C. Loschen, A. Migani, S. T. Bromley, F. Illas and K. M. Neyman, *Phys. Chem. Chem. Phys.*, 2008, **10**, 5730–5738.
21 C. A. C. Richard, S. A. French, A. A. Sokol, A. A. Al-Sunaidi and S. M. Woodley, *J. Comput. Chem.*, 2008, **13**, 2234–2249.
22 A. Erlebach, K. Heinz-Dieter, J. Grabow, F. A. Müller and M. Sierka, *Nanoscale*, 2015, **7**, 2960–2969.
23 C. Adamo and V. Barone, *J. Chem. Phys.*, 1999, **110**, 6158–6169.
24 V. Blum, R. Gehrke, F. Hanke, P. Havu, V. Havu, X. Ren, K. Reuter and M. Scheffler, *Phys. Commun.*, 2009, **180**, 2175–2196.
25 S. Bhattacharya, B. H. Sonin, C. J. Jumonville, L. M. Ghiringhelli and N. Marom, *Phys. Rev. B: Condens. Matter*, 2015, **91**, 241115.
26 Z.-W. Qu and G.-J. Kroes, *J. Phys. Chem. C*, 2007, **111**, 16808–16817.
27 P. Persson, J. C. M. Gebhardt and S. Lunell, *J. Phys. Chem. B*, 2003, **107**, 3336–3339.
28 O. Miroshnichenko, S. Auvinen and M. Alatalo, *Phys. Chem. Chem. Phys.*, 2015, **17**, 5321–5327.
29 G. Wulff, *Z. Kristallogr.*, 1901, **34**, 449–530.
30 P. Persson, R. Bergström and S. Lunell, *J. Phys. Chem. B*, 2000, **104**, 10348.
31 S. Auvinen, M. Alatalo, H. Haario, J.-P. Jalava and R.-J. Lamminmäki, *J. Phys. Chem. C*, 2011, **115**, 8484–8493.
32 R. Johnston, *Masters Series in Physics and Astronomy*, Taylor and Francis, London, 2002.
33 A. S. Barnard and P. Zapol, *J. Chem. Phys.*, 2004, **121**, 4276.
34 A. S. Barnard and L. A. Curtiss, *Nano Lett.*, 2005, **5**, 1261–1266.
35 S. Hamad, C. R. A. Catlow, S. M. Woodley, S. Lago and J. A. Mejias, *J. Phys. Chem. B*, 2005, **109**, 15741–15748.
36 M. Calatayud, L. Maldonado and C. Minot, *J. Phys. Chem. C*, 2008, **112**, 2008.
37 M. Calatayud and C. Minot, *J. Phys. Chem. C*, 2009, **113**, 12186–12194.
38 O. A. Syzgantseva, P. Gonzalez-Navarrete, M. Calatayud, S. Bromley and C. Minot, *J. Phys. Chem. C*, 2011, **115**, 15890–15899.
39 L. Tang, L. Linwei, J. Zhao and R. Qiu, *J. Comput. Chem.*, 2011, **33**, 163.
40 N. Marom, M. Kim and J. R. Chelikowsky, *Phys. Rev. Lett.*, 2012, **108**, 106801.
41 M. Y. Chen and D. A. Dixon, *J. Chem. Theory Comput.*, 2013, **9**, 3189–3200.
42 S. G. Neogi and P. Chaudhury, *J. Comput. Chem.*, 2014, **35**, 51–61.
43 M. Matsui and M. Akaogi, *Mol. Simul.*, 1991, **6**, 239–244.
44 E. Flikkema and S. T. Bromley, *Chem. Phys. Lett.*, 2003, **378**, 622–629.
45 D. J. Wales and J. P. K. Doye, *J. Phys. Chem. A*, 1997, **101**, 5111.
46 J. P. Perdew, K. Burke and M. Ernzerhof, *Phys. Rev. Lett.*, 1996, **77**, 3865–3868.
47 A. Sokol, C. R. A. Catlow, M. Miskufova, S. A. Shevlin, A. A. Al-Sunaidi, A. Walsh and S. M. Woodley, *Phys. Chem. Chem. Phys.*, 2010, **12**, 8438–8445.
48 E. Flikkema and S. T. Bromley, *J. Phys. Chem. B*, 2004, **108**, 9638–9645.
49 S. T. Bromley and E. Flikkema, *Phys. Rev. Lett.*, 2005, **95**, 185505.
50 F. Aguilera-Granja, A. Vega and L. Balbás, *J. Chem. Phys.*, 2016, **144**, 234312.
51 E. Flikkema and S. T. Bromley, *Phys. Rev. B: Condens. Matter*, 2009, **80**, 035402.
52 A. Wood, M. Giersig, M. Hilgendorff, A. Vilas-Campos, L. M. Liz-Marzán and P. Mulvaney, *Aust. J. Chem.*, 2003, **56**, 1051–1057.
53 M. A. Zwijnenburg, *Nanoscale*, 2011, **3**, 3780.
54 Debyer website: https://github.com/wojdyr/debyer. Debyer is a general program for calculating the XRD patterns and pair-distribution functions of nanoparticles.
55 M. Mattensi, J. S. de Almeida, L. Dubrovinsky, N. Dubrovinskaia, B. Johansson and R. Ahuja, *Phys. Rev. B: Condens. Matter*, 2004, **70**, 212101.
56 H. C. Choi, H.-J. Ahn, Y. M. Jung, M. K. Lee, H. J. Shin, S. B. Kim and Y.-E. Sung, *Appl. Spectrosc.*, 2004, **58**, 598.
57 S.-L. Hwang, P. Shen, H.-T. Chu and T.-F. Yui, *Science*, 2000, **288**, 321–324.
58 H. Zhang and J. F. Banfield, *J. Phys. Chem. B*, 2000, **104**, 3481.

3.1.3.3 When Anatase Nanoparticles Become Bulklike: Properties of Realistic Nanoparticles in the 1−6 nm Size Range from All Electron Relativistic Density Functional Theory Based Calculations

* UNKNOWN * | MPSJCA | JCA10.0.1465/W Unicode | ct-2017-00085p.3d (R3.6.i12 HF02:4458 | 2.0 alpha 39) 2016/10/28 09:46:00 | PROD-JCAVA | rq_8236741 | 3/02/2017 14:24:03 | 10 | JCA-DEFAULT

JCTC Journal of Chemical Theory and Computation — Article

pubs.acs.org/JCTC

When Anatase Nanoparticles Become Bulklike: Properties of Realistic TiO_2 Nanoparticles in the 1−6 nm Size Range from All Electron Relativistic Density Functional Theory Based Calculations

Oriol Lamiel-Garcia,[†] Kyoung Chul Ko,[†,‡] Jin Yong Lee,[‡] Stefan T. Bromley,[†,§] and Francesc Illas*[,†]

[†]Departament de Ciència de Materials i Química Física & Institut de Química Teòrica i Computacional (IQTCUB), Universitat de Barcelona, C/Martí i Franquès 1, 08028 Barcelona, Spain

[‡]Department of Chemistry, Sungkyunkwan University, Suwon 16419, Korea

[§]Institució Catalana de Recerca i Estudis Avançats (ICREA), 08010 Barcelona, Spain

Supporting Information

ABSTRACT: All electron relativistic density functional theory (DFT) based calculations using numerical atom-centered orbitals have been carried out to explore the relative stability, atomic, and electronic structure of a series of stoichiometric TiO_2 anatase nanoparticles explicitly containing up to 1365 atoms as a function of size and morphology. The nanoparticles under scrutiny exhibit octahedral or truncated octahedral structures and span the 1−6 nm size range. Initial structures were obtained from a Wulff construction, thus exhibiting the most stable (101) and (001) anatase surfaces. Final structures were obtained from geometry optimization with full relaxation of all structural parameters using both generalized gradient approximation (GGA) and hybrid density functionals. Results show that, for nanoparticles of a similar size, octahedral and truncated octahedral morphologies have comparable energetic stabilities. The electronic structure properties exhibit a clear trend converging to the bulk values as the size of the nanoparticles increases but with a marked influence of the density functional employed. Our results suggest that electronic structure properties, and hence reactivity, for the largest anatase nanoparticles considered in this study will be similar to those exhibited by even larger mesoscale particles or by bulk systems. Finally, we present compelling evidence that anatase nanoparticles become effectively bulklike when reaching a size of ∼20 nm diameter.

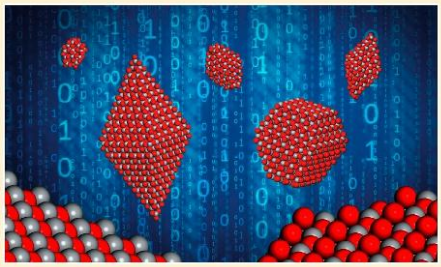

1. INTRODUCTION

Titanium dioxide (TiO_2) nanoparticles are at the heart of large number of technological applications,[1] including solar cells,[2,3] environmental cleanup,[4,5] self-cleaning surfaces,[6] and photocatalysis.[7−10] In particular, H_2 production from photocatalytic water splitting using TiO_2 nanoparticles[11,12] constitutes a promising clean and sustainable alternative to fossil fuels. Unfortunately, the rather large band gap (>3.0 eV)[13] of the most common polymorphs of titanium dioxide (anatase, rutile, and brookite) means that ultraviolet (UV) radiation is required for electronic excitation. This hinders general use as only ∼10% of the incoming photons from sunlight have enough energy to be absorbed and hence to participate in the photocatalytic process. Suitable modifications of titanium dioxide are thus actively being sought to overcome this constraint.

Several strategies, from nanostructuring[1,14] to doping with different types of elements,[15−17] have been proposed to reduce the band gap of TiO_2 so as to render the materials photocatalytic active under sunlight. The metastable anatase phase has been found to be stable in the form of nanoparticles. In turn these nanoparticles exhibit the highest photocatalytic activity, including water splitting reaction under certain conditions,[2,18−25] yet with too low activity under sunlight. The origin of the higher photocatalytic activity of anatase nanoparticles is largely unknown and likely to be the result of many factors including morphology, size, and possibly the presence of point defects and/or adsorbates. Thus, new techniques have been developed aimed at controlling the shape and size of anatase nanoparticles with the goal of optimizing their photocatalytic activity.[26] Nevertheless, experimental conditions make it difficult to discern between the different effects of size and shape and those introduced by the synthesis conditions.

To complement experiments, theoretical models can be used to investigate the effect of different morphologies for a given composition or vary the composition for a given morphology. A large amount of useful information has been gathered from electronic structure calculations of extended models of TiO_2 bulk polymorphs, including defects and/or dopants,[27−36] and of several well-defined surfaces.[37−39] However, these models lack

Received: January 26, 2017
Published: February 23, 2017

DOI: 10.1021/acs.jctc.7b00085
J. Chem. Theory Comput. XXXX, XXX, XXX−XXX

effects arising from the finite size and shape of the TiO_2 nanoparticles. To take these effects into account requires explicitly modeling $(TiO_2)_n$ nanoparticles which is computationally expensive and so far largely limited to the electronic ground state and small clusters with n in the 8−38 range.[40−48] The study of these species results in useful information although one must realize that rather small to moderately large $(TiO_2)_n$ nanoclusters typically exhibit a significant number of nonbulklike energetically low lying isomers. Since this implies that experimental measurements may provide information over an ensemble of particles rather than on the most stable structural ground state, it is necessary to investigate the properties of different isomers of TiO_2 nanoparticles. This is analogous to the bulk case of TiO_2 polymorph engineering, where similarly energetically stable yet distinct crystal structures lead to different modifications of band edges and hence band gaps due to varying local coordination.[49]

The ground state and excited electronic structure of specific low energy $(TiO_2)_n$ nonbulklike clusters in the size range n = 1−15 have been studied in detail,[41,47] but information regarding larger particles is almost inexistent with the exception of a recent study by some of us dealing with ground and excited states of small TiO_2 clusters including the most stable isomers and the low lying ones and also considering larger anatase bulk-cut $(TiO_2)_n$ particles with n up to 84.[50] The transition from nanoclusters, without a regular atomic structure, to nanocrystals exhibiting the crystal structure of the known polymorphs has also been theoretically estimated recently, and results indicate that anatase-like crystallinity emerges in titania nanoparticles of approximately 2−3 nm diameter.[51]

To help close the gap between nanoclusters and periodic models, Barnard et al.[52] developed a self-consistent tight-binding (SCTB) model that was found to be able to mimic the results obtained from density functional theory (DFT) based calculations of a moderately sized $(TiO_2)_{35}$ nanoparticle. These authors subsequently employed this SCTB approach to investigate the relative stability and atomic structure of $(TiO_2)_n$ anatase-like particles having different realistic bulk-cut morphologies exhibiting the lowest energy surfaces with n up to 455 (i.e., 1365 atoms). Unfortunately, the computational burden required to carry out explicit density functional theory based calculations for such large systems prevented reaching a more accurate description, and the details of the electronic structure based properties of these large nanoparticles remain unknown. Nevertheless, the advent of new powerful supercomputers containing thousands of cores together with the existence of newly developed computational codes which are able to fully exploit this architecture should provide the appropriate framework to undertake this challenge. The aim of the present work is precisely to provide a detailed study of the atomic and electronic structure of realistic $(TiO_2)_n$ nanoparticles, encompassing the models used by Barnard et al.[52] among others, and hence explore the convergence of stability and electronic structure related properties as a function of size and shape using a unified, consistent, and numerically accurate theoretical approach.

2. COMPUTATIONAL DETAILS

The DFT based calculations for the TiO_2 nanoparticles described in this study were carried out using the highly parallel FHI-AIMS code which is able to handle thousands of atoms with O(N) scaling.[53−55] The calculations explicitly include all electrons, and relativistic effects are accounted for at the zeroth order regular approximation (ZORA).[56,57] The atomic structures of the different nanoparticles considered in the present work were optimized at the DFT level using the Perdew-Bruke-Ernzerhof[58] (PBE) implementation of the Generalized Gradient Approximation (GGA) using a light-tier-1 numerical atom-centered orbitals (NAO) basis with quality similar to that obtained with valence triple-ζ plus polarization Gaussian Type Orbitals (GTO) as illustrated in the next section. In most cases, tight-binding optimized structures[52,59] were used as starting points which facilitates the convergence of the geometry optimization. The energy threshold for self-consistency was chosen as 10^{-5} eV. In the geometry optimization, all atoms were allowed to relax until the atomic forces were smaller than 0.001 eV/Å.

To improve the description of the electronic structure of these systems and to overcome the well-known underestimation of the band gap associated with calculations using GGA functionals,[28,60] we performed single point calculations using the optimized PBE structures with the PBE0 and PBEx hybrid functionals. The latter includes an empirically chosen 12.5% of Hartree−Fock exchange (instead of the 25% of the PBE0) so as to properly describe the electronic structure of stoichiometric and reduced rutile and anatase polymorphs/nanoparticles of TiO_2.[61,62] The single point calculations with the hybrid functionals were carried out using the same light-tier1 basis set and the same electronic convergence criteria of 10^{-5} eV for the total energy.

All calculations presented in this work were carried out the Marenostrum supercomputer of the Barcelona Super Supercomputer Center (BSC) using 1024 cores with a time limitation of 72 h per run. Within this constraint the hybrid (PBEx and PBE0) DFT based calculations for the ground state of the largest nanoparticle and the PBE open shell spin polarized calculations for the cation and anion were unfeasible. Yet, the trends from the series of calculations lead to meaningful and sound conclusions as described in detail in the forthcoming sections.

3. DEFINING THE TIO_2 ANATASE NANOPARTICLES

Ten different stoichiometric $(TiO_2)_n$ nanoparticles have been modeled with n ranging from 10 to 455 TiO_2 units hence containing up to 1365 atoms. The initial structure of these nanoparticles was obtained via Wulff constructions.[63,64] This approach relates the shape of the nanoparticle to the area of the surfaces exposed and of their relative stability. For the anatase phase of titania, the two most stable surfaces are the (101) and (001), respectively.[65] Restricting the morphology of the three-dimensional nanoparticles to those exhibiting these two surfaces leads to two kinds of structures, a first set exhibiting only the (101) surface and displaying octahedral (O_h) symmetry and a second set simultaneously exhibiting (101) and (001) surfaces displaying a truncated octahedral (TO_h) shape. In the following we will refer to both sets of nanoparticles as O_h and TO_h, and they are schematically shown in Figure 1.

Lu et al.[66] have been able to stabilize anatase nanoparticles exhibiting a large amount of the less stable (001) surface using fluorine. This finding has been later rationalized from DFT calculations and *ab initio* thermodynamics showing that F stabilizes the (001) surface and destabilizes the (101) ones.[67] Lu et al. also found that particles exhibiting the (001) facets present a higher photocatalytic activity than the nanoparticles presenting (101) surfaces only. This justifies the choice of

DOI: 10.1021/acs.jctc.7b00085
J. Chem. Theory Comput. XXXX, XXX, XXX−XXX

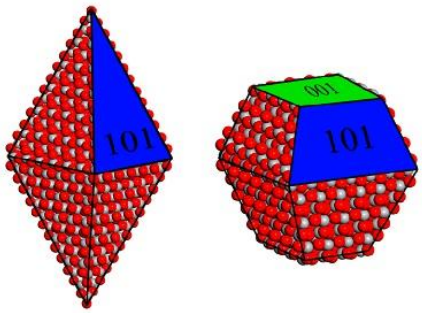

Figure 1. Schematic representation of the octahedral and cuboctahedral TiO_2 anatase nanoparticles featuring (101) and (001) surfaces.

nanoparticles studied which are displayed in Figure 2. The dimensions of these nanoparticles are between 1.3 and 6.1 nm high and 0.5−3 nm wide as measured from nucleus to nucleus or 1.6−6.4 nm high and 0.8−3.3 nm wide considering twice the O (1.52 Å) van der Waals radii,[68] as suggested by other authors.[69] Clearly, the size and shape of the nanoparticles studied in this work approach the size of experimentally synthesized nanoparticles used to probe photocatalytic water splitting.[26]

4. RESULTS AND DISCUSSION

Assessing the Quality of the NAO Basis Set Used. To assess the quality of the light-tier1 NAO basis set we compare the PBE total energy of the Ti atom and of the O_2 and TiO_2 molecules with those obtained using the widely used standard 6-311G** and TZVP basis sets. Table 1 reports the calculated energies corresponding to the formation of the TiO_2 molecule from Ti and O_2. For a proper comparison, the NAO results in Table 1 have been calculated without taking the relativistic effects into account. The calculations for the two molecules were carried out at the experimental geometry.

Table 1. Total Nonrelativistic PBE Energy of the Ti Atom (Triplet State), O_2 (Triplet State), and TiO_2 (Singlet State) As Obtained with a NAO Light-Tier1 and the GTO 6-311G and TZVP Basis Sets**

	total energy (Hartrees)		
	NAO (light-tier1)	6-311G**	TZVP
Ti	−848.3777	−848.3571	−848.3800
O_2	−149.6646	−149.6600	−149.6765
TiO_2	−998.1397	−998.0971	−998.1415
$Ti + O_2 \rightarrow TiO_2$	−0.0974	−0.0800	−0.0850

Results in Table 1 show that the energies obtained with the NAO light-tier1 basis set are always lower than those obtained with the 6-311G** GTO basis set by at least 0.004 hartree and are slightly higher than those obtained with the TZVP GTO basis set. Consequently, one can safely conclude that this NAO basis set is of triple-z plus polarization quality which provides a good compromise between accuracy and computational cost, especially given the large size of the systems treated in the present work and the high computational cost of calculations with hybrid density functionals.

Stability and Atomic Structure as a Function of Size, Shape, and Functional. In this section we analyze the convergence of relative stability and structure of the modeled nanoparticles, as a function of size and shape, taking also into account the effect of the DFT method used. First, we note that the optimization of the bulk cut nanoparticles preserves the initial shape with well-defined surfaces except in the smallest particles. In the case of the O_h particles, two different types of nearly degenerate local minima are found differing essentially in the position of the two apical oxygen atoms. In one type, the apical Ti−O bond preserves its direction as in the bulk

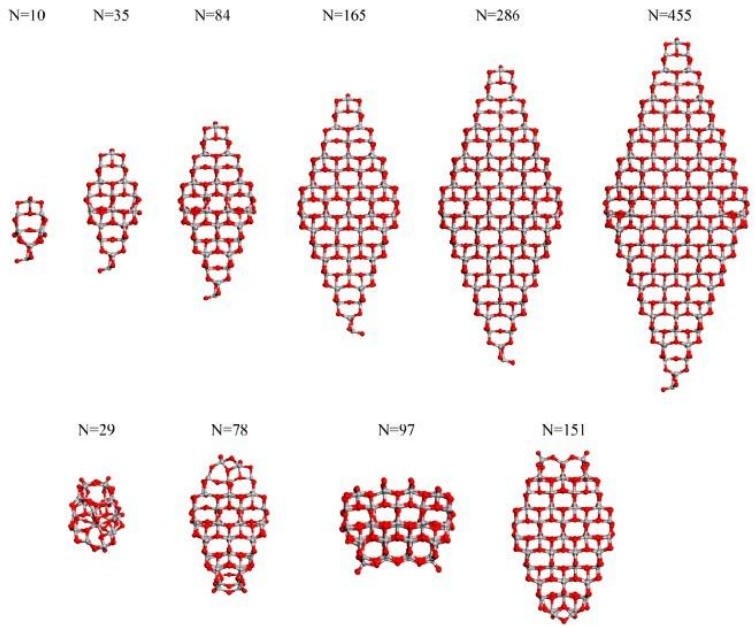

Figure 2. Octahedral (top) and cuboctahedral (bottom) $(TiO_2)_n$ nanoparticles considered in the present work.

DOI: 10.1021/acs.jctc.7b00085
J. Chem. Theory Comput. XXXX, XXX, XXX−XXX

structure, whereas in the other the Ti−O apical bond is tilted relative to the long axis of the nanoparticle (see Figure 3).

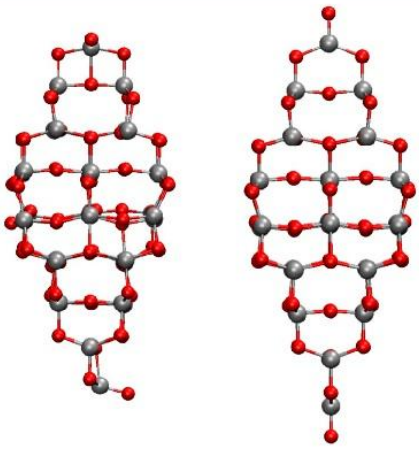

Figure 3. Two types of local minima found for the O_h type $(TiO_2)_n$ nanoparticles: tilted apical Ti−O bonds (left) and bulklike straight apical Ti−O bonds (right).

Nevertheless, for each of the O_h nanoparticles, the difference of energy per TiO_2 unit relative to anatase bulk ($\Delta E/n$) between these two stable geometries is minor (~0.009 eV/unit) except for the case of the smallest $(TiO_2)_{10}$ nanoparticle where, as expected, the small size implies large surface reconstruction/distortion effects leading to a larger energy/unit difference (0.12 eV/unit). Because of the small difference in the energy/unit of these two types of isomers (see Figure S1 in the Supporting Information), further analysis of the stability with respect to the size and the functional used will focus on the structures with the tilted apical Ti−O bonds. Results regarding the more symmetric local minima are provided in the Supporting Information.

Figure 4 plots the $\Delta E/n$ values for the optimized $(TiO)_n$ structures of the O_h and O_hT nanoparticles as obtained from calculations using the PBE functional. For comparison Figure 4 also reports the corresponding $\Delta E/n$ values for the unrelaxed bulk cut structures as well as for some of the structures as relaxed from the tight-binding method of Barnard et al.[52] which were made available by these authors. Figure 4 shows that, in all cases, $\Delta E/n$ drops rapidly with size especially in the range of the smaller nanoparticles; the largest energy decrease of 0.47 eV/unit corresponds to the increase in nanoparticle size from $(TiO_2)_{10}$ to $(TiO_2)_{35}$. With further increases in nanoparticle size, $\Delta E/n$ continues to decrease asymptotically with the decrease in $\Delta E/n$ being only 0.06 eV/unit when going from $(TiO_2)_{286}$ to $(TiO_2)_{455}$. Within the nanoparticle size range we consider $\Delta E/n$ is still significant due to the presence of terminating surfaces which necessarily introduce an energy cost relative to the infinite bulk. The $\Delta E/n$ values by PBE for fully relaxed O_h and TO_h particles approximately follow the same curve in spite of the fact that the former contains (101) facets only and the latter includes also two less stable (001) facets. This is also clear from the formation energy plots in Figure S2 calculated with respect to Ti(s) and O_2(g) where values for O_h and TO_h particles follow the same trend.

From Figure 4 the variation in $\Delta E/n$ produced by relaxation of the atomic structure from the bulk cut to the PBE optimized

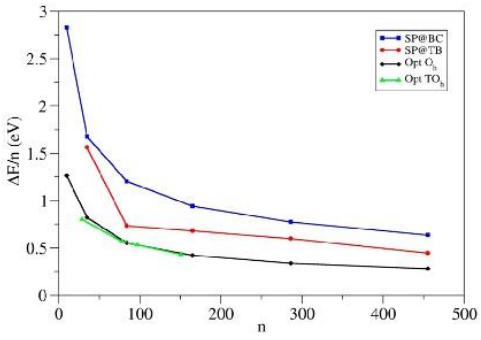

Figure 4. Energy per TiO_2 unit relative to anatase ($\Delta E/n$) for the different O_h and TO_h $(TiO_2)_n$ nanoparticles studied in the present work as obtained from calculations using the PBE functional. For comparison, the values corresponding to the unrelaxed structure cut from bulk and to the tight-binding relaxed structures from Barnard et al. are also shown.[52] Blue squares correspond to single point calculations using the bulk cut structures (SP@BC), red dots correspond to single point calculations using the tight-binding relaxed structures (SP@TB), black diamonds correspond to the optimized O_h structures (Opt O_h), and green triangles correspond to the optimized TO_h structures (Opt TO_h).

structure can also be observed. This relaxation energy is very large for the smaller particles and asymptotically decreases for the larger ones as their internal structure converges to that of the bulk. Figure 4 also shows that the relaxation is much smaller when the initial structure has been previously optimized using the tight binding method of Barnard et al.[52] although further relaxation is still required to obtain the PBE minimum energy structure. In this sense, the tight binding method can be regarded as an efficient and economic way to provide suitable starting structures for subsequent more accurate calculations.

In order to assess the influence of the density functional on the relative stability of the nanoparticles modeled, we have calculated the energies of the nanoparticles using the PBEx and PBE0 functionals using fixed geometries obtained from optimizations at the PBE level. For the relatively large nanoparticles considered in the present work, geometry optimization with the hybrid functionals is excessively demanding. Calculations with the hybrid functionals were excessively demanding for the $(TiO_2)_{455}$ particle, and some PBEx and PBE0 results for this particle have been extrapolated from corresponding data calculated for the $(TiO_2)_{286}$ nanoparticle. An indication of the influence of the functional is provided by comparing the change in $\Delta E/n$ when going from the original bulk cut to the PBE-optimized structure for each functional. For PBE, this change in $\Delta E/n$ for $(TiO_2)_{10}$ is 1.26 eV/unit, whereas for $(TiO_2)_{455}$ the corresponding $\Delta E/n$ decrease is about 0.28 eV/unit. The corresponding values for the PBEx hybrid functional are 1.39 eV/unit and 0.32 eV/unit, and for the PBE0 functional the values are 1.54 eV/unit and 0.39 eV/unit, respectively. The discussion so far relied on the structures optimized with the PBE functional. In the absence of polarons,[70] as is the case here, PBE and PBEx lead to the same optimized structure as proven for both stoichiometric anatase and rutile.[61] Hence we can safely assume that for the stoichiometric particles under scrutiny the PBEx and PBE0 functionals will also lead to almost equivalent optimized structures. Consequently, it is acceptable to claim that trends in $\Delta E/n$ are rather independent of the density functional method used. Nevertheless, for a given

DOI: 10.1021/acs.jctc.7b00085
J. Chem. Theory Comput. XXXX, XXX, XXX−XXX

particle, $\Delta E/n$ values decrease from PBE to PBEx and are followed by the PBEx and PBE0 subsequently. The effect of the functional is a consequence of the higher localization of the molecular orbitals with increasing the amount of nonlocal Fock exchange in the functional.

To assess the convergence of structure with respect to the size of the nanoparticles we focus now on two structural parameters: (i) the average Ti−O distance and (ii) the average coordination of the Ti and O atoms. In both cases we take the values of bulk anatase as the converged limit for large nanoparticles. The smallest $(TiO_2)_n$ nanoparticles with $n < 35$ have an average Ti−O distance significantly below the bulk value but which rapidly converges to the bulk value as the size of the nanoparticles increases (Figure 5, top panel). A similar trend is found for the coordination of the Ti and O atoms, but in this case the average coordination for Ti (Figure 5, middle panel) and O (Figure 5, bottom panel) converges to the bulk value more slowly. This is a result of the presence of a significant proportion of surface atoms always exhibiting lower coordination than those in the bulk.

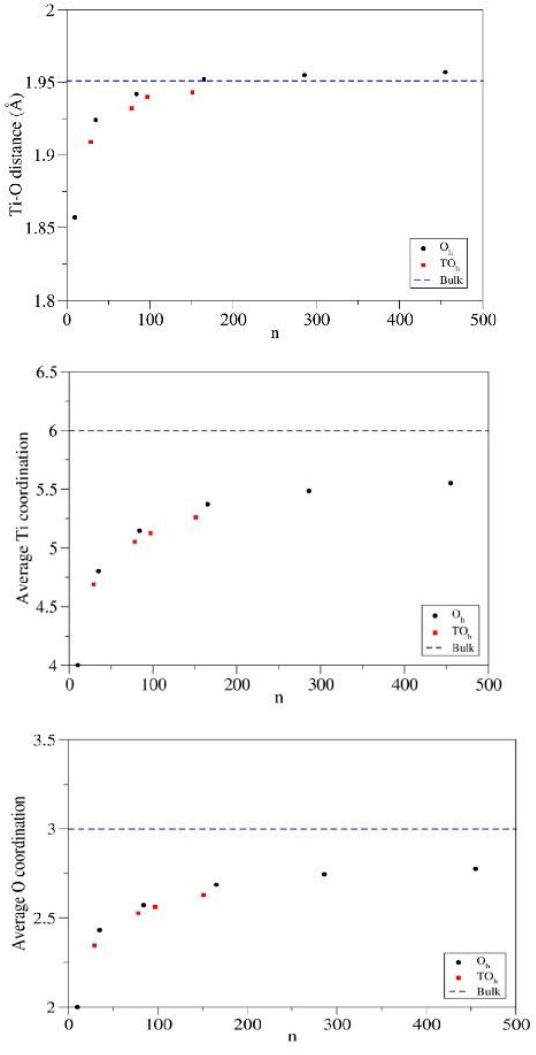

Figure 5. Average Ti−O distance (top panel), Ti coordination (middle panel), and O coordination (bottom panel) for the considered $(TiO_2)_n$ nanoparticles as a function of n. Black dots correspond to O_h, and red squares correspond to TO_h nanoparticles. The blue discontinuous lines correspond to the bulk values.

Electronic Structure Related Properties as a Function of Size, Shape, and Functional. One of the main features of TiO_2 is its photocatalytic activity, which is necessarily directly related to the electronic structure of the material in its different forms. Here, we discuss the electronic structure of the nanoparticles again focusing on the influence of size and shape and taking into account the effect of the choice of the density functional. In particular we investigate the band gap of these materials and consider both the optical and electronic gaps of the different $(TiO_2)_n$ nanoparticles following the strategy employed recently by Cho et al.[50] In all cases we use the anatase bulk values for the band gap as reference. This is justified since surface effects on the band gap of anatase have been reported to be very small. For instance, for TiO_2 nanoparticles with a diameter of 7.6 to 24 nm, the band bending from the center to the surface is only 0.004 eV only.[71]

The optical gap (O_{gap}) corresponds to the energy needed to excite an electron from the highest occupied molecular orbital (HOMO) energy level to the lowest unoccupied molecular orbital (LUMO) and is experimentally measurable from optical spectroscopy. On the other hand, the electronic gap (E_{gap}) is defined as the energy difference between the vertical ionization potential (VIP) and the vertical electron affinity (VEA) and is measured with the help of photoemission and inverse photoemission experiments. For an ideal infinite system with well delocalized valence and conduction bands both values coincide (i.e., in the absence of excitons). In fact, small excitonlike excitations have been found in rutile and anatase, but the corresponding excitation energies are of the order of a few meV only.[72−74] In the case of relatively small finite systems O_{gap} is lower than E_{gap} because of the electrostatic stabilization of the electron−hole pair interaction in the exciton state. The difference between these two energy gaps is commonly defined as the exciton binding energy and provides a measure of how bulklike a given nanoparticle of a certain size is with respect to its electronic structure.[50]

Let us start with the trends exhibited by O_{gap} which has been calculated simply as the energy difference of the corresponding Kohn−Sham energies. This is of course an approximation since an accurate treatment of the HOMO−LUMO excitation would require configuration interaction, time dependent DFT (TD-DFT), or GW many body quasi particle calculations. These levels of calculation are unfeasible for systems of the size considered in the present work. As such, the usual approach to estimating the band gap of bulk solids involves using the Kohn−Sham energy eigenvalues from band structure calculations. Since the main purpose of the present work is to explore the convergence of O_{gap} toward the bulk, it is reasonable to compare O_{gap} values for the nanoparticles and for the bulk using this widely used approach. This methodological choice is also justified from explicit TD-DFT calculations of the lowest singlet to singlet transition on $(TiO_2)_{35}$ and $(TiO_2)_{84}$ particles showing that, for a given functional, the HOMO−LUMO gap follows the same trends as those gaps obtained from TD-DFT.[50] However, because of the well-known effect of the density functional on the position of the Kohn−Sham energy levels, also evidenced in recent work,[61] O_{gap} values have been obtained using the PBE, PBEx, and PBE0 functionals, and

DOI: 10.1021/acs.jctc.7b00085
J. Chem. Theory Comput. XXXX, XXX, XXX−XXX

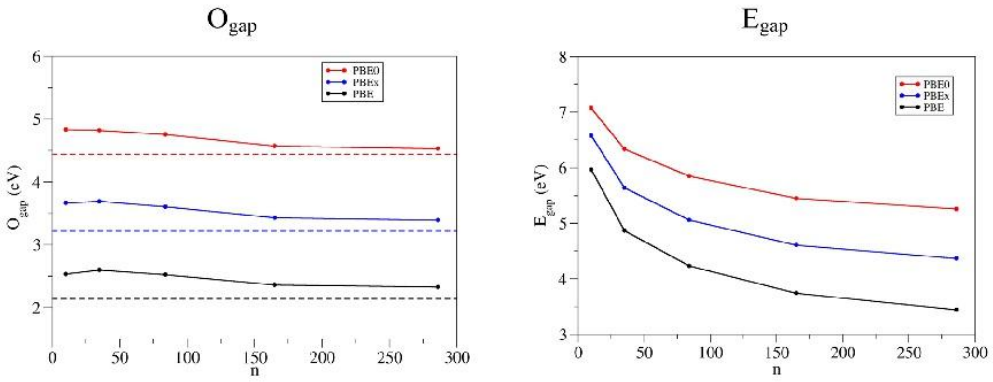

Figure 6. Optical (O_{gap}) and electronic (E_{gap}) gap calculated values for the octahedral $(TiO_2)_n$ nanoparticles as a function of n. Black, blue, and red correspond to PBE, PBEx, and PBE0, respectively, at optimized PBE geometries. The discontinuous line refers to the bulk value calculated at the same level of theory.

results for the O_h set of particles are summarized in Figure 6. Here, we recall that PBE severely underestimates the anatase experimental band gap of 3.2 eV, PBE0 overestimates it, and PBEx has been empirically adjusted to reproduce the experimental value for bulk TiO_2.[61] We note that the PBEx calculated O_{gap} values of $(TiO_2)_{84}$ and $(TiO_2)_{455}$ particles with O_h morphology, corresponding to nanoparticles with 3 and 6 nm apical diameters, are consistent with the experimentally estimated O_{gap} values of anatase nanoparticles with 3 and 6 nm sizes assumed to have a spherical shape.[75] The calculated and experimental O_{gap} values are 3.61 and 3.50 eV for the 3 nm nanoparticle and 3.34 and 3.34 eV for the 6 nm one, respectively. Hence, it appears that the PBEx functional also predicts reasonable O_{gap} values for TiO_2 nanoparticles. The same trend between functionals is observed for the O_{gap} values in Figure 6 where the most salient feature is perhaps the weak dependence of this quantity with respect to nanoparticle size. This confirms that the electronic structure converges faster than the energy ($\Delta E/n$) related properties.

Figure 6 also reports the E_{gap} values for the O_h set of particles as obtained with the three different considered functionals. The results in Figure 6 show not only that E_{gap} values are also strongly dependent on the functional used but also that they are markedly dependent on the particles size. As found for O_{gap}, lower values are obtained when using the PBE functional, higher energies for PBE0, with those corresponding to the PBEx functional in between. With respect to O_{gap}, the E_{gap} values rapidly decrease and asymptotically converge to the values of the anatase bulk band gap. For comparison and to assess the influence of the shape of the nanoparticle in this important property, Figure 7 collects the O_{gap} and E_{gap} values for the complete set of particles studied as predicted from the calculations using the PBEx hybrid functional[61] (the results for the largest particle are extrapolated as indicated above). Analysis of Figure 7 shows that, as far as electronic structure is concerned, size dominates over shape. However, for a given size O_{gap} and E_{gap} noticeably vary with shape suggesting that it may be able to tune the electronic properties by modifying the nanoparticle morphology.

Finally, we focus on the exciton binding energy (ΔE_{ex}) defined as E_{gap}-O_{gap}. The magnitude of ΔE_{ex} provides a direct measure of convergence of electronic properties toward the bulk since, in the absence of excitons as is the case in TiO_2,[72−74] the magnitude of ΔE_{ex} must tend to zero. Figure 8 plots ΔE_{ex} as a function of the number of TiO_2 units in the nanoparticles. Since E_{gap} decreases sharply with size and O_{gap}

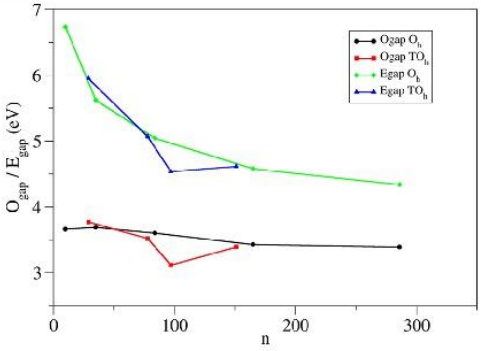

Figure 7. Optical (O_{gap}) and electronic (E_{gap}) gap calculated values for the whole set of $(TiO_2)_n$ nanoparticles, O_h and TO_h, as a function of n as predicted from the PBEx calculations at the PBE optimized geometry. Black dots and red squares refer to O_{gap} for O_h and TO_h nanoparticles, respectively. Green diamonds and blue triangles correspond to E_{gap} values for O_h and TO_h nanoparticles, respectively.

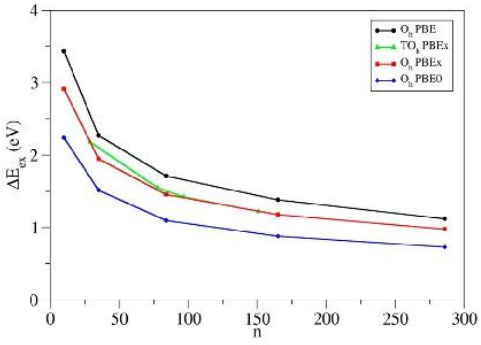

Figure 8. Exciton binding energy for the whole set of $(TiO_2)_n$ nanoparticles, O_h and TO_h, as a function of n as predicted from the different considered density functionals. Black dots, red squares, and blue diamonds correspond to O_h nanoparticles at PBE, PBEx, and PBE0 levels, respectively. Green triangles correspond to PBEx results for TO_h nanoparticles.

DOI: 10.1021/acs.jctc.7b00085
J. Chem. Theory Comput. XXXX, XXX, XXX−XXX

decreases more gradually, ΔE_{ex} exhibits a decreasing trend with size moving from energy values of about 3 eV at the PBEx level to less than 1 eV for the largest ones. This latter value fits well with predictions based on extrapolating results from smaller particles.[50] In addition, the present results allow one to define the size at which the TiO_2 nanoparticles will exhibit a bulk electronic structure. To this end, and following the strategy used in our previous work,[50] Figure 9 plots ΔE_{ex} for the

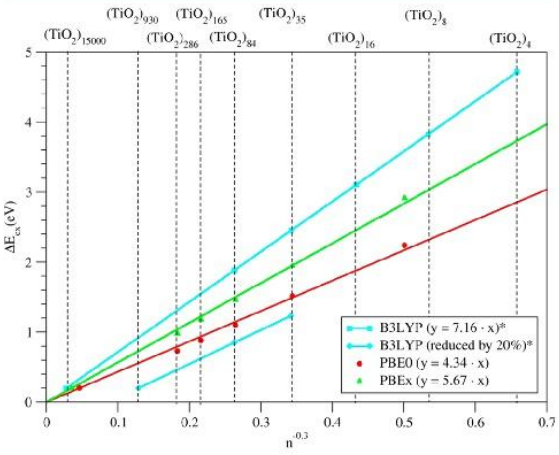

Figure 9. Exciton binding energy for the O_h set of $(TiO_2)_n$ nanoparticles as a function of $n^{-1/3}$ as predicted from the PBE0 and PBEx hybrid density functionals. Red circles and green triangles correspond to values obtained with the PBE0 and PBEx hybrid functionals, respectively. Blue lines correspond to the nonrelativistic B3LYP/6-31G(d) values for a set of smaller particles (upper blue line) and to the values scaled by 20% (bottom blue line) to take into account the overestimation of the band gap at the B3LYP level as taken from ref 50.

$(TiO_2)_n$ particles with O_h morphology as a function of $n^{-1/3}$. Consistent with the results of previous work,[50] the data in Figure 9 follow linear trends. The present PBE0 and PBEx fit lines lying in between those for smaller particles predicted by nonrelativistic B3LYP calculations within a standard GTO basis set of 6-31G(d) quality and the same B3LYP results scaled down by 20% to empirically correct for the B3LYP overestimate of band gap of anatase. The linear plots in Figure 9 allow one to make a prediction of the number of TiO_2 units a particle should have to have an exciton shift within the limits of accuracy of experiment (taken to be approximately ±0.1 eV). Thus, assuming that an exciton shift of or smaller than 0.2 eV is indicative of bulk behavior, the trends in Figure 9 indicate that this limit is reached by O_h particles of 22810, 15000, and 10218 TiO_2 units for the PBE0, B3LYP, and PBEx hybrid functionals, with a clear trend following the amount of Fock exchange (25, 20, and 12.5%) included in the functionals. In terms of TiO_2 units this may appear as a rather broad range, but this is very much reduced when focusing on the particle size. For the $(TiO_2)_n$ particles with O_h morphology a linear relationship exists between the particle height and $n^{1/3}$ (see Figure S3 in the Supporting Information). From this relationship one can readily find that the height of particles of 22810, 15000, and 10218 units is 18.1, 20.6, and 23.8 nm, respectively. Therefore, one can safely conclude that the onset size for bulklike electronic properties is of ∼20 nm apical diameter in an anatase O_h nanoparticle exhibiting the most stable (101) surfaces, a prediction in full agreement with previous indications extracted from significantly smaller nanoparticles.[50]

5. CONCLUSIONS

A systematic study has been presented of the atomic and electronic structure of realistic $(TiO_2)_n$ nanoparticles with $n \leq 455$ from relativistic, all electron density fucntional theory based calculations using a sufficiently large atom-centered numerical orbital basis set. Three different density functionals have been used, each differing in the amount of Fock exchange included (0% in PBE to 25% in PBE0). Interestingly, the main conclusions regarding qualitative trends in relative stability and electronic structure are consistent and independent of the functional used.

The energy per TiO_2 unit $(\Delta E/n)$ of the systems studied decreases as the size of the particle increases, as expected, with size effects dominating over morphology. In fact, octahedral and truncated octahedral nanoparticles exhibit similar size dependent stabilities. Note, however, that for very small sizes the truncated octahedral nanoparticles are similarly stable, or even more stable, than the octahedral nanoparticles. However, at larger sizes the effect of the different surfaces starts to become more important, and the octahedral nanoparticles become more energetically stable than the truncated nanoparticles.

Comparing the level of theory used in the calculations and the different starting point geometries, we can see that nanoparticles directly cut from the bulk are highly metastable and still require significant optimization of their structure. Part of this structural relaxation is well captured by the tight-binding approach of Barnard et al.,[52] although further optimization at the PBE level still has a considerable effect on the structure and energetic stability.

Regarding the electronic structure, the main conclusions are that the optical gap only varies slightly with size, whereas the electronic gap quickly converges with size to the value of the bulk band gap of anatase calculated at the same level of theory. This is confirmed by the explicit calculation of the exciton binding energy that shows smooth convergence toward zero (bulk behavior) for O_h particles of ∼20 nm between the apical corner sites. This implies that nanoparticles of size equal or larger than the largest ones studied in the present work would present electronic structure features, and hence photocatalytic activity, similar to that expected for bulk like anatase samples.

A final caveat is necessary here since the overall study presented in this work holds for TiO_2 nanoparticles in gas phase or in vacuum, whereas photocatalysis, especially water splitting, takes place in an aqueous environment. The presence of water will likely result in heavily hydroxylated nanoparticles with possible effects on both atomic and electronic structure trends. The effect of water on this type of nanoparticle is being currently studied in our laboratory.

■ ASSOCIATED CONTENT

Supporting Information

The Supporting Information is available free of charge on the ACS Publications website at DOI: 10.1021/acs.jctc.7b00085.

Energy per unit for the bent and symmetric O_h nanoparticles, formation energy of the O_h and TO_h particles as a function of size, particle height as a function of $n^{(1/3)}$ for the O_h particles, Cartesian coordinates of all TiO_2

DOI: 10.1021/acs.jctc.7b00085
J. Chem. Theory Comput. XXXX, XXX, XXX−XXX

particles as optimized at the PBE level using the NAO light-tier1 basis set (PDF)

AUTHOR INFORMATION

Corresponding Author

*E-mail: francesc.illas@ub.edu.

ORCID

Jin Yong Lee: 0000-0003-0360-5059

Francesc Illas: 0000-0003-2104-6123

Funding

This research was supported by the Spanish MINECO/FEDER CTQ2015-64618-R grant and, in part, by Generalitat de Catalunya (grants 2014SGR97 and XRQTC) and by the NOMAD Center of Excellence project, which received funding from the European Union's Horizon 2020 research and innovation programme under grant agreement No 676580. J.Y.L. acknowledges the financial support by the Ministry of Science, ICT and Future Planning, subjected project to the project EDISON (Education-research Integration through Simulation On the Net, Grant No. 2012M3C1A6035359). K.C.K. acknowledges the financial support by the Basic Science Research Program through the National Research Foundation of Korea (NRF) funded by the Ministry of Education (NRF-2016R1A6A3A11933303). O.L.G is grateful to the Universitat de Barcelona for a predoctoral grant, and F.I. acknowledges additional support from the 2015 ICREA Academia Award for Excellence in University Research. Computational time at the Marenostrum supercomputer has been provided by the Barcelona Supercomputing Centre through grants from Red Española de Supercomputación and the COMPHOTOCAT project 2014112608 of the Partnership for Advanced Computing in Europe (PRACE).

Notes

The authors declare no competing financial interest.

ACKNOWLEDGMENTS

The authors are very much indebted to Prof. Peter Zapol for having made available the TB-DFT optimized structures reported in ref 52 and to Prof. Volker W. Blum for continuous support on efficient use of the FHI-AIMS code.

REFERENCES

(1) Chen, X.; Mao, S. S. Titanium Dioxide Nanomaterials: Synthesis, Properties Modifications and Applications. *Chem. Rev.* **2007**, *107*, 2891−2959.

(2) O'Regan, B.; Gratzel, M. A Low-Cost, High-Efficiency Solar Cell Based on Dye-Sensitized Colloidal TiO_2 Films. *Nature* **1991**, *353* (6346), 737−740.

(3) Gratzel, M. Photoelectrochemical Cells. *Nature* **2001**, *414* (6861), 338−344.

(4) Hoffmann, M. R.; Martin, S. T.; Choi, W.; Bahnemann, D. W. Environmental Applications of Semiconductor Photocatalysis. *Chem. Rev.* **1995**, *95*, 69−96.

(5) Mills, A.; Davies, R. H.; Worsley, D. Water-Purification by Semiconductor Photocatalysis. *Chem. Soc. Rev.* **1993**, *22*, 417−425.

(6) Yaghoubi, H.; Taghavinia, N.; Alamdari, E. K. Self Cleaning TiO_2 Coating on Polycarbonate: Surface Treatment, Photocatalytic and Nanomechanical Properties. *Surf. Coat. Technol.* **2010**, *204*, 1562−1568.

(7) Fox, M. A.; Dulay, M. T. Heterogeneous Photocatalysis. *Chem. Rev.* **1993**, *93*, 341−357.

(8) Xu, H.; Ouyang, S.; Liu, L.; Reunchan, P.; Umezawa, N.; Ye, J. Recent Advances in TiO_2-Based Photocatalysis. *J. Mater. Chem. A* **2014**, *2*, 12642−12661.

(9) Hashimoto, K.; Irie, H.; Fujishima, A. TiO_2 Photocatalysis: A Historical Overview and Future Prospects. *Jpn. J. Appl. Phys.* **2005**, *44*, 8269−8285.

(10) Fujishima, A.; Zhang, X.; Tryk, D. A. TiO_2 Photocatalysis and Related Surface Phenomena. *Surf. Sci. Rep.* **2008**, *63*, 515−582.

(11) Chen, X. B.; Shen, S. H.; Guo, L. J.; Mao, S. S. Semiconductor-Based Photocatalytic Hydrogen Generation. *Chem. Rev.* **2010**, *110*, 6503−6570.

(12) Kudo, A.; Miseki, Y. Heterogeneous Photocatalyst Materials for Water Splitting. *Chem. Soc. Rev.* **2009**, *38*, 253−278.

(13) Kavan, L.; Gratzel, M.; Gilbert, S. E.; Klemenz, C.; Scheel, H. J. Electrochemical and Photoelectrochemical Investigation of Single-Crystal Anatase. *J. Am. Chem. Soc.* **1996**, *118*, 6716−6723.

(14) Fernandez-Garcia, M.; Martinez-Arias, A.; Hanson, J. C.; Rodriguez, J. A. Nanostructured Oxides in Chemistry: Characterization and Properties. *Chem. Rev.* **2004**, *104*, 4063.

(15) Asahi, R.; Morikawa, T.; Ohwaki, T.; Aoki, K.; Taga, Y. Visible-Light Photocatalysis in Nitrogen-doped Titanium Oxides. *Science* **2001**, *293*, 269−271.

(16) Asahi, R.; Morikawa, T.; Irie, H.; Ohwaki, T. Nitrogen-Doped Titanium Dioxide as Visible-Light-Sensitive Photocatalyst: Designs, Developments, and Prospects. *Chem. Rev.* **2014**, *114*, 9824−9852.

(17) Calatayud, D.; Jardiel, T.; Peiteado, M.; Illas, F.; Giamello, E.; Palomares, F.; Fernández Hevia, D.; Caballero, A. Synthesis and Characterization of Blue Faceted Anatase Nanoparticles Through Extensive Fluorine Lattice Doping. *J. Phys. Chem. C* **2015**, *119*, 21243−21250.

(18) Chen, X.; Shen, S. H.; Guo, L. J.; Mao, S. S. Semiconductor-based Photocatalytic Hydrogen Generation. *Chem. Rev.* **2010**, *110*, 6503−6570.

(19) Pelaez, M.; Nolan, N. T.; Pillai, S. C.; Seery, M. K.; Falaras, P.; Kontos, A. G.; Dunlop, P. S. M.; Hamilton, J. W. J.; Byrne, J. A.; O'Shea, K.; Entezari, M. H.; Dionysiou, D. D. A Review on the Visible Light Active Titanium Dioxide Photocatalysts for Environmental Applications. *Appl. Catal., B* **2012**, *125*, 331−349.

(20) Hoffmann, M. R.; Martin, S. T.; Choi, W.; Bahnemann, D. W. Environmental Applications of Semiconductor Photocatalysis. *Chem. Rev.* **1995**, *95*, 69−96.

(21) Fox, M. A.; Dulay, M. T. Heterogeneous Photocatalysis. *Chem. Rev.* **1993**, *93*, 341−357.

(22) Ravelli, D.; Dondi, D.; Fagnoni, M.; Albini, A. Photocatalysis. A Multi-faceted Concept for Green Chemistry. *Chem. Soc. Rev.* **2009**, *38*, 1999−2011.

(23) Kudo, A.; Miseki, Y. Heterogeneous Photocatalyst Materials for Water Splitting. *Chem. Soc. Rev.* **2009**, *38*, 253−278.

(24) Yuliati, L.; Yoshida, H. Photocatalytic Conversion of Methane. *Chem. Soc. Rev.* **2008**, *37*, 1592−1602.

(25) Chen, X.; Shen, S. H.; Guo, L. J.; Mao, S. S. Semiconductor-based Photocatalytic Hydrogen Generation. *Chem. Rev.* **2010**, *110*, 6503−6570.

(26) Liu, G.; Yang, H. G.; Pan, J.; Yang, Y. Q.; Lu, G. Q. M.; Cheng, H. M. Titanium Dioxide Crystals with Tailored Facets. *Chem. Rev.* **2014**, *114*, 9559−9612.

(27) Mattioli, G.; Filippone, F.; Alippi, P.; Bonapasta, A. Ab Initio Study of the Electronic States Induced by Oxygen Vacancies in Rutile and Anatase TiO_2. *Phys. Rev. B: Condens. Matter Mater. Phys.* **2008**, *78*, 241201.

(28) Di Valentin, C.; Pacchioni, G. Spectroscopic Properties of Doped and Defective Semiconducting Oxides from Hybrid Density Functional Calculations. *Acc. Chem. Res.* **2014**, *47*, 3233−3241.

(29) Morgan, B. J.; Watson, G. W. Intrinsic n-type Defect Formation in TiO_2: A Comparison of Rutile and Anatase from GGA+U Calculations. *J. Phys. Chem. C* **2010**, *114*, 2321−2328.

(30) Stausholm-Møller, J.; Kristoffersen, H. H.; Hinnemann, B.; Madsen, G. K. H.; Hammer, B. DFT+U Study of Defects in Bulk Rutile TiO_2. *J. Chem. Phys.* **2010**, *133*, 144708.

DOI: 10.1021/acs.jctc.7b00085
J. Chem. Theory Comput. XXXX, XXX, XXX−XXX

(31) Mattioli, G.; Alippi, P.; Filippone, F.; Caminiti, R.; Bonapasta, A. Deep versus Shallow Behavior of Intrinsic Defects in Rutile and Anatase TiO_2 Polymorphs. *J. Phys. Chem. C* **2010**, *114*, 21694−21704.
(32) Finazzi, E.; Di Valentin, C.; Pacchioni, G.; Selloni, A. Excess Electron States in Reduced Bulk Anatase TiO_2: Comparison of Standard GGA, GGA+U, and Hybrid DFT Calculations. *J. Chem. Phys.* **2008**, *129*, 154113.
(33) Islam, M. M.; Bredow, T.; Gerson, A. Electronic Properties of Oxygen-Deficient And Aluminum-Doped Rutile TiO_2 from First Principles. *Phys. Rev. B: Condens. Matter Mater. Phys.* **2007**, *76*, 045217.
(34) Janotti, A.; Varley, J. B.; Rinke, P.; Umezawa, N.; Kresse, G.; Van de Walle, C. G. Hybrid Functional Studies of the Oxygen Vacancy in TiO_2. *Phys. Rev. B: Condens. Matter Mater. Phys.* **2010**, *81*, 085212.
(35) Deák, P.; Aradi, B.; Frauenheim, T. Quantitative Theory of the Oxygen Vacancy and Carrier Self-Trapping in Bulk TiO_2. *Phys. Rev. B: Condens. Matter Mater. Phys.* **2012**, *86*, 195206.
(36) Tosoni, S.; Lamiel-Garcia, O.; Fernández-Hevia, D.; Doña, J. M.; Illas, F. Electronic Structure of F-doped Bulk Rutile, Anatase and Brookite Polymorphs of TiO_2. *J. Phys. Chem. C* **2012**, *116*, 12738−12746.
(37) Lazzeri, M.; Vittadini, A.; Selloni, A. Structure and Energetics of Stoichiometric TiO_2 Anatase Surfaces. *Phys. Rev. B: Condens. Matter Mater. Phys.* **2001**, *63*, 155409.
(38) Gong, X. Q.; Selloni, A. Reactivity of Anatase TiO_2 Nanoparticles: The Role of the Minority (001) surface. *J. Phys. Chem. B* **2005**, *109*, 19560−19562.
(39) Morgan, B. J.; Watson, G. W. A DFT+U Description of Oxygen Vacancies at the TiO_2 Rutile (110) Surface. *Surf. Sci.* **2007**, *601*, 5034−5041.
(40) Auvinen, S.; Alatalo, M.; Haario, H.; Jalava, J. P.; Lamminmäki, R. J. Size and Shape Dependence of the Electronic and Spectral Properties in TiO_2 Nanoparticles. *J. Phys. Chem. C* **2011**, *115*, 8484−8493.
(41) Li, S. G.; Dixon, D. A. Molecular Structures and Energetics of the (TiO2)n (n = 1−4) clusters and their anions. *J. Phys. Chem. A* **2008**, *112*, 6646−6666.
(42) Aguilera-Granja, F.; Vega, A.; Balbas, L. C. New structural and electronic properties of $(TiO_2)_{10}$. *J. Chem. Phys.* **2016**, *144*, 234312.
(43) Auvinen, S.; Alatalo, M.; Haario, H.; Vartiainen, E.; Jalava, J. P.; Lamminmaki, R. J. Refractive Index Functions of TiO_2 Nanoparticles. *J. Phys. Chem. C* **2013**, *117*, 3503−3512.
(44) Berardo, E.; Hu, H. S.; van Dam, H. J. J.; Shevlin, S. A.; Woodley, S. M.; Kowalski, K.; Zwijnenburg, M. A. Describing Excited State Relaxation and Localization in TiO2 Nanoparticles Using TD-DFT. *J. Chem. Theory Comput.* **2014**, *10*, 5538−5548.
(45) Persson, P.; Christof, J.; Gebhardt, M.; Lunell, S. The Smallest Possible Nanocrystals of Semiionic Oxides. *J. Phys. Chem. B* **2003**, *107*, 3336−3339.
(46) Shevlin, S. A.; Woodley, S. M. Electronic and Optical Properties of Doped and Undoped $(TiO_2)_n$ Nanoparticles. *J. Phys. Chem. C* **2010**, *114*, 17333−17343.
(47) Fernando, A.; Dimuthu, K. L.; Weerawardene, M.; Karimova, N. V.; Aikens, C. M. Quantum Mechanical Studies of Large Metal, Metal Oxide, and Metal Chalcogenide Nanoparticles and Clusters. *Chem. Rev.* **2015**, *115*, 6112−6216.
(48) Berardo, E.; Hu, H. S.; Shevlin, S. A.; Woodley, S. M.; Kowalski, K.; Zwijnenburg, M. A. Modeling Excited States in TiO_2 Nanoparticles: On the Accuracy of a TD-DFT Based Description. *J. Chem. Theory Comput.* **2014**, *10*, 1189−1199.
(49) Buckeridge, J.; Butler, K. T.; Catlow, C. R. A.; Logsdail, A. J.; Scanlon, D. O.; Shevlin, S. A.; Woodley, S. M.; Sokol, A. A.; Walsh, A. Polymorph Engineering of TiO_2: Demonstrating How Absolute Reference Potentials Are Determined by Local Coordination. *Chem. Mater.* **2015**, *27*, 3844−3851.
(50) Cho, D.; Ko, K. C.; Lamiel García, O.; Bromley, S. T.; Lee, J. Y.; Illas, F. Effect of Size and Structure on the Ground and Excited State Electronic Structure of TiO_2 Nanoparticles. *J. Chem. Theory Comput.* **2016**, *12*, 3751−3763.
(51) Lamiel Garcia, O.; Cuko, A.; Calatayud, M.; Illas, F.; Bromley, S. T. Predicting Size-Dependent Emergence of Crystallinity in Nanomaterials: Titania Nanoclusters Versus Nanocrystals. *Nanoscale* **2017**, *9*, 1049−1058.
(52) Barnard, A. S.; Erdin, S.; Lin, Y.; Zapol, P.; Halley, J. W. Modeling the Structure and Electronic Properties of TiO_2 Nanoparticles. *Phys. Rev. B: Condens. Matter Mater. Phys.* **2006**, *73*, 205405.
(53) Blum, V.; Gehrke, R.; Hanke, F.; Havu, P.; Havu, V.; Ren, X.; Reuter, K.; Scheffler, M. Ab Initio Molecular Simulations with Numeric Atom-centered Orbitals. *Comput. Phys. Commun.* **2009**, *180*, 2175−2196.
(54) Havu, V.; Blum, V.; Havu, P.; Scheffler, M. Efficient O(N) Integration for All-electron Electronic Structure using Numerically Tabulated Basis Functions. *J. Comput. Phys.* **2009**, *228*, 8367−8379.
(55) Ren, X.; Rinke, P.; Blum, V.; Wieferink, J.; Tkatchenko, A.; Sanfilippo, A.; Reuter, K.; Scheffler, M. Resolution-of-identity Approach to Hartree-Fock, Hybrid Density Functionals, RPA, MP2, and GW with Numeric Atom-centered Orbital Basis Functions. *New J. Phys.* **2012**, *14*, 053020.
(56) Chang, C.; Pelissier, M.; Durand, M. Regular Two-Component Pauli-Like Effective Hamiltonians in Dirac Theory. *Phys. Scr.* **1986**, *34*, 394.
(57) van Lenthe, E.; Baerends, E. J.; Snijders, J. G. Relativistic Regular Two-component Hamiltonians. *J. Chem. Phys.* **1993**, *99*, 4597.
(58) Perdew, J. P.; Burke, K.; Ernzerhof, M. Generalized Gradient Approximation Made Simple. *Phys. Rev. Lett.* **1996**, *77*, 3865−3868.
(59) The tight-binding structures were kindly provided by Peter Zapol, private communication.
(60) Sousa, C.; Tosoni, S.; Illas, F. Theoretical Approaches to Excited States Related Phenomena in Oxide Surfaces. *Chem. Rev.* **2013**, *113*, 4456−4495.
(61) Ko, K. C.; Lamiel-García, O.; Lee, J. Y.; Illas, F. Performance of a Modified Hybrid Functional in the Simultaneous Description of Stoichiometric and Reduced TiO_2 Oolymorphs. *Phys. Chem. Chem. Phys.* **2016**, *18*, 12357.
(62) Kim, S.; Ko, K. C.; Lee, J. Y.; Illas, F. Single oxygen vacancies of $(TiO_2)_{35}$ as a prototype reduced nanoparticle: implication for photocatalytic activity. *Phys. Chem. Chem. Phys.* **2016**, *18*, 23755.
(63) Wulff, G. On the question of speed of growth and dissolution of crystal surfaces. *Z. Kristallogr.* **1901**, *34*, 449−530.
(64) Bromley, S. T.; Moreira, I. De P.R.; Neyman, K.-M.; Illas, F. Approaching nanoscale oxides: models and theoretical methods. *Chem. Soc. Rev.* **2009**, *38*, 2657−2670.
(65) Lazzeri, M.; Vittadini, A.; Selloni, A. Structure and energetics of stoichiometric TiO_2 anatase surfaces. *Phys. Rev. B: Condens. Matter Mater. Phys.* **2001**, *63*, 155409.
(66) Yang, H. G.; Sun, C. H.; Qiao, S. Z.; Zou, J.; Liu, G.; Smith, S. C.; Cheng, H. M.; Lu, G. Q. Anatase TiO_2 Single Crystals with a Large Percentage of Reactive Facets. *Nature* **2008**, *453*, 638−641.
(67) Lamiel-Garcia, O.; Tosoni, S.; Illas, F. Relative Stability of F-Covered TiO_2 Anatase (101) and (001) Surfaces from Periodic DFT Calculations and ab Initio Atomistic Thermodynamics. *J. Phys. Chem. C* **2014**, *118*, 13667−13673.
(68) Bondi, A. van der Waals Volumes and Radii. *J. Phys. Chem.* **1964**, *68*, 441.
(69) Duanmu, K.; Friedrich, J.; Truhlar, D. G. Thermodynamics of Metal Nanoparticles: Energies and Enthalpies of Formation of Magnesium Clusters and Nanoparticles as Large as 1.3 nm. *J. Phys. Chem. C* **2016**, *120*, 26110−26118.
(70) Di Valentin, C.; Finazzi, E.; Pacchioni, G.; Selloni, A.; Livraghi, S.; Paganini, M. C.; Giamello, E. N-doped TiO_2: Theory and experiment. *Chem. Phys.* **2007**, *339*, 44−56.
(71) Zhang, Z.; Yates, J. T., Jr. Band bending in semiconductors: chemical and physical consequences at surfaces and interfaces. *Chem. Rev.* **2012**, *112*, 5520−5551.
(72) Pascual, J.; Camassel, J.; Mathieu, H. Fine Structure in the Intrinsic Absorption Edge of TiO_2. *Phys. Rev. B: Condens. Matter Mater. Phys.* **1978**, *18*, 5606−5614.

DOI: 10.1021/acs.jctc.7b00085
J. Chem. Theory Comput. XXXX, XXX, XXX−XXX

786 (73) Tang, H.; Levy, F.; Berger, H.; Schmid, P. E. Urbach tail of
787 anatase TiO_2. *Phys. Rev. B: Condens. Matter Mater. Phys.* **1995**, *52*,
788 7771−7774.
789 (74) Kang, W.; Hybertsen, M. S. Quasiparticle and Optical Properties
790 of Rutile and Anatase TiO_2. *Phys. Rev. B: Condens. Matter Mater. Phys.*
791 **2010**, *82*, 085203.
792 (75) Almquist, C. B.; Biswas, P. Role of Synthesis Method and
793 Particle Size of Nanostructured TiO_2 on Its Photoactivity. *J. Catal.*
794 **2002**, *212*, 145−156.

DOI: 10.1021/acs.jctc.7b00085
J. Chem. Theory Comput. XXXX, XXX, XXX−XXX

Overview:

With the aim of studying the stability and electronic properties of bulk-like and non-bulk-like TiO_2 nanostructures we performed DFT calculations on a set of representative nanoparticles of the two families. We found that the smaller nanoclusters, in the size range of 0.5 – 3.2 nm diameter, to present electronic structure features which depend more on their structure and morphology than their size. This can be explained by the large and irregular potential energy surface presented in this range of nanostructures and especially for this material. This leads to very different structures with very different electronic properties in a small range of energetic stability. This suggests that as the difference in energetic stability for a same size is relatively narrow, several isomers of each size need to be studied to derive from them their electronic properties.

In the range of structures studied in the work presented in the first part of the chapter the exciton binding energy is significant, with or without the inclusion of solvent. This is especially important for the smallest nanoclusters and has been observed to change with size. From these results we can extract that, for a certain size we can expect a bulk like behavior where the exciton binding energy becomes almost zero. Another important conclusion is that the free charge carriers calculated for these clusters are thermodynamically able to perform the water splitting reaction. However the systems that present a more stable exciton state are only able to do it when the solvation effect is taken into account.

In the second article presented in this chapter we provide new ground state candidates for nanoclusters with sizes between 11 and 38 TiO_2 units. They have been found to be more stable than all the candidates previously reported on the literature and in good agreement with the trend shown for smaller sizes. Also crystalline nanoclusters up to 84 units (252 atoms) were also studied in this work, finding the nanocrystal of 38 units to be significantly metastable in comparison with the non-crystalline nanoclusters. This is an indication that using nanocrystals models of this size as a representative model of these systems should be done with caution. The nanocrystals of this size and smaller are found to present a higher energy than the correspondingly sized amorphous systems. Another important conclusion extracted from this work comes from the extrapolating of the fitting of the energetic stability of both types of structures, nanoclusters and nanocrystalline TiO_2 structures. The predicted stability extrapolated for larger sizes of

both types of systems indicates that the crossover point where the order of stability changes between the nanoclusters to the nanocrystals should be around 125 units (375 atoms). By applying the Wulff construction models and the previous knowledge from the other nanocrystals modeled, we can predict that this size corresponds to nanoparticles of around 2.6 nm depending on the morphology of the nanoparticle. This is an important size to know where the amorphous spherical nanoclusters become less stable than the crystalline bulk-like nanoparticles. This gives a valuable information about when to use each nanoparticle model approach in order to accurately predict the properties of the systems studied.

Continuing with the results obtained from the study of the evolution of the electronic and energetic properties of TiO_2 nanoparticles with size in the nanocrystals regime we can extract several important conclusions. Firstly find that the geometrical features like Ti-O distances, oxygen average coordination and titanium average coordination quickly converge to the bulk values with size. Also it has been shown that the stability of the octahedral nanocrystals and truncated octahedral nanocrystals is similar. The energy per TiO_2 unit ($\Delta E/n$) of the systems studied decreases as the size of the particle increases, as expected, with size effects dominating over morphology.

Otherwise the convergence of the electronic properties is much slower than the energetic stability. Showing that the optical gap (HOMO-LUMO gap) remains almost constant as the size increases but with small fluctuations. Meanwhile the electronic gap converges much faster with size. This is very interesting as it indicates the reduction of the exciton binding energy with size. This points to a convergence to bulk structure electronic properties with size and allows us to predict at which range of size the nanocrystals would show bulk like properties. We estimate that this size would be around 15000 TiO_2 units.

Chapter 4.2

Zinc Oxide (ZnO)

3.2 Zinc oxide (ZnO)

Zinc oxide (ZnO) in its wurtzite phase has become a very popular material for diverse technological applications (e.g. semiconductors, transistors, photodetectors, blue and UV-light laser diodes, gas sensors, etc.) due to its unique semiconducting properties. ZnO has relatively large exciton binding energies and presents a band gap of around 3.4 eV, enabling ultraviolet light absorption. These features motivated our study of ZnO.

Apart from this large range of technological applications, recently there has been an increased from interest the scientific community in catalytical properties of ZnO. This material is already used in sulphur vulcanization processes, methanol synthesis, dissociation of water and sulphur hydride, and others.[70–75]The catalytic and specific electronic properties shown by ZnO makes it a very promising photocatalyst. There have been an increasing number of publications studying the photocatalytic activity of ZnO in the last decades, finding interesting applications related to dye decomposition, alcohol photodegradation, and water splitting reactions.[76]

The photocatalytic activity of this ZnO is still under study and a matter of debate. The features related with the activity are still not clear and several experimental works relate the photocatalytic activity with structural factors. Many studies carried out in recent years explored very different morphologies for ZnO nanoparticles, finding different photocatalytic activity response depending on the type of structure presented by the nanoparticles. This points to structural features and characteristics being an important key point related with the photoactivity.

A wide range of different ZnO structures can be obtained by changing the methodology used during the synthesis process. Regarding this fact, it has been pointed out that the presence of a higher ratio of polar surfaces with respect to other stable non-polar surfaces implies a higher photoactivity. These results present in the literature motivated us to study the importance of the $(000\bar{1})$ polar surfaces of ZnO on its photocatalytic activity compared to other stable non-polar surfaces for wurtzite ZnO like the $(10\bar{1}0)$ and $(11\bar{2}0)$ surfaces.

Following the research on ZnO, and motivated by the variety of stable polymorphs presented by ZnO reported in the literature like we have studied a variety of polymorphs and nanostructures. Wurtzite (WZ) is the most stable polymorph of ZnO for large

periodic systems. The body centered tetragonal (BCT) structure has been predicted to be a very stable crystal structure when ZnO is presented as several layers or thin films. For smaller finite systems another type of nanostructures has been reported to be especially stable in the literature. Here cage-like nanostructures formed from graphene-like layers are found to be stable. These structure consists in hexagonal layers of ZnO include that include some Zn_2O_2 motifs in their structure which allows them to fold into a cage-like shape, that in some cases can contain another smaller cage-like structure inside. We refer to them as single-layered cages (SC) and multi-layered cages nanocages (MC). Another crystalline structure(SOD-ZnO) based on these tacking of small $Zn_{12}O_{12}$ single-layered sodalite cages has also been predicted to rather stable and is also studied.

This wide landscape of different stable structures for ZnO and the evidences in the literature that the crossover between the smaller very stable nanocages and WZ type clusters is not clear, motivated us to perform a study to elucidate the preference of stability of all these polymorphs mentioned previously at different sizes, to know which kind of structures is more stable respect to the others depending on their size. The results obtained from this systematic study that covers the range of a few ZnO units to over 1000 units is presented in the following manuscript.

3.2.1 Morphology effects in photoactive ZnO nanostructures: photooxidative activity of polar surface

Journal of Materials Chemistry A

PAPER

View Article Online
View Journal

Cite this: DOI: 10.1039/c5ta01111f

Morphology effects in photoactive ZnO nanostructures: photooxidative activity of polar surfaces†

Ana Iglesias-Juez,*[a] Francesc Viñes,[b] Oriol Lamiel-García,[b] Marcos Fernández-García[a] and Francesc Illas*[b]

A series of ZnO nanostructures with variable morphology were prepared by a microemulsion method and their structural, morphological, and electronic properties were investigated by a combined experimental and theoretical approach using microscopy (high resolution transmission electron microscopy) and spectroscopic (X-ray diffraction, Raman, and UV-visible) tools, together with density functional theory calculations. The present experimental and computational study provides a detailed insight into the relationship between surface-related physicochemical properties and the photochemical response of ZnO nanostructures. Specifically, the present results provide evidence that the light-triggered photochemical activity of ZnO nanostructures is related to the predominance of highly-active (polar) surfaces, in particular, the amount of Zn-terminated (0001) surfaces, rather than band gap sizes, carrier mobilities, and other variables usually mentioned in the literature. The computational results highlight the oxidative capability of polar surfaces, independently of the degree of hydration.

Received 10th February 2015
Accepted 12th March 2015

DOI: 10.1039/c5ta01111f

www.rsc.org/MaterialsA

1. Introduction

Wurtzite zinc oxide (ZnO), also known as zinczite, is a material of technological interest mostly due to its peculiar optical and electronic properties: ZnO displays high electron mobilities and thermal conductivities, and a direct bandgap (~3.4 eV) with large exciton binding energies (~60 meV),[1–3] stimulating its usage in a great deal of technological devices including semiconductors,[4] field-effect transistors,[5] photodetectors,[6] blue- and UV-light emitting and laser diodes,[7–9] gas sensors,[10–12] piezoelectric generators,[13] transparent electrodes,[14] and cells for solar light harvesting.[15–17]

As long as its chemistry is concerned, ZnO has recently become the focus of many research endeavours considering it as a possible catalyst for a variety of reactions.[18] Apart from its long-standing use in rubber sulphur vulcanization[19] and its promoter key role in methanol synthesis when using the ternary copper-based $Cu/ZnO/Al_2O_3$ catalyts,[20–22] ZnO has been suggested as a suitable catalyst for water[23] and sulphur hydride[24] dissociations, desulfurization processes,[25,26] the water gas shift reaction,[27] CO_2 activation,[28] and, finally, for the conversion of maleic anhydride into 1,4-butanediol.[29,30]

At the overlap of the catalytic potential and the above-commented UV-light absorption capability one unfolds the photocatalytic aspect. ZnO has been a long-time posed material for light-triggered catalysis, with many studies even pointing a better quantum and reaction yield than titanium oxide (TiO_2).[31,32] The number of studies tackling the photocatalytic usage of ZnO bloomed in the last decade; mainly on dye decomposition[33–36] but also for the treatment of volatile organic compounds,[37] peroxide synthesis,[38] water splitting,[39] and alcohol photodegradation.[40,41]

Nevertheless, the photocatalytic process is far from being mastered, and the aspects governing the catalytic activity and selectivity are still a matter of debate. Hitherto many experimental works have addressed the issue of relating the photocatalytic activity with structural factors by sampling a plethora of ZnO morphologies; from single crystal surfaces,[42] to thin films,[35] powders,[32] nanostructures featuring a great diversity of sizes and shapes (*e.g.* rods, disks, rings, screw caps, burgers, tubes, hourglasses, trigonal prisms, toilet brushes, spheres, abalone shells, and so on),[37,41,43–48] and, eventually, nanoparticles with well-defined facets.[31,33,44,45] From such studies many aspects affecting the photochemical process can be invoked. For instance, concerning the acid brown 14 dye degradation, it has been shown that media acidity seems to affect the reaction, but whereas a basic medium enhances the yield for ZnO it hinders the yield for TiO_2 photocatalyst.[31] Surprisingly, recent studies did not reveal any correlation

[a]Instituto de Catálisis y Petroleoquímica, CSIC, c/Marie Curie 2, Cantoblanco, 28049 Madrid, Spain. E-mail: ana.iglesias@icp.csic.es

[b]Departament de Química Física & Institut de Química Teòrica i Computacional (IQTCUB), Universitat de Barcelona, c/Martí i Franquès 1, 08028 Barcelona, Spain. E-mail: francesc.illas@ub.edu

† Electronic supplementary information (ESI) available. See DOI: 10.1039/c5ta01111f

between the photochemical activity and the nanoparticle size[33] or surface area.[41]

Furthermore, relatively few of these studies analyse in detail the direct relation between the ZnO morphology and the enhanced photocatalytic activity. The nanostructured morphology (primary/secondary particle size and shape) of the catalyst can be controlled depending on the synthesis method, the solvent employed, the addition of capping agents, and/or eventually the growing conditions.[37,41,43,49] The synthesized oxide may feature distinct polar/nonpolar facet ratios depending on the experimental procedure, and this is often argued to be a key aspect on the photochemical catalytic activity. However, the discussion remains open to a large extent. On one hand, Mclaren and coworkers[33] have shown that a higher proportion of polar surfaces, *i.e.* hexagonal disk-like nanoparticles, show a higher photocatalytic activity towards the methylene blue dye decomposition, in line with the results of Li *et al.* for the *N*-formylation of aniline.[43] In the former work[33] it is posed that the Zn-terminated (0001) polar surface is responsible for the high catalytic activity, backed by the study of Xu and colleagues on phenol degradation.[41]

The idea behind such hypothesis is that such a surface—together with the O-terminated $(000\bar{1})$—is the most unstable one, *i.e.* it exhibits the highest surface energy, and so is prone to attach the reactants, although this explanation neglects the photochemical aspect. However, other authors[33,41,43] also speculate on the possible critical role of surface oxygen vacancies on ZnO surfaces. Nonetheless, pristine polar surfaces suffer from an electric dipole instability issue, and in fact, do feature a variety of reconstructions which generally involve surface vacancies.[50,51] Last but not least, although in some cases the role of nonpolar surfaces is ruled out,[33,41] Kislov *et al.* have recently shown that the nonpolar surfaces of ZnO present the highest photochemical activity for the methyl orange dye degradation.[42]

As long as the alcohol photodegradation is concerned, little is known on the key aspects governing the photocatalytic activity. Typically phenol is used as a probe molecule for liquid-phase photodegradation studies whereas isopropanol is the test case in the gas-phase counterpart.[52] Regardless of that, isopropanol is commonly used as a liquid-phase hydroxyl scavenger additive.[53,54] The previous studies of phenol photodegradation on ZnO nanostructures point out that the Zn-terminated (0001) polar surface is the most catalytically active,[41] and that ZnO nanoparticles exhibit a superior activity than TiO_2 ones.[55] This enhanced activity is also observed in the pioneering work of Kulkarni and Wachs on the photooxidation of isopropanol, in which it was found that ZnO selectively converts isopropanol into acetone *via* dehydrogenation.[32] In this latter work the pivotal role of acid/basic sites on the catalytic activity and specificity was posed.

In the present work we explore the relationship between the ZnO morphology and the chemical activity in a series of nanometric samples and analyse the structural/electronic and chemical differences encountered for different nanostructures as a function of the specific surface planes exposed to the media, either naked or hydrated, but also, for polar terminations, including surface defects. To this end, ZnO wurtzite nanoparticles were synthesized by means of a microemulsion method and have been characterized by X-Ray Diffraction (XRD) patterns and High-Resolution Transmission Electron Microscopy (HR-TEM) images together with Density Functional (DF) calculations on reliable model systems. The information obtained was used to rationalize the chemical properties exhibited by ZnO nanostructures in the photoelimination of isopropanol vapour. The structural and electronic characteristics of the polar/nonpolar faces are at the origin of the reactive response of ZnO nanoparticles but many details are, as above described, unknown. Here we attempt to address this issue and found evidence that the exposure of polar surfaces and, more explicitly, of Zn-terminated (0001) surfaces, is at the heart of the ZnO activity.

2. Experimental section

2.1. Experimental details

Materials were prepared using a microemulsion method using *n*-heptane (Scharlau) as the organic medium, Triton X-100 ($C_{14}H_{22}O(C_2H_4O)_n$) (Aldrich) as the surfactant, and hexanol (Aldrich) as the cosurfactant. Zn was introduced from the nitrate from (Aldrich). Water/Zn molar ratio was fixed at 110 and water/surfactant molar ratio was varied from 36 (sample **A**), to 18 (sample **B**), and finally 9 (sample **C**). After introduction of Zn into the aqueous phase and 30 min of stirring, a double quantity of tetramethylammonium-hydroxide was introduced from the aqueous phase of a similar microemulsion. The resulting mixture was stirred for 24 h, centrifuged, and the separated solid precursors rinsed with methanol and dried at 110 °C for 12 h. The Brunauer–Emmett–Teller (BET) surface areas and average pore volume and sizes were measured by nitrogen physisorption (Micromeritics ASAP 2010). The samples present a BET area of 47, 25, and 23 $m^2\ g^{-1}$ for **A**, **B**, and **C** materials, respectively. XRD profiles were obtained with a Seifert D-500 diffractometer using Ni-filtered Cu Kα radiation with a 0.02° step and fitted using the Von Dreele approach to the Le Bail method.[56]

HR-TEM were recorded on a JEOL 2100F TEM/STEM microscope. Specimens were prepared by dripping an ethanol suspension of the samples to be investigated onto a copper grid supporting a perforated carbon film. Raman spectroscopy was also carried out to explore the structural characteristics of the ZnO nanostructures. Raman spectra were acquired using a Horiba iH320 spectrometer and He:Ne laser excitation (632.8 nm). UV-visible diffuse reflectance spectroscopy experiments were performed with a Shimadzu UV2100 apparatus with a nominal resolution of *ca.* 1 nm using $BaSO_4$ as the reference. Band gap analysis was carried out following standard procedures (for a direct band gap semiconductor) by plotting $(h\nu A)^2$ (where $h\nu$ = excitation energy and A = absorption coefficient) *vs.* energy.

2.2. Computational details

Different slab models have been constructed to simulate the ZnO nanoparticle facets. From the present (see below) and

previous XRD studies[16,33,37,41,45] it is clear that wurtzite ZnO preferentially displays the nonpolar $(10\bar{1}0)$ and $(11\bar{2}0)$ surfaces, and the Zn- and O-terminated (0001) and $(000\bar{1})$ polar surfaces, respectively. Nonpolar surfaces can perfectly feature an unreconstructed termination whereas polar surfaces suffer from a well-known surface energy instability issue. Considering ZnO as an ionic material (with the caveat that is in the fringe region of ionic compounds), the different charged terminations of the polar surfaces exhibit a net dipole moment, which *de facto* increases with the separation between them. This introduces an electrostatic component to the surface energy that diverges with the surface separation.[57,58]

There are various ways to nullify this dipole moment. The bulk cut termination may exist involving a charge transfer from the electron-rich O-terminated $(000\bar{1})$ surface to the electron-poor Zn-terminated (0001) surface. However, despite such charge transfer is feasible for systems with few layers, it becomes unrealistic for the systems contemplated here. So, for nanometer-sized ZnO (0001)/$(000\bar{1})$ systems it has been found that pristine terminations must feature 1/4 ML of surface vacancies to compensate the under/overcharge.[59] Many previous studies reveal a variety of surface reconstructions as a function of O_2 and H_2 pressure.[50,51,60] Besides this, it has been found that when fully hydrogenated/hydrated both polar surfaces show a perfect (1×1) arrangement, *i.e.* apparently no surface defects.[61–63] Because of this, we decided to consider the ideal pristine polar surface models only as a conceptual reference for dehydrogenation/dehydration processes, thus allowing for decoupling desorption from the surface reconstruction (vacancy formation) process.

To ascertain how the electronic structure affects the photochemical activity we investigated pristine nonpolar surfaces and polar surfaces with surface vacancies. Moreover, following the previous investigations,[64] we considered also fully hydrated ZnO surfaces, *e.g.* saturation coverage, which imply one half coverage of the surface Zn atoms by hydroxyls on the (0001) surface, one half coverage of the surface O atoms by H on the $(000\bar{1})$ surface, a mixed H_2O dissociated situation for the nonpolar $(10\bar{1}0)$ surface, and a fully dissociated situation for the nonpolar $(11\bar{2}0)$ surface, these being the most stable situations, also featuring almost the same density of adsorbed water molecules per surface area—fragments, *i.e.*, hydroxyl and atomic H groups coming from a water molecule scission in the case of polar surfaces—, in particular, 0.05 fragments $Å^{-2}$ for (0001)/$(000\bar{1})$ polar surfaces, and 0.06 and 0.07 H_2O molecules $Å^{-2}$ for $(10\bar{1}0)$ and $(11\bar{2}0)$ surfaces, respectively. Further details on these structures and their stability are found in ref. 64 and references therein. Note in passing by that surface slab models were constructed, for the sake of convenience, from the orthorhombic bulk unit cell, sketched in Fig. 1, containing 8 atoms (4O + 4Zn) instead of the usual hexagonal bulk unit cell, containing 4 atoms (2O + 2Zn).

Following a widely used computational scheme, 8-layer slabs have been used to represent each of the four surfaces, in which the uppermost four layers are completely allowed to relax whereas the bottommost four layers are kept fixed as in the bulk-optimized positions—*a.k.a.* 4 + 4 approximation—. The

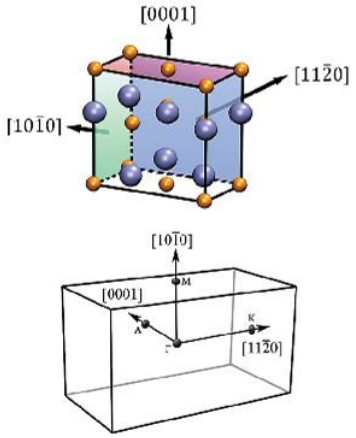

Fig. 1 Crystallographic wurtzite bulk ZnO on the orthorhombic unit cell showing the preferential surface orientations (upper image) and the corresponding reciprocal unit cells (lower image).

present tests and several past studies by different working groups reveal that such slab widths and relaxation approximation are enough to ensure converged results of surface properties.[65–75] Note however that cleavage energies of polar surfaces are actually derived with an extrapolation to infinite slab thickness.[66,67,69]

Vacancy-free pristine surfaces have been modeled using (1×1) primitive unit cells. For polar surfaces containing vacancies and for hydrated surfaces larger supercells have been employed. The (001) polar surfaces simulating 1/4 vacancies on both O- and Zn-terminations have been constructed using a (1×2) supercell based on the orthorhombic cell depicted in Fig. 1, which relates to the primitive $p(1 \times 1)$ unit cell through the $\begin{pmatrix} 2 & 0 \\ -1 & 2 \end{pmatrix}$ matrix transformation of the unit cell vectors. For both terminations, this supercell contains four surface atoms and, for each termination, one surface atom has been removed, thus modeling the 1/4 vacancy concentration at each termination, while maintaining the ZnO stoichiometry as well. The 1/2 coverage of hydroxyls on the (0001) surface and the 1/2 coverage of H on the $(000\bar{1})$ surface has been modelled using the (1×1) orthorhombic unit cell obtained from the primitive one through a $\begin{pmatrix} 1 & 0 \\ -1 & 2 \end{pmatrix}$ matrix transformation.

The H_2O mixed dissociated situation on the nonpolar $(10\bar{1}0)$ surface, as profusely studied both experimentally and theoretically, has been modeled using a (2×1) unit cell,[64,76,77] whereas a (1×1) unit cell is adequate for the fully dissociated situation on the nonpolar $(11\bar{2}0)$ surface.[64] A minimum vacuum of 1 nm was applied in the surface direction to avoid interaction between repeated slabs. A counter dipole was set in the middle of the vacuum gap to compensate long-range dipole–dipole interactions among repeated slabs for pristine polar surfaces. An optimal Monkhorst-Pack **k**-points grid of $17 \times 17 \times 1$ has been used for the ZnO surface calculations, guaranteeing an energy convergence below 0.01 kJ mol^{-1} as tested using denser grids.

The present DF calculations were performed with the VASP code,[78] carrying out periodic Kohn–Sham calculations for the above-described surface slab models. The projector augmented wave method has been used to represent atomic core effect on the valence electron density.[79] This representation of the core states allows one to obtain converged results—variations in energy below 0.01 kJ mol^{-1}—with a cut-off kinetic energy of 415 eV for the plane-wave basis set. Geometry optimizations were performed using a conjugated gradient algorithm and applying a tetrahedron smearing method with Blöchl corrections. The structural optimization was finalized when forces acting on atoms were below 0.01 kJ mol^{-1} pm^{-1}. Unless stated otherwise, all calculations were carried out in a non spin-polarized fashion. All DF calculations have been carried out using the Perdew–Burke–Ernzerhof (PBE) exchange correlation (xc) functional.[80] This xc functional has proven to deliver a realistic description of bulk ZnO and low-index Miller surface structures.[57,60,61,64]

Note that PBE, among other xc functionals, severely underestimates materials bandgap. Indeed, the bandgap for ZnO is here computed to be 0.83 eV, quite small compared to the experimental value of 3.4 eV,[1–3] but in line with previous PBE values of 0.83 eV of Alkauskas and Pasquarello,[81] and of 0.9 eV of Moreira *et al.*[82] This drawback can be compensated by using hybrid xc functionals, in which the incorporation of Hartree–Fock exchange counteracts this deficiency. For instance, ZnO bandgap calculated using the Becke–Lee–Yang–Parr (B3LYP)[83] xc is 3.34 eV,[84] quite close to the experimental value. Another way of solving this issue is to carry many body GW calculations, which deliver a bulk ZnO value of 3.08 eV.[85] More importantly, a direct proportionality of GW and PBE bandgap values was found in this latter study, which, applied to our calculated value, provides a bandgap of 3.32 eV, quite close to the experimental value. This allows discussion of computationally more economic PBE-based bandgaps, which are nevertheless connected to correct values.

Surface energies for the (4 + 4) slabs have been obtained following a procedure detailed in the past (see *e.g.* ref. 86). In summary, the surface energy of the truncated bulk slab, γ^{fix}, is defined as;

$$\gamma^{\mathrm{fix}} = \frac{E^{\mathrm{fix}}_{\mathrm{slab}} - E_{\mathrm{bulk}}}{2A} \quad (1)$$

where $E^{\mathrm{fix}}_{\mathrm{slab}}$ is the total energy of the slab unit cell containing two equal surfaces, and E_{bulk} is the total energy of the slab atoms in the bulk environment. A is the area of each surface created within the slab unit cell. Given that γ^{fix} is known, one can extract the surface energy of a relaxed surface, γ^{rel}, from the following equation:

$$\gamma^{\mathrm{rel}} = \frac{E^{\mathrm{rel}}_{\mathrm{slab}} - E_{\mathrm{bulk}}}{A} - \gamma^{\mathrm{fix}} \quad (2)$$

where $E^{\mathrm{rel}}_{\mathrm{slab}}$ is the total energy of the relaxed slab—here with only one of its surfaces being relaxed. Alternatively, one could calculate the relaxation energy per unit area, γ^{relax}, according to:

$$\gamma^{\mathrm{relax}} = \frac{E^{\mathrm{rel}}_{\mathrm{slab}} - E^{\mathrm{fix}}_{\mathrm{slab}}}{A} \quad (3)$$

and then adding the relaxation energy to γ^{fix}.

Thus, this procedure for computing surface energies is valid for the nonpolar surfaces and for asymmetric employed slabs. However, it cannot be used for polar surfaces because, inevitably, both surface terminations are different and present in the slab calculation. For the polar surfaces where both terminations are relaxed we define the cleavage energy, E_{cleav}, as:

$$E_{\mathrm{cleav}} = \frac{E^{\mathrm{real}}_{\mathrm{slab}} - E_{\mathrm{bulk}}}{A} \quad (4)$$

Note that within this definition relaxed surface energies of nonpolar surfaces are equal to half of their cleavage energy. For this latter systems, both surface and cleavage energies are well converged—variations below 0.1 J m^{-2}—already for a slab thickness of 8 layers.[87] For the polar surfaces cleavage energies have been calculated for various slab thicknesses—up to 14 layers, each layer containing a ZnO unit—where all atomic layers were relaxed. The given value is extrapolated to infinite thickness, following a procedure described elsewhere.[65–67] For any nonpolar surface, fully hydrated surface energy, $\gamma^{\mathrm{H_2O}}$, has been calculated by subtracting the water adsorption energy, $E^{\mathrm{H_2O}}_{\mathrm{ads}}$, per A area unit. The values are taken from the previous study using the same computational level.[64]

$$\gamma^{\mathrm{H_2O}} = \gamma^{\mathrm{rel}} - \frac{E^{\mathrm{H_2O}}_{\mathrm{ads}}}{A} \quad (5)$$

The fully hydrated cleavage energy, $E^{\mathrm{H_2O}}_{\mathrm{cleav}}$, of polar (0001)/(000$\bar{1}$) surfaces have been obtained similarly, although the H_2O adsorption energy has been introduced assuming that OH groups are solely adsorbed on the (0001) surface, whereas H groups are adsorbed on the (000$\bar{1}$) surface. Thus:

$$E^{\mathrm{H_2O}}_{\mathrm{cleav}} = E_{\mathrm{cleav}} - \frac{E^{\mathrm{OH}/(0001)}_{\mathrm{ads}} + E^{\mathrm{H}/(000\bar{1})}_{\mathrm{ads}}}{A} \quad (6)$$

Electron/hole pair conductivity is explained based on the effective masses, estimated in a first approximation assuming a parabolic dispersion of the Conduction Band (CB) maximum and the Valence Band (VB) minimum, in the form:

$$E(\mathbf{k}) = \frac{\hbar^2|\mathbf{k}|}{2m^*} \quad (7)$$

where $E(\mathbf{k})$ is the band energy around its stationary point, here arbitrarily defined as $\mathbf{k} = 0$, *i.e.* at Γ point; $\hbar$ is the reduced Planck constant, $\mathbf{k}$ is the $\mathbf{k}$-vector distance, and m^* is the effective mass. In this sense, the effective masses are obtained from the curvature of the band minima or maxima adjusted to a second degree polynom, as done in previous related studies.[88] For that, the bandstructure within the irreducible Brillouin zone has been sampled from the Γ point—at which the direct band gap is found—towards **A**, **M**, and **K** points, which correspond in real space to [0001], [10$\bar{1}$0], and [11$\bar{2}$0] directions, see Fig. 1. During the bandstructure sampling a $\mathbf{k}$-point density of 0.02 points nm^{-1} or better was used.

The electronic structure has been also studied based on the Density Of States (DOS) or, more specifically, the projected DOS. In this case, an energy resolution of 0.05 eV was employed, and the projection was carried out over the surface and near surface atoms, including the adsorbates upon when found. For a proper comparison of VB and CB of the different surfaces and situations, the bands were aligned using the vacuum energy level as the zero energy reference.

3. Results and discussion

The XRD patterns of ZnO samples obtained with the microemulsion method by varying the surfactant to water ratio are shown in Fig. 2. Table 1 summarizes some characterization results obtained from XRD and other techniques concerning the structural and morphological properties. All synthesized samples present XRD patterns ascribable to the characteristic wurtzite ZnO structure,[89] and their average primary particle size diminished with the increase of the surfactant agent concentration used during the microemulsion method (Table 1). More importantly for our purposes, we can see that the $(10\bar{1}0)/(0002)$ XRD intensity ratio varies from 0.69 for sample **B** to 0.89 for sample **C** evidencing a morphology modification among the sample series. A decrease of such a ratio indicates a morphology variation in which the stacking along the crystallographic *c* axis is favoured, consequently leading to an increase in the extension of nonpolar planes at the surface, or, viewed from another perspective, to a decrease of the polar *vs.* nonpolar surface extension. According to the present XRD results the proportion of polar surfaces would grow from sample **B** to **A** and then become maximum for **C**.

Such a morphology evolution throughout our sample series was studied in detail using HR-TEM. The TEM images of the sample with higher surfactant concentration, **A** (Fig. 3a), show rounded (hexagonal-like) ZnO nanoparticles with sizes around 5 nm. Decreasing of surfactant concentration leads to increasing average particle size (Table 1) and a drastic effect on the shape (Fig. 3). Sample **B** presents more elongated forms (Fig. 3b) while those in sample **C** display sharp needle-like structures (Fig. 3c).

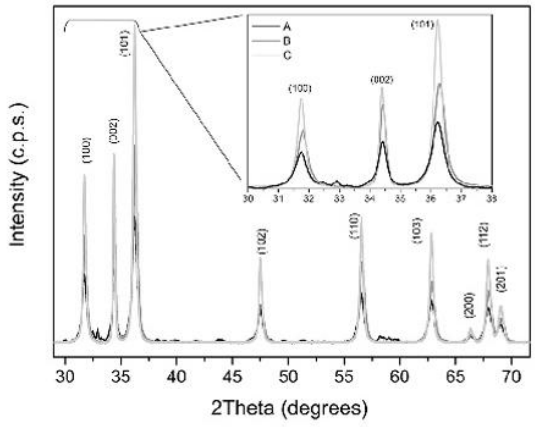

Fig. 2 XRD patterns of the synthesized A, B, and C samples.

Table 1 Water to surfactant molar ratio microemulsion parameter values (*w*), primary particle size (size, in nm) calculated from XRD data, and BET areas (A_{BET}, in $m^2\ g^{-1}$), $(10\bar{1}0)/(0002)$ diffraction peaks intensity (*I*) ratio, and band gap energy (eV) measured from UV-visible data

Parameter/sample	A	B	C
W	9	18	36
Size	4.1	7.5	8.5
A_{BET}	35	25	23
I	0.78	0.69	0.89
Band gap	3.35	3.33	3.31

Extra images from other individual crystals of the studied samples show that the present results are representative of other areas and presents a valid statistical impression, as shown in the ESI.†

For sample **A**, a hexagonal-disk type morphology becomes more evident from high resolution images. Fig. 4a shows a magnified HR-TEM image and the corresponding Fast Fourier Transform (FFT) diffraction pattern for the selected area. The analysis of FFT diffraction patterns indicates a [0001] zone axis and consequently the ZnO-disk morphology mainly exposed at the surface layer of polar $(0001)/(000\bar{1})$ planes and, in less proportion, $(10\bar{1}0)$ facets. For a brick-type morphology like in sample **B**, a high resolution image and the corresponding FFT diffraction pattern (Fig. 4b) indicate the presence of well-defined nanostructures displaying a $[10\bar{1}0]$ zone axis, similar to those found in the literature.[45] This would correspond to slightly elongated particles along the *c* crystallographic orientation and presenting larger contribution of nonpolar $(10\bar{1}0)$ than polar $(0001)/(000\bar{1})$ plane types. Fig. 4c presents HR-TEM images for sample **C** and the corresponding FFT diffraction pattern of the selected zone of the needle entities. The analysis unequivocally identifies a [0001] zone axis, so the nanostructure grows in a direction perpendicular to the crystallographic *c* axis exposing polar $(0001)/(000\bar{1})$ and nonpolar $(10\bar{1}0)$ facets along the needle particulate surface layer. The analysis is representative of the other crystals present in the samples, as shown in the ESI.†

The TEM analysis provides a clear view of the morphology evolution among our samples. The anisotropic growth evidenced in the XRD patterns is then clarified using the TEM analysis (Fig. 3 and 4). Such morphology differences are customarily justified on the basis of the different surface free energies of the crystallographic planes. During nucleation and growth at preparation states, a fast growing plane generally tends to disappear or has limited expression/extension at the end of the preparation, allowing larger expression of slow growing planes, typically having lower surface energy.[90]

To support this, DF based calculations of the surface energies have been carried out, although, for the present purposes, a more important quantity is the estimated cleavage energies, obtained following the procedure above-described. Thus, DF cleavage energies for the vacancy-free $(0001)/(000\bar{1})$, $(11\bar{2}0)$, and $(10\bar{1}0)$ surfaces, are, respectively, 3.31, 1.78, and 1.70 J m^{-2}.

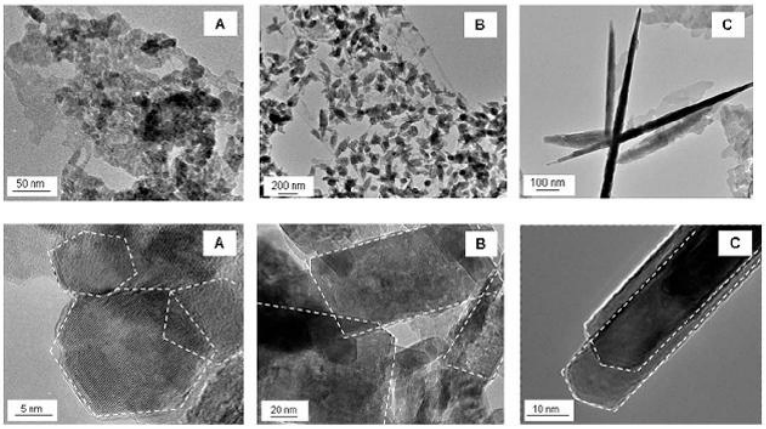

Fig. 3 TEM images corresponding to samples A, B, and C.

Note that the cleavage energy of the polar surfaces is very close to those previously reported[65,66] at the PBE level of 3.41 J m^{-2} and goes along with the infinite thickness slab B3LYP value of ~4 J m^{-2}.[67] The calculated cleavage energies of the $(11\bar{2}0)$ and $(10\bar{1}0)$ surfaces are very similar to previous PBE results[66] of 1.7 and 1.6 J m^{-2}, respectively. Furthermore, the present results match the preference in stability of the $(10\bar{1}0)$ surface with respect to the $(11\bar{2}0)$ by ~0.1 J m^{-2}.[66]

According to this, in the low water (high surfactant) regime, such as in sample **A**, the most stable structure should feature small pristine polar $(0001)/(000\bar{1})$ facets, and large nonpolar $(10\bar{1}0)$ and $(11\bar{2}0)$ facets. Based on these results and, as generally reported, the growth of ZnO crystals preferentially would occur along the [0001] direction to form rod-like structures, which is not the case in our samples. The explanation arises when computing realistic models of polar surfaces with vacancies. The present value of cleavage energy for the $(0001)/(000\bar{1})$ surface containing 1/4 ML vacancies is 1.07 J m^{-2}. This would suggest that $(0001)/(000\bar{1})$ facets containing vacancies would be the most exposed surface, with lower ratio of nonpolar planes. This matches hexagonal nanodisk structures obtained at high surfactant concentration employed in the preparation of sample **A**, which dominantly exposes polar (0001) and $(000\bar{1})$ surfaces.

However the fully hydrated cleavage energies explain a different tale: they are, for vacancy-free $(0001)/(000\bar{1})$, $(11\bar{2}0)$, and $(10\bar{1}0)$ surfaces, respectively, 0.76, −0.31, and −0.34 J m^{-2}. Thus, this reveals that in systems with more water content—like in sample **B**—all surfaces can become hydrated and consequently further and strongly stabilized. It is worth noting that under such conditions the largest stabilization results for nonpolar surfaces, and therefore, these should be the ones most exposed. This matches the brick-wall structures of sample **B** obtained using standard water/oil values (*e.g.* a ratio between 12 and 20) of microemulsion parameters.[91] The elongated nanocubes predominantly expose nonpolar $(11\bar{2}0)$ and $(10\bar{1}0)$ surfaces, in perfect agreement with the order of stability of the different surfaces as derived from DF calculations (Fig. 3).

It is known that the use of capping agents may play a key role in morphology control. Depending on the nature of the capping molecules, they can be preferentially adsorbed on different ZnO surfaces. These adsorbed moieties can prevent contact between the growth units at particular surfaces and thus, direct the growth in other spatial directions. A large number of studies

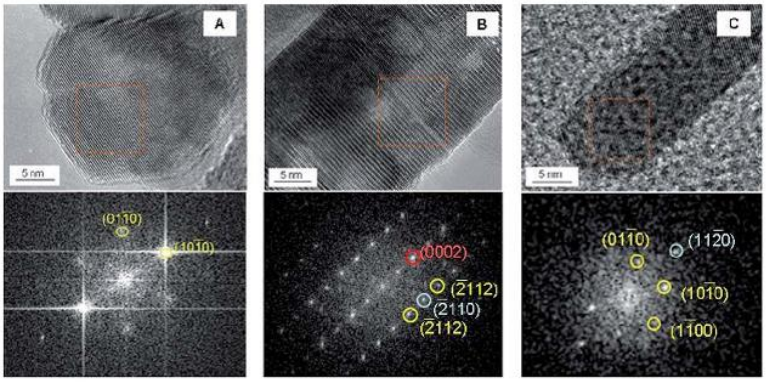

Fig. 4 HR-TEM images and FFT diffraction patterns (from locations marked with a red colour box) corresponding to samples A, B, and C.

published in this field support this statement.[20,21] For example, citrate anions with –COO^- and –OH groups are preferentially adsorbed on the positively charged Zn terminated (0001) surface, preventing contact between the growth unit and the (0001) crystal surface. Under these conditions, a ZnO crystal would grow primarily along the other six symmetric directions (the so-called preferential equatorial growth).

This is a reasonable explanation for the morphologies obtained in sample **C**, which otherwise, due to the low surfactant concentration—water saturation conditions—, should feature completely water saturated surfaces, and a morphology similar to sample **B**. However, in **B** the growth appears to be governed by the thermodynamics, whereas in **C** kinetics seems to play a key role. Take for instance a ZnO nanoparticle with all surfaces fully hydrated due to the capping effect of H_2O, OH, or H moieties. In order to grow in a particular surface direction, a moiety must desorb of the surface to allow a ZnO growing unit to be inserted. Desorption can be difficult in water rich conditions, *i.e.* the desorbed water molecule can easily be replaced by another water molecule. However, the limiting step seems to be still the desorption energy.

In the case of (0001)/(000$\bar{1}$) polar surfaces the desorption is more problematic; on one hand, it would imply desorption of hydroxyls from the (0001) surface, or H atoms in the (000$\bar{1}$) case. Here we conceptually considered the simultaneous desorption of both moieties from both surface terminations to form a water molecule in the media, and thus, leaving both surfaces free to further grow, thus allowing a more fair comparison with the other surfaces. On the other hand, moiety desorption is considered leaving the polar surfaces naked and pristine, *i.e.* free of vacancies. This is done because when fully hydrated, polar surfaces are found to feature a regular vacancy-free (1 × 1) pattern.[61–63] Therefore, we decided to separate desorption from a possible posterior vacancy formation process, which is out of the present discussion. One must keep in mind, however, that when water would be removed from the polar surfaces, they would unavoidably reconstruct forming vacancies. Present calculations reveal desorption energies to be 2.55, 2.04, and 2.09 J m^{-2}, for vacancy-free (0001)/(000$\bar{1}$), (10$\bar{1}$0), and (11$\bar{2}$0) surfaces, respectively. Thus, the capping effect is largest on polar surfaces, a fact that explains why sample **C** presents principally (0001) and (000$\bar{1}$) surfaces with even a largest polar/nonpolar facet ratio than sample **A**.

Table 2 Lighthole (m^h) and electron (m^e) effective masses, in units of free electron effective mass, 1 × $10^{-2}m_0$, for wurtzite ZnO along [0001], [10$\bar{1}$0], and [11$\bar{2}$0] directions, and averaged bulk value

Direction	[0001]	[10$\bar{1}$0]	[11$\bar{2}$0]	Bulk
m^e	0.37	0.37	0.42	0.38
m^h	0.40	0.45	0.41	0.42

Having explained the morphology based on the synthesis media and growing conditions, we now focus on the photocatalytic aspect. For isopropanol photooxidation it is well known that the initial radical attack is carried out by hole-related species.[92] The alcohol degradation assisted by UV light irradiation is based on the principle that UV light creates electron/hole (e^-/h^+) pairs within the semiconductor. Holes generated in the VB are capable of oxidizing the alcohol substrate and the CB electrons are capable of reducing oxygen present in air. The generated e^-/h^+ pairs suffer competitive fates concerning their recombination or involvement in chemical steps. The efficient separation of photogenerated electron/hole pairs is one of the important factors in the reaction.

As well-known, the relative energy of VB and CB levels determines the (potential) transfer path(s) of photoexcited holes and electrons, which can directly influence their fate as charge recombination and/or chemically related species. Primary size and shape are important morphological parameters affecting the photoactivity by influencing VB and CB levels. Size is rather important but the crystalline dimension range here explored (Table 2; average dimension between 4 and 8 nm) would indicate that changes in valence and conduction band edge positions are rather limited.[93] In fact, calculation of the band gap in our samples using UV-visible data gives a constant value within

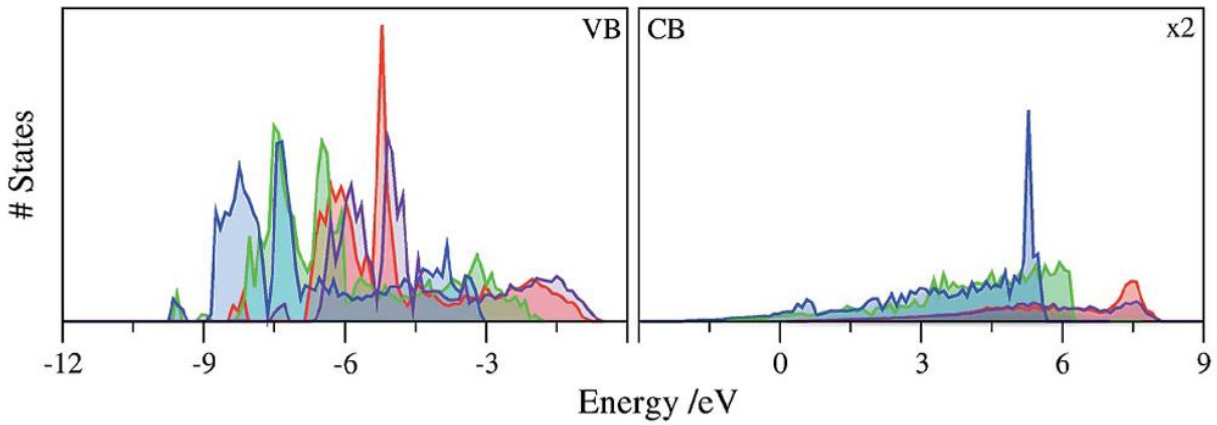

Fig. 5 Density of states of VB and CB of the fully hydrated nonpolar (10$\bar{1}$0) and (11$\bar{2}$0) facets (green and blue), and of the polar (0001) and (000$\bar{1}$) planes (violet and red).

the experimental error (Table 1). It thus seems that here shape would be an important morphological aspect driving the chemical performance of charge carriers. Shape effects in photocatalysis of TiO_2 and ZnO have been the subject of a significant number of publications, summarized in recent review articles,[94,95] and here we focus on the specific grounds of this important issue.

Electron/hole effective masses for bulk wurtzite ZnO along (0001), $(10\bar{1}0)$, and $(11\bar{2}0)$ directions have been calculated following the procedure detailed in the Methods section for the orthorhombic wurtzite bulk cell (Fig. 1), and values are encompassed in Table 2. The results indicate that charge mobility has no significant differences (maximum of *ca.* 10%) as a function of orientation. However, DF calculations performed to estimate the CB and VB bands based on DOS of different hydrated surface facets (Fig. 5) show a different energy ordering for VB end- and CB start-edges: the VB end-edge of the facets of ZnO crystals follows the order $(0001) > (000\bar{1}) > (10\bar{1}0) > (11\bar{2}0)$, and, in contrast, the corresponding CB end-edge follows an inverse order of $(11\bar{2}0) < (10\bar{1}0) < (000\bar{1}) < (0001)$. In the case of pristine nonpolar surfaces and polar surfaces displaying a concentration of 1/4 ML of vacancies, the ordering is similar; the VB end-edge follows the trend, $(0001) > (000\bar{1}) \sim (10\bar{1}0) > (11\bar{2}0)$, and so the inverse order for CB end-edge, $(11\bar{2}0) < (10\bar{1}0) \sim (000\bar{1}) < (0001)$, see ESI.†

Indirectly the VB plots in Fig. 5 show that work function values for different surface terminations differ within a range of 1.2 eV, which is in line with variations of up to 0.8 eV as found in the literature.[96] Note that the ZnO work function is generally accepted to be around 4.3 eV, as found for nanocrystalline thin films.[97] Indeed, variations between different surface terminations are well below this value, and also smaller than the changes in the work function produced by adsorption of polar molecules upon, found to vary the work function by up to 2.9 eV.[98–100]

Coming back to Fig. 5, it indicates that the (0001) facets are those that feature the maximum stabilization of photogenerated holes, followed by the $(000\bar{1})$ surface. Compared to $(10\bar{1}0)$ and $(11\bar{2}0)$ facets, holes are more stable at these polar surfaces thereby making them more prone than the nonpolar ones to photooxidation steps involving organic compounds. On the other hand, electrons are more stable on the nonpolar surface, suggesting that these constitute better active sites for photoreduction. This argument holds for fully hydrated surfaces, but, as shown in the ESI,† such hole/electron stability is maintained on dehydrated surfaces as well. Thus, one could argue that such a difference in stability is kept at any degree of ZnO nanoparticle surface hydration.

Note that holes/electrons would be generated on all the surfaces, although a transfer among surfaces would be favorable given the different stability. If such a transfer would not be inhibited, holes would accumulate on polar surfaces, and electrons on nonpolar ones. Thus, the presence of both types of surfaces would allow the photogenerated e^-/h^+ pairs to be separated for a longer time, hindering the recombination rate and making ZnO more effective in the photocatalytic degradation of isopropanol. However such hypothesis neglects the dipole energy barriers to be overcome at junctions between surfaces, the band bending, and also charge unbalance effects. These as well as dynamical aspects are no doubt of interest but they are out of the scope of the present work, and will require further investigation.

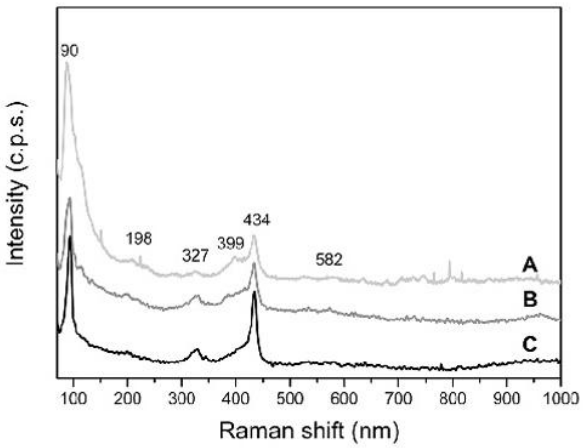

Fig. 6 Raman spectra of samples A, B, and C.

Experiments have been carried out on samples **A–C** to rule out first inhomogeneity issues in between samples. Raman scattering is an effective technique to investigate the crystallization, structure, and defects in nanostructured materials. Measurements were performed on different points of these materials to check homogeneity and it was observed that Raman spectra thus recorded are rather similar. According to group theory, hexagonal wurtzite ZnO belongs to the *P*63*mc* space group, the optical phonons at the **Γ** point of the Brillouin zone are $A_1 + 2B_1 + E_1 + 2E_2$. Both A_1 and E_1 modes are polar and split into transverse TO and longitudinal optical LO phonons and are Raman active, whereas the B_1 modes are Raman inactive (silent modes). The two nonpolar E_2 modes (E_{2low}, E_{2high}) are only Raman active. Fig. 6 shows the Raman spectra for the three samples discussed in this work. A sharp peak at 433–453 cm^{-1}

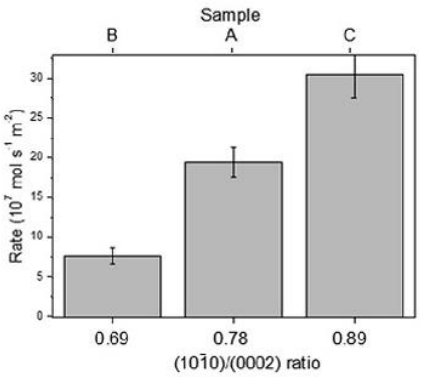

Fig. 7 Normalized (per surface area) isopropanol photooxidation rate of samples A, B, and C.

can be assigned to the E_2 high mode of nonpolar optical phonons, which is the characteristic peak of the hexagonal wurtzite phase. Other E_2 related mode peaks appear at 90 cm^{-1} (E_{2low}), 195 cm^{-1} ($2E_{2low}$) and 331–327 cm^{-1} to (E_{2high}–E_{2low}), the last two due to multiple phonon scattering processes. The peak at 383 cm^{-1} corresponds to the A_1 transverse optical (TO) mode. A small peak at 580 cm^{-1} attributed to the E_1 (LO) mode has also been observed. Generally, it is believed that the E_1 (LO) mode is related to the structural defects (oxygen vacancies, zinc interstitials, free carriers, *etc.*) in ZnO. The low intensity of the E_{2high} peak and the absence of significant differences among the presented spectra suggest that the samples exhibit well crystalline hexagonal wurtzite entities without substantial differences in lattice/defect related structural properties.

Finally, Fig. 7 presents the normalized photooxidation rate of the samples (*e.g.* rates eliminating the effect of different surface areas of the samples) as a function of $(10\bar{1}0)/(0002)$ XRD intensity ratio. A "natural" order evolves from this graph; needle crystals (sample **C**) showing much higher activity than flat crystals (sample **A**), and these two structures displaying larger activity than brick structures (sample **B**). These results highlight the requirement of the presence of polar surfaces for obtaining high photocatalytic performance. This, in combination with the present DF-based photochemical activity trends, and considering, as above-mentioned, the h^+ key role in the process, indicates that isopropanol photoelimination is likely to occur on polar ZnO nanoparticle facets, independently of the degree of hydration. In particular, the Zn-terminated (0001) surface is the one with *a priori* better photooxidation activity. This rules out the effect of water displacement by isopropanol as a key factor.

Thus, apparently, the exposure of polar surfaces, in particular the Zn-terminated (0001) surface, appears to be a key factor for the photooxidation capability of ZnO nanostructures. This result further supports the previous work of Maclaren and coworkers,[33] showing that a higher proportion of polar surfaces is needed for a good organic compound decomposition, although here needle-like structures show a better activity than previous[33] and present hexagonal disk-like nanoparticles. Besides, the key role of (0001) surfaces is also in line with previous studies on alcohol degradation.[41] This shows why sample **C**, showing the higher ratio of (0001) surfaces, maximizes the isopropanol photooxidation rate as seen in Fig. 7. To obtain such a high ratio of polar surfaces, one needs to synthesize ZnO nanoparticles in a water rich environment. Thus, this shape comparison under the same conditions allows one to figure out which polar surface is the best to improve the photocatalytic power of a ZnO-based nanoparticle material.

4. Conclusions

A series of ZnO nanostructures were prepared by a microemulsion method using a single pot procedure. A multitechnique XRD, Raman, TEM, UV-visible experimental study combined with DF calculations allowed us to provide a complete structural, morphological, and electronic analysis of the materials. The nanostructured ZnO entities displayed disk-, brick-, and needle-like morphologies as the surfactant to water ratio of the microemulsion procedure continuously decreases from *ca.* 40 to 10 values.

The analysis of the chemical response of such ZnO nanostructures in the photoelimination of isopropanol was rationalized in terms of the structural/electronic properties of the nanosolids. The combined experimental and theoretical approach was able to provide evidence that the process is better carried out on polar surfaces, independently of the degree of hydration, and consequently, ruling out the effect of water displacement by isopropanol adsorption. Furthermore, the key role played by the ratio between polar and nonpolar facets exposed at the external surface of the ZnO nanomaterial is disclosed. It is shown that maximization of activity is not obtained by physicochemical properties (*e.g.* defects, band gap energy, *etc.*) previously described in the literature, but by maximizing the exposure to the external solid surface of polar surfaces in general, and the ZnO Zn-terminated (0001) surface in particular. This is shown to be grounded in the preferential stability of holes upon light excitation at (0001) surfaces. This feature would be relevant for all photodegradation processes and thus hold general validity for ZnO nanomaterials.

Acknowledgements

We are indebted to one of the reviewers for truly enlightening discussion beyond that required in usual peer review reports, whose comments have been crucial to reach a physically sound interpretation. The authors also thank Dr A.B. Hungría for discussion of TEM results. Financial support by Spanish MICINN/MINECO research grants CTQ2010-14872/BQU and CTQ2012-30751 and, in part, by *Generalitat de Catalunya* grants 2014SGR97 and XRQTC is acknowledged. O.G.L. thanks the *Universitat de Barcelona* for a predoctoral APIF fellowship; F.V. and A.I.J. thank the MINECO for a postdoctoral *Juan de la Cierva* grant (JCI-2010-06372) and for a postdoctoral *Ramón y Cajal* contract, respectively. F.I. acknowledges additional support from the 2009 ICREA.

References

1 A. Mang, K. Reimann and S. Rübenacke, *Solid State Commun.*, 1995, **94**, 251–254.
2 D. C. Reynolds, D. C. Look, B. Jogai, C. W. Litton, G. Cantwell and W. C. Harsch, *Phys. Rev. B: Condens. Matter Mater. Phys.*, 1999, **60**, 2340–2344.
3 A. B. Djurisic and Y. H. Leung, *Small*, 2006, **2**, 944–961.
4 C. G. Van de Walle and A. Janotti, *Rep. Prog. Phys.*, 2009, **72**, 126501.
5 J. Goldberger, D. J. Sirbuly, M. Law and P. Yang, *J. Phys. Chem. B*, 2005, **109**, 9–14.
6 H. Kind, H. Q. Yan, B. Messer, M. Law and P. D. Yang, *Adv. Mater.*, 2002, **14**, 158.
7 D. M. Bagnall, Y. F. Chen, Z. Zhu, T. Yao, S. Koyama, M. Y. Shen and T. Goto, *Appl. Phys. Lett.*, 1997, **70**, 2230–2232.

8 V. L. Colvin, M. C. Schlamp and A. P. Alivisatos, *Nature*, 1994, **370**, 354–357.
9 M. H. Huang, S. Mao, H. Feick, H. Q. Yan, Y. Y. Wu, H. Kind, E. Weber, R. Russo and P. D. Yang, *Science*, 2001, **292**, 1897–1899.
10 C. S. Rout, A. R. Raju, A. Govindaraj and C. N. R. Rao, *Solid State Commun.*, 2006, **138**, 136–138.
11 W. Göpel, *Prog. Surf. Sci.*, 1985, **20**, 9–103.
12 S. Polarz, A. Roy, M. Lehmann, M. Driess, F. E. Kruis, A. Hoffmann and P. Zimmer, *Adv. Funct. Mater.*, 2007, **17**, 1385–1391.
13 Z. L. Wang and J. H. Song, *Science*, 2006, **312**, 242–246.
14 P. Duran, F. Capel, J. Tartaj and C. Moure, *Adv. Mater.*, 2002, **14**, 137–141.
15 J. F. Gnichwitz, R. Marczak, F. Werner, N. N. Lang, N. Jux, D. M. Guldi, W. Peukert and A. Hirsch, *J. Am. Chem. Soc.*, 2010, **132**, 17910–17920.
16 R. Marczak, F. Werner, R. Ahmad, V. Lobaz, D. M. Guldi and W. Peukert, *Langmuir*, 2011, **27**, 3920–3929.
17 B. O'Regan and M. Grätzel, *Nature*, 1991, **353**, 737–739.
18 C. Wöll, *Prog. Surf. Sci.*, 2007, **82**, 55–120.
19 P. Nieuwenhuizen, *Appl. Catal., A*, 2001, **207**, 55–120.
20 S. Polarz, J. Strunk, V. Ischenko, M. W. E. van den Berg, O. Hinrichsen, M. Muhler and M. Driess, *Angew. Chem., Int. Ed.*, 2006, **45**, 2965–2969.
21 S. A. French, A. A. Sokol, S. T. Bromley, C. R. A. Catlow, S. C. Rogers, F. King and P. Sherwood, *Angew. Chem., Int. Ed.*, 2001, **40**, 4437–4440.
22 M. Kurtz, J. Strunk, O. Hinrichsen, M. Muhler, K. Fink, B. Meyer and C. Wöll, *Angew. Chem., Int. Ed.*, 2005, **44**, 2790–2794.
23 B. Meyer, D. Marx, O. Dulub, U. Diebold, V. Kunat, D. Langenberg and C. Wöll, *Angew. Chem., Int. Ed.*, 2004, **43**, 6642–6645.
24 J. A. Rodriguez and A. Maiti, *J. Phys. Chem. B*, 2000, **104**, 3630–3638.
25 T. Jirsak, J. Dvorak and J. A. Rodriguez, *J. Phys. Chem. B*, 1999, **103**, 5550–5559.
26 J. Dvorak, T. Jirsak and J. A. Rodriguez, *Surf. Sci.*, 2001, **479**, 155–168.
27 O. Hinrichsen, K. Kochlöfl and M. Muhler, in *Handbook of Heterogeneous Catalysis*, ed G. Ertl, H. Knözinger and J. Weitkamp, VCH, Weinheim, Germany, 2nd edn, 2008.
28 Y. Wang, R. Kováčik, B. Meyer, K. Kotsis, D. Stodt, V. Stämmler, H. Qiu, F. Träger, D. Langenberg, M. Muhler and C. Wöll, *Angew. Chem., Int. Ed.*, 2007, **46**, 7315–7318.
29 S. Girol, T. Strunskus, M. Muhler and C. Wöll, *J. Phys. Chem. B*, 2004, **108**, 13736–13745.
30 M. Messori and A. Vaccari, *J. Catal.*, 1994, **150**, 177–185.
31 S. Sakthivel, B. Neppolian, M. V. Shankar, B. Arabindoo, M. Palanichamy and V. Murugesan, *Sol. Energy Mater. Sol. Cells*, 2003, **77**, 65–82.
32 D. Kulkarni and I. E. Wachs, *Appl. Catal., A*, 2002, **237**, 121–137.
33 A. Mclaren, T. Valdes-Solis, G. Li and S. C. Tsang, *J. Am. Chem. Soc.*, 2009, **131**, 12540–12541.
34 H. Wagata, K. Katsumata, N. Ohashi, M. Sakai, A. Nakajima, A. Fujishima, K. Okada and N. Matsushita, *Photochem. Photobiol.*, 2011, **87**, 1009–1015.
35 T. Pauporte and J. Rathousky, *J. Phys. Chem. C*, 2007, **111**, 7639–7644.
36 N. Daneshvar, D. Salari and A. R. Khataee, *J. Photochem. Photobiol., A*, 2004, **162**, 317–322.
37 Z. R. Tian, J. A. Voigt, J. Liu, B. McKenzie, M. J. McDermott, M. A. Rodriguez, H. Konishi and H. Xu, *Nat. Mater.*, 2003, **2**, 821–826.
38 C. Kormann, D. W. Bahnemann and M. R. Hoffmann, *Environ. Sci. Technol.*, 1988, **22**, 798–806.
39 K. Maeda and K. Domen, *Chem. Mater.*, 2010, **22**, 612–623.
40 A. A. Khodja, T. Sehili, J. F. Pilichowski and P. Boule, *J. Photochem. Photobiol., A*, 2001, **141**, 231–239.
41 L. Xu, Y. L. Hu, C. Pelligra, C. H. Chen, L. Jin, H. Huang, S. Sithambaram, M. Aindow, R. Joesten and S. L. Suib, *Chem. Mater.*, 2009, **21**, 2875–2885.
42 N. Kislov, J. Lahiri, H. Verma, D. Y. Goswanni, E. Stefanakos and M. Batzill, *Langmuir*, 2009, **25**, 3310–3315.
43 G. R. Li, T. Hu, G. L. Pan, T. Y. Yan, X. P. Gao and H. Y. Zhu, *J. Phys. Chem. C*, 2008, **112**, 11859–11864.
44 L. Vayssieres, *Adv. Mater.*, 2003, **15**, 464–466.
45 C. Lizandara-Pueyo, S. Siroky, M. R. Wagner, A. Hoffmann, J. S. Reparaz, M. Lehmann and S. Polarz, *Adv. Funct. Mater.*, 2011, **21**, 295–304.
46 Z. L. Wang, *ACS Nano*, 2008, **2**, 1987–1992.
47 C. Lizandara-Pueyo, M. C. Morant-Minana, M. Wessig, M. Krumm, S. Mecking and S. Polarz, *RSC Adv.*, 2012, **2**, 5298–5306.
48 J. Yang, J. Wang, X. Li, J. Lang, F. Liu, L. Yang, H. Zhai, M. Gao and X. Zhao, *J. Alloys Compd.*, 2012, **528**, 28–33.
49 S. Polarz, A. Roy, M. Merz, S. Halm, D. Schröder, L. Schneider, G. Bacher, F. E. Kruis and M. Driess, *Small*, 2005, **5**, 540–552.
50 J. V. Lauritsen, S. Porsgaard, M. K. Rasmussen, M. C. R. Jensen, R. Bechstein, K. Meinander, B. S. Clausen, S. Helveg, R. Wahl, G. Kresse and F. Besenbacher, *ACS Nano*, 2011, **5**, 5987–5994.
51 M. Valtiner, M. Todorova, G. Grundmeier and J. Neugebauer, *Phys. Rev. Lett.*, 2009, **103**, 065502.
52 G. Colón, P. Sampedro, M. Fernández-García, H. Chen, J. C. Hanson and J. A. Rodriguez, *Langmuir*, 2008, **24**, 11111–11118.
53 C. Richard, F. Bosquet and J.-F. Pilichowski, *J. Photochem. Photobiol., A*, 1997, **108**, 45–49.
54 C. Richard and P. Boule, *Sol. Energy Mater. Sol. Cells*, 1995, **38**, 431–440.
55 F. Xu, P. Zhang, A. Navrotsky, Z. Y. Yuan, T. Z. Ren, M. Halasa and B. L. Su, *Chem. Mater.*, 2007, **19**, 5680–5686.
56 A. Le Bail, H. Duroy and J. L. Fourquet, *Mater. Res. Bull.*, 1988, **23**, 447–452.
57 J. Goniakowski, F. Finocchi and C. Noguera, *Rep. Prog. Phys.*, 2008, **71**, 016501.
58 C. Noguera, *J. Phys.: Condens. Matter*, 2000, **12**, R367.
59 G. Kresse, O. Dulub and U. Diebold, *Phys. Rev. B: Condens. Matter Mater. Phys.*, 2003, **68**, 245409.

60 O. Dulub, U. Diebold and G. Kresse, *Phys. Rev. Lett.*, 2003, **90**, 016102.
61 V. Stämmler, K. Fink, B. Meyer, D. Marx, M. Kunat, U. Burghaus, S. Gil-Girol and C. Wöll, *Phys. Rev. Lett.*, 2003, **90**, 106102.
62 M. Kunat, S. Gil-Girol, U. Burghaus and C. Wöll, *J. Phys. Chem. B*, 2003, **107**, 14350–14356.
63 T. Becker, S. Hövel, M. Kunat, C. Boas, U. Burghaus and C. Wöll, *Surf. Sci.*, 2001, **486**, 502–506.
64 F. Viñes, A. Iglesias-Juez, F. Illas and M. Fernández-García, *J. Phys. Chem. C*, 2014, **118**, 1492.
65 G. Kresse, O. Dulub and U. Diebold, *Phys. Rev. B: Condens. Matter Mater. Phys.*, 2003, **68**, 245409.
66 B. Meyer and D. Marx, *Phys. Rev. B: Condens. Matter Mater. Phys.*, 2003, **67**, 035403.
67 A. Wander, F. Schedin, P. Steadman, A. Norris, R. McGrath, T. S. Turner, G. Thornton and N. M. Harrison, *Phys. Rev. Lett.*, 2001, **86**, 3811–3814.
68 A. Wander and N. M. Harrison, *Surf. Sci.*, 2000, **457**, L342–L346.
69 N. H. Moreira, G. Dolgonos, B. Aradi, A. L. da Rosa and T. Frauenheim, *J. Chem. Theory Comput.*, 2009, **5**, 605–614.
70 H. Li, L. K. Schirra, J. Shim, H. Cheun, B. Kippelen, O. L. A. Monti and J.-L. Bredas, *Chem. Mater.*, 2012, **24**, 3044–3055.
71 S. Nénon, R. Méreau, S. Salman, F. Castet, T. V. Regemorter, S. Clima, D. Beljonne and J. Cornil, *J. Phys. Chem. Lett.*, 2012, **3**, 58–63.
72 D. J. Cooke, A. Marmier and S. C. Parker, *J. Phys. Chem. B*, 2006, **110**, 7985–7991.
73 F. Labat, I. Ciofini and C. Adamo, *J. Chem. Phys.*, 2009, **131**, 044708.
74 B. Meyer, H. Rabaa and D. Marx, *Phys. Chem. Chem. Phys.*, 2006, **8**, 1513–1520.
75 A. Wander and N. M. Harrison, *J. Chem. Phys.*, 2001, **115**, 2312–2316.
76 B. Meyer, D. Marx, O. Dulub, U. Diebold, M. Kunat, D. Langenberg and C. Wöll, *Angew. Chem., Int. Ed.*, 2004, **43**, 6642.
77 O. Dulub, B. Meyer and U. Diebold, *Phys. Rev. Lett.*, 2005, **95**, 136101.
78 G. Kresse and J. Furthmüller, *Phys. Rev. B: Condens. Matter Mater. Phys.*, 1996, **54**, 11169–11186.
79 P. E. Blöchl, *Phys. Rev. B: Condens. Matter Mater. Phys.*, 1994, **50**, 17953–17979.
80 J. P. Perdew, K. Burke and M. Ernzerhof, *Phys. Rev. Lett.*, 1996, **77**, 3865–3868.
81 A. Alkauskas and A. Pasquarello, *Phys. Rev. B: Condens. Matter Mater. Phys.*, 2011, **84**, 125206.
82 N. H. Moreira, G. Dogonos, B. Aradi, A. L. da Rosa and T. J. Frauenheim, *J. Chem. Theory Comput.*, 2009, **5**, 605.
83 A. D. Becke, *J. Chem. Phys.*, 1993, **98**, 5648.
84 C. H. Patterson, *Phys. Rev. B: Condens. Matter Mater. Phys.*, 2006, **74**, 144432.
85 I. Demiroglu, S. Tosoni, F. Illas and S. T. Bromley, *Nanoscale*, 2014, **6**, 1181.
86 F. Viñes, C. Sousa, P. Liu, J. A. Rodriguez and F. Illas, *J. Chem. Phys.*, 2005, **122**, 174709.
87 N. L. Marana, V. M. Longo, E. Longo, J. B. L. Martins and J. R. Sambrano, *J. Phys. Chem. A*, 2008, **112**, 8958–8963.
88 S. Z. Karazhanov, P. R. Ravindran, A. Kjekshus, H. Fjellvag, U. Grossner and B. G. Svensson, *J. Appl. Phys.*, 2006, **100**, 043709.
89 F. Decremps, F. Datchi, A. M. Saitta, A. Polian, S. Pascarelli, A. Di Cicco, J. P. Itié and F. Baudelet, *Phys. Rev. B: Condens. Matter Mater. Phys.*, 2003, **68**, 104101.
90 X. Feng, L. Feng, M. Jin, J. Zhai, L. Jiang and D. Zhu, *J. Am. Chem. Soc.*, 2004, **126**, 62–63.
91 V. Uskokovic and M. Drofenik, *Surf. Rev. Lett.*, 2005, **12**, 239–277.
92 M. A. Henderson, *Surf. Sci. Rep.*, 2011, **66**, 185–297.
93 L. Zhang, L. Ying, C. Wang, N. Lun, Y. Qui and D. Xing, *J. Phys. Chem. C*, 2010, **114**, 9561–9568.
94 A. Kubacka, M. Fernández-García and G. Colón, *Chem. Rev.*, 2012, **112**, 1555–1614.
95 A. Iglesias-Juez, A. Kubacka, G. Colón and M. Fernández-García, Photocatalytic nanooxides: the case of TiO_2 and ZnO, in *Catalysis by Nanoparticles*, New and of the Future Developments in Catalysis Series, ed. S. Suib, Elservier, Amsterdam, 2013, ISBN: 978-0-44-453874-1.
96 R. Schlesinger, Y. Xu, O. T. Hofmann, S. Winkler, J. Frisch, J. Niederhausen, A. Vollmer, S. Blumstengel, F. Henneberger, P. Rinke, M. Scheffler and N. Koch, *Phys. Rev. B: Condens. Matter Mater. Phys.*, 2013, **87**, 155311.
97 S. Gutmann, M. Conrad, M. A. Wolak, M. M. Beerbom and R. Schlaf, *J. Appl. Phys.*, 2012, **111**, 123710.
98 O. T. Hofmann, J.-C. Deinert, Y. Xu, P. Rinke, J. Stähler, M. Wolf and M. Scheffler, *J. Chem. Phys.*, 2013, **139**, 174701.
99 W. A. Tisdale, M. Muntwiler, D. J. Norris, E. S. Aydil and X.-Y. Zhu, *J. Phys. Chem. C*, 2008, **112**, 14682–14692.
100 I. Lange, S. Reiter, M. Pätzel, A. Zykov, A. Nefedov, J. Hildebrandt, S. Hecht, S. Kowarik, C. Wöll, G. Heimel and D. Neher, *Adv. Funct. Mater.*, 2014, **24**, 7014–7024.

3.2.2 Size dependent structural and polymorphic transitions in ZnO: from Clusters to Bulk

Nanoscale

PAPER

View Article Online
View Journal

Cite this: DOI: 10.1039/c7nr02818k

Size dependent structural and polymorphic transitions in ZnO: from nanocluster to bulk†

Francesc Viñes, [a] Oriol Lamiel-Garcia, [a] Francesc Illas [a] and Stefan T. Bromley [*a,b]

We report on an extensive survey of $(ZnO)_N$ nanostructures ranging from bottom-up generated nanoclusters to top-down nanoparticles cuts from bulk polymorphs. The obtained results enable us to follow the energetic preferences of structure and polymorphism in $(ZnO)_N$ systems with N varying between 10–1026. This size range encompasses small nanoclusters with 10s of atoms and nanoparticles with 100s of atoms, which we also compare with appropriate bulk limits. In all cases the nanostructures and bulk systems are optimized using accurate all-electron, relativistic density functional theory based calculations with numeric atom centered orbital basis sets. Specifically, sets of five families of $(ZnO)_N$ species are considered: single-layered and multi-layered nanocages, and bulk cut nanoparticles from the sodalite (SOD), body centered tetragonal (BCT), and wurtzite (WZ) ZnO polymorphs. Using suitable fits to interpolate and extrapolate these data allows us to assess the size-dependent energetic stabilities of each family. With increasing size our results indicate a progressive change in energetic stability from single-layered to multi-layered cage-like nanoclusters. For nanoparticles of around 2.6 nm diameter we identify a transitional region where multi-layered cages, SOD, and BCT nanostructures are very similar in energetic stability. This transition size also marks the size regime at which bottom-up nanoclusters give way to top-down bulk-cut nanoparticles. Eventually, a final crossover is found where the most stable WZ-ZnO polymorph begins to energetically dominate at $N \sim 2200$. This size corresponds to an approximate nanoparticle diameter of 4.7 nm, in line with experiments reporting the observation of wurtzite crystallinity in isolated ligand-free ZnO nanoparticles of 4–5 nm size or larger.

Received 20th April 2017,
Accepted 25th June 2017

DOI: 10.1039/c7nr02818k

rsc.li/nanoscale

Introduction

Zinc oxide (ZnO) has attracted much attention from both theoretical and experimental researchers largely due to its huge technological potential in fields such as optoelectronics and photocatalysis.[1,2] Although in such applications ZnO is very often used as a nanosized or nanostructured material, the underlying atomic ordering is almost always that of a stable bulk crystal polymorph; either wurtzite (WZ-ZnO) or zinc blende.[3,4] In this sense, the majority of experimentally fabricated nanoscale ZnO structures can be thought of as top-down (*i.e.* reduced size bulk-like) systems. Conversely, many theoretical studies and a few experimental studies of nano-ZnO start from monomeric ZnO or nano-ZnO "building blocks", and investigate how the structures and properties of the growing nano-system vary in a bottom-up manner upon the progressive addition of the respective sub-units. Deposition of ZnO monomers on weakly interacting surfaces, for example, is theoretically predicted to lead to the growth of graphene-like nanoclusters (*i.e.* two-dimensional sheets formed mainly by tessellated Zn_3O_3 hexagonal rings).[5] Other calculations have further indicated that very thin unsupported infinite films of ZnO energetically prefer to form a new non-bulk-like polymorph (layered-ZnO) formed of graphene-like layers.[6] With increasing film thickness other polymorphs (such as the Body Centered Tetragonal phase – BCT-ZnO) are predicted to energetically compete with, and become more stable than, this layered phase, until eventually the bulk WZ-ZnO phase becomes most stable.[7,8] Particular top-down cuts of the WZ-ZnO crystal to form nanoparticles (NPs) and nanowires with high aspect ratios (*e.g.* long thin nanowires or flat wide NPs) are likewise predicted to be unstable to layer formation.[9,10] The thickness dependent transition between layered-ZnO and bulk-like ZnO thin films has been confirmed by detailed bottom-up surface science experiments studying the growth of ZnO on metal surfaces.[11,12]

[a]Departament de Ciència de Materials i Química Física & Institut de Química Teòrica i Computacional (IQTCUB), Universitat de Barcelona, c/ Martí i Franquès 1, 08028 Barcelona, Spain. E-mail: s.bromley@ub.edu
[b]Institució Catalana de Recerca i Estudis Avançats (ICREA), 08010 Barcelona, Spain

†Electronic supplementary information (ESI) available. See DOI: 10.1039/c7nr02818k

Bottom-up theoretical investigations of isolated low energy ZnO nanoclusters have also revealed the propensity of nanoscale ZnO to form graphene-like layers. Specifically, many studies report calculations confirming that the most stable structure of $(ZnO)_N$ nanoclusters in the approximate size range $8 \leq N \leq 28$ is cage-like.[13–21] These clusters can be considered to be formed from finite graphene-like sheets which also contain four-membered Zn_2O_2 rings to facilitate the necessary curvature to form closed single-layered cages. The preference for $(ZnO)_N$ nanoclusters for $8 \leq N \leq 23$ to exhibit cage-like isomers has further been confirmed by collaborative experimental–theoretical cluster beam studies.[22] $(ZnO)_N$ nanoclusters for $28 < N \leq 108$ are predicted to energetically favor either: (i) single-layered cages, or (ii) cages encapsulating smaller nanoclusters. Especially for the larger nanoclusters in this size range, where the interior nanocluster is itself a smaller cage, these species can be viewed as double-layered cages. Double-layered cages were first theoretically proposed as low energy cluster isomers for ZnS.[23,24] Cluster beam experiments finding anomalously high abundances of $(ZnO)_N$ clusters with N = 34, 60, and 78 were also initially taken to be evidence of double-layered cages.[25] Although the most stable isomer of $(ZnO)_{34}$ does not appear to be a double-layered cage,[26] the 12@48 (ref. 16, 21, 27 and 28) and 18@60 (ref. 21) isomers—where we use the notation $X@Y$ to indicate a $(ZnO)_{X+Y}$ cluster constituted by a $(ZnO)_X$ cage encapsulated within a $(ZnO)_Y$ cage—have been shown to be very low energy cluster isomers. It is found that symmetry plays an important role in the stability of single- and double-layered cages. For example, the single-layered $(ZnO)_N$ octahedral cages for N = 12, 48, 108 (T_h symmetry), N = 16, 36, 64, 100 (T_d symmetry), and N = 28 (T symmetry) are all candidate global minima.[21] Similarly, double-layered cages which use these cages and maintain octahedral symmetry (*e.g.* N = 32 (4@28), 60 (12@48), 80 (16@64)) are also found to be very stable.[21] The particularly high energetic stability of these symmetric species has led to them being proposed as building blocks for cluster-assembled ZnO bulk polymorphs.[28–32] Of such materials, sodalite (SOD-ZnO) based on the union of single-layered octahedral $(ZnO)_{12}$ cages is found to be particularly stable (only 0.15 eV per ZnO higher in energy than wurtzite).[29] Based on this stability, symmetric finite assemblies of $(ZnO)_{12}$ cages following the stacking pattern in SOD-ZnO, have also been proposed as alternative global minima structures for $(ZnO)_N$ sizes N = 60, 78, 96.[27] For $(ZnO)_N$ nanoclusters in the size range $108 < N \leq 168$ only double-layer and triple-layer cages have thus far been proposed as potential global minima. We note that the global minimum for the $(ZnO)_{168}$ nanocluster has been proposed to be a triple-layer 12@48@108 cage based on three octahedral nanoclusters.[21]

There have been few attempts to extrapolate from this non-bulk-like nanocluster size regime to WZ-ZnO bulk phase in order to estimate the cluster-to-bulk transition size. Based on comparing the energetic stabilities per ZnO unit of single-layered cages with respect to bulk-like clusters cut from the WZ-ZnO crystal, the cage-to-WZ-ZnO crossover size has been reported by Zhao *et al.* to be >26 units, and by Woodley *et al.* to be between 75 (ref. 33)–120 (ref. 34) ZnO units. As is noted in these studies, these estimates are rather approximate due the fact that that the cluster-to-bulk crossover will not actually be directly from single-layered cages to WZ-ZnO. Using the most extensive set of cage-like clusters thus far reported,[21] extrapolating the cohesive energies per unit of the single-layered cages to infinite size results in a limiting "bulk" cohesive energy that is much lower than that of bulk WZ-ZnO.[21] This clearly indicates that other more stable species are involved in filling the energy gap between single-layered cages and WZ-ZnO with increasing cluster size. From the discussion above, we know that, with increasing size, the stability of single-layered cages will be first superseded by multi-layered cages, and then perhaps by other cluster types at intermediate sizes, before bulk-like WZ-ZnO clusters become the most stable form of ZnO. Taking the energies of double- and triple-layered cages also into account when extrapolating to infinite size leads to a limiting "bulk" cohesive energy which is closer to, but still significantly lower than, that of WZ-ZnO.[21] Even by selecting the few most stable "magic" clusters, containing a small set of single-, double-, and triple-layered cages, the extrapolated cohesive energy limit is still 0.187 eV per ZnO above of that of bulk WZ-ZnO.[21] Tens of metastable bulk polymorphs have been calculated to lie in the energy range <0.19 eV per ZnO relative to WZ-ZnO.[8,29,35,36] The BCT-ZnO and SOD-ZnO low density polymorphs are of particular interest in this respect as they are both particularly low in energy with respect to their density[36] and have thus been studied with respect to being possible targets for stabilization under negative pressure conditions.[37–39] This strongly suggests that nanoclusters based on cuts from such phases will be become energetically competitive with layered cages with increasing nanocluster size, and may provide natural smooth crossover phases from cluster-to-bulk.

In this study we accurately evaluate the energetic stabilities of $(ZnO)_N$ nanoclusters with N = 10–1026 using all electron, relativistic, density functional theory (DFT) based calculations. In this unprecedented size range, in addition to considering bottom-up generated single-, double, and triple-layered cages, we also take top-down cuts from three bulk polymorphs: SOD-ZnO, BCT-ZnO, and WZ-ZnO. By tracking the energetic stability of these species with size we are able to follow the gradual transition from non-bulk-like cage nanoclusters through metastable polymorphic cuts and eventually to bulk WZ-ZnO.

Methodology

All reported nanoclusters and nanoparticles were fully optimized with no symmetry contraints employing all electron, relativistic, density functional theory (DFT) based calculations using the FHI-AIMS code.[40] The electronic density was expanded using a "light-tier-1" basis of numerical atom-centered orbitals (NAO), approximately providing results of a

similar or higher quality to those obtained with valence triple-zeta plus polarization Gaussian type orbitals.[41] In the case of ZnO, recent work has established that the quality of this NAO basis set is even higher than that of the aug-cc-pVDZ,[42] in line with systematic studies of these NAO basis sets.[43] The Perdew–Burke–Ernzerhof (PBE)[44] Generalized Gradient Approximation (GGA) functional was used throughout. Previous studies have confirmed the reliability of GGA functional respect to experimental data for structural, mechanical and energetic properties of ZnO in both bulk[42,45,46] and nanofilms.[8,12] GGA functionals have also been extensively confirmed in their treatment of structure and relative energetics of a wide range ZnO clusters[17] and low density ZnO polymorphs.[35] In all calculations, scalar-relativistic effects were taken into account using the zero order regular approximation (ZORA).[47,48]

Herein, we focus on five families of $(ZnO)_N$ nanostructures of both a bottom-up type: (1) single-layered cages, and (2) multi-layered cages; and those derived from top-down cuts from the respective bulk polymorph: (3) SOD-ZnO, (4) BCT-ZnO, and (5) WZ-ZnO – see Fig. 1. We found that the structures of low energy single-layered $(ZnO)_N$ cages for sizes $N \leq 60$ could be derived using basin hopping global optimization

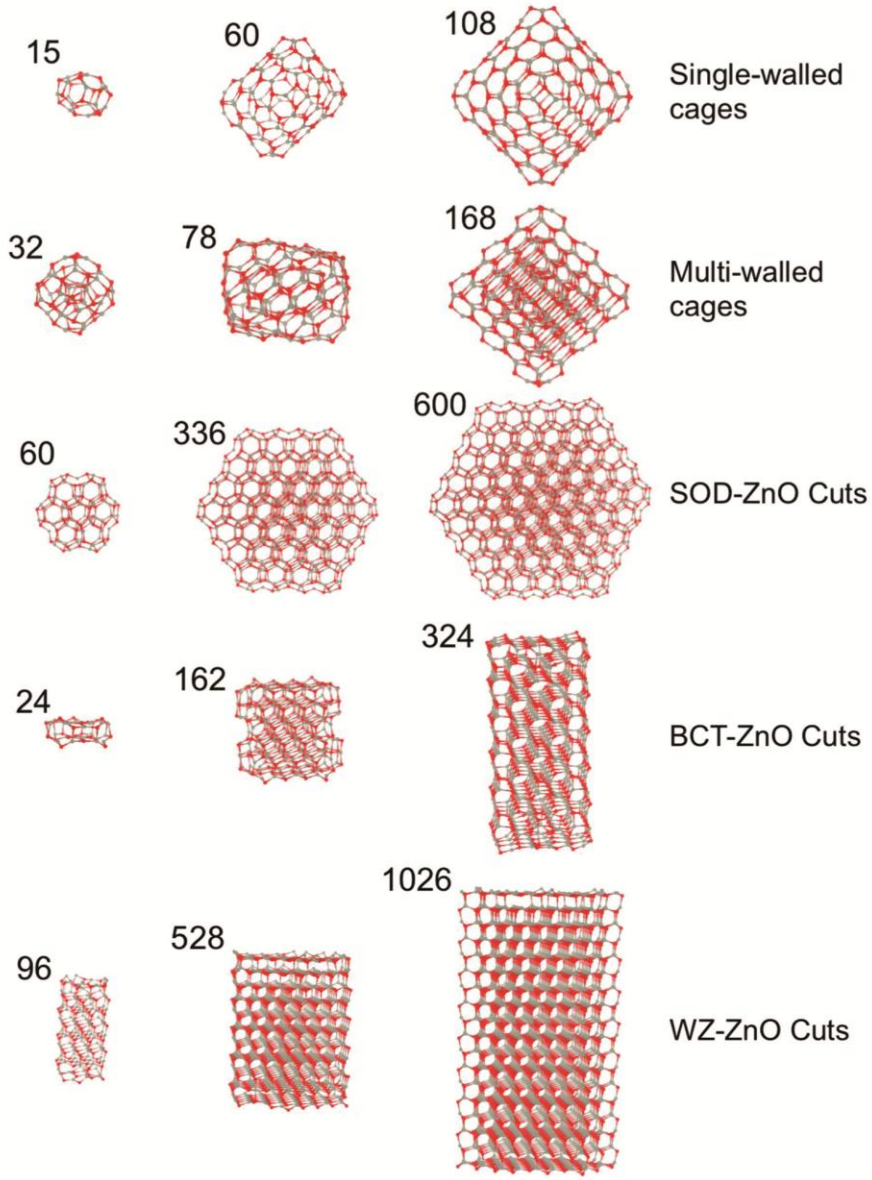

Fig. 1 Examples of different sized $(ZnO)_N$ species from each of the five families of nanostructures considered, where the numbers relate to the number of ZnO units in the corresponding nanostructure. Grey and red spheres denote Zn and O atoms, respectively.

approach[49] together with an interatomic potential parameterized for MgO but with ionic charges chosen to bias the energy landscape towards cages.[29,50] For larger single-layered and multi-layered nanoparticles we employed low energy $(ZnO)_N$ structures from previous works.[21,28] For the $(ZnO)_N$ nanoparticles of SOD-ZnO, we employed a previously reported stable bulk-cut with size N = 60 (ref. 27) and further made seven new larger cuts with N = 162–600. All these latter SOD-ZnO bulk-cuts were created maintaining the low energy symmetric $(ZnO)_{60}$ nanocluster as a core. For both BCT-ZnO and WZ-ZnO we used the Wulff construction to obtain initial geometries for the bulk cuts. Due to the similar hexagonal structure of WZ-ZnO and BCT-ZnO in both cases, the surface stability ordering of WZ-ZnO was employed to build up the Wulff-derived nanoparticles.[51] We note that the (0001) polar facets of the WZ-ZnO nanoparticles formally induce a finite dipole over the nanoparticle. Calculations were thus carried out with both reconstructed (*i.e.* with facet ion vacancies to compensate the dipole) and clean facets. Both pristine and reconstructed polar facets were considered for the WZ-ZnO nanoparticles, as the energy differences between these two scenarios were minor. For BCT-ZnO, $(ZnO)_N$ nanoparticles with up to N = 324 were created. We note that for $(ZnS)_N$ nanoparticles of a similar size, bottom-up computational studies have predicted the emergence of the BCT structure.[24] For WZ-ZnO, the known most stable ZnO polymorph with increasing size, we extended our nanoparticle size range to N = 1026. A selection of $(ZnO)_N$ nanoclusters from each of these five families can found in Fig. 1.

Results and discussion

Properties of nanoclusters evolve as a function of size. Following the spherical cluster approximation,[52] where internal degrees of freedom of the cluster are ignored, one can show that the surface area to "bulk" ratio of a cluster is proportional to $N^{-1/3}$. It is found that many generic properties, $G(N)$, of simple closed-packed clusters (*e.g.* total energies, ionisation energies, melting temperatures) can be approximately fitted by a scaling law of the following type:[51]

$$G(N) = G_{\text{bulk}} + a_1 N^{-1/3}, \quad (1)$$

where G_{bulk} is a characteristic constant value of the property in question for the corresponding bulk phase of the cluster. Taking into account that real clusters are comprised of bonded aggregates of atoms/ions, higher order terms (*i.e.* $a_2(N^{-1/3})^2$, $a_3(N^{-1/3})^3$ ...) can become more significant contributions to $G(N)$.[53] For the case when $G(N)$ is the total (free) energy of the cluster, for example, the second order term can be largely ascribed to compressive effects due to surface stress.[54,55]

In Fig. 2a and b we plot our calculated total energies of a range of $(ZnO)_N$ nanoclusters with respect to $N^{-1/3}$ together

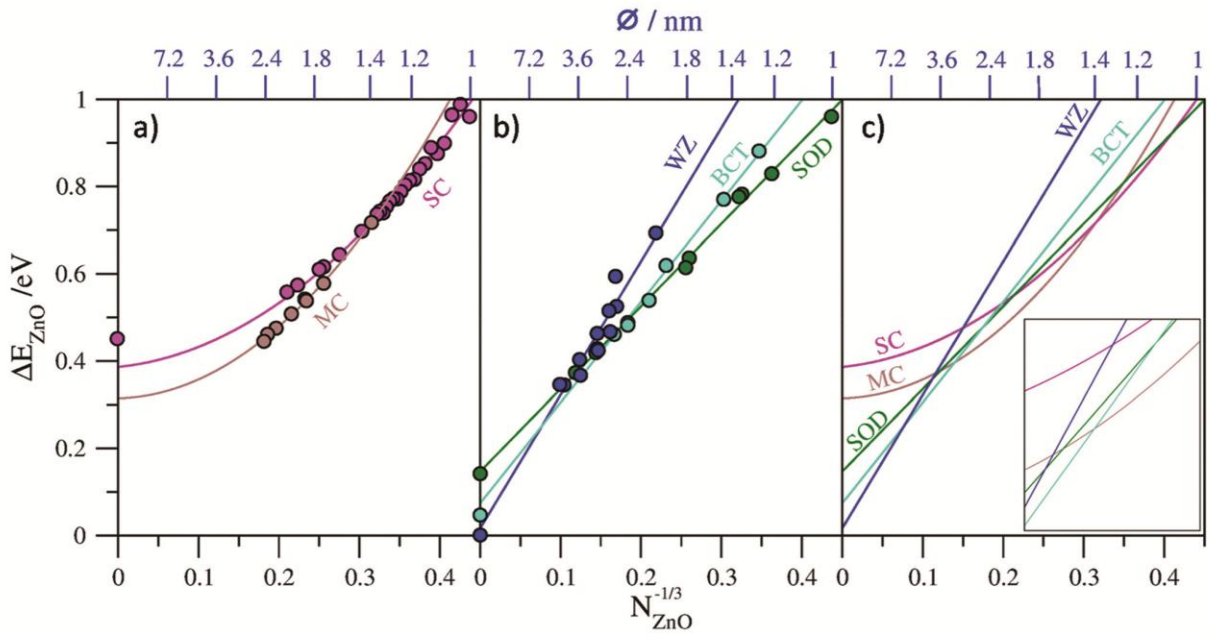

Fig. 2 Plots of calculated relative energies of nanoclusters/nanoparticles and bulk phases with respect to $N^{-1/3}$ (lower x-axes) and approximate diameter (upper x-axes, see main text for details): (a) data for single-layered cages (SC) and multi-layered cages (MC) with corresponding second order fit lines and the calculated energy of an infinite single layer, (b) data for bulk-cut nanoparticles of SOD-ZnO (SOD), BCT-ZnO (BCT), and WZ-ZnO (WZ) phases with corresponding first order fit lines and the calculated energies of the respective bulk phases, (c) collated plot of fit lines for all five families of nanocluster considered.

Table 1 Limiting bulk energies per ZnO unit from extrapolated fits to the calculated size *versus* energy data are reported for first order fits (column 2) and second order fits (column 3). Note: all energies are given with respect to that for bulk WZ-ZnO. The R^2 values for each corresponding fit are given in parentheses. Relative energies for explicit calculations of bulk phases are reported in column 4. The differences in energy between the extrapolated values and the explicit bulk calculations are reported in column 5 with respect to the first and second order fits, respectively

Nanocluster type	Bulk limiting energy from extrapolated first order fit (eV per ZnO)	Bulk limiting energy from extrapolated second order fit (eV per ZnO)	Explicit calculation of bulk energy (eV per ZnO)	Energy differences (eV per ZnO)
WZ-ZnO cuts	0.016 (0.918)	0.155 (0.925)	0.00	+0.016/+0.155
BCT-ZnO cuts	0.074 (0.993)	0.174 (0.995)	0.046	−0.028/+0.128
SOD-ZnO cuts	0.146 (0.996)	0.124 (0.996)	0.129	+0.017/−0.005
Multi-walled cages	0.085 (0.992)	0.314 (0.999)	—	—/—
Single-walled cages	0.113 (0.979)	0.386 (0.987)	0.465	−0.352/−0.079

with lines fitted to the data. In all cases we use the energy per ZnO unit (eV per ZnO) with respect to the calculated total energy per unit of bulk WZ-ZnO as, obviously, obtained from the same computational setup as indicated below. For the top-down bulk-cut nanoclusters we found that a first order linear fit to the data could be made with corresponding coefficients of determination (R^2) of 0.996 for SOD-ZnO, 0.993 for BCT-ZnO, and 0.918 for WZ-ZnO. As a further check we compared the energy corresponding to the extrapolated bulk limit of each fit (*i.e.* for $N^{-1/3} \rightarrow 0$) with the explicitly calculated energy of the respective bulk phase from a periodic calculation using exactly the same level of theory and code as used for the nanoclusters. The comparison between the extrapolated bulk energies and the explicitly calculated bulk energies (see Table 1) shows a very good match, with the differences between these two values being <0.03 eV per ZnO in all cases. We note that although the high R^2 values tend to indicate that these linear fits are formally "good", as shown in Table 1, second order fits also give very similar R^2 values but can also give significantly different limiting energies. For WZ-ZnO and BCT-ZnO, for example, the bulk limiting energies from extrapolated second order fits are >0.125 eV per ZnO higher than the respective explicitly calculated bulk energies. This clearly shows that these fits are not trustworthy as guides to the trends in energetic stability for increasingly larger nanoclusters. For SOD-ZnO we find that both first and second order fits to the nanocluster data give exactly the same R^2 values and respectively extrapolate to slightly above (+0.017 eV per ZnO) and slightly below (−0.005 eV per ZnO) the explicitly calculated bulk energy of SOD-ZnO. Although either fit is physically acceptable, examining the second order fitting equation reveals that it is dominated by the linear first order term. Importantly, this implies that both fit lines are negligibly different over the size range where SOD-ZnO nanoclusters could be energetically competitive with the lowest energy nanoclusters, and thus does not affect our results.

For the bottom-up generated single- and multi-layered nanoclusters, linear fits to the respective data also resulted in high R^2 values (see Table 1). In the case of the single-layered cages we can also take the infinite "bulk" limit to correspond to a flat, infinite in two dimensions, single layer of ZnO. Comparing the explicitly calculated energy of this layer with that obtained from the extrapolated limit of the linear fit results in a large mismatch (−0.352 eV per ZnO), showing that a linear fit is physically inappropriate. Conversely, a second order fit to the single-layered nanocluster energy data gives a very slightly improved R^2 value, but, more significantly, has an extrapolated infinite limiting energy that is relatively close (+0.079 eV per ZnO) to the calculated energy of a single ZnO layer. Considering that single-layered cages are, in a sense, only made from bonded networks of surface atoms, it is perhaps not surprising that higher order terms related to the surface stress contributions to the total energy are required for a physically improved fit.

For the multi-layered cages, unlike in the case of the single-layered cages, size increase does not imply a corresponding overall layer flattening, as, with growth, one retains more and more closed inner layers of ZnO, all concentric around a single point. As such, a limiting infinite onion-like cage is not amenable to calculation *via* periodic DFT calculations and we cannot provide an explicit calculation of the bulk limit in order to guide the physical appropriateness of our fit to the data. First and second order fits to the multi-layered cage data both give high R^2 values but yield very different extrapolated bulk limiting energies of 0.085 eV per ZnO and 0.314 eV per ZnO respectively with respect to WZ-ZnO. Double- and triple-layered cages are clearly energetically preferred over single-layered cages for the largest cage-like nanoclusters sizes we consider, which is understandable due to the attractive interlayer interactions between concentric cages. This strongly implies that the infinite bulk limit of multi-layered cages should be lower in energy than a single infinite layer; a constraint that is satisfied by both fits. We also note that the limiting infinite extrapolations of both fits also yield energies lower than that from the corresponding limit of the second order fit to the single-layer cage data (see Fig. 2a). The set of multi-layered cages we employ only contains a limited number of double- and triple-layered cages and thus does not sample cages with higher numbers of layers. Infinite limiting extrapolations to only these sub-classes of multi-layered cages is complicated by the fact that free-standing bilayers and trilayers of ZnO tend to relax to very weakly interacting planar layers[6,56] which do not capture the stronger distortion-inducing interactions between the layers in multi-layered cages.[28] However, a bulk ZnO polymorph with strongly interacting planar hexagonal layers, known as the 5–5 (ref. 57) or hexagonal[29,37] phase,

hereafter referred to as hex-ZnO, has been shown computationally to be stable. The hex-ZnO phase can be thought of as a limit to which the outer layers of multi-layered particle approach with increasing size. Clearly, however, any such particle will always retain its growing concentric core of closed layers and thus will always be higher in energy than a perfect stacking of interacting planar layers as in hex-ZnO. Consistent with previous reports[8,29] herein we calculate the (bulk) hex-ZnO polymorph to be metastable with respect to WZ-ZnO by 0.14 eV per ZnO, which we thus take as a lower bound for the limiting energy for multi-layered cages. Following the above, the extrapolated infinite limiting energy of any fit to the data for multi-layered ZnO cages should ideally lay between 0.14–0.465 eV per ZnO. As the second order fit is most consistent with this criterion, we consider this fit in the remainder. We note that the set of multi-layered cages, although classed as a single family herein, is unlike the other families considered as it really corresponds to a range of cages of with different shapes and numbers of layers. As such, a higher order fit may be better able to account for this variability (*e.g.* as used to track the energetics of $(TiO_2)_N$ nanoclusters[35]) and yield an even more physically realistic extrapolated value. However, without more criteria to use as a guide, we use the second order fit.

In Fig. 2c we collate all fit lines for the five considered families of nanoclusters in order to provide an approximate guide to the evolution of nanocluster structure/polymorph and energetic stability with respect to size. We note that the nanocluster diameters with respect to $N^{-1/3}$ on the upper *x*-axes in Fig. 2a–c are approximate values which take the diameter of a sphere of N units of ZnO, where the volume occupied by a ZnO unit is taken to be that in bulk WZ-ZnO. Although only providing an approximate estimate of size, this measure is used as it is generally applicable to all nanocluster families. We note also that this approximation is clearly most accurate for the case of spherical WZ-ZnO nanoparticles. For the very smallest nanocluster sizes in the range $12 \leq N \leq 14$ the fit line with the lowest energy appears to imply that the SOD-ZnO polymorphic phase is most stable. This, however, is rather misleading as it really is just a result of the high energetic stability of the N = 12 single-walled sodalite cage which was used in the fit for SOD-ZnO. For $N \geq 15$ the fit line corresponding to the single-layered cages is found to persistently be the lowest in energy up to N = 37, where we find a stability crossover to multi-layered cages. We note that this crossover size corresponds quite well with the size of the first double-layered cage global minimum for N = 32 (*i.e.* 4@28). The fit lines predict that multi-layered cage nanoclusters are the most stable type of nanocluster up to a crossover to BCT-ZnO occurring at N = 364, where the nanocluster diameter is approximately 2.6 nm. In this sense the crossover represents a transition from aperiodic bottom-up nanoclusters to top-down bulk cuts from periodic crystal polymorphs. Interestingly, at this nanocluster size, the fit line for SOD-ZnO nanoclusters comes within 0.014 eV per ZnO of the point of crossover (see inset to Fig. 2c) indicating that SOD-ZnO nanoclusters are energetically competitive around this size. Due to the uncertainty involved in the fits, it could well be that SOD-ZnO nanoclusters in this size regime are the most energetically stable species, or at least potentially realizable metastable species. Previous work has indeed suggested that SOD-ZnO nanoclusters could become more stable that other types of clusters for specific sizes for $N <$ 100.[27] For nanoparticle diameters in the approximate range 2.6–4.7 nm those based on cuts from the BCT-ZnO polymorph are predicted to be the most energetically stable. As noted above, the emergence of the BCT phase has also been predicted to occur in bottom-up modelling studies of ZnO nanofilms[7,8] and in moderately sized $(ZnS)_N$ nanoparticles up to ~4 nm diameter.[24] Experimentally, a reversible phase transition between the BCT-ZnO lattice and WZ-ZnO could be activated in ZnO($10\bar{1}0$) surfaces,[58] further confirming the small energy difference between the two phases. Finally, our fits predict nanoparticles based on cuts from the bulk WZ-ZnO polymorph to be most energetically favored for nanoclusters with $N > 2200$ corresponding to nanoclusters with approximate diameters >4.7 nm. We note that the smallest isolated ligand-free ZnO nanoparticles reported to exhibit the wurtzite crystallographic structure are of typically 4–5 nm diameter,[59,60] consistent with our prediction.

Although our study is not exhaustive with respect to the nanostructure types considered, our selection is based on the most probable low energy structures and polymorphic phases likely to be encountered for nanoscale ZnO based on the current literature. Likewise, although our fits are necessarily based on sets of data points which are limited by current knowledge and computational constraints, our calculations represent the most comprehensively broad collection of DFT-optimised ZnO nanoclusters and nanoparticles yet reported. Moreover, considering that our collection includes all electron, relativistic, DFT calculations of nanoclusters with up to 2052 atoms, our work makes available an accurately calculated dataset for nanoscale ZnO up to an unprecedented size (the full set of calculated data is made available in the ESI†). On the basis of our data, and the fits thereof, our work thus provides the first attempt at a comprehensive description of the size-dependent structural and polymorphic evolution of low energy ZnO species from nanocluster to bulk.

Conclusions

We consider a comprehensive set of all-electron, relativistic, DFT based calculations of five families of ZnO nanoclusters: (A) single-layered nanocages, (B) multi-layered nanocages, (C) SOD-ZnO bulk-cuts, (D) BCT-ZnO bulk cuts, and (E) WZ-ZnO bulk-cuts. Using these data and explicit calculations of relevant bulk phases, we use appropriate fits and their extrapolations to estimate the size-dependent energetic stability of each nanocluster family. Our fits indicate a progressive change in energetic stability of the nanocluster families following the series A → B → (B/C/D) → D → E, where (B/C/D) indicates a region of transition (ø ~ 2.6 nm) where multi-layered cages and bulk-

cuts of both SOD-ZnO and BCT-ZnO are very similar in energetic stability. This transition size also marks the point at which bottom-up clusters give way to top-down bulk-cuts. Eventually, our results indicate a final crossover to cuts from the most stable WZ-ZnO polymorph will occur at about 2200 ZnO units corresponding to an approximate nanoparticle diameter of 4.7 nm, in line with previous experiments reporting wurtzite ZnO for nanoparticles of 4–6 nm size or bigger.[58,59]

Acknowledgements

This research was supported by the Spanish MINECO/FEDER CTQ2015-64618-R grant and, in part, by Generalitat de Catalunya (grants 2014SGR97 and XRQTC) and by the NOMAD Center of Excellence project, which received funding from the European Union's Horizon 2020 research and innovation programme under grant agreement no 676580. O. L. G. is grateful to the Universitat de Barcelona for a predoctoral grant; and F. I. acknowledges additional support from the 2015 ICREA Academia Award for Excellence in University Research. F. V. thanks MINECO for postdoctoral Ramón y Cajal (RyC) research contract (RYC-2012-10129). Computational time at the Marenostrum supercomputer has been provided by the Barcelona Supercomputing Centre through grants from Red Española de Supercomputación and the COMPHOTOCAT project 2014112608 of the Partnership for Advanced Computing in Europe (PRACE).

References

1 A. Janotti and C. G. Van de Walle, *Rep. Prog. Phys.*, 2009, **72**, 126501.
2 C. Klingshirn, *Phys. Status Solidi B*, 2007, **244**, 3027–3073.
3 X. Wang, J. Song and Z. L. Wang, *J. Mater. Chem.*, 2007, **17**, 711–720.
4 Z. L. Wang, *J. Phys.: Condens. Matter*, 2004, **16**, R829–R858.
5 I. Demiroglu, S. M. Woodley, A. A. Sokol and S. T. Bromley, *Nanoscale*, 2014, **6**, 14754–14765.
6 C. L. Freeman, F. Claeyssens, N. L. Allan and J. H. Harding, *Phys. Rev. Lett.*, 2006, **96**, 066102.
7 B. J. Morgan, *Phys. Rev. B: Condens. Matter*, 2009, **80**, 174105.
8 I. Demiroglu and S. T. Bromley, *Phys. Rev. Lett.*, 2013, **110**, 245501.
9 L. Zhang and H. Huang, *Appl. Phys. Lett.*, 2007, **90**, 023115.
10 B. Wen and R. Melnik, *Chem. Phys. Lett.*, 2008, **466**, 84–87.
11 C. Tusche, H. L. Mayerheim and J. Kirschner, *Phys. Rev. Lett.*, 2007, **99**, 026102.
12 G. Weirrum, G. Barcaro, A. Fortunelli, F. Weber, R. Schennach, S. Surnev and F. Netzer, *J. Phys. Chem. C*, 2010, **114**, 15432–15439.
13 E. C. Behrman, R. K. Foehrweiser, J. R. Myers, B. R. French and M. E. Zandler, *Phys. Rev. A*, 1994, **49**, R1543.
14 J. M. Matxain, J. E. Fowler and J. M. Ugalde, *Phys. Rev. A*, 2000, **62**, 053201.
15 A. C. Reber, S. N. Khanna, J. S. Hunjan and M. R. Beltran, *Eur. Phys. J. D*, 2007, **43**, 221–224.
16 M. Zhao, Y. Xia, Z. Tan, X. Liu and L. Mei, *Phys. Lett. A*, 2007, **372**, 39–43.
17 B. Wang, S. Nagase, J. J. Zhao and G. Wang, *J. Phys. Chem. C*, 2007, **111**, 4956–4963.
18 A. A. Al Sunaidi, A. A. Sokol, C. R. A. Catlow and S. M. Woodley, *J. Phys. Chem. C*, 2008, **112**, 18860–18875.
19 I. A. Sarsari, S. J. Hashemifar and H. Salamati, *J. Phys.: Condens. Matter*, 2012, **24**, 505502.
20 G. Malloci, L. Chiodo, A. Rubio and A. Mattoni, *J. Phys. Chem. C*, 2012, **116**, 8741–8746.
21 M. Chen, T. P. Straatsma, Z. Fang and D. Dixon, *J. Phys. Chem. C*, 2016, **120**, 20400–20418.
22 J. Heinzelmann, A. Koop, S. Proch, G. F. Ganteför, R. Łazarski and M. Sierka, *J. Phys. Chem. Lett.*, 2014, **5**, 2642–2648.
23 E. Spano, S. Hamad and C. R. A. Catlow, *J. Phys. Chem. B*, 2003, **107**, 10337–10340.
24 S. Hamad and C. R. A. Catlow, *J. Cryst. Growth*, 2006, **294**, 2–8.
25 A. Dmytruk, I. Dmitruk, I. Blonskyy, R. Belosludov, Y. Kawazoe and A. Kasuya, *Microelectron. J.*, 2009, **40**, 218–220.
26 X. Wang, B. Wang, L. Tang, L. Sai and J. Zhao, *Phys. Lett. A*, 2010, **374**, 850–853.
27 B. Wang, X. Wang and J. Zhao, *J. Phys. Chem. C*, 2010, **114**, 5741–5744.
28 M. R. Farrow, J. Buckeridge, C. R. A. Catlow, A. J. Logsdail, D. O. Scanlon, A. A. Sokol and S. M. Woodley, *Inorganics*, 2014, **2**, 248–263.
29 J. Carrasco, F. Illas and S. T. Bromley, *Phys. Rev. Lett.*, 2007, **99**, 235502.
30 Y. Yong, B. Song and P. He, *J. Phys. Chem. C*, 2011, **115**, 6455–6461.
31 S. M. Woodley, M. B. Watkins, A. A. Sokol, S. A. Shevlin and C. R. A. Catlow, *Phys. Chem. Chem. Phys.*, 2009, **11**, 3176–3185.
32 A. A. Sokol, M. R. Farrow, J. Buckeridge, A. J. Logsdail, C. R. A. Catlow, D. O. Scanlon and S. M. Woodley, *Phys. Chem. Chem. Phys.*, 2014, **16**, 21098–21105.
33 C. R. A. Catlow, S. T. Bromley, S. Hamad, M. Mora-Fonz, A. A. Sokol and S. M. Woodley, *Phys. Chem. Chem. Phys.*, 2010, **12**, 786–811.
34 C. R. A. Catlow, S. A. French, A. A. Sokol, A. A. Al-Sunaidi and S. M. Woodley, *J. Comput. Chem.*, 2008, **29**, 2234–2249.
35 I. Demiroglu, S. Tosoni, F. Illas and S. T. Bromley, *Nanoscale*, 2014, **6**, 1181–1187.
36 M. A. Zwijnenburg, F. Illas and S. T. Bromley, *Phys. Rev. Lett.*, 2010, **104**, 175503.
37 W. Sangthong, J. Limtrakul, F. Illas and S. T. Bromley, *Phys. Chem. Chem. Phys.*, 2010, **12**, 8513–8520.
38 J. Wang, A. J. Kulkarni, M. Zhou, K. Sarasamak and S. Limpijumnong, *Phys. Rev. Lett.*, 2006, **97**, 105502.
39 D. Stradi, F. Illas and S. T. Bromley, *Phys. Rev. Lett.*, 2010, **105**, 045901.

40 V. Blum, R. Gehrke, F. Hanke, P. Havu, V. Havu, X. Ren, K. Reuter and M. Scheffler, *Phys. Commun.*, 2009, **180**, 2175–2196.
41 O. Lamiel-Garcia, K. C. Ko, J. Y. Lee, S. T. Bromley and F. Illas, *J. Chem. Theory Comput.*, 2017, **13**, 1785–1793.
42 F. Viñes and F. Illas, *J. Comput. Chem.*, 2017, **38**, 523–529.
43 I. Y. Zhang, X. Ren, P. Rinke, V. Blum and M. Scheffler, *New J. Phys.*, 2013, **15**, 123033.
44 J. P. Perdew, K. Burke and M. Ernzerhof, *Phys. Rev. Lett.*, 1996, **77**, 3865–3868.
45 M. Kalaya, H. H. Karta, S. Özdemir Karta and T. Çağın, *J. Alloys Compd.*, 2009, **484**, 431–438.
46 M. P. Molepo and D. P. Joubert, *Phys. Rev. B: Condens. Matter*, 2011, **84**, 094110.
47 C. Chang, M. Pelissier and P. Durand, *Phys. Scr.*, 1986, **34**, 394–404.
48 E. van Lenthe, E. J. Baerends and J. G. Snijders, *J. Chem. Phys.*, 1994, **101**, 9783.
49 D. J. Wales and J. P. K. Doye, *J. Phys. Chem.*, 1997, **101**, 5111–5116.
50 C. Roberts and R. L. Johnston, *Phys. Chem. Chem. Phys.*, 2001, **3**, 5024–5034.
51 A. Iglesias-Juez, F. Viñes, O. Lamiel-García, M. Fernández-García and F. Illas, *J. Mater. Chem. A*, 2015, **3**, 8782–8792.
52 R. Johnston, Masters Series in Physics and Astronomy, in *Atomic and Molecular Clusters*, Taylor and Francis, London, 2002.
53 O. Lamiel-Garcia, A. Cuko, M. Calatayud, F. Illas and S. T. Bromley, *Nanoscale*, 2017, **9**, 1049–1058.
54 A. S. Barnard and P. Zapol, *Phys. Rev. B: Condens. Matter*, 2004, **70**, 235403.
55 A. S. Barnard and P. Zapol, *J. Chem. Phys.*, 2004, **121**, 4276.
56 I. Demiroglu and S. T. Bromley, *J. Phys.: Condens. Matter*, 2015, **28**, 224007.
57 J. C. Schön and M. Jansen, *Comput. Mater. Sci.*, 1995, **4**, 43.
58 M.-R. He, R. Yu and J. Zhu, *Angew. Chem., Int. Ed.*, 2012, **51**, 7744.
59 D. Hapiuk, B. Masenelli, K. Masenelli-Varlot, D. Tainoff, O. Boisron, C. Albin and P. Mélinon, *J. Phys. Chem. C*, 2013, **117**, 10220–10227.
60 Y. Liu, D. Wang, Q. Peng, D. Chu, X. Liu and Y. Li, *Inorg. Chem.*, 2011, **50**, 5841.

Overview:

In this chapter DFT calculations where performed to study the stability and properties of different ZnO nanostructures. We found that ZnO nanoparticles with a higher proportion of polar surfaces exposed present a higher photocatalytic activity in the isopropanol photoelimination. Both experiments and theoretical studies indicate that the process is better carried out on polar surfaces, without taking into account the hydration of these polar surfaces. It seems that water can be displaced by the isopropanol without difficulties. Otherwise the high activity is not directly related with the pysicoquemical properties of the surface like defect states, of modification of the band gap, but on the stabilization of the holes generated during the photoexcitation process in the $(000\bar{1})$ surfaces. This fact is very important for all the photodegradation processes of ZnO in its different shapes.

Continuing with the ZnO stability studies presented in this chapter we performed DFT calculations on 5 different families of ZnO structures, the single-layered nanocages (SC), multi-layered nanocages (MC), sodalite based nanoparticles (SOD), body centered tetragonal structures (BCT), wurtzite bulk nanoparticles (WZ) and the respective bulk phases. We could fit the calculated data obtained for the different structures to study the evolution of stability with size, finding interesting changes in the ordering of stabilities. For the smaller size clusters the SC cages are preferred, followed by the MC cages that become more stable when the size increases. When reaching the range of 2.6 nm of nanoparticle diameter we observed very similar energetic stability for MC cages, SOD type structures and BCT structures. At this size the bottom-up clusters give way to the region dominated by top-down nanocrystals. Beyond this point the BCT structure eventually leads to crossover of stability with the wurtzite bulk cuts at about 2200 ZnO units corresponding to nanoparticles of 4.7 nm which is in good agreement with experimental studies that have reported the wurtzite ZnO structure for bare nanoparticles in this range of size.

Chapter 4

Conclusions

4.Conclusions

In this work computational calculations based on DFT methodology have been performed in order to study the TiO_2 and ZnO systems. By analyzing the energetics, electronic structure and geometrical features obtained from these calculations we extracted important information for future development of photocatalytic materials based on ZnO and TiO_2

Regarding studies for bulk TiO_2

The geometric features of the three TiO_2 polymorphs, rutile, anatase, brookite have been shown to be well described by the GGA, GGA+U and hybrid functionals, leading to accurate results of the structural parameters. However the GGA functional fails to well describe the electronic structure of these systems and significantly underestimates the band gap. Hybrid functionals give a reasonably good description of the electronic structure (i.e. closer to the experimental values) but slightly overestimating the band gap. Once the U value is empirically defined, the GGA+U functional can provide a good description of the band gap of the material which is essential for photocatalytical studies.

The effect of fluorine doping on TiO_2 has been studied using the GGA+U methodology previously mentioned. The calculations show that F-doping of all polymorphs is thermodynamically favorable. Regarding the electronic structure of the doped titania polymorphs, the presence of substitutional F atoms leads to Ti^{3+} states that lay in the gap. In the case of rutile and brookite the states lay near the conduction band and do not represent a big modification of the photocatalytic activity. In the case of anatase the states fall in the middle of the band gap, which leads to a reduction of the band gap and possibly increase of the photocatalytic activity.

We performed a study of the effect of modified hybrid functionals on the description of the electronic structure of TiO_2 and reduced TiO_2. The results obtained indicate that modifying the PBE0 functional in a way that it has 12.5% of Fock exchange (PBEx) enables it to reproduce very accurately the experimental values for the band gaps, lattice parameters and thermodynamic energies for the clean bulk systems. In the case of the reduced systems the PBEx functional also describes correctly the systems with oxygen vacancies defects, leading to results that confirm the previously reported experimental

results. This confirms this approach as a suitable methodology to describe TiO_2 systems and will be used in future works.

We continued performing a systematic study of the effect of varying the parameters of the HSE functional on the electronic structure and band gap of a representative set of metal oxides. We found that the band gap obtained from the calculations is linearly dependent with the amount of Fock exchange included in the calculation and the screening parameter has the contrary effect. There is not a unique combination of parameter values that leads to good electronic structure description for all the materials at same time. However, one can use the linear dependence between the amount of Fock exchange and the band gap and the inverse relation between the screening parameter and the band gap in order to find the set of parameters able to describe properly the band gap of any one of these semiconductors accurately.

Regarding the effect of fluorine in the electronic structure of bulk and surfaces of TiO_2: relevance to photocatalytic activity:

We performed DFT based calculations to study the capability of fluorine atoms to diffuse trough the rutile anatase and brookite bulk structures. The diffusion of the fluorine atoms is controlled by the size of the diffusion channels but even more determining is the structural flexibility of the different bulk polymorphs. For anatase the [100] direction was found to present an almost negligible barrier, and the diffusion through this channel is almost thermodynamically favorable. In the case of brookite, the fluorine diffusion is kinetic and thermodynamically unfavorable. Meanwhile for rutile the [110] diffusion is thermodynamically unfavorable but the barrier found is extremely small which indicates that it is kinetically favorable. Thus, the incorporation of fluorine into anatase from the gas phase seems not to be the rate-limiting step of the process.

We also performed periodic density functional theory based calculations with the GGA+U functional in order to study the interaction of fluorine with the anatase TiO_2 (101) and (001) surfaces as function of the coverage, and how this affect to the stability of the mentioned surfaces. In both cases, the adsorption of the fluorine is exothermic and oxidizes the surface of the substrate due to the charge transfer from the nearest oxygen to the F atom. The coverage does not have a strong effect on the adsorption energy and there is only a small reduction of this energy as the coverage increases. The free energy analysis revealed a change in stability as the coverage increases; changing

the order of stability between the [101] and the [001] surfaces. We found that with no F atoms adsorbed the [101] surface is more stable but as the coverage increases the [001] surface become more stable. The results mentioned can explaining the increasing proportion of [001]/[101] surface presented by the nanoparticles when are synthetized in presence of fluorine.

In the same line, the adsorption of the trifluoroacetic acid on anatase surfaces was also studied by mean of DFT calculations. We found that the interaction between the acid and the [101] surface is relatively weak, with almost no distortion of its optimal gas phase geometry. On the other hand the interaction between the trifluoroacetic acid molecule and the [001] surface is much stronger leading to the dissociation of the molecule into trifluoroacetate that is adsorbed on top of the Ti atom and the H atom that is adsorbed on top of the nearest O atom. This explains the stabilization of the [001] surface with respect to the [101] surface found experimentally. These results are useful in order to develop new synthesis methods to improve the photocatalytic activity of TiO_2 nanoparticles.

Regarding TiO_2 clusters and nanoparticles

To study the effect of size and structure on the electronic structure of TiO_2 nanoparticles we performed DFT and TDDFT calculations on a set of bulk like and non-bulk-like nanoparticles. We found that that the electronic structure is more dependent on the structure than the size, especially in the smaller non-bulk-like nanoparticles. In the range of sizes studied in this work, the exciton state is stable in vacuum and with solvent. The electronic structure data obtained shows that the free charge carrier state of the TiO_2 nanoparticles studied here is able to drive photocatalytic water splitting, at least from a thermodynamic point of view. However, for the more stable exciton state, water splitting is only favored when the presence of water is taken into account.

Further research was done to predict at which size the crystalline nanoparticles (top down approach) become more stable than the non-bulk like nanoclusters (bottom up approach). We analyzed a set of nanoclusters in the range of N=1-38 (from global optimization and data-mining) and some nanocrystals up to N=84 modeled following the Wulff construction methodology. From comparing the results obtained from the two

sets we can conclude that in the range of N= 1-38 the nanoclusters are significantly more stable than the correspondingly sized nanocrystals. This points to the fact that using nanocrystals as computational models of large nanoparticles of bulk systems in this range of size can be inaccurate and lead to artifacts. By fitting the data from both sets we could extrapolate that the crossover in stability between the two types of nanostructures would occur at approximately 125 TiO_2 units, which corresponds to a nanoparticle size of 2-2.6 nm.

After finding the crossover of energetic stability between non-bulk like nanoclusters and nanoparticles we continued our research by investigating the system size when the electronic properties of nanocrystals converge to the values of the respective bulk. This research was carried out by calculation the electronic properties and relative stability of a set of nanocrystals in the sizes range between 10 and 455 TiO_2 units exhibiting the [101] and [001] surfaces. The energy per unit decreases with size as expected, for both truncated octahedral nanoparticles and octahedral nanoparticles. The results obtained regarding the electronic gap and the optical gap show how the former gap converges fast with size meanwhile the optical gap remains almost constant as the size of the nanocrystals increases. If we examine the exciton binding energy we can observe that it converges to zero (bulk value) quickly. Taking this into account, and by fitting the data of the binding energies we extrapolate that for nanoparticles with around 15000 TiO_2 units the binding energy will be close enough to the bulk value to expect their electronic properties be almost identical to that of the bulk.

All these results combined represent advances in the knowledge of the behavior of TiO_2 especially as function of size and structure. The studies of the fluorine, and fluoroacetic interaction with TiO_2 can help to design nanoparticles with a desired shape. The studies on nanoclusters and nanoparticles are especially important to know which size is needed in order to have certain properties and thus to improve photocatalytic performance of this material.

Regarding Zinc Oxide (ZnO)

DFT calculations performed to study the electronic structure and stability of ZnO surfaces confirmed the experimental findings that relate the activity in the isopropanol photoelimination process with the exposure of the $(000\bar{1})$ ZnO polar surface. The maximization of the photoelimination activity is reached when maximizing the exposure of these polar surfaces, especially the $(000\bar{1})$ surface. This information is very useful to understand other similar photodegradation processes where ZnO is involved.

Following the study on the stability of ZnO nanostructures, we performed an extensive study of the stability presented by different nanostructures derived from ZnO stable polymorphs and especially stable nanoclusters. The goal of this study is to elucidate the order of stability of the different type of structures as function of their size. The five families of ZnO nanoclusters studied were: (A) single-layered nanocages, (B) multi-layered nanocages, (C) SOD-ZnO bulk-cuts, (D) BCT-ZnO bulk cuts, and (E)WZ-ZnO bulk-cuts. The results obtained show the following evolution: The single layered nanocages are the most stable for the smaller sized structures and as the size increases they become less stable than the multi-layered nanocages. For larger sizes the multilayered nano-cages, the SOD-ZnO bulk-cuts and the BCT-ZnO bulk cuts become almost equally stable in a transition region (ø $\sim$ 2.6 nm). When the size increases further BCT-ZnO bulk cuts become more stable and a finally a crossover to cuts from the most stable WZ-ZnO polymorph will occur at about 2200 ZnO units. This latter size corresponds to approximately 4.7 nm size which is in agreement with 4-6 nm WZ-ZnO nanoparticles previously reported by experiments.

Chapter 5

Contributions to publications

5. Contribution to publications

The results of this thesis are presented as a compendium of nine publications which are co-authored by more than just the author. This chapter describes the contribution of the author of this thesis to each of the publications.

"*Electronic structure of f-doped bulk rutile, anatase, and brookite polymorphs of* TiO_2*.Tosoni, S., Lamiel-Garcia, O., Fernandez Hevia, D., Doña, J. M. & Illas, F. J. Phys. Chem. C****116,*** *12738–12746 (2012)."*

Contribution: Carrying out part of the DFT calculations on TiO_2 bulks and F-doped systems, analyzing the calculated data.

"Performance of a modified hybrid functional in the simultaneous description of stoichiometric and reduced TiO_2 *polymorphs. Ko, K. C., Lamiel-García, O., Lee, J. Y. & Illas, F. Phys. Chem. Chem. Phys.****18,*** *12357–12367 (2016)."*

Contribution: Carrying out part of the DFT calculations and analyzing the calculated data.

"Systematic study of the effect of HSE functional internal parameters on the electronic structure and band gap of a representative set of metal oxides. Viñes, F., Lamiel-Garcia, O., Chul Ko, K., Yong Lee, J. & Illas, F.; J. Comput. Chem. 1–9 (2017)."

Contribution: Carrying out part of the DFT calculations on several systems and analyzing the calculated data.

"Theoretical study of atomic fluorine diffusion through bulk TiO_2 *polymorphs. Tosoni, S., Lamiel-Garcia, O., Fernandez Hevia, D. & Illas, F.; J. Phys. Chem. C****117,*** *5855–5860 (2013)"*

Contribution: Carrying out part of the DFT calculations and analyzing the calculated data.

*"Relative stability of F-covered TiO_2anatase (101) and (001) surfaces from periodic DFT calculations and ab initio atomistic thermodynamics. Lamiel-Garcia, O., Tosoni, S. & Illas, F.; J. Phys. Chem. C**118,** 13667–13673 (2014)."*

Contribution: Carrying out part of the DFT calculations and analyzing the calculated data.

*"Adsorption properties of trifluoroacetic acid on anatase (101) and (001) surfaces: a density functional theory study. Lamiel-Garcia, O., Fernandez-Hevia, D., Caballero, A. C. & Illas, F.; Phys. Chem. Chem. Phys.**17,** 23627–33 (2015)."*

Contribution: Carrying out all the DFT calculations, analyzing the calculated data and writing the theoretical part of the manuscript.

"Effect of Size and Structure on the Ground-State and Excited-State Electronic Structure of TiO_2 Nanoparticles. Cho, D.; Ko, K. C.; Lamiel-Garcia, O.; Bromley, S. T.; Lee, J. Y.; Illas, F.; J. Chem. Theory Comput.12, 3751–3763. (2016)."

Contribution: Providing the structures to study, carrying out part of the DFT calculations and analyzing the calculated data.

*"Predicting size-dependent emergence of crystallinity in nanomaterials: titania nanoclusters versus nanocrystals. Lamiel-Garcia, O., Cuko, A., Calatayud, M., Illas, F. & Bromley, S. T.; Nanoscale**9,** 1049–1058 (2016)."*

Contribution: Providing some of the global optimized nanoclusters and carrying out part of the DFT calculations and analyzing the calculated data.

"When Anatase Nanoparticles Become Bulklike: Properties of Realistic TiO_2 Nanoparticles in the 1–6 nm Size Range from All Electron Relativistic Density Functional Theory Based Calculations. Lamiel-Garcia, O., Ko, K. C., Lee, J. Y., Bromley, S. T. & Illas, F.; J. Chem. Theory Comput.(2017)"

Contribution: Carrying out part of the DFT calculations, analyzing the calculated data and writing the manuscript.

Chapter 6

Resum en català

6.1 Introducció:

En aquesta memòria es presenten els resultats mes rellevants corresponents a la tesis doctoral amb el nom "Desenvolupament de models per nanopartícules de TiO_2 i ZnO en photocatalysis". En la qual s'han estudiat l'estabilitat d'aquests sistemes i les seves propietats electròniques mes rellevants, mitjançant càlculs computacionals basats en el funcional de la densitat.

Durant els últims anys l'òxid de titani (TiO_2) ha guanyat molta rellevància en la comunitat científica degut a les seves grans propietats electròniques molt útils en diferents camps de la ciència. Aquestes s'ha trobat especialment interessant en el camp de la fotocatàlisis i en la interacció d'aquest material amb la llum. En particular algunes de les aplicacions actuals mes destacables son la seva utilització en els processos de purificació d'aire i aigua mitjançant processos fotocatalítics, la seva utilització en la fabricació de materials que es poden netejar per si sols.[77,78]Totes aquestes aplicacions queden completades amb la que per nosaltres resulta la principal motivació per realitzar aquest estudi. La possibilitat que presenta aquest material per aprofitar l'energia solar per tal de transformar-la en energia química capaç de obtindre H_2 i O_2 a partir de l'aigua, sense necessitat d'aplicar una energia extra. Aquest fet obre les portes a la possibilitat d'obtenir H_2 com a combustible a partir de l'aigua de forma neta i respectuosa amb el medi ambient. Per aquest motiu en els últims anys el nombre d'investigacions en aquest camp ha augmentat molt considerablement en els últims anys.

L'origen de l' interès en aquest tipus de materials en el camp de la fotocatàlisis va començar al voltant dels anys 60 quan diversos grups d'investigació que investigaven processos fotoinduits en sòlids (com el TiO_2 i ZnO) van descobrir que certes molècules com l'aigua i l'oxigen s'adsorbien i desorbien de al superfície d'aquests semiconductors. Aquest fenomen va ser explicat anys després per la teoria de la banda d.[1–3] Poc després d'aquests descobriments S. Kato y F Masuo van reportar la primera reacció fotocatalitzada per l'òxid de titani; la oxidació de tetralin en fase liquida irradiat amb llum UV.[4]Aquest resultat va disparar l' interès de la comunitat científica cap a l'òxid de titani. Descobrint en els anys següents diferents reaccions en fase gas basades en l'òxid de titani irradiat amb llum UV.[5–8] Però no va ser fins l'any 1972 quan es va publicar el treball de Fujishima i Honda, on es va donar a conèixer la capacitat de aquest material per poder du a terme la reacció de descomposició fotocatalítica de

l'aigua, quan s'irradiava amb llum UV amb una reducció del corrent aplicat necessari en el procés.[9] Des d'aquell moment i fins l'actualitat s'han realitzat gran nombre d' investigacions enfocades en aquesta capacitat especial que presenta, l'òxid de titani.[10–13,77–80]

Intentant proposar possibles mecanismes de reacció. Estudiant la activitat photocatalitica d'aquest material en diferents fases però sobretot enfocats a com es pot augmentar l'activitat d'aquest material. Ja que per aquest procés necessita de radiació UV i la quantitat de llum d'aquesta longitud d'ona que arriba a la superfície de la terra es escassa. Per aquest motiu es busca modificar l'estructura electrònica del material per tal de reduir-ne el seu *band gap* per tal que pugui aprofitar la llum en l'espectre visible. Per tal de trobar fotocatalitzadors eficients s'han realitzar nombrosos estudis utilitzant, utilitzant semiconductors col·loïdals, barreges binaries d'òxids, nanopartícules metàl·liques suportades sobre òxids, o dopant el sistema amb diferents ions metàl·lics i no metàl·lics.[13,14,79–85]

Aquest mateix fet es pot aplicar al òxid de zinc (ZnO), un altre semiconductor amb propietats electròniques similars a les presentades per l'òxid de titani ja que l' òxid de zinc presenta un *band gap* de 3.4 eV, molt similar al de l'òxid de titani. Les investigacions relacionades amb aquest material que involucren processos fotocatalítics i altre aplicacions tecnològiques han augmentat en els últims anys com el cas dels estudis sobre transistors, fotodetectors, elèctrodes transparents, sensors de gasos i generadors piezoelèctrics.[21–29]

En tots dos casos les aplicacions tecnològiques estan relacionades amb les propietats de l'estructura electrònica del material i per tant un ampli coneixement d'aquesta es necessari per tal d'augmentar l'eficiència d'aquests fotocatalitzadors. Tot i això els detalls de quins factors de l'estructura electrònica del material son necessaris per tal de du a terme aquests processos de forma eficient o els mecanismes d'aquetes reaccions no estan clars i hi ha moltes preguntes que encara no tenen resposta. Com per exemple, perquè certes nanopartícules son mes actives que d'altres? Quines son les característiques que fan un catalitzador mes actiu? Com es pot modificar aquest material per tal de millorar la seva eficiència? Que fa que aquestes nanopartícules tinguin una activitat diferent del *bulk*?

Molts treballs teòrics s'han dut a terme en els últims anys amb l' intenció de respondre a aquetes preguntes, en la majoria d'aquests casos els models utilitzats son models periòdics que assumeixen una simetria infinita perfecte que no es una descripció realista per les nanopartícules. Per sort en els últims anys la capacitat de càlcul i els diversos codis computacionals han millorat exponencialment y en l'actualitat tenim mètodes molt mes sofisticats que poden aplicar-se a models molt mes realistes. Aprofitant això, la idea d' aqueta tesis es combinar els models periòdics i models on s'estudien explícitament nanopartícules de gran mida per tal de clarificar alguns d'aquests punts importants respecte l'estructura electrònica dels sistemes (nano)TiO_2 i (nano)ZnO.

6.2 Metodologia

Els resultats presents en aquesta tesis s'han obtingut mitjançant càlculs basats en la teoria del funcional de la densitat (DFT). Que te origen als anys 20, en el model del gas d'electrons desenvolupat per Thomas i Fermi.[35,36] que posteriorment va ser revisat i millorat per Dirac[86] i Bloch[56] tot i que formalment la metodologia del funcional de la densitat no va aparèixer com a tal fins que Hohenberg i Kohn van enunciar els seus teoremes.[37] Aquests plantegen que l'energia d'un sistema queda determinada per la densitat electrònica del mateix i està relacionada mitjançant un cert potencial extern. i un hamiltonià electrònic i que qualsevol densitat de proba donarà sempre una energia superior a la del estat fonamental. Enunciat d'una altre manera la densitat real del sistema es la que minimitza l'energia del funcional.

Anys mes tard Kohn i Sham[33] van plantejar l'aproximació que consisteix en que un sistema d'electrons interaccionant per un sistema d'electrons sense interacció i que aquesta es pot descriure per un terme de correlació i intercanvi inclòs al funcional. Arribant així a l'expressió del funcional que inclou: L'energia cinètica del sistema, el terme de repulsió coulombica i l'esmentat terme de intercanvi i correlació. A partir d'aquest esquema comú s'han desenvolupat gran nombre de funcionals de diferents tipus. Els LDA[38,39] que calculen el terme d'intercanvi a partir de la densitat, GGA[40–42] que ho calculen a partir del gradient de la densitat y els híbrids[40,41,44] que a mes del esmentat anteriorment contenen una part d'intercanvi Hartree Fock. D'altre banda també hi ha models que inclouen correccions semi-empíriques per tal de millorar la descripció electrònica com es el cas del DFT+U[51]. En el cas d'aquest treball aquestes ultimes metodologies s'han utilitzat per tal d'obtenir una descripció correcta dels estats electrònics del TiO_2 i ZnO ja que aquesta informació es crucial en aquesta investigació.

En el nostre cas s'han realitzat càlculs utilitzant els models periòdics. Els quals utilitzen les ones planes com a funcions de base i pseudopotencials per descriure els electrons interns. També s'han realitzat càlculs de sistemes finits (clústers i nanopartícules) on no eren necessàries les condicions periòdiques. En aquest cas els càlculs s'han realitzat tenint en compte explícitament tots els electrons i utilitzant orbitals atòmics numèrics (NAO) com a funcions de base[53].

Per tal de poder comparar sistemes diferents i veure l'efecte que tenen sobre aquests variables termodinàmiques com composició pressió o temperatura, s'han aplicat la

metodologia *ab initio* thermodynamics[59] als resultats obtinguts dels càlculs DFT aquesta metodologia consisteix en aplicar la termodinàmica estadística per tal de obtindré resultats de la termodinàmica del sistema.

Per tal de dissenyar les nanoestructures utilitzades en els estudis realitzats en aquesta tesis s'han utilitzat dos models teòriques. Per les nanopartícules mes petites que presenten propietats geomètriques no cristal·lines s'ha utilitzat l'aproximació anomenada aproximació *bottom up* on a partir d'algoritmes d'optimització global, concretament el mètode *basin hopping*[57] amb ell s'han trobat alguns dels candidats a estructures mes estables per els sistemes estudiats. D'altre banda per tal de modelitzar les nanopartícules de major mida que ja presenten cristal·linitat similar a la del *bulk* s'ha utilitzat el model de Wulff[58] que està basat en l'idea que les nanopartícules cstital·lines tendiran a exposar una major area de les superfícies mes estables. Seguint aquesta idea un pot construir una nanopartícula que minimitzi d'aquesta manera l'energia superficial de forma que presenti una major estabilitat.

6.3 Resultats:

6.3.1 Estudis del *bulk* de TiO_2

En aquest capítol es mostra un resum dels resultats de l' inici de aquesta tesis. Els primers estudis realitzats estan motivats per la necessitat de trobar un model computacional capaç de descriure l'estructura electrònica de l'òxid de titani sòlid *(bulk).*

Aquest punt es especialment important ja que la capacitat de l'òxid de titani d'absorbir llum esta relacionada directament amb el *band gap* del material i aquest depèn de la seva estructura electrònica. Per aquest motiu s'ha realitzat l'estudi previ del funcionament de diferents funcionals en la descripció de l'estructura electrònica de Rutil, Anatasa i Brookita. Els funcionals utilitzats els podem separar en grups. Els funcionals GGA (PW91 i PBE) GGA+U (PBE+U) híbrids (B3LYP, PBE0 i HSE06).

Tots tres tipus de funcionals descriuen prou correctament les geometries i els paràmetres de *bulk* d'aquests sistemes. Els funcionals que millor ho descriuen son els híbrids seguits dels GGA i per últims els GGA+U. D'altre banda l'estructura electrònica no està ben descrita pels funcionals GGA com era d'esperar. Aquests subestimen de forma considerable el *band gap* en tots els polimorfs de l' òxid de titani, tal com era d'esperar. Aquesta descripció millora al utilitzar els mètodes GGA+U on després d'ajustar els paràmetres semi-empirics del model (U = 6 eV per als orbitals Ti(3d) i O(2p)) els resultats del *band gap* milloren molt considerablement sense un augment del cost computacional. D'altre banda els funcionals híbrids donen valors prou propers al *band gap* del TiO_2 en alguns casos lleugerament superiors als experimentals però en aquest cas si que hi ha un augment del cost computacional important.

A partir dels resultats obtinguts s'ha utilitzat la metodologia DFT+U per tal d'estudiar l'efecte que te el dopatge amb fluor en l'estructura electrònica dels tres polimorfs. Els resultats obtinguts d'aquests càlculs indiquen que els estats electrònics deguts al fluor es situen en tots els casos en la regió del *band gap*. Això combinat amb el fet que la inserció del fluor dins la xarxa cristal·lina del sòlid es termodinàmicament favorable fa que aquest efecte sigui encara molt mes important ja que permet reduir el valor del *band gap* i això permet que el material pugui absorbir llum amb una longitud d'ona propera al visible lo qual es molt interessant per tal d'augmentar el rendiment d'aquest.

Basant-nos en aquests resultats i motivats per trobar una metodologia capaç de descriure correctament l'estructura electrònica del TiO_2 i els estats electrònics deguts a vacants d'oxigen, s'ha realitzat un estudi sobre la descripció que donen els funcionals híbrids modificats de l'estructura electrònica del sòlid i del sòlid reduït.

En aquest estudi s'ha observat una dependència lineal entre el tant per cent d'intercanvi Hartree Fock utilitzat i el valor del *band gap* del material. D'aquesta manera s'ha pogut obtenir un valor d'intercanvi tal que descrigui el *band gap* de forma correcta. Utilitzant un 12.5% d'intercanvi Hartree Fock, els valors obtinguts per al *band gap* de Rutil i Anatasa son 2.91 i 3.02 eV. Aquests valors son molt similars als experimentals que per aquests dos polimorfs son 3.03 i 3.20 eV respectivament. Tanmateix els paràmetres estructurals i energetics com l'entalpia de formació també estan descrits amb menys d'un 2% d'error per l'Anatasa i 4% d'error per al Rutil.

D'aquesta manera hem validat el funcionament d'aquest funcional modificat i establert una metodologia de càlcul capaç de descriure correctament les característiques mes destacables d'aquest sistema. Un cop aconseguit això s'ha realitzat un estudi de l'efecte de les vacants d'oxigen en l'òxid de titani. Els estats electrònics derivats de vacants d'oxigen en el cas del Rutil mostren un comportament raonable. Els estats es troben lleugerament per sota la banda de conducció (~1 eV) lo qual està en concordança amb els resultats trobats a la literatura[87]. En el cas de l'Anatasa els estats es troben també lleugerament per sota de la banda de conducció (~0.5 eV) lo qual també coincideix qualitativament amb els resultats trobats a la literatura.

Motivats per aquests resultats també varem estudiar l'efecte que tenen els paràmetres d'intercanvi i apantallament (*screening*) del funcional HSE en la descripció de l'estructura electrònica i *band gap* d'un ser mes ampli d'òxids metàl·lics (TiO_2, ZrO_2, CuO_2, ZnO, MgO, SnO_2, and $SrTiO_3$). Amb l'esperança de trobar un set de paràmetres tal que permeti descriure al mateix temps els diferents òxids metàl·lics.

En aquest treball s'han variat els valors dels paràmetres d'apantallament i intercanvi de Hartree Fock per tal de veure com afecten en la descripció del *band gap*. Hem observat, que com era d'esperar, una dependència lineal entre valor del *band gap* obtingut al càlcul i la quantitat d'intercanvi de Hartree Fock utilitzada. De la mateixa forma que havíem observat en els treballs anteriors. D'altre manera el paràmetre d'apantallament es comporta de forma contraria. En augmentar el seu valor reduïm el *band gap* obtingut.

Tot i no trobar un set de paràmetres únic que permetin descriure acuradament els diferents òxids esmentats. Si que hem observat que ajustant aquests dos paràmetres podem obtenir un funcional que descrigui amb una bona precisió l'estructura electrònica de qualsevol sistema. Però no hi ha una única combinació que descrigui eficientment tots els sistemes a l'hora.

6.3.2 Efecte del fluor atomic en l'estructura electronica del bulk i superficies de TiO_2: importancia per l'activitat fotocatalitica.

En aquest capítol es resumeixen els resultats obtinguts del estudi de les interaccions entre el fluor i l'òxid de titani. Aquest estudi ha estat motivat per els treballs experimentals previs on s'ha comprovat que en presencia de fluor durant la síntesis de les nanopartícules d'òxid de titani. Aquest millora considerablement la seva eficiència fotocatalítica. Per aquest motiu primerament s'ha estudiat la difusió del fluor dins la xarxa estructural del sòlid. Ja que la difusió del fluor dins l'estructura cristal·lina es un pas clau en el procés de dopatge del TiO_2

S'ha estudiat la difusió del fluor en els diferents canals perpendiculars a les superfícies mes estables d'Anatasa, Rutil i Brookita. Observant que la facilitat del fluor per difondre depèn inicialment de la mida del canal, però no exclusivament, ja que la flexibilitat de l'estructura es clau per tal de permetre la relaxació com a resposta de la presencia del fluor. En el cas de l'Anatasa en la direcció [100] mostra una barrera quasi inexistent i sembla gairebé afavorida termodinàmicament. En el cas de la Brookita, que presenta una estructura mes rígida i compacta, la difusió de fluor esta desafavorida tant cinètica com termodinàmicament. En el cas del Rutil es un punt intermedi entre Anatasa i Brookita. En la direcció [110] la barrera per la difusió es gairebé 0. Però d'altre banda el complex F-TiO_2 està desafavorit termodinàmicament.

Els resultats obtinguts apunten a que la inserció i difusió del Fluor en les estructures cristal·lines no son la etapa limitant del procés de dopatge.

Un cop finalitzat aquest primer estudi vam estudiar com afecta l'adsorció de fluor a l'estabilitat de les superfícies (101) i (001) de l'òxid de titani. Aquest estudi ha estat motivat per els resultats experimentals que apuntaven que, una presencia de fluor durant el procés de síntesis de les nanopartícules modificava la seva geometria. Augmentant l'àrea de la superfície menys estable però mes activa (001) en detriment de l'àrea exposada de la superfície (101).

Per dur a terme aquest estudi es va analitzar l'energia d'adsorció del fluor a totes dues superfícies i com aquesta variava en funció del recobriment. Veient com el fluor s'adsorbeix exotèrmicament en totes dues superfícies i que aquest procés ve acompanyat d'una oxidació del substrat degut a la transferència de carrega cap a l'àtom

de fluor procedent de l'àtom d'oxigen mes proper. Tal com indiquen els anàlisis de la densitat d'spin. L' interacció es entre el fluor y la superfície es mes forta per la superfície (001) lo qual no es sorprenent ja que aquesta superfície es la menys estable i mes reactiva.

Amb aquests resultats s'ha aplicat el formalisme *ab initio thermodynamics* per tal de poder estudiar l'estabilitat de les dues superfícies del recobriment a 298,15K i 1 bar de pressió de F_2. Els resultats obtinguts en aquesta part demostren com segons el recobriment augmenta, l'estabilitat de les dues superfícies s'intercanvia, passant a mostrar una major estabilitat la superfície (001) en front la habitualment mes estable (101).

Degut als resultats obtinguts en l'estudi anterior i tenint en compte els problemes industrials de l' utilització d'àcid fluohidric en la síntesis de nanopartícules hem realitzat un estudi en col·laboració amb un grup experimental per estudiar l'efecte d'una altre molècula amb fluor. Els nostres col·laboradors han observat experimentalment que la presencia d'ácid trifluoroacetic durant la síntesis també modifica la morfologia de les nanopartícules. Per aquest motiu s'ha estudiat l' interacció d'aquesta molècula amb les superfícies (101) i (001) de l'òxid de titani.

Els resultats d'aquest estudi ens indiquen que l' interacció d'aquesta molècula es diferent per a totes dues superfícies. En el cas de la superfície (101) la interacció amb l'àcid es dèbil mantenint una estructura molt similar a la que presenta en fase gas. D'altre banda per la superfície (001) l' energia d'adsorció es considerablement superior. Tant que en el procés d'adsorció l'àcid es dissocia en el trifluoroacetat que s'adsorbeix fortament per els oxígens als àtoms de titani de la superfície i l'àtom d'hidrogen que s'adsorbeix en un àtom d'oxigen proper. Aquesta diferent afinitat per les dues superfícies pot explicar la diferent morfologia presentada per les nanopartícules quan es sintetitzen en presencia d'aquest àcid. Ja que la forta interacció amb la superfície (001) pot impedir el creixement de la superfície (101) augmentant així l'àrea exposada de la superfície amb major activitat fotocatalítica.

6.3.3 Resultats dels clústers i nanopartícules d'òxid de titani

Un cop finalitzats els estudis dels sistemes periòdics estudiats en els capítols anteriors, i degut a que experimentalment l'òxid de titani nanoestructurat acostuma a presentar morfologies diferents a sòlid amb millors propietats fotocatalítiques, Per aquest motiu passem a estudiar-les ja que les propietats que poden presentar poden ser molt diferents a les que presenten els sistemes periòdics a mes aquestes propietats son mes fàcilment relacionables amb els resultats experimentals que acostumen a ser utilitzant pols de TiO_2. Aquests motius han motivat l'estudi de l'estabilitat i propietats electròniques (tant en l' estat fonamental com dels estats excitats). Per dur a terme aquest treball s'han realitzat càlculs DFT i TDDFT de nanopartícules de TiO_2 de diferent mida. En aquest treball s'han estudiat dues famílies de sistemes nanoestructurats. Una família formada per estructures amb uns quants àtoms amb geometries clarament no cristal·lines (que anomenarem nanoclusters) i d'altre banda una família d'estructures amb una mida mes gran que si presenten cristal·linitat (nanopartícules), les primeres han estat obtingudes mitjançant mètodes d'optimització global[57] mentre que les nanopartícules han estat obtingudes mitjançant les construccions de Wulff[58] i tenint en compte les energies superficials de l'Anatasa, ja que es el polimorf mes habitual en les nanopartícules amb major activitat fotocatalítica.

Les nanopartícules de menor mida (en un rang entre 0.5 – 3.2 nm) presenten unes grans diferencies en la seva estructura electrònica entre diferents morfologies d'una mateixa mida, diferencies mes grans que no pas entre diferents mides de nanopartícula. Això pot se degut a la irregularitat en la superfície d'energia potencial que presenten les nanoestructures d'aquesta mida. Obtenint propietats electròniques molt variades entre diferents els diferents isòmers que tanmateix presenten estabilitats molt similars. D'aquesta manera per tal de obtenir una descripció complerta del comportament electrònic de nanopartícules d'aquestes mides caldria fer un estudi molt exhaustiu de diferents isòmers per cada certa mida per tal de poder extrapolar aquestes propietats a sistemes mes grans.

En el rang d'estructures presentades en aquest treball l'energia de lligadura de l'excitó es considerable tant en el els càlculs on s'ha tingut en compte l'efecte del dissolvent (aigua) com en els casos sense dissolvent. Aquest efecte es important en els clústers de mida petita pro canvia en augmentar la mida. D'aquests resultats podem extreure que

per a una certa mida podem esperar un comportament similar al *bulk* quan l'energia de lligadura es gairebé zero. Una altre conclusió important es que els portadors de carrega calculats per aquests clústers son capaços de trencar la molècula d'aigua. Però els sistemes que presenten un excitó mes estable nomes poden dur a terme reacció quan es te en compte l'efecte del dissolvent.

En el següent treball realitzat durant aquesta tesis proporcionem nous candidats a estructura mes estable per els nanoclusters amb mides entre 11 y 38 unitats de TiO_2. Els candidats presentats han resultat ser mes estables que les estructures anteriorment presents a la literatura i estan d'acord amb els tendències mostrades per a mides mes petites. També s'han estudiat estructures cristal·lines que contenen fins a 84 unitats de TiO_2 (252 àtoms) trobant el nanocristall de 38 unitats resulta ser metastable en comparació amb els nanoclusters no cristal·lins. Aquest es un indicatiu que d'utilització de models nanocristal·lins d'aquesta mida pot ser perillós. Els nanocristalls d'aquesta mida i mes petits han demostrat presentar una energia major que les estructures amorfes de la mateixa mida.

Una altre conclusió important que podem extreure d'aquest treball be de l'extrapolació de l'ajust de les energies per les dues famílies d'estructures. L'estabilitat predita per a sistemes mes grans de totes dues famílies indican un creuament d'estabilitat entre nanoclusters i nanocristalls al voltant de 125 unitats (375 àtoms). D'aquesta manera i utilitzant els models de Wulff per una generar un nanocristall d'aquesta mida indiquen que tindria una mida aproximada de 2.6 nm depenent de la morfologia exacta. Aquest es un punt important a conèixer ja que ens indica el punt on les estructures nanocristalines guanyen en estabilitat als clústers amorfs. Això dona una informació molt important de cara a l'elecció de models per estudiar els sistemes de diferent mida.

Un cop trobat aquest punt de canvi d'estabilitat hem continuat l'estudi utilitzant nanocristals de mida superior per tal d'estudiar la tendència de les seves propietats quan augmenta la seva mida per tal de poder predir en quin punt les propietats electròniques d'aquestes nanopartícules convergeixen amb les del sòlid. Per aquest motiu s'han modelitzat diferents nanopartícules amb mides compreses entre 10 unitats de TiO_2 i 455, seguint sempre les construccions de Wulff per al disseny dels nanocristalls. Els resultats obtinguts de l'estudi de l'evolució de l'estructura electrònica i propietats

energètiques de les nanopartícules de TiO_2 amb mida dintre del regim de nanocristalls es resumiran a continuació.

En aquest estudi s'ha observat com les característiques geomètriques, com les distancies Ti-O, coordinació promig d'àtoms de titani i oxigen convergeixen rapidament als valors del *bulk* en augmentar la mida de les nanopartícules (tenint en compte que les coordinacions promig sempre seran menors a la del bulk degut a la menor coordinació dels àtoms superficials. També s'ha demostrat que l'estabilitat de la nanopartícules amb forma d'octaedre i octaedre truncat per les puntes es molt similar en aquest rang. D'altre banda com era d'esperar s'ha observat que l'energia per unitat de TiO_2 dels sistemes estudiats decreix ràpidament en augmentar la mida de les partícules. Observant la dominancia de l'efecte de la mida per damunt del efecte de la morfologia.

D'altre banda la convergència de les propietats electròniques es molt mes lenta que la de l'estabilitat energètica. Mostrant com el gap òptic (HOMO-LUMO) no varia quasi quan augmentem la mida del sistema. Mentre que el gap electrònic convergeix molt mes ràpidament. Això es molt interessant i comporta una reducció de l'energia de lligadura de l'excitó amb la mida del sistema. Això apunta a una convergència de l'estructura electrònica cap a l'estructura electrònica del sòlid amb el mida que ens permet poder predir aproximadament el rang de mida en el que els nanocristalls presentaran propietats com les del sòlid periòdic. Hem estimat que això succeeix aproximadament al voltant de partícules amb 15000 unitats de TiO_2.

6.3.4 Zinc oxide (ZnO)

L'òxid de zinc en la fase wurtzita ha esdevingut un material molt popular degut a les seves propietats tecnològiques (semiconductors, transistors, fotodetectors, etc) a causa de les seves propietats característiques com a semiconductor. El ZnO presenta una energia de lligadura de l'excitó considerablement gran i presenta un *band gap* de 3.4 eV, permetent així l'absorció de llum UV. Aquests factors han motivat l'estudi presentat a continuació sobre l'òxid de zinc.

L'activitat fotocatalítica del ZnO segueix sent un motiu de debat. Les característiques relacionades amb l'activitat no son clares i diversos experiments relacionen l'activitat a factors estructurals. Un gran nombre de morfologies diferents es poden obtenir canviant la metodologia durant el procés de síntesis. Relacionat amb aquest fet s'ha apuntat a que un major ràtio de superfícies polars respecte les altres superfícies no polars mes estables implica una activitat major. Aquests resultats experimentals han motivat una col·laboració amb teòric-experimental per tal d'estudiar l'importància de la superfície de l'òxid de zinc en la seva activitat fotocatalítica comparada amb superfícies no polars mes estables com la $(10\bar{1}0)$ i $(11\bar{2}0)$.

Per dur a terme aquest estudi hem realitzat càlculs basats en el funcional de la densitat per tal d'estudiar la major activitat presentada per les nanopartícules amb major area de superfície polar exposada. Els estudis teòrics i experimentals realitzats indiquen que el procés de la fotoeliminació del isopropanol es du a terme en aquestes superfícies polars. Sembla que l'aigua pot ser desplaçada d'aquesta superfície amb certa facilitat per l'isopropanol facilitant així el procés. D'altre banda l'alta activitat mostrada no sembla estar directament relacionada amb propietats fisicoquimíques de la superfície com podrien ser la presencia de vacants o la modificació del *band gap*, si no que sembla apuntar a que el causant d'aquest augment d'activitat está relacionat amb l'estabilitat dels forats generats Durant el procés de fotoxidació en la superfície polar $(000\bar{1})$. El coneixement d'aquesta dada es de gran importància per altres processos de fotodegradació que involucren el ZnO.

Continuant amb l'estudi de l'òxid de zinc I motivats per la gran varietat de polimorfs estables que presenta aquest material. Com la Wurtzita (WZ) l'estructura tetragonal centrada en el cos (BCT) especialment estable quan l'òxid de zinc es presenta en forma

de capes fines. També per sistemes mes petits s'han trobat alters tipus d'estructures especialment estables com les nanocaixes, tenen una estructura de capes hexagonals que formen una caixa i en alguns casos contenen també una caixa de mida mes petita al seu interior. Ens referirem a aquestes estructures com a caixes d'una sola capa (SC) i caixes de múltiples capes (MC). També cal destacar una estructura cristal·lina anomenada Sodalita (SOD-ZnO) que esta basada en la unió de petites unitats de $Zn_{12}O_{12}$ acoblades unes amb alters.

Per aquest motiu hem realitzat un estudi sistemàtic d'un gran nombre d'estructures de les 5 famílies d'estructures d'òxid de zinc mencionades anteriorment (SC, MC; SOD, BCT WZ). Estudiant-ne la seva estabilitat energètica respecte els seus *bulks*. A partir dels resultats d'estabilitat obtinguts podem ajustar les dades per tal d'obtenir l'evolució de l'ordre d'estabilitat de les diferents estructures. Hem observat que per a la mida mes petita les caixes d'una sola capa (SC) son les mes estables seguides de les caixes de múltiples capes (MC) que es converteixen en les estructures mes estables en augmentar la mida de les partícules. En arribar a mides properes a 2.6 nm observem que les caixes de múltiples capes (MC), les estructures de tipus Sodalita (SOD) i les estructures BCT presenten estabilitats molt similars. En aquest punt les estructures de tipus nanocristalines. Inicialment sent mes estable les estructures tipus BCT per posteriorment cedir el lideratge en estabilitat a les estructures de tipus Wurtzita (WZ). Això succeeix aproximadament al voltant de partícules amb 2200 unitats de ZnO. El que correspon a nanopartícules d' aproximadament 4.7 nm lo qual coincideix amb les estructures experimentals reportades per aquesta mida de partícula.

6.4 Conclusions

En aquest treball s'han realitzat càlculs basats en el funcional de la densitat per tal d'estudiar els sistemes de TiO_2 i ZnO. Mitjançant l'anàlisi de les seves estabilitats energètiques i les característiques de la seva estructura electrònica. D'aquests càlculs hem extret conclusions importants de cara al desenvolupament de materials fotocatalitzadors basats en ZnO i TiO_2.

Algunes conclusions importants extretes dels estudis del *bulk* de TiO_2 es comenten a continuació. Primerament hem observat com els funcionals GGA fallen en descriure l'estructura electrònica d'aquest material i que suposa una millora quan s'aplica la correcció semi-empirica de GGA+U. D'altre banda els funcionals híbrids donen prou bons resultats. Especialment quan es modifica la quantitat d' intercanvi de Hartree Fock utilitzada en el funcional. De manera que hem pogut trobar una metodologia on utilitzant una modificació del funcional PBE0 amb un 12.5% d'intercanvi hem pogut descriure de forma adequada els nostres sistemes.

Un altre fet important es el relacionat de la interacció del fuor amb l'òxid de titani. En cas de que s'utilitzi com a dopant. Aquest causa l'aparició d'alguns estats electrònics en el *band gap* del TiO_2 aconseguint així reduir-lo, provocant que el material pugui absorbir llum mes propera al espectre visible i per tant, augmentant-ne potencialment la seva activitat. També de l'estudi de l'adsorció de fluor i àcid fluoroacetic traiem la conclusió que: En el cas del fluor es capaç de modificar l'estabilitat de les superfícies del òxid de titani. Augmentant així la proporció de la superfície (001) que es mes reactiva. De forma similar succeeix amb l'àcid fluoroacetic. També augmenta la proporció d'aquesta superfície i per tant augmenta l'activitat de les nanopartícules però en aquest cas es degut a la forta interacció que hi ha entre la molècula d'àcid i el TiO_2

En relació a les nanopartícules hem pogut observar l'ordre d'estabilitat entre les partícules cristal·lines i no cristal·lines en un rang que va entre uns pocs àtoms fins mes de 1000. Amb aquests resultants hem pogut deduir el punt on les nanopartícules cristal·lines comencen a ser mes estables que les amorfes i també en quin punt les nanopartícules cristal·lines comencen a presentar un comportament similar al del *bulk*, aproximadament cap als 15000 unitats.

En relació al òxid de zinc hem observat com en el cas de les nanopartícules de Wurtzita utilitzades per la fotodegradació del isopropanol. La seva activitat esta relacionada amb l'àrea de superfície polar exposada per la nanopartícula. De manera que nanopartícules amb major superfície polar presentaran una activitat major I no nomes això si no que aquest fet està mes relacionat amb els factors estructurals que no amb les característiques electròniques d'aquesta superfície en concret.

També gracies al estudi dels diferents polimorfs d'òxid de zinc hem pogut aportar un mapa d'estabilitats que cobreix un rang molt ampli de mides de particular desde uns pocs àtoms fins a milers. D'aquesta manera podem saber quin es el model mes adient en el cas de voler estudiar nanopartícules d'una certa mida. O d'altre banda sabent les propietats d'aquests sistemes podem escollir un mida de particular que doni com a resultat el tipus d'estructura adient.

Chapter 7

Bibliography

7. Bibliography

1. DOERFFLER, W. Heterogeneous photocatalysis I. The influence of oxidizing and reducing gases on the electrical conductivity of dark and illuminated zinc oxide surfaces. *J. Catal.* **3,** 156–170 (1964).

2. Barry, T. I. & Stone, F. S. The Reactions of Oxygen at Dark and Irradiated Zinc Oxide Surface. *Proc. R. Soc. London A Math. Phys. Eng. Sci.* **255,** (1960).

3. Kennedy, D. R., Ritchie, M. & Mackenzie, J. The photosorption of oxygen and nitric oxide on titanium dioxide. *Trans. Faraday Soc.* **54,** 119 (1958).

4. Kato, S. & Mashio, F. Titanium Dioxide-Photocatalyzed Liquid Phase Oxidation of Tetralin. *J. Soc. Chem. Ind. Japan* **67,** 1136–1140 (1964).

5. STEINBACH, F. Photosensitized Oxidation of Carbon Monoxide on Semi-conductors supported on Silver. *Nature* **215,** 152–153 (1967).

6. Tanaka, K. & Blyholder, G. Photocatalytic reaction on zinc oxide. II. Oxidation of carbon monoxide with nitrous oxide and oxygen. *J. Phys. Chem.* **76,** 1807–1814 (1972).

7. Yoneyama, H., Toyoguchi, Y. & Tamura, H. Reduction of methylene blue on illuminated titanium dioxide in methanolic and aqueous solutions. *J. Phys. Chem.* **76,** 3460–3464 (1972).

8. BICKLEY, R. Photoadsorption and photocatalysis at rutile surfaces I. Photoadsorption of oxygen. *J. Catal.* **31,** 389–397 (1973).

9. Fujishima, A. & Honda, K. Electrochemical photolysis of water at a semiconductor electrode. *Nature* **238,** 37–8 (1972).

10. Schrauzer, G. N. & Guth, T. D. Photocatalytic reactions. 1. Photolysis of water and photoreduction of nitrogen on titanium dioxide. *J. Am. Chem. Soc.* **99,** 7189–7193 (1977).

11. HALMANN, M. Photoelectrochemical reduction of aqueous carbon dioxide on p-type gallium phosphide in liquid junction solar cells. *Nature* **275,** 115–116 (1978).

12. Anpo, M. *et al.* Photocatalysis on Native and Platinum-Loaded TiO_2 and ZnO Catalysts —Origin of Different Reactivities on Wet and Dry Metal Oxides—. *Bull. Chem. Soc. Jpn.* **64,** 543–551 (1991).

13. Moser, J. & Graetzel, M. Light-induced electron transfer in colloidal semiconductor dispersions: single vs. dielectronic reduction of acceptors by conduction-band electrons. *J. Am. Chem. Soc.* **105,** 6547–6555 (1983).

14. Anpo, M. Photocatalysis on small particle TiO_2 catalysts. reaction intermediates and reaction mechanisms. *Res. Chem. Intermed.* **11,** 67–106 (1989).

15. Anpo, M., Kawamura, T., Kodama, S., Maruya, K. & Onishi, T. Photocatalysis on titanium-aluminum binary metal oxides: enhancement of the photocatalytic activity of titania species. *J. Phys. Chem.* **92,** 438–440 (1988).

16. Bahnemann, D. W., Kormann, C. & Hoffmann, M. R. Preparation and characterization of quantum size zinc oxide: a detailed spectroscopic study. *J. Phys. Chem.* **91,** 3789–3798 (1987).

17. Kiwi, J. & Graetzel, M. Projection, size factors, and reaction dynamics of colloidal redox catalysts mediating light induced hydrogen evolution from water. *J. Am. Chem. Soc.* **101,** 7214–7217 (1979).

18. Kawai, T. & Sakata, T. Photocatalytic decomposition of gaseous water over TiO_2 and TiO_2—RuO_2 surfaces. *Chem. Phys. Lett.* **72,** 87–89 (1980).

19. Sato, S. & White, J. M. Photoassisted water-gas shift reaction over platinized titanium dioxide catalysts. *J. Am. Chem. Soc.* **102,** 7206–7210 (1980).

20. Demiroglu, I. Effect of Dimensionality and Polymorphism on the properties of ZnO. *TDX (Tesis Dr. en Xarxa)* (2014).

21. Segets, D. *et al.* Experimental and Theoretical Studies of the Colloidal Stability of Nanoparticles−A General Interpretation Based on Stability Maps. *ACS Nano* **5,** 4658–4669 (2011).

22. Durán, P., Capel, F., Tartaj, J. & Moure, C. A Strategic Two-Stage Low-Temperature Thermal Processing Leading to Fully Dense and Fine-Grained Doped-ZnO Varistors. *Adv. Mater.* **14,** 137–141 (2002).

23. Wang, Z. L. & Song, J. Piezoelectric Nanogenerators Based on Zinc Oxide Nanowire Arrays.

24. Rout, C. S., Raju, A. R., Govindaraj, A. & Rao, C. N. R. Hydrogen sensors based on ZnO nanoparticles. *Solid State Commun.* **138,** 136–138 (2006).

25. Colvin, V. L., Schlamp, M. C. & Alivisatos, A. P. Light-emitting diodes made from cadmium selenide nanocrystals and a semiconducting polymer. *Nature* **370,** 354–357 (1994).

26. Bagnall, D. M. *et al.* Optically pumped lasing of ZnO at room temperature. *http://oasc12039.247realmedia.com/RealMedia/ads/click_lx.ads/www.aip.org/pt/adcenter/pdfcover_test/L-37/549665608/x01/AIP-PT/APL_ArticleDL_042617/FYI_HouseBanner_1640x440_v3.jpg/434f71374e315a556e61414141774c75?x* (1998). doi:10.1063/1.118824

27. Bai, Z. *et al.* High sensitivity, fast speed and self-powered ultraviolet photodetectors based on ZnO micro/nanowire networks. *Prog. Nat. Sci. Mater. Int.* **24,** 1–5 (2014).

28. Goldberger, J., Sirbuly, D. J., Law, M. & Yang, P. ZnO Nanowire Transistors. *J. Phys. Chem. B* **109,** 9–14 (2005).

29. Janotti, A. & Van De Walle, C. G. Fundamentals of zinc oxide as a semiconductor. *Rep. Prog. Phys* **72,** 126501–29 (2009).

30. Nakata, K. & Fujishima, A. TiO 2 photocatalysis: Design and applications. *J. Photochem. Photobiol. C Photochem. Rev.* **13,** 169–189 (2012).

31. Leyland, N. S. *et al.* Highly Efficient F, Cu doped TiO_2 anti-bacterial visible light active photocatalytic coatings to combat hospital-acquired infections. *Sci. Rep.* **6,** 24770 (2016).

32. Szabo, A. & Ostlund, N. S. *Modern quantum chemistry : introduction to advanced electronic structure theory*. (Dover Publications, 1996).

33. Kohn, W. & Sham, L. J. Self-Consistent Equations Including Exchange and Correlation Effects. *Phys. Rev.* **140,** A1133–A1138 (1965).

34. Parr, R. G. & Yang, W. *Density-functional theory of atoms and molecules*. (Oxford University Press, 1989).

35. Thomas, L. H. The calculation of atomic fields. *Math. Proc. Cambridge Philos. Soc.* **23,** 542 (1927).

36. Fermi, E. Eine statistische Methode zur Bestimmung einiger Eigenschaften des Atoms und ihre Anwendung auf die Theorie des periodischen Systems der Elemente. *Zeitschrift f*[illegible] *Phys.* **48,** 73–79 (1928).

37. Hohenberg, P. & Kohn, W. Inhomogeneous Electron Gas. *Phys. Rev.* **136,** B864–B871 (1964).

38. Vosko, S. H., Wilk, L. & Nusair, M. Accurate spin-dependent electron liquid correlation energies for local spin density calculations: a critical analysis. *Can. J. Phys.* **58,** 1200–1211 (1980).

39. Cole, L. A. & Perdew, J. P. Calculated electron affinities of the elements. *Phys. Rev. A* **25,** 1265–1271 (1982).

40. Becke, A. D. Density-functional exchange-energy approximation with correct asymptotic behavior. *Phys. Rev. A* **38,** 3098–3100 (1988).

41. Lee, C., Yang, W. & Parr, R. G. Development of the Colle-Salvetti correlation-energy formula into a functional of the electron density. *Phys. Rev. B* **37,** 785–789 (1988).

42. Perdew, J. P. *et al.* Atoms, molecules, solids, and surfaces: Applications of the generalized gradient approximation for exchange and correlation. *Phys. Rev. B* **46,** 6671–6687 (1992).

43. Perdew J. P, B. K. & Ernzerhof, M. Generalized Gradient Approximation Made Simple. *Phys. Rev. Lett.* **77,** 3865–3868 (1996).

44. Perdew, J. P., Ernzerhof, M. & Burke, K. Rationale for mixing exact exchange with density functional approximations. *http://oasc12039.247realmedia.com/RealMedia/ads/click_lx.ads/www.aip.org/pt/adcenter/pdfcover_test/L-37/20939943/x01/AIP-PT/JCP_ArticleDL_0117/PTBG_orange_1640x440.jpg/434f71374e315a556e61414141774c75?x* (1998). doi:10.1063/1.472933

45. Hubbard, J. Electron Correlations in Narrow Energy Bands. *Proc. R. Soc. London A Math. Phys. Eng. Sci.* **276,** (1963).

46. Hubbard, J. Electron Correlations in Narrow Energy Bands. II. The Degenerate Band Case. *Proc. R. Soc. London A Math. Phys. Eng. Sci.* **277,** (1964).

47. Hubbard, J. Electron Correlations in Narrow Energy Bands. III. An Improved Solution. *Proc. R. Soc. London A Math. Phys. Eng. Sci.* **281,** (1964).

48. Hubbard, J. Electron Correlations in Narrow Energy Bands. IV. The Atomic Representation. *Proc. R. Soc. London A Math. Phys. Eng. Sci.* **285,** (1965).

49. Hubbard, J. Electron Correlations in Narrow Energy Bands. V. A Perturbation Expansion About the Atomic Limit. *Proc. R. Soc. London A Math. Phys. Eng. Sci.* **296,** (1967).

50. Hubbard, J. Electron Correlations in Narrow Energy Bands. VI. The Connexion with Many-Body Perturbation Theory. *Proc. R. Soc. London A Math. Phys. Eng. Sci.* **296,** (1967).

51. Dudarev, S. L., Botton, G. A., Savrasov, S. Y., Humphreys, C. J. & Sutton, A. P. Electron-energy-loss spectra and the structural stability of nickel oxide: An LSDA+U study. *Phys. Rev. B* **57,** 1505–1509 (1998).

52. Slater, J. C. Atomic Shielding Constants. *Phys. Rev.* **36,** 57–64 (1930).

53. Blum, V. *et al.* Ab initio molecular simulations with numeric atom-centered orbitals. *Comput. Phys. Commun.* **180,** 2175–2196 (2009).

54. Hamann, D. R., Schlüter, M. & Chiang, C. Norm-Conserving Pseudopotentials. *Phys. Rev. Lett.* **43,** 1494–1497 (1979).

55. Blöchl, P. E. *Projector augmented-wave method*. *Physical Review B* **50,** 17953–17979 (American Physical Society, 1994).

56. Bloch, F. Über die Quantenmechanik der Elektronen in Kristallgittern. *Zeitschrift für Phys.* **52,** 555–600 (1929).

57. Wales, D. J. & Doye, J. P. K. Global Optimization by Basin-Hopping and the Lowest Energy Structures of Lennard-Jones Clusters Containing up to 110 Atoms.

58. Wulff, G. XXV. Zur Frage der Geschwindigkeit des Wachsthums und der Auflösung der Krystallflächen. *Zeitschrift für Krist. - Cryst. Mater.* **34,** 449–530 (1901).

59. Reuter, K. & Scheffler, M. First-Principles Atomistic Thermodynamics for Oxidation Catalysis: Surface Phase Diagrams and Catalytically Interesting Regions. *Phys. Rev. Lett.* **90,** 46103 (2003).

60. Bromley, S. T., Moreira, I. D. P. R., Neyman, K. M. & Illas, F. Approaching nanoscale oxides: models and theoretical methods. *Chem. Soc. Rev.* **38,** 2657–2670 (2009).

61. de P. R. Moreira, I., Illas, F. & Martin, R. L. Effect of Fock exchange on the electronic structure and magnetic coupling in NiO. *Phys. Rev. B* **65,** 155102 (2002).

62. Jimmy C. Yu, *,†, Jiaguo Yu, †,‡, Wingkei Ho, †, Zitao Jiang, † and & Zhang†, L. Effects of F- Doping on the Photocatalytic Activity and Microstructures of Nanocrystalline TiO_2 Powders. (2002). doi:10.1021/CM020027C

63. Di Valentin, C. & Pacchioni, G. Trends in non-metal doping of anatase TiO_2: B, C, N and F. *Catal. Today* **206,** 12–18 (2013).

64. Harb, M., Sautet, P. & Raybaud, P. Anionic or Cationic S ‑ Doping in Bulk Anatase TiO$_2$: Insights on Optical Absorption from First Principles Calculations. *J. Phys. Chem. C* **117,** 8892–8902 (2013).

65. Deng, Q., Han, X., Gao, Y. & Shao, G. Remarkable optical red shift and extremely high optical absorption coefficient of V-Ga co-doped TiO 2. *J. Appl. Phys.* **112,** 13523 (2012).

66. Asahi, R., Morikawa, T., Ohwaki, T., Aoki, K. & Taga, Y. Visible-Light Photocatalysis in Nitrogen-Doped Titanium Oxides. *Science (80-.).* **293,** 269–271 (2001).

67. Han, X., Kuang, Q., Jin, M., Xie, Z. & Zheng, L. Synthesis of titania nanosheets with a high percentage of exposed (001) facets and related photocatalytic properties. *J. Am. Chem. Soc.* **131,** 3152–3153 (2009).

68. Lamiel-Garcia, O., Tosoni, S. & Illas, F. Relative stability of F-covered TiO_2 anatase (101) and (001) surfaces from periodic DFT calculations and ab initio atomistic thermodynamics. *J. Phys. Chem. C* **118,** 13667–13673 (2014).

69. Calatayud, D. G. *et al.* Highly photoactive anatase nanoparticles obtained using trifluoroacetic acid as an electron scavenger and morphological control agent. *J. Mater. Chem. A* **1,** 14358 (2013).

70. French, S. A. *et al.* From CO2 to Methanol by Hybrid QM/MM Embedding This work was supported by EU Esprit IV project 25047. S.A.F. is grateful to ICI and Synetix for funding. K. Waugh, L. Whitmore, S. Cristol, and P. Sushko are thanked for their helpful insights. QM/MM=quantum. *Angew. Chemie Int. Ed.* **40,** 4437 (2001).

71. Kurtz, M. *et al.* Active Sites on Oxide Surfaces: ZnO-Catalyzed Synthesis of Methanol from CO and H_2. *Angew. Chemie Int. Ed.* **44,** 2790–2794 (2005).

72. Meyer, B. *et al.* Partial Dissociation of Water Leads to Stable Superstructures on the Surface of Zinc Oxide. *Angew. Chemie Int. Ed.* **43,** 6641–6645 (2004).

73. Nieuwenhuizen, P. J. Zinc accelerator complexes. *Appl. Catal. A Gen.* **207,** 55–68 (2001).

74. Rodriguez*, J. A. & Maiti, A. Adsorption and Decomposition of H2S on MgO(100), NiMgO(100), and ZnO(0001) Surfaces: A First-Principles Density Functional Study. (2000). doi:10.1021/JP000011E

75. Polarz, S. *et al.* On the Role of Oxygen Defects in the Catalytic Performance of Zinc Oxide. *Angew. Chemie Int. Ed.* **45,** 2965–2969 (2006).

76. Maeda, K. & Domen, K. Solid Solution of GaN and ZnO as a Stable

Photocatalyst for Overall Water Splitting under Visible Light ? *Chem. Mater.* **22,** 612–623 (2010).

77. Mills, A. & Le Hunte, S. An overview of semiconductor photocatalysis. *J. Photochem. Photobiol. A Chem.* **108,** 1–35 (1997).

78. Linsebigler, A. L. *et al.* Photocatalysis on TiO_2 Surfaces: Principles, Mechanisms, and Selected Results. *Chem. Rev.* **95,** 735–758 (1995).

79. Grätzel, M. *Energy resources through photochemistry and catalysis*. (Academic Press, 1983).

80. Nenadovic, M. T., Rajh, T. & Micic, O. I. Size quantization in small semiconductor particles. *J. Phys. Chem.* **89,** 397–399 (1985).

81. Reiche, H. & Bard, A. J. Heterogeneous photosynthetic production of amino acids from methane- ammonia-water at platinum/titanium dioxide. Implications in chemical evolution. *J. Am. Chem. Soc* **101,** 3127–3128 (1979).

82. Yoneyama, H., Koizumi, M. & Tamura, H. Photolysis of Water on Illuminated Strontium Titanium Trioxide. *Bull. Chem. Soc. Jpn.* **52,** 3449–3450 (1979).

83. Kiwi, J., Borgarello, E., Pelizzetti, E., Visca, M. & Grätzel, M. Cyclic Water Cleavage by Visible Light: Drastic Improvement of Yield of H2 and O2 with Bifunctional Redox Catalysts. *Angew. Chemie Int. Ed. English* **19,** 646–648 (1980).

84. Heller, A., Aharon-Shalom, E., Bonner, W. A. & Miller, B. Hydrogen-evolving semiconductor photocathodes: nature of the junction and function of the platinum group metal catalyst. *J. Am. Chem. Soc.* **104,** 6942–6948 (1982).

85. Borgarello, E., Kiwi, J., Graetzel, M., Pelizzetti, E. & Visca, M. Visible light induced water cleavage in colloidal solutions of chromium-doped titanium dioxide particles. *J. Am. Chem. Soc.* **104,** 2996–3002 (1982).

86. Dirac, P. A. M. The Quantum Theory of the Electron. *Proc. R. Soc. London A Math. Phys. Eng. Sci.* **117,** (1928).

87. Gerosa, M., Di Valentin, C., Onida, G., Bottani, C. E. & Pacchioni, G. Anisotropic Effects of Oxygen Vacancies on Electrochromic Properties and Conductivity of γ-Monoclinic WO_3. *J. Phys. Chem. C* **120,** 11716–11726 (2016).